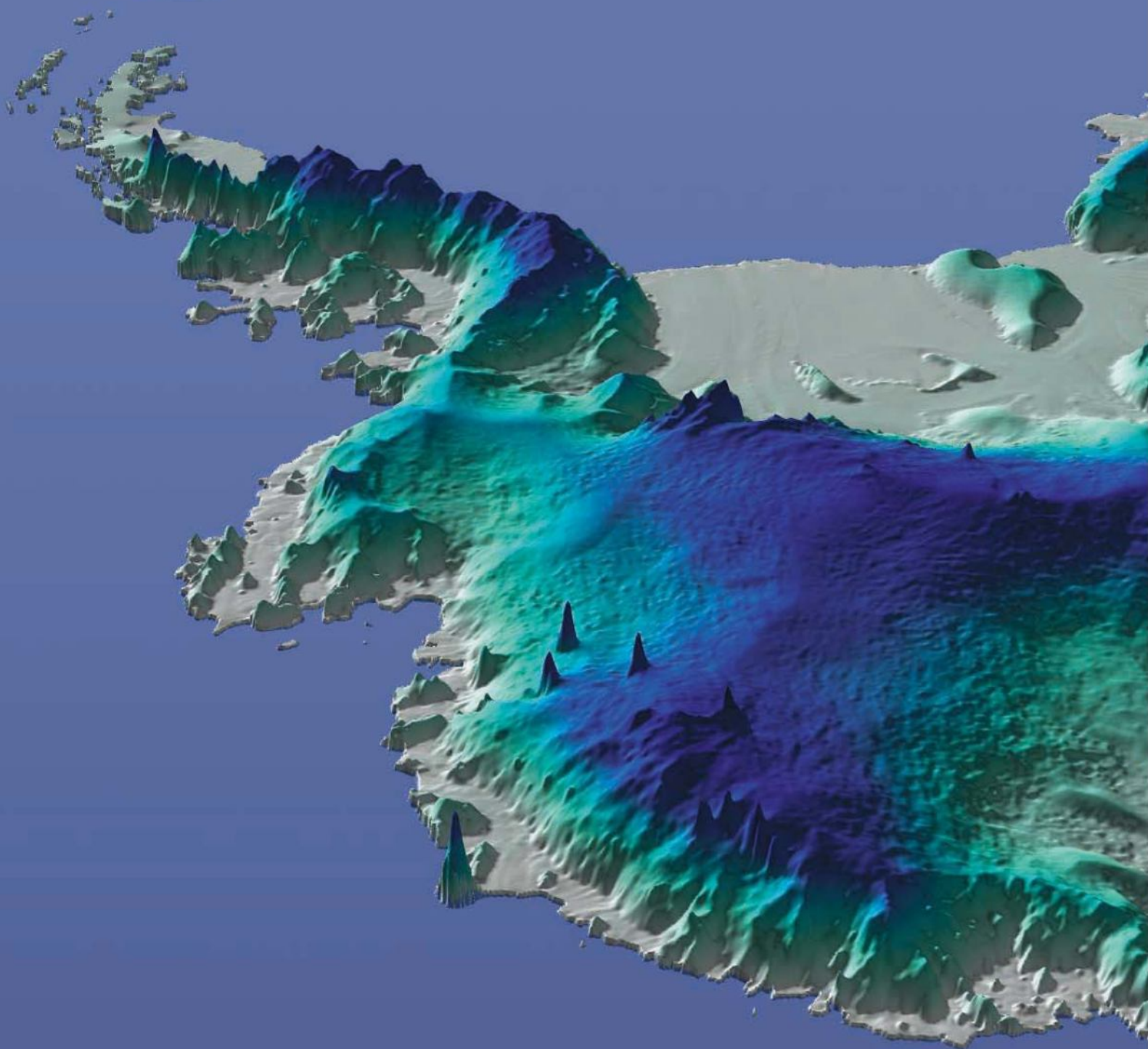
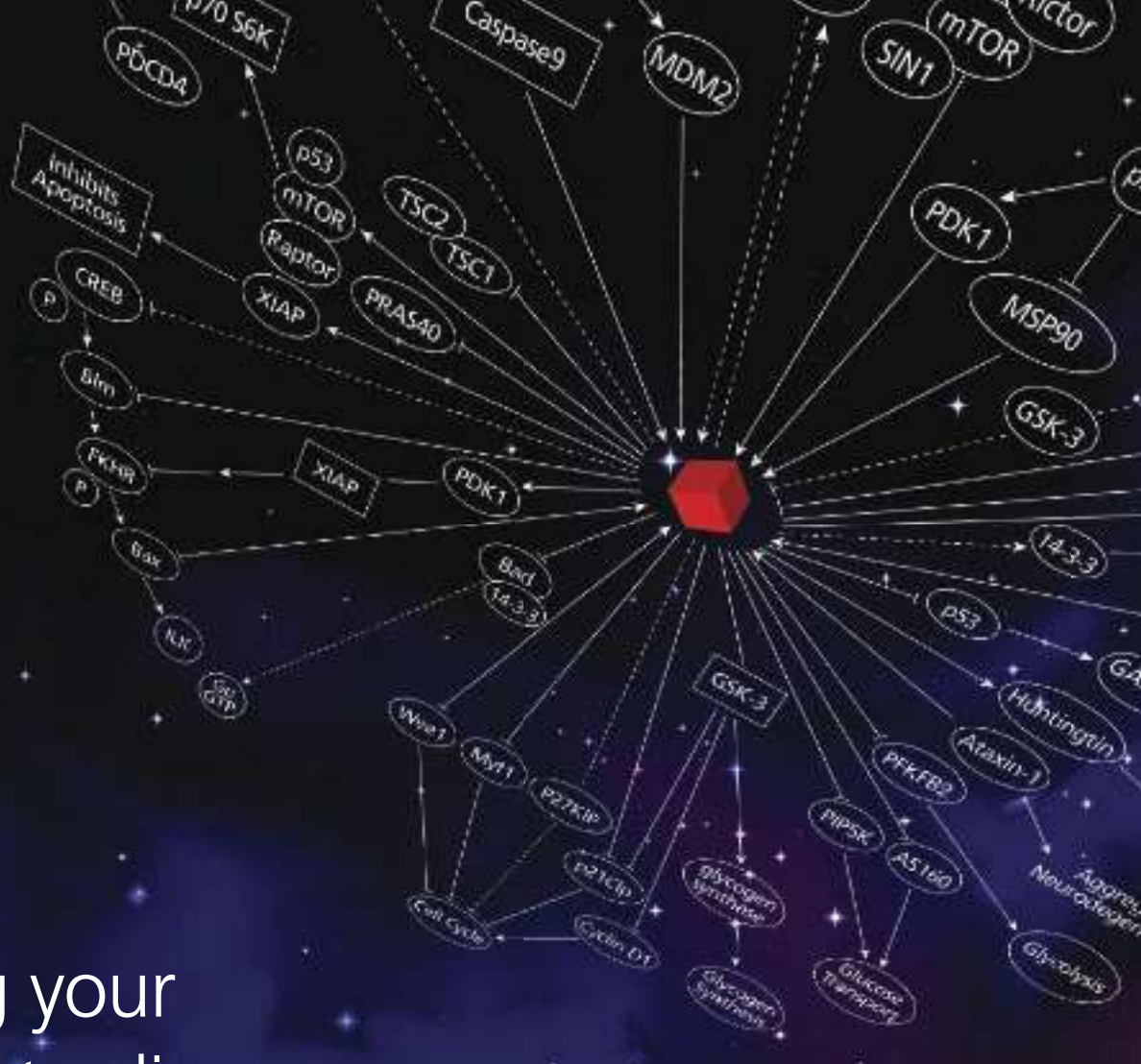


15 May 2009 | \$10

Science





Mapping your pathway to discovery.

Move beyond the boundaries of the known. Built on the solid Sigma foundation of quality and reliability, our cell biology portfolio is backed by a universe of experience, knowledge and biological data.

- 16,000+ Antibodies
- Highly Validated Prestige Antibodies® Powered by Atlas Antibodies
- New Precisio™ Active Human Kinases
- 3,000+ Bioactive Small Molecules
- LOPAC® Libraries of Pharmacologically Active Compounds
- Navigate by Gene, Disease, Tissue or Pathway via Your Favorite Gene powered by Ingenuity



For a closer look at cell biology content you can count on visit
sigma.com/cellbiology



Our Innovation, Your Research — Shaping the Future of Life Science

Precisio is a trademark of Sigma-Aldrich Biotechnology LP and Sigma-Aldrich Co.
LOPAC and Prestige Antibodies are registered trademarks of Sigma-Aldrich Biotechnology LP and Sigma-Aldrich Co.



cell sciences®

www.CytokineCenter.com

Cytokine Center

Browse our web site with over 1300 proteins, including recombinant cytokines, growth factors, chemokines and neurotrophins. Daily shipping and competitive pricing are offered. Bulk quantities of many proteins available.



PROTEINS

4-1BBL
4-1BB Receptor
6 Ckine
ACAD8
ACAT2
gAcrp30/Adipolean
Activin A
Activin B
ACY1
ADAT1
Adiponectin
ADRP
AITRL
Akt1
Alpha-Feto Protein (AFP)
Alpha-Galactosidase A
Angiopoietin-1 (Ang-1)
Angiopoietin-2 (Ang-2)
Angiostatin K1-3
Annexin-V
apo-SAA
Apolipoprotein A-1
Apolipoprotein E2
Apolipoprotein E3
Apolipoprotein E4
APRIL
Artemin
ATF2
Aurora A
Aurora B
BAFF
BAFF Receptor
BCA-1 / BLC / CXCL13
BCMA
BD-1
BD-2
BD-3
BDNF
Betacellulin
Bivalirudin
BMP-2
BMP-4
BMP-6
BMP-7
BMP-13
sBMPR-1A
Brain Natriuretic Protein
BRAK
Breast Tumor Antigen
C5a
C5L2 Peptide
C-10
C-Reactive Protein
C-Src
Calbindin D-9K
Calbindin D-28K
Calbindin D-29K
Calmodulin
Calcitonin Acetate
Carbonic Anhydrase III
Carcino-embryonic Antigen
Cardiotrophin-1
Caspase-3
Caspase-6
CD4
CD14
CD22
CD40 Ligand / TRAP

CD95 / sFas Ligand
CD105 / Endoglin
CHIPS
CNTF
Collagen
CREB
CTACK / CCL27
CTGF
CTGFL / WISP-2
CTLA-4 / Fc
CXCL16
CYR61
Cytokeratin 8
DEP-1
Desmopressin
Disulfide Oxidoreductase
E-selectin
ECGF
EGF
Elafin / SKALP
EMAP-II
ENA-78 / CXCL5
Endostatin
Enteropeptidase
Eotaxin / CCL11
Eotaxin-2
Eotaxin-3 (TSC)
EPHB2
EPHB4
Epigen
Epiregulin
Eptifibatide
Erk-2
Erythropoietin (EPO)
Exodus-2
Fas Ligand
Fas Receptor
FGF-1 (acidic)
FGF-2 (basic)
FGF-4
FGF-5
FGF-6
FGF-7 / KGF
FGF-8
FGF-9
FGF-10
FGF-16
FGF-17
FGF-18
FGF-19
FGF-20
sFGFR-1 (IIIc) / Fc Chimera
sFGFR-2 (IIIc) / Fc Chimera
sFGFR-3 / Fc Chimera
sFGFR-4 / Fc Chimera
sFlt-1 (native)
sFlt-1 (D3)
sFlt-1 (D4)
sFlt-1 (D5)
sFlt-1 (D7)
Flt3-Ligand
sFlt-4
sFlt-4 / Fc Chimera
Follistatin
FSH
Fractalkine / CX3C
G-CSF
 α -Galactosidase A
Galectin-1

Galectin-3
Gastrointestinal CA
GCP-2
GDF-3
GDF-9
GDF-11
GDNF
GLP-1
Glucagon
GM-CSF
Goserelin
GPBB
Granzyme B
GRO α
GRO β
GRO γ
GRO/MGSA
Growth Hormone
Growth Hormone BP
GST-p21/WAF-1
HB-EGF
HCC-1
HGF
Histidyl-tRNA synthetase
Histrelin
HRG1- β 1
I-309
I-TAC
IFN- α
IFN- α A
IFN- α 2a
IFN- α 2b
IFN- β
IFN- γ
IFN-Omega
IGF-I
IGF-II
proIGF-II
IGFBP-1
IGFBP-2
IGFBP-3
IGFBP-4
IGFBP-5
IGFBP-6
IGFBP-7
IL-1 α
IL-1 β
IL-2
IL-3
IL-4
sIL-4 Receptor
IL-5
IL-6
sIL-6 Receptor
IL-7
IL-8 (72 a.a.)
IL-8 (77 a.a.)
IL-9
IL-10
IL-11
IL-12
IL-13
IL-13 analog
IL-15
IL-16 (121 a.a.)
IL-16 (130 a.a.)
IL-17
IL-17B
IL-17D

IL-17E
IL-17F
IL-19
IL-20
IL-21
IL-22
IL-31
Insulin
IP-10
JE
JNK2a1
JNK2a2
KC / CXCL1
KGF
L-asparaginase
LAG-1
LALF Peptide
LAR-PTP
LBP
LC-1
LD-78 β
LDH
LEC / NCC-4
Leptin
LIGHT
LIX
LKM
LL-37
Lungkine / CXCL15
Lymphotactin
sLYVE-1
M-CSF
MCP-1 (MCAF)
MCP-2
MCP-3
MCP-4
MCP-5
MDC (67 a.a.)
MDC (69 a.a.)
MDH
MEC
Mek-1
MIA
Midkine
MIG / CXCL9
MIP-1 α / CCL3
MIP-1 β / CCL4
MIP-3 / CCL23
MIP-3 α / CCL20
MIP-3 β / CCL19
MIP-4 (PARC) / CCL18
MIP-5 / CCL15
MMP-3
MMP-7
MMP-13
Myostatin
Nanog
NAP-2
Neurturin
NFAT-1
 β -NGF
NOGGIN
NOV
NP-1
NT-1/BCSF-3
NT-3
NT-4
Ocreotide
Oncostatin M
Osteoprotegerin (OPG)
OTOR
Oxytocin
p38- α
PAI-1
Parathyroid Hormone
PDGF-AA
PDGF-AB
PDGF-BB
PDGF-CC
Persephin
PF-4
PIGF-1

PIGF-2
PKA α -subunit
PKC- α
PKC- γ
Pleiotrophin
PLGF-1
Polymyxin B (PMB)
PRAS40
PRL-1
PRL-2
PRL-3
Prokineticin-2
Prolactin
Protirelin
PTHrP
PTP1B
PTP-IA2
PTP-MEG2
PTP-PEST
sRANK
sRANKL
RANTES
RELM- α
RELM- β
Resistin
RPTP β
RPTP γ
RPTP μ
SCF
SCGF- α
SCGF- β
SDF-1 α
SDF-1 β
Secretin
SF20
SHP-2
STAT1
c-Src
TACI
TARC
TC-PTP
TECK
TFF2
TGF- α
TGF- β 1
TGF- β 2
TGF- β 3
Thymosin α 1
sTIE-1/Fc Chimera
sTIE-2/Fc Chimera
TL-1A
TNF- α
TNF- β
sTNF-receptor Type I
sTNF-receptor Type II
TPO
sTRAIL R-1 (DR4)
sTRAIL R-2 (DR5)
TRAIL/Apo2L
TSG
TSH
TSLP
TWEAK
TWEAK Receptor
Urokinase
EG-VEGF
VEGF121
VEGF145
VEGF165
VEGF-C
VEGF-C 1125
VEGF-E
HB-VEGF-E
sVEGFR-1
sVEGFR-2
sVEGFR-3
Visfatin
WISP-1
WISP-2
WISP-3
WNT-1

480 Neponset Street, Building 12A, Canton, MA 02021 • TEL (781) 828-0610 • EMAIL info@cellsciences.com

CALL TOLL FREE (888) 769-1246 • FAX (781) 828-0542 • VISIT www.cellsciences.com

www.cellsciences.com

Biacore systems

from inspiration
...to publication

Highest quality, information-rich interaction data from Biacore™ systems deepen your understanding of molecular mechanisms and interaction pathways and enable you to add function to structure.

Select the perfect solution for your application and draw conclusions with confidence – from the company that continues to set the standard for label-free protein interaction analysis.

For further information or register to have one of our scientific experts contact you, please visit www.gelifesciences.com/biacore-science



Biacore T100
unmatched performance



Biacore X100
ready to run research system



Biacore Flexchip
array-based comparative profiling



imagination at work

EDITORIAL

- 855 Translational Careers
N. Andrews et al.

NEWS OF THE WEEK

- 864 Stimulus Spending Looms Large as Obama Charts a Course for Science
>> Science Podcast
- 864 Navigating Treacherous Waters
- 867 Stimulus Funding Elicits a Tidal Wave of 'Challenge Grants'
- 867 From the *Science* Policy Blog
- 868 Newsmaker Interview:
Texas Transplant Alfred Gilman
Guides \$3 Billion Cancer Project
- 869 Austria's Possible CERN Withdrawal
Rattles Physicists
- 869 From *Science's* Online Daily News Site
- 870 Flu Researchers Train Sights on
Novel Tricks of Novel H1N1
- 871 Swine Flu Names Evolving Faster
Than Swine Flu Itself

NEWS FOCUS

- 872 'Vengeance' Bites Back at Jared Diamond
- 875 Carbon Sheets an Atom Thick Give Rise
to Graphene Dreams
Relativistic Physics in the Lab
- 878 Two Missions Go in Search of
A Watery Lunar Bonanza

LETTERS

- 880 Politics Still in Play
L. S. Thompson
Invest in Postdocs
K. G. Hoff
Mining the Data on Coal
M. Lardelli
Conference Covered Climate
from All Angles
M. Hulme et al.

BOOKS ET AL.

- 883 Animal Spirits
G. A. Akerlof and R. J. Shiller,
reviewed by M. Baddeley
- 884 Browsings

POLICY FORUM

- 885 The Cholera Crisis in Africa
S. Bhattacharya et al.

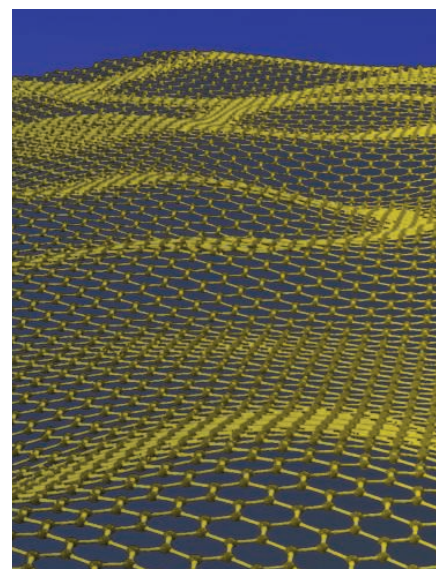
PERSPECTIVES

- 886 Seasons and Life Cycles
H. Steltzer and E. Post
>> Perspective p. 887
- 887 Phenology Feedbacks on Climate Change
J. Peñuelas et al.
>> Perspective p. 886
- 888 Ice Sheet Stability and Sea Level
E. R. Ivins
>> Research Article p. 901
- 890 Ovulation Signals
R. Duggavathi and B. D. Murphy
>> Report p. 938
- 891 Photovoltaics Power Up
R. M. Swanson
- 892 Two Beams Squeeze Feature Sizes
in Optical Lithography
J. W. Perry
>> Reports pp. 910, 913, and 917
- 893 Crossing the Line
T. Kidd
>> Report p. 944

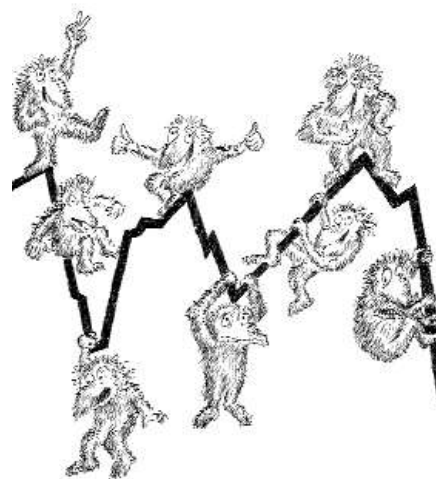
REVIEW

- 895 The Tail of Integrins, Talin, and Kindlins
M. Moser et al.

CONTENTS continued >>



page 875



page 883



COVER

Shaded perspective view of a surface topography of the West Antarctic Ice Sheet looking toward the Filchner-Ronne Ice Shelf and Antarctic Peninsula at the upper left. Floating ice shelves at the surface are in gray; the grounded ice sheet is shaded green to blue with increasing elevation. The topography was used to determine the volume of ice above sea level, as described on page 901.

Image: David Vaughan, British Antarctic Survey

DEPARTMENTS

- 851 This Week in *Science*
- 857 Editors' Choice
- 860 *Science* Staff
- 863 Random Samples
- 959 New Products
- 960 *Science* Careers

Making improvements in life possible

QIAGEN is making improvements in life possible in:

- Molecular diagnostics
- Pharma
- Animal and veterinary testing
- Genetic identity and forensics
- Life science research



Sample & Assay Technologies

BREVIA

- 900** A Key Role for Similarity in Vicarious Reward
D. Mobbs et al.
A functional magnetic resonance imaging study reveals the interactions within the brain that modulate feelings of reward on seeing a similar person win a contest.
>> *Science Podcast*

RESEARCH ARTICLES

- 901** Reassessment of the Potential Sea-Level Rise from a Collapse of the West Antarctic Ice Sheet
J. L. Bamber et al.
A collapse of the West Antarctic Ice Sheet would raise global sea level by 3.2 meters, but with large regional variations.
>> *Perspective p. 888; Science Podcast*
- 904** Input-Specific Spine Entry of Soma-Derived Vesl-15 Protein Conforms to Synaptic Tagging
D. Okada et al.
The protein Vesl-15 fulfills the synaptic tagging hypothesis for the maintenance of input-specific action of neuronal networks.

REPORTS

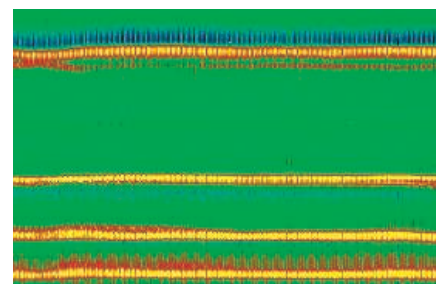
- 910** Achieving $\lambda/20$ Resolution by One-Color Initiation and Deactivation of Polymerization
L. Li et al.
Polymerization activated by a pulsed light beam was halted by a continuous beam of the same color in a surrounding halo.
>> *Perspective p. 892*
- 913** Two-Color Single-Photon Photoinitiation and Photoinhibition for Subdiffraction Photolithography
T. F. Scott et al.
Polymerization activated by a beam of light was halted by inhibitors generated by a surrounding halo of a different color.
>> *Perspective p. 892*
- 917** Confining Light to Deep Subwavelength Dimensions to Enable Optical Nanopatterning
T. L. Andrew et al.
Molecules that photoisomerize and change in transparency are used to define narrow features on photoresists.
>> *Perspective p. 892*
- 921** Size and Shape of Saturn's Moon Titan
H. A. Zebker et al.
Titan's poles lie at lower elevations than the equator, perhaps explaining its high-latitude hydrocarbon lakes.
- 924** Observing the Quantization of Zero Mass Carriers in Graphene
D. L. Miller et al.
Scanning tunneling microscopy on graphene reveals non-equally spaced Landau energy levels induced by a magnetic field.

- 927** Direct Detection of Abortive RNA Transcripts in Vivo
S. R. Goldman et al.
RNA polymerase engages in abortive transcription in bacteria, a process that may help to regulate gene expression.
- 929** The Nuclear DNA Base 5-Hydroxymethylcytosine Is Present in Purkinje Neurons and the Brain
S. Kriaucionis and N. Heintz
The genome of mammals contains appreciable amounts of a previously undescribed modified DNA base.
- 930** Conversion of 5-Methylcytosine to 5-Hydroxymethylcytosine in Mammalian DNA by MLL Partner TET1
M. Tahiliani et al.
Methylated C bases, an important epigenetic mark in genomic DNA, can be enzymically converted to 5-hydroxymethylcytosine.
- 935** A Functional Role for Transposases in a Large Eukaryotic Genome
M. Nowacki et al.
The ciliate *Oxytricha* uses transposase genes to influence thousands of DNA rearrangements required for proper development.
- 938** MAPK3/1 (ERK1/2) in Ovarian Granulosa Cells Are Essential for Female Fertility
H.-Y. Fan et al.
Targeted disruption of the kinases derails the molecular events that mediate induction of female reproductive development.
>> *Perspective p. 890*
- 941** Cell Movements at Hensen's Node Establish Left/Right Asymmetric Gene Expression in the Chick
J. Gros et al.
Asymmetric gene expression is passively set up in the early chick embryo by cell rearrangements.
- 944** A Frazzled/DCC-Dependent Transcriptional Switch Regulates Midline Axon Guidance
L. Yang et al.
A single receptor in *Drosophila* is involved in two molecular strategies that coordinate axon guidance.
>> *Perspective p. 893*
- 948** Fictive Reward Signals in the Anterior Cingulate Cortex
B. Y. Hayden et al.
Single neurons in the monkey cingulate cortex respond to fictive and experienced outcomes in the same way.
- 951** Extinction-Reconsolidation Boundaries: Key to Persistent Attenuation of Fear Memories
M.-H. Monfils et al.
Behavioral manipulations can reverse a learned fearful association in rats.

CONTENTS continued >>



pages 890 & 938



page 924



page 951

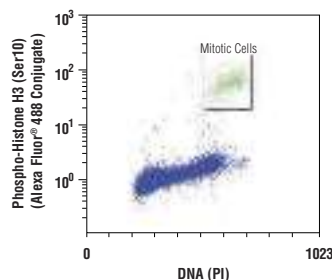
Alexa Fluor® Conjugated Antibodies

from Cell Signaling Technology®

Unparalleled product quality, validation and technical support.

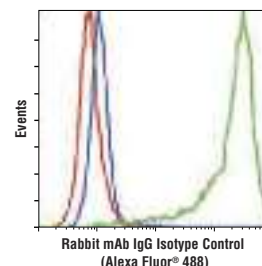
- ∴ The highest quality antibodies provide you with the brightest signal and the lowest background.
- ∴ Extensive validation by our in-house conjugation group means optimization is not left up to you, the user.
- ∴ Technical support provided by our conjugation group translates into a thorough, fast and accurate response.
- ∴ High quality custom conjugations of our off-the-shelf antibodies also available contact drugdiscovery@cellsignal.com.

▲ Confocal immunofluorescent analysis of rat brain using **GFAP (GA5) Mouse mAb (Alexa Fluor® 488 Conjugate) #3655** (green) and **Neurofilament-L (DA2) Mouse mAb #2835** (red). Blue pseudocolor = **DRAQ5® #4084** (fluorescent DNA dye).



◀ Flow cytometric analysis of Jurkat cells using **Phospho-Histone H3 (Ser10) (D2C8) Rabbit mAb (Alexa Fluor® 488 Conjugate) #3465** compared to propidium iodide (DNA content). The box indicates phospho-histone H3 positive cells.

Flow cytometric analysis of Jurkat cells, untreated (blue) or IFN- α -treated (green), using **Phospho-S6 Ribosomal Protein (Ser235/236) (D57.2.2E) Rabbit mAb (Alexa Fluor® 488 Conjugate) #4803**, compared to **Rabbit (DA1E) mAb IgG Isotype Control (Alexa Fluor® 488 Conjugate) #2975** (red).



for quality products you can trust...

www.cellsignal.com



Cell Signaling
TECHNOLOGY®

SCIENCEONLINE

SCIENCEXPRESS

www.sciencexpress.org

Synapse- and Stimulus-Specific Local Translation During Long-Term Neuronal Plasticity

D. O. Wang et al.

Live-cell microscopy reveals local translation during long-term facilitation of *Aplysia* sensory-motor synapses.
10.1126/science.1173205

Diversity and Complexity in DNA Recognition by Transcription Factors

G. Badis et al.

A broad survey of transcription factors reveals that related proteins can have multiple and differing DNA binding specificities.
10.1126/science.1162327

A Vital Role For Interleukin-21 in the Control of a Chronic Viral Infection

J. S. Yi et al.

The cytokine interleukin-21 has a profound impact on virus-specific T cell responses to chronic infections in mice.
10.1126/science.1175194

Determining the Dynamics of Entanglement

O. Jiménez Fariás et al.

The evolution of quantum mechanically entangled photon pairs can now be measured as they interact with their environment.
10.1126/science.1171544

Pd-Pt Bimetallic Nanodendrites with High Activity for Oxygen Reduction

B. Lim et al.

The catalytic activity of platinum is enhanced through a growth process that creates nanocrystals with high surface area.
10.1126/science.1170377

Pandemic Potential of a Strain of Influenza A (H1N1): Early Findings

C. Fraser et al.

An international collaborative effort has analyzed the initial dynamics of the swine flu outbreak.
10.1126/science.1176062

SCIENCENOW

www.sciencenow.org

Highlights From Our Daily News Coverage

Neutron Stars: Billions of Times Stronger Than Steel

A neutron star's surface is so dense it might shake up spacetime.

Sometimes, Nice Guys Finish First

Study of homicidal tribe shows aggressive warriors have less reproductive success.

Sun's Behavior Flummoxes Solar Scientists

New prediction pushes back timing and intensity of solar activity, but not everyone is on board.

SCIENCESIGNALING

www.sciencesignaling.org

The Signal Transduction Knowledge Environment

RESEARCH ARTICLE: TRPM1 Forms Ion Channels Associated with Melanin Content in Melanocytes

E. Oancea et al.

Newly identified TRPM1 isoforms that mediate current are highly conserved, present intracellularly, and associated with melanin content.

PERSPECTIVE: The Quest for Long-Distance Signals in Plant Systemic Immunity

J. E. Parker

Infected plant tissues generate diffusible signals that prime defenses in the rest of the plant.

PERSPECTIVE: The Yin and Yang of Synaptic Active Zone Assembly

S. J. Sigrist

An antagonist of two protein-protein interactions required for synapse formation has been identified in *C. elegans*.

PRESENTATION: Integrative Analysis of Genome-Wide RNA Interference Screens

J. D. Berndt et al.

By integrating RNAi screens with protein-protein interaction data, drug-protein interaction data, or disease-genotype data, researchers can focus their efforts on the best hits.

GLOSSARY

Find out what CoA, PAO, and WW mean in the world of cell signaling.

E-LETTER: Paradigm Shift

J. S. Torday and V. K. Rehan

Torday and Rehan discuss the recent *Science Signaling* editorial by Searls.

SCIENCECAREERS

www.sciencemag.org/career_magazine

Free Career Resources for Scientists

Traversing the Bridge Years

S. Brass

Bridging clinical training and a research career requires careful, strategic thinking.

>> *Editorial p. 855*

Tooling Up: Six Classic Lines of Bull

D. Jensen

Some of the things you hear during a job search are about as silly as a bad pickup line.

SCIENCEPODCAST

www.sciencemag.org/multimedia/podcast

Free Weekly Show

Download the 15 May *Science* Podcast to hear about how the brain reacts to vicarious reward, potential sea-level rise from collapsing ice sheets, monies budgeted for U.S. science, and more.



SCIENCESIGNALING
Controlling skin color.



SCIENCECAREERS
Crossing between clinical training and research.

ORIGINSBLOG

blogs.sciencemag.org/origins

A History of Beginnings

SCIENCEINSIDER

blogs.sciencemag.org/scienceinsider

Science Policy News and Analysis

SCIENCE (ISSN 0036-8075) is published weekly on Friday, except the last week in December, by the American Association for the Advancement of Science, 1200 New York Avenue, NW, Washington, DC 20005. Periodicals Mail postage (publication No. 484460) paid at Washington, DC, and additional mailing offices. Copyright © 2009 by the American Association for the Advancement of Science. The title SCIENCE is a registered trademark of the AAAS. Domestic individual membership and subscription (51 issues): \$146 (\$174 allocated to subscription). Domestic institutional subscription (51 issues): \$835; Foreign postage extra: Mexico, Caribbean (surface mail) \$55; other countries (air assist delivery) \$85. First class, airmail, student, and emeritus rates on request. Canadian rates with GST available upon request, GST #1254 88122. Publications Mail Agreement Number 1069624. **Printed in the U.S.A.**

Change of address: Allow 4 weeks, giving old and new addresses and 8-digit account number. **Postmaster:** Send change of address to AAAS, P.O. Box 96178, Washington, DC 20090-6178. **Single-copy sales:** \$10.00 current issue, \$15.00 back issue prepaid includes surface postage; bulk rates on request. **Authorization to photocopy** material for internal or personal use under circumstances not falling within the fair use provisions of the Copyright Act is granted by AAAS to libraries and other users registered with the Copyright Clearance Center (CCC) Transactional Reporting Service, provided that \$20.00 per article is paid directly to CCC, 222 Rosewood Drive, Danvers, MA 01923. The identification code for *Science* is 0036-8075. *Science* is indexed in the *Reader's Guide to Periodical Literature* and in several specialized indexes.

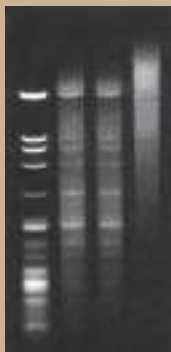


ADVANCING SCIENCE. SERVING SOCIETY

IN A WORD, TRUST.

T4 DNA Ligase

New England Biolabs is dedicated to providing our customers with guaranteed enzyme performance. Our recombinant T4 DNA Ligase is the most extensively used ligase for cloning experiments and other applications, including sample preparation and next generation sequencing. It is available at exceptional value, and an even greater value when purchased in large quantities for high throughput technologies. For cohesive, blunt, simple or complex reactions, make T4 DNA Ligase from NEB your first choice.



0 0.1 0.2 1.0
T4 DNA Ligase (µl)
Ligation of blunt-ended HaeIII fragments of Lambda DNA using various amounts of T4 DNA Ligase (400,000 cohesive end units/ml) in a 20 µl reaction volume. Reactions were incubated for 30 minutes at 16°C.



0 10 20 30 60
Time (min)
Ligation of HindIII fragments (4-base overhang) of Lambda DNA using 1 cohesive end unit (1 µl of 1:400 dilution) of T4 DNA Ligase. Reactions were incubated at 25°C.

Advantages:

Quality - Highly pure enzyme with no lot-to-lot variation

Convenience - Choose original T4 DNA Ligase or the Quick Ligation Kit to meet the demands of a variety of reaction conditions


Flexibility - Active at room temperature or 16°C; reaction times run from 5 minutes to overnight

Robustness - Active in a variety of reaction buffers

T4 DNA Ligase*

Regular Concentration M0202S/L
For standard cloning reactions

High Concentration M0202T/M
For large or difficult constructs

Quick Ligation™ Kit*  M2200S/L
For ligation of cohesive or blunt-end DNA fragments in 5 minutes at room temperature

 = Recombinant

*NEB ligase products are BSA-free

For more information regarding customization and OEM opportunities, please contact oem@neb.com

New England Biolabs, Inc. is an ISO 9001 certified company

 **NEW ENGLAND**
BioLabs[®] Inc.
enabling technologies in the life sciences

CLONING & MAPPING

DNA AMPLIFICATION
& PCR

RNA ANALYSIS

PROTEIN EXPRESSION
& ANALYSIS

GENE EXPRESSION
& CELLULAR ANALYSIS

www.neb.com



<< Editing the Genome

The ciliate *Oxytricha trifallax* has an unusual genome with the coding regions of genes (the exons) scattered through the genome. The exons are then somehow knitted together following transcription prior to their translation into proteins. As part of this process *Oxytricha* eliminates all transposable elements, stripping the genome down to 5% of the original germline DNA during development. **Nowacki et al.** (p. 935, published online 16 April) show that germline-limited transposases appear to be important for these large-scale DNA rearrangements.

Synaptic Tag Tagged

Input-dependent synaptic plasticity is critical for the reproducible activation of a specific neuronal assembly encoding a particular memory. The synaptic tagging hypothesis, which suggests how input specificity is maintained in late-phase synaptic plasticity, attempts to explain the persistence of long-term memory. However, it has been difficult to identify proteins that behave as the hypothesis predicts. **Okada et al.** (p. 904) investigated if the regulated spine entry of a late-phase-related somatically synthesized plasticity-related protein, Vesl-15, works as a synaptic tag. Vesl-15 protein was carried from the soma to every dendrite and recruited into spines by synaptic activation in an input-specific manner. Spine entry was protein-synthesis independent, was NMDA receptor dependent, and had a persistent lifetime of activation. These results provide long-sought evidence for the input-specific capturing of a plasticity-related protein as postulated by the synaptic tagging hypothesis.

Collapse and Rise

The West Antarctic Ice Sheet (WAIS) is thought to be inherently unstable and susceptible to rapid collapse if it reaches a certain warming threshold. Although such an event is considered unlikely, to predict the consequences of collapse it is important to know how much sea level would rise in such a case. The WAIS is thought to contain enough ice to raise sea level by 5 to 7 meters were it to collapse. **Bamber et al.** (p. 901, see the cover; see the Perspective by **Ivins**) have reassessed that number, on the basis of better data on the geometry of the WAIS, and conclude that its sudden collapse would raise sea level by about 3.2 meters, on average, with large and important regional variations.

Although this is only about half as much as previously thought, its impact on coastal areas would still be devastating.

Tales of Talin, Kindlin, and Integrin

The integrins are receptors on the surface of animal cells that mediate attachment to the extracellular matrix. Integrins also act as signaling molecules, activating signaling pathways when they bind to their ligands in the matrix. Furthermore, integrins can communicate signals from the inside to the outside of the cell when signals within the cell alter the affinity of integrins for their extracellular ligands. **Moser et al.** (p. 895) review recent advances in understanding the roles of the proteins talin and kindlin in such bidirectional signaling and how they influence the function of integrins in health and disease.

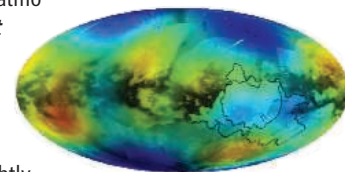
Subwavelength Patterning

Microscopists have recently achieved fluorescence imaging at subwavelength resolution by focusing one beam of light in a halo around another beam, thereby quenching the glow of fluorescent dyes in all but the very center of the illuminated spot. Three studies have now adapted this approach to photolithography (see the Perspective by **Perry**). **Andrew et al.** (p. 917, published online 9 April) coated a photoresist with molecules that, upon absorbing the ultraviolet etching beam, isomerized to a transparent layer but returned to the initially opaque form upon absorption of visible light. Applying an interference pattern with ultraviolet peaks superimposed on visible nodes restricted etching to narrow regions in the center of these nodes,

yielding lines of subwavelength width. **Scott et al.** (p. 913, published online 9 April) used a central beam to activate polymerization initiators, while using a halo-shaped surrounding beam to trigger inhibitors that would halt polymerization. **Li et al.** (p. 910, published online 9 April) found that use of a different initiator molecule allowed both beams to share the same wavelength (800 nanometers), with a relatively weak quenching beam lagging a highly intense initiating beam slightly in time. Both the latter techniques produced three-dimensional features honed to subwavelength dimensions.

Global Analysis of Titan

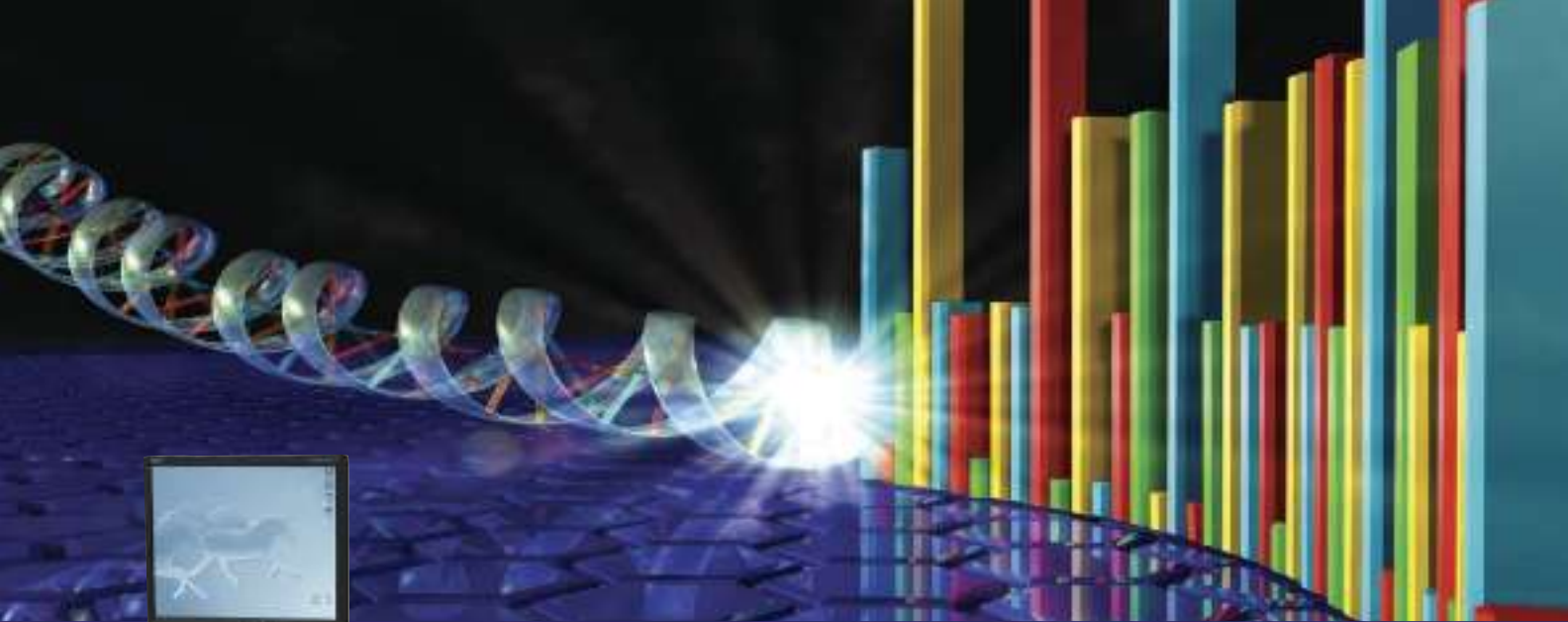
In its orbit around Saturn, the Cassini spacecraft passes regularly by the planet's largest moon, Titan. Using a radar instrument to peer through the moon's thick atmosphere, **Zebker et al.** (p. 921, published online 2 April) developed a global model of Titan. Titan is slightly oblate, so that its poles have lower elevations than the equator, which may explain why the moon's hydrocarbon lakes are located at high latitudes.



Identifying Abortive Initiation

During transcription initiation in vitro, the RNA polymerase enzyme typically engages in cycles of synthesis and release of short RNA transcripts

Continued on page 853

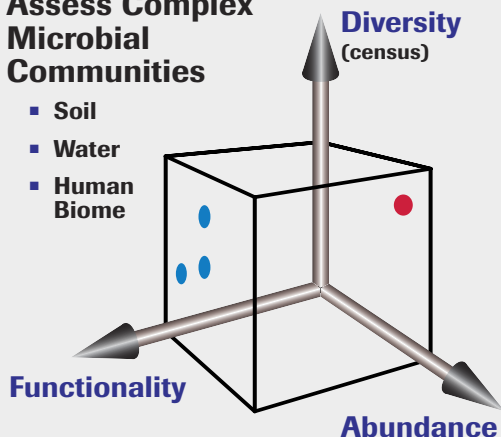


www.roche-applied-science.com

Genome Sequencer FLX System Characterize Your Metagenomic Samples

Assess Complex Microbial Communities

- Soil
- Water
- Human Biome



The power of metagenomic studies using the **Genome Sequencer FLX**. In a single instrument run, determine what microbial members of a community are present, annotate their function, and detect relative abundances. As indicated by the blue and red circles in the diagram, the combination of these variables enables the establishment of a signature profile for a specific environment, reflecting its relative health.

With more than 360 peer-reviewed publications, including more than 70 metagenomic studies, the Genome Sequencer FLX System is changing the way we view the microbial world.

Discover what microbial organisms are present.

- "Microbial population structures in the deep marine biosphere." Roesch *et al.*, ISME Journal 1: 283–290 (2008).
- "Pyrosequencing enumerates and contrasts soil microbial diversity." Huber *et al.*, Science 318: 97–100 (2007).

Determine the signature profile of an environment.

- "Functional metagenomic profiling of nine biomes." Dinsdale *et al.*, Nature 452: 629–632 (2008).
- "Globally distributed uncultivated oceanic N_2 -fixing cyanobacteria lack oxygenic photosystem II." Zehr *et al.*, Science 322: 1110 (2008).

Identify viral pathogens – quickly and accurately.

- "A new arenavirus in a cluster of fatal transplant-associated diseases." Palacios *et al.*, New England Journal of Medicine 358: 991–998 (2008).
- "A metagenomic survey of microbes in honey bee colony collapse disorder." Cox-Foster *et al.*, Science 318: 283–287 (2007).

Visit www.454.com for more information and to view a selection of these and other published references.

454
SEQUENCING

For life science research only. Not for use in diagnostic procedures.
454, 454 LIFE SCIENCES, 454 SEQUENCING, and GS FLX TITANIUM are trademarks of Roche. Other brands or product names are trademarks of their respective holders.
© 2009 Roche Diagnostics. All rights reserved.

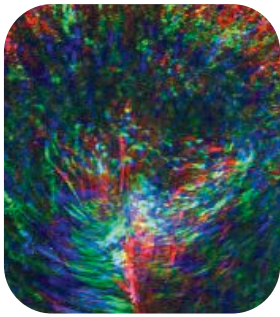
Roche Diagnostics
Roche Applied Science
Indianapolis, Indiana



("abortive initiation") before breaking interactions with promoter DNA and beginning transcription elongation. Using hybridization methods developed to detect microRNAs, **Goldman *et al.*** (p. 927) directly detected products of abortive initiation in bacterial cells *in vivo*. Abortive initiation increased when interactions between RNA polymerase and the promoter were strengthened or when transcription was prevented. Thus, products of abortive initiation may help to regulate gene expression.

Regulating Oocyte Maturation

Understanding exactly how ovarian follicles mature to generate fertile eggs is key to many aspects of fertility treatment. When the pituitary surge of luteinizing hormone (LH) binds to its receptor on granulosa cells of preovulatory follicles, a cascade of signaling events triggers granulosa cells to become luteal cells and the oocyte to resume meiosis. **Fan *et al.*** (p. 938; see the Perspective by **Duggavathi and Murphy**), using the mouse as a model system, targeted disruption of the kinases ERK1 and ERK2 selectively in granulosa cells. The kinases were essential *in vivo* mediators of LH induction of ovulation and luteinization.



Migration and Asymmetry

Although vertebrates show asymmetry in internal body organization, the earliest steps toward establishing different anatomies on the left and right sides are not conserved. How this is achieved in birds has been especially confusing. **Gros *et al.*** (p. 941, published online 9 April) show that in chicks some of the earliest left-right asymmetric domains of gene expression, including those of *Sonic hedgehog* (*Shh*) and *Fibroblast growth factor 8* (*Fgf8*), are produced passively. Genes are activated in bilateral cell populations, followed by rearrangements that shuffle *Shh*-expressing cells.

Stop-Go Axon Crossing

Developing axons may or may not cross the body's midline according to a balance between repulsive and attractive guidance factors. As an axon first approaches the midline, a repressive receptor encoded by the *comm* gene is inactivated by relocation within the cell. After the axon crosses the midline, the repressive receptor is reactivated, keeping the axon from crossing back. **Yang *et al.*** (p. 944, published online 26 March; see the Perspective by **Kidd**) now show that in *Drosophila* the *comm* gene is regulated by the attractive receptor known as Frazzled. The Frazzled protein thus functions in two ways: It initiates attraction in response to a ligand and it activates transcription of the *comm* gene, keeping the repressive signal out of the action.

The Path Not Taken

People readily recognize that unchosen actions have consequences and adjust their behavior accordingly. The ability to recognize fictive outcomes is thought to be a necessary component of regret, and disruptions in this ability may cause anxiety and problem gambling. Do animals engage in this same process? **Hayden *et al.*** (p. 948) provided monkeys with information about what rewards unchosen options would have given. The monkeys' behavior depended strongly on these fictive outcomes. Responses of single neurons in the anterior cingulate cortex, which monitors outcomes of rewarding decisions and guides subsequent changes in behavior, were recorded while monkeys performed the task. Nearly half the neurons in the sample responded to both experienced and fictive outcomes. Thus, the anterior cingulate cortex does not simply monitor the consequences of actions, but represents outcomes in a more abstract manner that incorporates both real and fictive information.

Reversing Pavlov

Memories of fearful associations, such as hearing a tone before receiving a low-voltage shock, are labile when they are retrieved, such that the association can be extinguished or reconsolidated. **Monfils *et al.*** (p. 951, published online 2 April) demonstrate that applying a standard extinction treatment (sounding the tone multiple times in the absence of any shocks) within a window of time during which reconsolidation would normally occur has the effect of overwriting the original memory. Rats treated in this fashion display much lower levels of renewal (fear induced by sounding the tone once by itself), reinstatement (fear induced by giving the shock once by itself), and spontaneous recovery.



Meet your new lab partner.

The new Thermo Scientific NanoDrop 2000 and 2000c Spectrophotometers offer true micro-sample analysis, with sample size capability as low as 0.5 μ l and a measurement time of less than five seconds. Either of these is the perfect instrument for all your quantitation needs—DNA, RNA, proteins and more. Providing full spectrum UV-Vis results, both instruments can analyze samples with concentrations greater than 15,000 ng/ μ l (dsDNA) without dilutions. Innovative software makes it easy to build your own methods, design reports and export data. And with both pedestal and cuvette capability, the NanoDrop™ 2000c is the one spectrophotometer that does it all.

Test-drive the NanoDrop 2000 or 2000c in your own lab!*

Visit www.nanodrop.com to schedule your test-drive. Try out an instrument and run your own samples. It's completely free.

* Available only in US and Canada



Thermo Scientific NanoDrop 2000c

The only spectrophotometer that combines micro-volume pedestal technology and cuvette capability

Moving science forward

Thermo
S C I E N T I F I C

Part of Thermo Fisher Scientific

Translational Careers

Nancy Andrews is former president of the American Society for Clinical Investigation.

John E. Burris is president of the Burroughs Wellcome Fund.

Thomas R. Cech is former president of the Howard Hughes Medical Institute.

Barry S. Collier is president of the Society for Clinical and Translational Science.

William F. Crowley Jr. is chairman of the Clinical Research Forum and Foundation.

Elaine K. Gallin is program director for Medical Research at the Doris Duke Charitable Foundation.

Katrina L. Kelner is the editor of *Science Translational Medicine*.

Darrell G. Kirch is president of the Association of American Medical Colleges.

Alan I. Leshner is chief executive officer of the American Association for the Advancement of Science (AAAS) and executive publisher of *Science*.

Cynthia D. Morris is president of the Association for Clinical Research Training.

Freddy T. Nguyen is board chairman of the American Physician Scientists Association.

Jim Oates is past president of the American Federation for Medical Research.

Nancy S. Sung is board chair of the Health Research Alliance.

POWERED BY THE COMPUTATIONAL MUSCLE OF BIOINFORMATICS AND THE BROAD PERSPECTIVE of systems biology, advances in biomedical science now have the capacity to transform medicine. Yet to fully realize the health benefits of new scientific insight, we must ensure a vibrant flow of information between the basic sciences and clinical medicine. This takes both systems and people.

The U.S. government has made an unprecedented investment in the infrastructure required to support a new generation of translational researchers. Through the Clinical and Translational Science Award program (CTSA), the National Institutes of Health has created a national consortium that already includes 39 centers in 23 states with an annual funding commitment of \$500 million by 2012. Still in its infancy, this initiative seeks to shorten the time required to translate research results into therapies by many means, including training researchers and providing them with an academic home, developing tools for clinical research, streamlining regulatory processes, and fostering interdisciplinary and interinstitutional research. The potential is clear.

But people are the prerequisite for success. We need an array of innovative investigators whose expertise spans all the disciplines of basic discovery and medical science. As a counterpoint to federal efforts, our private, nonprofit organizations have addressed the human capital need in robust ways, training and funding physicians and other clinical scientists, and piloting models for interdisciplinary graduate training involving biologists, physical and computational scientists and engineers, as well as a wide range of clinical and public health professionals.

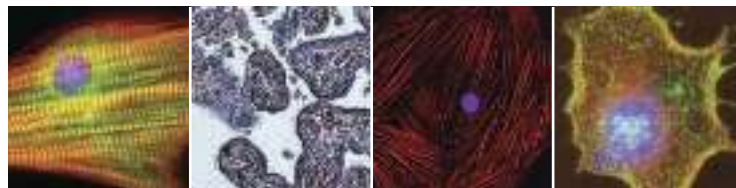
Beyond the rigorous research education essential for all scientists, translational scientists who will work at the boundaries of discovery and clinical science must possess an assortment of practical and logistical skills. They must understand the processes by which discoveries turn into therapies, as well as the evolving role of private industry. They must navigate the regulatory environment surrounding human-subjects research, work in teams and share the rewards of their work, and defer financial rewards while spending years in extra training to gain this knowledge. Existing investigators must learn new skills, but we must also attract new people and facilitate productive interactions among them.

The infrastructure envisioned by the CTSA initiative will provide access to resources of enormous value. But the most precious resource for translational research is the insights of individual investigators. All will benefit if these investigators participate in a coherent, communicative community. Incompatible communications infrastructures work against this aim. We need a means to connect people and transmit important information in a way that crosses the boundaries of individual subspecialties, institutions, and professional societies. Toward these ends—and in partnership with each of our organizations, and others that wish to join us—AAAS and *Science* are launching CTSciNet (<http://sciencecareers.org/ctscinet>), the Clinical and Translational Science Network. CTSciNet will combine a career-development Web portal for clinical and translational investigators with an experimental, evolving communications infrastructure, to be launched soon. The articles in CTSciNet will focus on educating trainees and new investigators in translational-research skills, in the spirit of *Science Careers*, which has served scientists since 1995. As it develops, CTSciNet's online professional network will connect clinical and translational science communities worldwide, leading to the formation of scientific relationships among student peers, mentors and protégés, and collaborators in academia and industry.

If it fulfills its potential, translational research will lead to better health for people. But translation is not one-way; the insights gained at the bedside, and from clinical and population-based studies, will spawn hypotheses, enabling scientists to probe the mechanisms of disease in new ways and ultimately enriching basic biology. Therefore, strengthening the support systems for those who will accomplish this multidirectional translation can only be good for science.

— N. Andrews, J. E. Burris, T. R. Cech, B. S. Collier, W. F. Crowley Jr., E. K. Gallin, K. L. Kelner, D. G. Kirch, A. I. Leshner, C. D. Morris, F. T. Nguyen, J. Oates, N. S. Sung





At Abcam we are dedicated to offering the best nuclear signaling antibodies in the world

Your most complete nuclear signaling resource

- Review articles
- Over 65 pathway downloads including the new Nucleocytoplasmic Transport Pathway
- More than 13,000 nuclear signaling-specific antibodies

www.abcam.com/nuclearsignal

Protocol Library

Abcam's scientific support team has written over 60 protocols for antibody-related applications.

www.abcam.com/protocol

Our Abpromise means 100% support

Get the reassurance of expert scientific support and replacement or refund if the product does not perform as we say it should.

www.abcam.com/abpromise



GEOLOGY

Andean Origins

The elevation of the Andes mountains has a tremendous influence on climate and ecology across South America, and their interaction with the atmosphere even tweaks Earth's rotation. Their past elevation and uplift history would have greatly influenced evolution and the development of ecosystems. The Andes were constructed by near-continuous subduction beneath South America for more than several hundred million years, and an uplift history might reveal or help elucidate specific tectonic events shaping the continent. Carrapa *et al.* compared dates from several techniques marking the original formation age and timing of rapid cooling of minerals now found in sedimentary rocks in the Central Andes. These ages reflect times of more rapid erosion of the Andes. The data are consistent with several episodes of uplift or exhumation including at about 350, 80 to 50, and 30 to 5 million years ago. Ehlers and Poulsen explored the relation between Andean uplift and paleoclimate of South America using a climate model and focusing on the past 10 million years or so. The simulations show that the lower Andes would have led to more drying of the Central Andes, but to more precipitation to the north. The magnitude of the results, while elucidating the importance of the Andes in climate, complicate the interpretation of stable isotope fossil plant data used to infer uplift history. — BH

Geology **37**, 407 (2009); *Earth Planet. Sci. Lett.* **281**, 238 (2009).

IMMUNOLOGY

T Cell Plasticity

CD4⁺ T helper cells are important mediators of humoral immunity. Different types of infection induce distinct helper lineages with characteristic profiles of cytokine expression. During an infection, CD4⁺ T cells interact with B cells in lymph node follicles where, through cell-cell interaction and cytokine secretion, they determine the classes of antibodies that B cells produce. CD4⁺ T cells that induce B cell class switching, termed T follicular helper cells, express distinct phenotypic markers regardless of infection type and were thus thought to be a dis-

tinct lineage of helper cells; however, one lineage of cells can induce the different classes of antibodies associated with immune response to distinct classes of pathogens.

Three studies by Reinhardt *et al.*, Zaretsky *et al.*, and King and Mohrs address this issue in the context of a helminth infection, which generates a classical T helper cell 2 (T_H2) immune response associated with interleukin-4 (IL-4) production. Using IL-4 reporter mice, the authors demonstrate that in the lymph node, most IL-4-producing T cells localize to B cell follicles. These cells are similar in phenotype to T follicular helper cells and are required for B cell class switching, but they also express T_H2-associated genes such as

GATA-3. In contrast, IL-4-producing cells outside of lymph nodes express T_H2-associated markers, but not T follicular helper cell-associated markers. These studies suggest that T follicular helper cells may not represent a distinct lineage, but rather differentiate from other T helper cell lineages and help to channel B cell responses via the secretion of lineage-specific cytokines. These studies also provide insight into how humoral and cellular immunity are coordinated because the same helper cytokines that induce humoral responses in the lymph node also drive cell-mediated immunity in the periphery. — KLM

Nat. Immunol. **10**, 385 (2009); *J. Exp. Med.* **206**, 10.1084/jem.20090303; 10.1084/jem.20090313 (2009).

ANIMAL BEHAVIOR

6 Heads Are Better than 2

A study of the gregarious house sparrow suggests that individuals in larger groups are swifter at solving new problems than those in smaller groups—findings that add a behavioral dimension to the ecological costs and benefits of group living. Using wild-caught birds that were then acclimatized to experimental aviaries, Liker and Bókonyi investigated whether group size affected the success rate at which birds

figured out how to obtain seeds from a familiar feeder when access was blocked with a transparent lid. The larger groups, which contained six birds, were able to dislodge the lids roughly 10 times as quickly as smaller groups of two birds—a pattern that was consistent across all individuals in the groups. Also, birds from urban environments were faster than birds from rural backgrounds. Increased success at problem-solving in larger groups may reflect a wider diversity of experience and skill among the individuals in the group and may constitute an adaptive advantage in complex habitats. — AMS

Proc. Natl. Acad. Sci. U.S.A. **106**, 10.1073/pnas.0900042106 (2009).



CHEMISTRY

Sources of Static

Contact electrification can be a nuisance (as in a static electricity shock) but can also be harnessed in applications such as photocopying. Many issues about this process are still unresolved—

Continued on page 859



LabTurbo®

THE POWER OF AUTOMATED SYSTEM FOR NUCLEIC ACID PURIFICATION

LabTurbo® 36 Compact

- Spin column automation
- 6-Channel pipette
- Processing of 1-36 samples per run in 90 minutes
- Ultrasonic fluid sensor
- Up-scalable sample input
- Compact size: 24W x 24D x 28H inch

LabTurbo® 96 Compact

- 96 spin column plate automation
- 24-Channel pipette
- Processing of 12-96 samples per run in 90 minutes
- Sample format: tube or 96-well plate
- Compact size: 34W x 31D x 39H inch

- ▶ Built-in touch screen
- ▶ Barcode documentation
- ▶ UV light sterilization
- ▶ Optimized protocols
- ▶ User-friendly Program
- ▶ Customizable
- ▶ Easy installation and maintenance



www.labturbo.com

Enter

Distributor wanted



TAIGEN Bioscience Corporation
TEL : +886-2-28891136 | FAX : +886-2-28836458
E-Mail : order@taigen.com



CB CE IVD

Continued from page 857

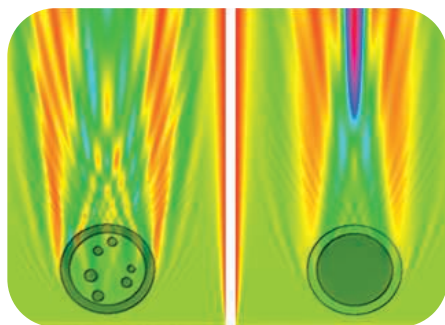
for example, in materials such as polymers, are the charges being transferred during rubbing electrons, or ions? Liu and Bard examined fresh samples of the thermoplastic poly(methyl methacrylate), or PMMA, which develops a positive charge if rubbed against Teflon. They found that the pristine PMMA tubing samples could undergo a number of reactions that are most readily explained as electron rather than ion transfers: plating out silver, copper, and palladium metal from ions in solution, for example, and reducing ferricyanide. Powdered samples increased the pH of aqueous solutions and generated hydrogen. The authors estimate that PMMA has a surface density of 5×10^{13} "cryptoelectrons," which could be recharged by contact with sodium amalgam, and further argue that the electrons occupy surface states created by damaged bonds, as opposed to states created by impurities. — PDS

J. Am. Chem. Soc. **131**, 6397 (2009).

CELL BIOLOGY

Nuclear Optics

In humans, the 3 billion nucleotides of DNA that constitute the genome would take up substantial cellular space if they were all stored in an open configuration; in a remarkable instance of molecular housekeeping, the DNA strands are instead packaged efficiently by the cell with proteins to form chromatin—a compressed material that can be straightforwardly confined to an



Light intensity (high, red/blue; low, green/orange) transmitted by conventional (left) and inverted (right) nuclei.

approximately 10- μ m-diameter membrane-bound nucleus. Some of the DNA needs to remain easily accessible to proteins and small molecules that together regulate gene expression and ensure the whole lot can be copied faithfully base by base, once per cell cycle. The vast majority of cells from both unicellular and multicellular organisms package transcriptionally inactive chromatin (heterochromatin) at the

nuclear periphery and the more active chromatin (euchromatin) in the center. Although the function of this segregation is debated, the pattern correlates with the timing of replication, which during S phase is generally later for heterochromatin, and is altered by changes in gene activity, as occurs during development.

In mammals, rod photoreceptor cells display the opposite pattern, with euchromatin found at the nuclear periphery. Solovei *et al.* have analyzed chromatin organization in rod cells from more than 30 mammalian species, including deer, rabbits, and pigs. They found the inverted pattern predominantly in nocturnal animals, and they demonstrated that this inversion has the consequence of improving photon transmission through the retina. In fact, the heterochromatin regions had a higher refractive index than the euchromatin, and the rod cell nuclei acted as converging lenses, indicating that the large-scale organization of euchromatin and heterochromatin can be usefully exploited to achieve specialized cellular functions. — HP*

Cell **137**, 356 (2009).

MATERIALS SCIENCE

Of Grains and Glasses

Most crystalline materials do not naturally form single crystals, but instead form ordered regions separated by thin grain boundaries. Although the boundaries may occupy only a small fraction of the volume, they can substantially affect the mechanical and electrical properties. Zhang *et al.* use simulations to explore the boundaries at high temperatures, where less is known about them experimentally, and specifically probe how atom mobility changes with temperature. They find that the motion of the atoms resembles that in glass-forming liquids. In particular, both materials show the cooperative motion of strings of atoms, with similar behavior in the size and motion of the strings over a range of temperatures, including the formation at low temperature of cages that trap atoms into localized oscillations. The authors believe their model can explain why grain boundary behavior is dependent on the mode of an applied stress, something that is not captured by conventional grain boundary migration theories. The nature of the strain (tensile or compressive), for example, alters the average chain length, which in turn influences the mobility. Similarly, impurities can either disrupt or enhance the formation of atom chains, and thus render the boundary region either a stronger or weaker glass former. — MSL

Proc. Natl. Acad. Sci. U.S.A. **106**, 10.1073/pnas.0900227106 (2009).

*Helen Pickersgill is a locum editor in *Science's* editorial department.

Call for Papers

Science Signaling

Science Signaling, published by the publisher of **Science**, AAAS, features top-notch, peer-reviewed, original research. The journal publishes leading-edge findings in cellular regulation including:

- Molecular Biology
- Development
- Immunology
- Neuroscience
- Microbiology
- Physiology and Medicine
- Pharmacology
- Biochemistry
- Cell Biology
- Bioinformatics
- Systems biology

Subscribing to **Science Signaling** ensures that you and your lab have the latest cell signal resources.

For more information visit
www.ScienceSignaling.org

Chief Scientific Editor

Michael B. Yaffe, M.D., Ph.D.

Associate Professor, Department of Biology
Massachusetts Institute of Technology

Submit your research at:
www.sciencesignaling.org/about/help/research.dtl

Science Signaling



1200 New York Avenue, NW
Washington, DC 20005

Editorial: 202-326-6550, FAX 202-289-7562

News: 202-326-6581, FAX 202-371-9227

Bateman House, 82-88 Hills Road
Cambridge, UK CB2 1LQ

+44 (0) 1223 326500, FAX +44 (0) 1223 326501

SUBSCRIPTION SERVICES For change of address, missing issues, new orders and renewals, and payment questions: 866-434-AAAS (2227) or 202-326-6417, FAX 202-842-1065. Mailing addresses: AAAS, P.O. Box 96178, Washington, DC 20090-6178 or AAAS Member Services, 1200 New York Avenue, NW, Washington, DC 20005

INSTITUTIONAL SITE LICENSES please call 202-326-6755 for any questions or information

REPRINTS: Author Inquiries 800-635-7181

Commercial Inquiries 803-359-4578

PERMISSIONS 202-326-7074, FAX 202-682-0816

MEMBER BENEFITS AAAS/Barnes&Noble.com bookstore www.aaas.org/bn; AAAS Online Store www.apisource.com/aaas/ code MKB6; AAAS Travels: Betchart Expeditions 800-252-4910; Apple Store www.apple.com/epstore/aaas; Bank of America MasterCard 1-800-833-6262 priority code FAA3YU; Cold Spring Harbor Laboratory Press Publications www.cshlpress.com/affiliates/aaas.htm; GEICO Auto Insurance www.geico.com/landingpage/go51.htm?logo=17624; Hertz 800-654-2200 CDP#343457; Office Depot hps.bsd.office depot.com/portalLogin.do; Seabury & Smith Life Insurance 800-424-9883; Subaru VIP Program 202-326-6417; VIP Moving Services www.vipmayflower.com/domestic/index.html; Other Benefits: AAAS Member Services 202-326-6417 or www.aaasmember.org.

science_editors@aaas.org (for general editorial queries)

science_letters@aaas.org (for queries about letters)

science_reviews@aaas.org (for returning manuscript reviews)

science_bookrevs@aaas.org (for book review queries)

Published by the American Association for the Advancement of Science (AAAS), *Science* serves its readers as a forum for the presentation and discussion of important issues related to the advancement of science, including the presentation of minority or conflicting points of view, rather than by publishing only material on which a consensus has been reached. Accordingly, all articles published in *Science*—including editorials, news and comment, and book reviews—are signed and reflect the individual views of the authors and not official points of view adopted by AAAS or the institutions with which the authors are affiliated.

AAAS was founded in 1848 and incorporated in 1874. Its mission is to advance science, engineering, and innovation throughout the world for the benefit of all people. The goals of the association are to: enhance communication among scientists, engineers, and the public; promote and defend the integrity of science and its use; strengthen support for the science and technology enterprise; provide a voice for science on societal issues; promote the responsible use of science in public policy; strengthen and diversify the science and technology workforce; foster education in science and technology for everyone; increase public engagement with science and technology; and advance international cooperation in science.

INFORMATION FOR AUTHORS

See pages 807 and 808 of the 6 February 2009 issue or access www.sciencemag.org/about/authors

EDITOR-IN-CHIEF **Bruce Alberts**

EXECUTIVE EDITOR

NEWS EDITOR

Monica M. Bradford

Colin Norman

MANAGING EDITOR, RESEARCH JOURNALS **Katrina L. Kelner**

DEPUTY EDITORS **R. Brooks Hanson, Barbara R. Jasny, Andrew M. Sugden**

EDITORIAL SENIOR EDITOR/PERSPECTIVES Lisa D. Chong; **SENIOR EDITORS** Gilbert J. Chin, Pamela J. Hines, Paula A. Kiberstis (Boston), Marc S. Lavine (Toronto), Beverly A. Purnell, L. Bryan Ray, Guy Riddihough, H. Jesse Smith, Phillip D. Szurmilo (Tennessee), Valda Vinson; **ASSOCIATE EDITORS** Kristen L. Mueller, Nicholas S. Wingington, Jake S. Yeston, Laura M. Zahn; **ONLINE EDITOR** Stewart Willis; **ASSOCIATE ONLINE EDITORS** Robert Frederick, Tara S. Marathe; **WEB CONTENT DEVELOPER** Martyn Green; **BOOK REVIEW EDITOR** Sherman J. Suter; **ASSOCIATE LETTERS EDITOR** Jennifer Sills; **EDITORIAL MANAGER** Cara Tate; **SENIOR COPY EDITORS** Jeffrey E. Cook, Cynthia Howe, Harry Jach, Barbara P. Ordway, Trista Wagoner; **COPY EDITORS** Chris Filiatreau, Lauren Kmeck; **EDITORIAL COORDINATORS** Carolyn Kyle, Beverly Shields; **PUBLICATION ASSISTANTS** Ramatoulaye Diop, Carlos L. Durham, Jai S. Granger, Jeffrey Hearn, Lisa Johnson, Scott Miller, Jerry Richardson, Jennifer A. Seibert, Brian White, Anita Wynn; **EDITORIAL ASSISTANTS** Emily Guise, Michael Hicks, Patricia M. Moore; **EXECUTIVE ASSISTANT** Sylvia S. Kihara; **ADMINISTRATIVE SUPPORT** Maryrose Madrid **NEWS DEPUTY NEWS EDITORS** Robert Coontz, Eliot Marshall, Jeffrey Mervis, Leslie Roberts; **CONTRIBUTING EDITORS** Elizabeth Culotta, Polly Shulman; **NEWS WRITERS** Yudhijit Bhattacharjee, Adrian Cho, Jennifer Couzin, David Grimm, Constance Holden, Jocelyn Kaiser, Richard A. Kerr, Eli Kintisch, Andrew Lawler (New England), Greg Miller, Elizabeth Pennisi, Robert F. Service (Pacific NW), Erik Stokstad; **INTERN** Jackie D. Grom; **CONTRIBUTING CORRESPONDENTS** Dan Charles, Jon Cohen (San Diego, CA), Daniel Ferber, Ann Gibbons, Robert Koenig, Mitch Leslie, Charles C. Mann, Virginia Morell, Evelyn Strauss, Gary Taubes; **COPY EDITORS** Linda B. Felaco, Melvin Gatling, Melissa Raimondi; **ADMINISTRATIVE SUPPORT** Scherraine Mack, Fannie Groom; **BUREAUS** New England: 207-549-7755, San Diego, CA: 760-942-3252, FAX 760-942-4979, Pacific Northwest: 503-963-1940

PRODUCTION DIRECTOR James Landry; **SENIOR MANAGER** Wendy K. Shank; **ASSISTANT MANAGER** Rebecca Doshi; **SENIOR SPECIALISTS** Steve Forrester, Chris Redwood; **SPECIALIST** Anthony Rosen; **PREFLIGHT DIRECTOR** David M. Tompkins; **MANAGER** Marcus Spiegler; **SPECIALIST** Jason Hillman

ART DIRECTOR Yael Kats; **ASSOCIATE ART DIRECTOR** Laura Creveling; **ILLUSTRATORS** Chris Bickel, Katharine Sutliff; **SENIOR ART ASSOCIATES** Holly Bishop, Preston Huey, Nayomi Kevitiyagala; **ART ASSOCIATE** Jessica Newfield; **PHOTO EDITOR** Leslie Blizard

SCIENCE INTERNATIONAL

EUROPE (science@science-int.co.uk) **EDITORIAL: INTERNATIONAL MANAGING EDITOR** Andrew M. Sugden; **SENIOR EDITOR/PERSPECTIVES** Julia Fahrenkamp-Uppenbrink; **SENIOR EDITORS** Caroline Ash, Stella M. Hurtle, Ian S. Osborne, Peter Stern; **ASSOCIATE EDITOR** Maria Cruz; **LOCUM EDITOR** Helen Pickersgill; **EDITORIAL SUPPORT** Deborah Dennison, Rachel Roberts, Alice Whaley; **ADMINISTRATIVE SUPPORT** John Cannell, Janet Clements, Louise Moore; **NEWS: EUROPE NEWS EDITOR** John Travis; **DEPUTY NEWS EDITOR** Daniel Clerly; **CONTRIBUTING CORRESPONDENTS** Michael Balter (Paris), John Bohannon (Vienna), Martin Enserink (Amsterdam and Paris), Gretchen Vogel (Berlin); **INTERN** Claire Thomas

ASIA Japan Office: Asca Corporation, Eiko Ishioka, Fusako Tamura, 1-8-13, Hirano-cho, Chuo-ku, Osaka-shi, Osaka, 541-0046 Japan; +81 (0) 6 202 6272, FAX +81 (0) 6 202 6271; asca@os.gulf.or.jp; **ASIA NEWS EDITOR** Richard Stone (Beijing: rstone@aaas.org); **CONTRIBUTING CORRESPONDENTS** Dennis Normile (Japan: +81 (0) 3 3391 0630, FAX +81 (0) 3 5936 3531; dnormile@gol.com); Hao Xin (China: +86 (0) 10 6307 4439 or 6307 3676, FAX +86 (0) 10 6307 4358; cindyhao@gmail.com); Pallava Bagla (South Asia: +91 (0) 11 2271 2896; pbagla@vsnl.com)

EXECUTIVE PUBLISHER **Alan I. Leshner**

PUBLISHER **Beth Rosner**

FULFILLMENT SYSTEMS AND OPERATIONS (membership@aaas.org); **DIRECTOR** Waylon Butler; **SENIOR SYSTEMS ANALYST** Jonny Blaker; **CUSTOMER SERVICE SUPERVISOR** Pat Butler; **SPECIALISTS** Latoya Casteel, LaVonda Crawford, Vicki Linton, April Marshall; **DATA ENTRY SUPERVISOR** Cynthia Johnson; **SPECIALISTS** Eintou Bowden, Tarrika Hill, William Jones

BUSINESS OPERATIONS AND ADMINISTRATION DIRECTOR Deborah Rivera-Wienhold; **ASSISTANT DIRECTOR, BUSINESS OPERATIONS** Randy Yi; **MANAGER, BUSINESS ANALYSIS** Michael LoBue; **MANAGER, BUSINESS OPERATIONS** Jessica Tierney; **FINANCIAL ANALYSTS** Priti Pamnani, Celeste Troxler; **RIGHTS AND PERMISSIONS: ADMINISTRATOR** Emilie David; **ASSOCIATE** Elizabeth Sandler; **MARKETING DIRECTOR** Ian King; **MARKETING MANAGER** Allison Pritchard; **MARKETING ASSOCIATES** Aimee Aponte, Alison Chandler, Mary Ellen Crowley, Julianne Wielga, Wendy Wise; **MARKETING EXECUTIVE** Jennifer Reeves; **MARKETING/MEMBER SERVICES EXECUTIVE** Linda Rusk; **DIRECTOR, SITE LICENSING** Tom Ryan; **DIRECTOR, CORPORATE RELATIONS** Eileen Bernadette Moran; **PUBLISHER RELATIONS, eRESOURCES SPECIALIST** Kiki Forsythe; **SENIOR PUBLISHER RELATIONS SPECIALIST** Catherine Holland; **PUBLISHER RELATIONS, EAST COAST** Phillip Smith; **PUBLISHER RELATIONS, WEST COAST** Philip Tsolakidis; **FULFILLMENT SUPERVISOR** Iqoo Edim; **FULFILLMENT COORDINATOR** Laura Clemens; **ELECTRONIC MEDIA: MANAGER** Elizabeth Harman; **PROJECT MANAGER** Trista Snyder; **ASSISTANT MANAGER** Lisa Stanford; **SENIOR PRODUCTION SPECIALISTS** Christopher Coleman, Walter Jones; **PRODUCTION SPECIALISTS** Nichele Johnston, Kimberly Oster

ADVERTISING DIRECTOR, WORLDWIDE AD SALES Bill Moran

PRODUCT (science_advertising@aaas.org); **MIDWEST/WEST COAST/W. CANADA** Rick Bongiovanni: 330-405-7080, FAX 330-405-7081; **EAST COAST/E. CANADA** Laurie Faraday: 508-747-9395, FAX 617-507-8189; **U. EUROPE/ASIA** Roger Gonçalves: TEL/FAX +41 43 243 1358; **JAPAN** Masuyoshi Yoshikawa: +81 (0) 3 3235 5961, FAX +81 (0) 3 3235 5852; **SENIOR TRAFFIC ASSOCIATE** Deandra Simms

COMMERCIAL EDITOR Sean Sanders: 202-326-6430

PROJECT DIRECTOR, OUTREACH Brianna Blaser

CLASSIFIED (advertise@sciencecareers.org); **U.S.: SALES MANAGER** Daryl Anderson: 202-326-6543; **INSIDE SALES REPRESENTATIVE** Tina Burks: 202-326-6577; **KEY ACCOUNT MANAGER/MIDWEST** Joribah Able; **EAST COAST** Alexis Fleming: 202-326-6578; **WEST/SOUTH CENTRAL** Nicholas Hintzbite: 202-326-6533; **SALES COORDINATORS** Rohan Edmonson, Shirley Young; **INTERNATIONAL: SALES MANAGER** Tracy Holmes: +44 (0) 1223 326525, FAX +44 (0) 1223 326532; **SALES** Susanne Kharraz, Dan Pennington, Alex Palmer; **JAPAN** Masuyoshi Yoshikawa: +81 (0) 3 3235 5961, FAX +81 (0) 3 3235 5852; **ADVERTISING SUPPORT MANAGER** Karen Foote: 202-326-6740; **ADVERTISING PRODUCTION OPERATIONS MANAGER** Deborah Tompkins; **SENIOR PRODUCTION SPECIALIST/GRAPHIC DESIGNER** Amy Hardcastle; **SENIOR PRODUCTION SPECIALIST** Robert Buck; **SENIOR TRAFFIC ASSOCIATE** Christine Hall; **PUBLICATIONS ASSISTANT** Mary Lagnaoui

AAAS BOARD OF DIRECTORS RETIRING PRESIDENT, CHAIR James J. McCarthy; PRESIDENT Peter C. Agre; PRESIDENT-ELECT Alice Huang; TREASURER David E. Shaw; CHIEF EXECUTIVE OFFICER Alan I. Leshner; BOARD ALICE GAST, Linda P. B. Katchi, Nancy Knowlton, Cherry A. Murray, Julia M. Phillips, Thomas D. Pollard, David S. Sabatini, Thomas A. Woolsey



ADVANCING SCIENCE, SERVING SOCIETY

SENIOR EDITORIAL BOARD

John I. Brauman, Chair, Stanford Univ.
Richard Lockard, Harvard Univ.
Robert May, Univ. of Oxford
Marcia McClurt, Monterey Bay Aquarium Research Inst.
Linda Partridge, Univ. College London
Vera C. Rubin, Carnegie Institution
Christopher R. Somerville, Univ. of California, Berkeley

BOARD OF REVIEWING EDITORS

Takuzo Aida, Univ. of Tokyo
Joanna Aizenberg, Harvard Univ.
Sonia Altizer, Univ. of Georgia
Daniel Altshuler, Broad Institute
Arturo Alvarez-Buylla, Univ. of California, San Francisco
Richard Amasino, Univ. of Wisconsin, Madison
Angelika Amon, MIT
Minrat O. Andrade, Max Planck Inst., Mainz
Kristi S. Anseth, Univ. of Colorado
John A. Bargh, Yale Univ.
Cornelia I. Bargmann, Rockefeller Univ.
Ben Barres, Stanford Medical School
Marisa Bartolomei, Univ. of Penn. School of Med.
Facundo Batista, London Research Inst.
Ray H. Baughman, Univ. of Texas, Dallas
Stephen J. Benkovic, Penn State Univ.
Toni Bissell, Wageningen Univ.
Mina Bissell, Lawrence Berkeley National Lab
Peer Bork, EMBL
Robert W. Boyd, Univ. of Rochester
Paul M. Brakefield, Leiden Univ.
Stephen Buratowski, Harvard Medical School
Joseph A. Burns, Cornell Univ.
William P. Butz, Population Reference Bureau
Mats Carlsson, Univ. of Oslo
Peter Carmeliet, Univ. of Leuven, VIB
Mildred Cho, Stanford Univ.
David Clapham, Children's Hospital, Boston
David Clary, Oxford University
J. M. Claverie, CNRS, Marseille
Jonathan D. Cohen, Princeton Univ.
Andrew Cossins, Univ. of Liverpool

Robert H. Crabtree, Yale Univ.
Wolfgang Cramer, Potsdam Inst. for Climate Impact Research
F. Fleming Crim, Univ. of Wisconsin
William Cumberland, Univ. of California, Los Angeles
Jeff L. Dangl, Univ. of North Carolina
Stanislav Dehaene, Collège de France
Edward DeLong, MIT
Emmanouil T. Dermitzakis, Wellcome Trust Sanger Inst.
Robert Desimone, MIT
Claude Desplan, New York Univ.
Dennis Discher, Univ. of Pennsylvania
Scott C. Doney, Woods Hole Oceanographic Inst.
W. Ford Doolittle, Dalhousie Univ.
Jennifer A. Doudna, Univ. of California, Berkeley
Julian Downward, Cancer Research UK
Denis Duboule, Univ. of Geneva/EPFL Lausanne
Christopher Dye, WHO
Gerhard Ertl, Fritz-Haber-Institut, Berlin
Mark Estelle, Indiana Univ.
Barry Everitt, Univ. of Cambridge
Paul G. Falkowski, Rutgers Univ.
Ernst Fehr, Univ. of Zurich
Tom Fenchel, Univ. of Copenhagen
Alain Fischer, INSERM
Scott E. Fraser, Cal Tech
Chris D. Frith, Univ. College London
Wulfraam Gerstner, EPFL Lausanne
Charles Godfrey, Univ. of Oxford
Diane Griffin, Johns Hopkins Bloomberg School of Public Health
Christian Haass, Ludwig Maximilians Univ.
Niels Hansen, Technical Univ. of Denmark
Dennis L. Hartmann, Univ. of Washington
Chris Hawkesworth, Univ. of Bristol
Martin Heimann, Max Planck Inst., Jena
James A. Hendler, Rensselaer Polytechnic Inst.
Ray Hilborn, Univ. of Washington
Michael E. Himmel, National Renewable Energy Lab
Kei Hirose, Tokyo Inst. of Technology
Ove Hoegh-Guldberg, Univ. of Queensland
Brigid L. M. Hogan, Duke Univ. Medical Center
Ronald R. Hoy, Cornell Univ.
Uli Ikkala, Helsinki Univ. of Technology
Meyer B. Jackson, Univ. of Wisconsin Med. School
Stephen Jackson, Univ. of Cambridge

Steven Jacobsen, Univ. of California, Los Angeles
Peter Jonas, Universität Freiburg
Barbara B. Kahn, Harvard Medical School
Daniel Kahne, Harvard Univ.
Gerard Karsenty, Columbia Univ. College of P&S
Bernhard Keimer, Max Planck Inst., Stuttgart
Elizabeth A. Kellog, Univ. of Missouri, St. Louis
Hanna Kokko, Univ. of Helsinki
Alan B. Krueger, Princeton Univ.
Lee Kump, Penn State Univ.
Nichelle A. Lazer, Univ. of Pennsylvania
David Lazer, Harvard Univ.
Virginia Lee, Univ. of Pennsylvania
Olle Lindvall, Univ. Hospital, Lund
Marcia C. Linn, Univ. of California, Berkeley
John Lis, Cornell Univ. of Tokyo
Richard Losick, Harvard Univ.
Ke Lu, Chinese Acad. of Sciences
Andrew P. MacKenzie, Univ. of St Andrews
Raul Madariaga, Ecole Normale Supérieure, Paris
Anna Magurran, Univ. of St Andrews
Charles Marshall, Harvard Univ.
Virginia Miller, Washington Univ.
Yasushi Miyashita, Univ. of Tokyo
Richard Morris, Univ. of Edinburgh
Edward Morse, Norwegian Univ. of Science and Technology
Naoto Nagasawa, Univ. of Cambridge
James Nelson, Stanford Univ. School of Med.
Timothy W. Nilsen, Case Western Reserve Univ.
Roeland Nolte, Univ. of Nijmegen
Helga Nowotny, European Research Advisory Board
Eric N. Olson, Univ. of Texas, SW
Stuart H. Orkin, Dana-Farber Cancer Inst.
Erin O'Shea, Harvard Univ.
Elinoir Ostrom, Indiana Univ.
Jonathan T. Overpeck, Univ. of Arizona
John Pendry, Imperial College
Simon Philoat, Univ. of Florida
Philippe Poulin, CNRS
Mary Power, Univ. of California, Berkeley
Molly Przeworski, Univ. of Chicago
Colin Renfree, Univ. of Cambridge
Trevor Robbins, Univ. of Cambridge
Barbara A. Romanowicz, Univ. of California, Berkeley
Edward M. Rubin, Lawrence Berkeley National Lab

Shimon Sakaguchi, Kyoto Univ.
Jürgen Sandkühler, Univ. of Vienna
David W. Schindler, Univ. of Alberta
Georg Schulz, Albert-Ludwigs-Universität
Paul Schulze-Lefert, Max Planck Inst., Cologne
Christine Seidman, Harvard Medical School
Terrence J. Sejnowski, The Salk Institute
Richard J. Shavelson, Stanford Univ.
David Sibley, Washington Univ.
Joseph Silk, Univ. of Oxford
Montgomery Slatkin, Univ. of California, Berkeley
Davor Solter, Inst. of Medical Biology, Singapore
Joan Steitz, Yale Univ.
Elisbeth Stern, ETH Zürich
Jerome Strauss, Virginia Commonwealth Univ.
Jürg Tschopp, Univ. of Lausanne
Derek van der Kooy, Univ. of Toronto
Bert Vogelstein, Johns Hopkins Univ.
Ulrich H. von Andrian, Harvard Medical School
Bruce D. Walker, Harvard Medical School
Christopher A. Walsh, Harvard Medical School
David A. Wardle, Swedish Univ. of Agric. Sciences
Graham Warren, Yale Univ. School of Med.
Colin Watts, Univ. of Dundee
Detlef Weigel, Max Planck Inst., Tübingen
Jonathan Weissman, Univ. of California, San Francisco
Wes Sessler, Univ. of Georgia
Ellen D. Williams, Univ. of Maryland
Ian A. Wilson, The Scripps Res. Inst.
Jerry Workman, Stowers Inst. for Medical Research
Xiaoliang Sunney Xie, Harvard Univ.
John R. Yates III, The Scripps Res. Inst.
Jan Zaenen, Leiden Univ.
Huda Zoghbi, Baylor College of Medicine
Maria Zuber, MIT

BOOK REVIEW BOARD

John Aldrich, Duke Univ.
David Bloom, Harvard Univ.
Angela Creager, Princeton Univ.
Richard Sweders, Univ. of Chicago
Ed Wasserman, DuPont
Lewis Wolpert, Univ. College London

CALL FOR PAPERS

Submit your research now to be
one of the first to be considered for
publication in the **inaugural issue of**
Science Translational Medicine!

Science Translational Medicine, to be published online weekly beginning in the fourth quarter 2009, focuses on the conversion of basic biomedical research into practical applications, thus bridging the research-to-application gap.

The editors of ***Science Translational Medicine*** are accepting manuscripts for review in the following areas:
cancer, cardiovascular disease, metabolism/diabetes/obesity, neuroscience/neurology/psychiatry, immunology/vaccines, infectious diseases, policy, behavior, bioengineering, physics, chemical genomics/drug discovery, imaging, applied physical sciences, medical nanotechnology, drug delivery, biomarkers, gene therapy/regenerative medicine, toxicology and pharmacokinetics, data mining, cell culture, animal, and human studies, medical informatics, and other interdisciplinary approaches to medicine.

Review the information for authors at
<http://sciencemag.org/marketing/stm/papers.dtl>

Recommend a subscription to your library:
www.sciencemag.org/cgi/recommend_subscription

Submit your research at
www.submit2scitranslmed.org

For more information, contact
Editor Katrina Kelner, Ph.D. at
scitranslmededitors@aaas.org

» **Elias A. Zerhouni, M.D.**
Chief Scientific Adviser
Senior Fellow, Global Health Program,
Bill & Melinda Gates Foundation
Former Director,
National Institutes of Health

» **Katrina L. Kelner, Ph.D.**
Editor
American Association for
the Advancement of Science

Advisory Board Members

Kenneth R. Chien, M.D., Ph.D.
Director, Cardiovascular Research Center,
Massachusetts General Hospital,
Harvard Stem Cell Institute,
Harvard Medical School

Harry C. Dietz, M.D.
Professor, Institute of Genetic Medicine,
Johns Hopkins Hospital
Investigator, Howard Hughes Medical Institute,
Johns Hopkins University School of Medicine

Jeffrey I. Gordon, M.D.
Director, Center for Genome Sciences,
Washington University in St. Louis,
School of Medicine

Philip Greenland, M.D.
Senior Associate Dean, Clinical and Translational
Research, Feinberg School of Medicine
Director, Northwestern University, Clinical and
Translational Sciences Institute
Former Editor, *Archives of Internal Medicine*

Joseph B. Martin, M.D.
Professor, Neurobiology and *Co-Chair*, Governance,
NeuroDiscovery Center, Harvard Medical School
Former Dean, Harvard Medical School

Elizabeth G. Nabel, M.D.
Chief and Principal Investigator, Nabel Lab,
Cardiovascular Branch, Vascular Biology Section
Director, National Heart, Lung, and Blood Institute,
National Institutes of Health



Integrating Medicine and Science

www.ScienceTranslationalMedicine.org

Submission
deadline
August 1

Rewarding brilliance since 1995.



The GE & Science Prize for Young Life Scientists. Because brilliant ideas build better realities.

Imagine standing on the podium at the Grand Hotel in Stockholm, making your acceptance speech. Imagine joining the ranks of those published in Science magazine and having your essay on your work in molecular biology read by your peers around the world. Imagine taking part in a seminar with the other Prize winners and Nobel Prize laureates and discussing your work with leaders in the field. Imagine what you could do with the \$25,000 prize money. Imagine what a brilliant start to your career, and where it could lead. Now stop imagining. If you were awarded your Ph.D in 2008, submit your 1000-word essay by August 1 and make it reality.

Want to build a better reality? Go to www.gelifesciences.com/science



GE & Science
Prize for Young
Life Scientists



imagination at work



* For the purpose of this prize, molecular biology is defined as "that part of biology which attempts to interpret biological events in terms of the physico-chemical properties of molecules in a cell".

(McGraw-Hill Dictionary of Scientific and Technical Terms, 4th Edition).

GE Healthcare Bio-Sciences AB, a General Electric Company.
Björkgatan 30, 751 84 Uppsala, Sweden.
© 2009 General Electric Company
- All rights reserved.

Busting the Bumblebee Bushwa



There's an old but persistent myth, based on calculations from 19th century aerodynamic theory, that bumblebees shouldn't be able to get their heavy bodies airborne with their teeny wings. Computer modelers have tried to explain how they do it, and now scientists at the University of Oxford have captured bumblebee flight *in vivo*.

Biomechanicist Richard Bomphrey and colleagues trained bees to fly between a hive and pollen-rich flowers in a smoky wind tunnel while high-speed video cameras captured the swirls of air, or vortices, over the beating wings. It turned out that bumblebees are very inefficient fliers. Unlike most flying animals, they "use the wings on each side independently," says Bomphrey, which

means that they do not connect the airflow over their wings into a single vortex that would speed them on. Such flight requires a lot of energy, supplied by bumblebees'

hefty thorax muscles and energy-rich diets.

Bomphrey speculates that the bees have sacrificed efficiency for "increased control whilst hovering at flowers." Or the large thorax needed to carry pollen may prevent airflow from linking over it. With this study, in the May issue of *Experiments in Fluids*, "we now have more information about the flows round bumblebee wings than any other animal," says co-author Adrian Thomas.

"The finding sounds indeed interesting," says biologist Fritz-Olaf Lehmann of the University of Ulm in Germany. But he cautions that three-dimensional flow measurements would be more informative than the 2D smoke trails that the Oxford group studied.

DNA on the Block

When J. Craig Venter became the first person to sequence his genome in 2001, it took his company, Celera Genomics, a year and cost \$100 million.

This week, a European man won an auction on eBay with a bid of \$69,000 to have his whole genome sequenced and analyzed by Knome Inc. in Cambridge, Massachusetts.

The company, which usually charges \$99,500 per genome, will donate the proceeds to the X PRIZE Foundation. "The cost of generating sequence data has been in an absolute free fall" as technology advances, says Knome CEO Jorge Conde. The foundation plans to push the process further by awarding \$10 million to the first team that can sequence 100 human genomes in 10 days for \$10,000 each.

One company promises a \$10,000 genome by next year and predicts that the figure will plunge to \$1000 in 5 years, says geneticist Yoav Gilad of the University of Chicago in Illinois. At such prices, researchers are salivating at the thought of finding out, for example, whether different populations evolved different versions of genes to adapt to various diseases or diets—research that will help usher in a bold new era of personalized medicine.

Chancellor Turnover At UC



Two University of California (UC) institutions are getting their first female chancellors this summer. At UC San Francisco, Susan Desmond-Hellmann, 51, (above) will replace J. Michael Bishop, 73, who is stepping down after 10 years. As a cancer researcher and executive at the pioneering biotech company Genentech, Desmond-Hellmann played a key role in ushering blockbuster cancer drugs—such as Herceptin, Rituxan, and Avastin—to market. Desmond-Hellmann, a hot commodity who shows up perennially on *Fortune's* list of powerful businesswomen, was leaving Genentech as part of the leadership shakeup following the company's acquisition by Swiss drugmaker Roche.

And last week, UC regents approved the appointment of Linda Katehi as chancellor of UC Davis. Katehi, 55, is currently a professor of electrical and computer engineering and provost at the University of Illinois, Urbana-Champaign.

Into the Depths

On 23 May, a new crewless submersible will leave Guam on a trip that will include an attempt to explore the deepest part of the world's oceans: the 11,000-meter Challenger Deep in the Pacific Ocean's Mariana Trench.

Nereus will have to withstand the pressure of roughly 1000 atmospheres—equivalent to "three SUVs standing on your big toe," says Andy Bowen of the Woods Hole Oceanographic Institution in Massachusetts, one of the designers.

There have been only two prior attempts to go this deep. In 1960, two men spent 20 minutes at the bottom in the bathyscaphe *Trieste*. In 1995, Japan's crewless submersible *Kaikyo* made a brief visit. *Nereus* will be the first equipped to roam around mapping Challenger Deep, with batteries enabling it to operate autonomously for 20 hours and cover about 70 kilometers, Bowen says. The vehicle, which carries stacks of disposable steel plates as ballast, will also be tethered to the mother ship by a 40-km-long fiber-optic cable for remote operation so that it can collect samples and send back pictures.

Nereus, ready for the abyss.



CREDITS (TOP TO BOTTOM): COURTESY OF UNIVERSITY OF OXFORD; UNIVERSITY OF CALIFORNIA; ROBERT ELDER/WOODS HOLE OCEANOGRAPHIC INSTITUTION

THE 2010 BUDGET

Stimulus Spending Looms Large as Obama Charts a Course for Science

Take a deep breath. That's what President Barack Obama seems to be telling nervous U.S. scientists in the detailed 2010 budget that he unveiled last week.

Despite the candidate's repeated assurances about the importance of investing in science, Obama's \$3.6 trillion budget request to Congress—his first since taking office in January—is hardly a call to arms. Overall spending on research would creep up by 0.6%, to \$59 billion, over the comparable appropriation for 2009. (The more commonly quoted figure for federal R&D, which includes weapons systems, would edge up 0.4%, to \$147.6 billion).

What that number doesn't include, however, is the unprecedented \$21 billion influx of research funding from the one-time stimulus package enacted in February (*Science*, 20 February, p. 992). The small percentage change also reflects large increases this year for some agencies that legislators approved belatedly in March (*Science*, 6 March, p. 1275). Then there's the fact that the new

Administration is still filling many positions and, as one lobbyist notes, "You need people to come up with new programs."

Take the National Institutes of Health (NIH), which received \$10.4 billion in stimulus funds that must be spent in the next 18 months. Its 2010 budget would rise to

\$30.8 billion, a 1.5% increase over a 2009 budget without the stimulus funding. "We didn't need additional resources," says Kathleen Sebelius, newly installed as head of the Department of Health and Human Services, of which NIH

is a part. Even so, Obama has proposed a controversial doubling of cancer research over 8 years, to \$11.5 billion, starting with a 5% jump in 2010.

The small overall increases for 2010 have put science advocates in a difficult position. They don't want to appear ungrateful for what's in the stimulus package, and even a small increase in the regular budget is better than nothing against a budget deficit topping \$1 trillion. But "we would like to have seen the strong support

for medical research expressed by President Obama matched by sizable funding increases [in the 2010 request]," said Richard Marchase, president of the Federation of American Societies for Experimental Biology in Bethesda, Maryland, in a statement about the proposed NIH budget. "While we appreciate that NIH received an incremental increase at a time when federal programs are facing cuts, and while the scientific community is immensely grateful for the investment in medical research that Congress and the president made through the Recovery Act, the budget still raises serious concerns about the sustainability of the biomedical research enterprise."

Getting a \$3 billion slice of the stimulus pie hasn't hurt the National Science Foundation (NSF), whose budget Obama has promised to double over 10 years as part of a commitment first made by Bush in 2007 to strengthen federal support for the physical sciences (see sidebar). The foundation would receive an increase of 8.5% in 2010, to \$7.04 billion. Within that total, its research account would grow by 12%, to \$5.73 billion. (Details had not been released at presstime.) The science and technology portion of the Environmental Protection Agency's budget would grow by 6.6%, to \$842 million, with more research into air toxics, human health, and ecosystems. And the U.S. Geological Survey's budget would

Online
sciencemag.org
Podcast
interview with
author Jeffrey Mervis.

NAVIGATING TREACHEROUS WATERS

Science lobbyists have cheered President Barack Obama's arrival at the helm of the U.S. ship of state for a host of reasons. One is the impressive scientific credentials of the new Administration's initial appointments. The list generally begins with Steven Chu, a physics Nobel laureate, and includes science adviser John Holdren, National Oceanic and Atmospheric Administration head Jane Lubchenco, and the co-chairs of the President's Council of Advisors on Science and Technology, medicine Nobel laureate Harold Varmus and genomics wizard Eric Lander. Another is Obama's repeated promise to "restore science to its rightful place." That's code for reversing the regulatory policies of the Bush years that seemed to ignore or distort the scientific analyses on which they were supposed to be based. And just last month, Obama received an ovation from the members of the National Academy of Sciences (NAS) by calling for 3% of the country's economy to be devoted to research, an unprecedented level of public and private spending on science.

But how long will that honeymoon last? Here are five areas that could cause friction between the new president and the research community.

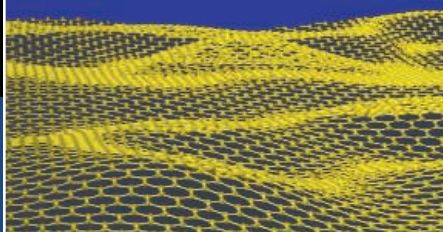


In addition to providing new funding, Obama has done plenty to befriend researchers concerned about global warming. He has stuck with his campaign promise to push for an 80% reduction by 2050 in 1990 greenhouse gas emissions. And an Environmental Protection Agency (EPA) ruling last month that those gases should be regulated under the Clean Air Act will give Obama leverage with Congress.

But there's also much concern that the president may ultimately be forced to choose a watered-down deal over no deal at all. An Administration official said last month that the Administration was considering a bargain in which emissions caps would begin in 2014 instead of 2012, and that one concession to large carbon emitters might be opening up oil drilling in U.S. waters. Holdren also indicated recently that Obama might be rethinking a campaign promise to have companies pay for all the emissions allowances allotted to them as part of a reduction scheme.

"It's too early to start whining," says atmospheric scientist Michael Oppenheimer of Princeton University. "But I'm concerned about what the White House might eventually agree to."

CREDIT: PHOTOS.COM



Graphene:
a material
in fashion

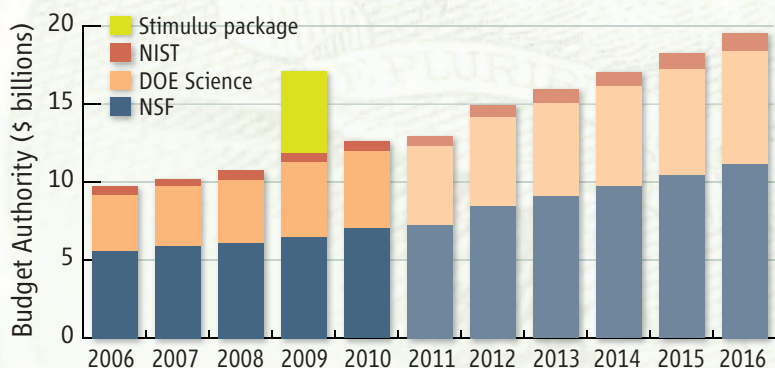
875



In search of water
on the moon

878

THE ERRATIC PACE OF DOUBLING



By the numbers. What would the president's promised 10-year budget doubling mean each year for the three agencies it covers? The Bush Administration was always careful to say it wanted to double overall spending by the National Science Foundation, the Department of Energy's (DOE's) Office of Science, and the National Institute of Standards and Technology by 2016. But the Obama White House has calculated each yearly step, for each agency. Budget cynics may not be surprised, but it turns out that most of the growth occurs in the last 5 years and that 2011 is projected to be a pretty tough year. DOE's science office would grow by only 1.6% in 2011, for example, and NSF by 2.9%. Double-digit increases would return the following year and beyond, however, with each agency winding up in 2016 with twice the amount it had received in 2006.

grow faster than inflation for the first time in years, receiving a 5% boost, to \$1.1 billion.

One agency whose science budget is getting a real shakeup is the Department of Energy (DOE). The president has requested \$280 million for a competition to pick eight Energy Innovation Hubs, each one focused on a different energy-related challenge aimed at reducing the country's carbon emissions and fostering energy independence. "This is something that I feel quite passionate about," said Energy Secretary Steven Chu about the hubs, which he described as little Bell Labs. Each would receive as much as \$135 million over 5 years. The 2010 budget

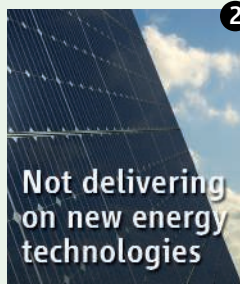
also includes \$10 million for a new agency, Advanced Research Projects Agency-Energy (ARPA-E), to identify and fund what Chu and others call "transformative research" on solutions to the country's energy needs. ARPA-E received \$400 million in the stimulus package.

DOE would also get \$115 million to begin educating students at all levels in clean-energy fields. That's six times the amount DOE now invests in training and would make the department a major player in federally funded science, technology, engineering, and math education. By comparison, the leader, NSF, would see its edu-

cation directorate grow by only \$13 million, to \$858 million. That bump would be more than absorbed by boosts for technology training at community colleges and a hike in the graduate research fellowship program. The latter addresses the president's promise to triple the size of the program, to 3000 new awards a year, by 2013.

The proposed 3.9% increase for DOE's Office of Science, to \$4.94 billion, takes into account the 19% leap that the office received in 2009, as well as the \$1.6 billion in the stimulus package. At the same time, the 2010 budget would also scale back some activities, notably the hydrogen vehicle program, a ▶

CREDITS: (TOP) OFFICE OF SCIENCE AND TECHNOLOGY POLICY; (BOTTOM) PHOTOS.COM



Not delivering
on new energy
technologies

2 When Obama promised NAS members last month that his Administration would make "the largest commitment to scientific research and innovation in American history," he predicted the payoff would include "solar cells as cheap as paint [and] green buildings that produce all the energy they consume." Chu has also painted a rosy picture of the technical breakthroughs that will lead the way to a low-carbon future.

But will there be a backlash when, as is likely, those breakthroughs don't materialize or have no practical impact before the next election? "There's no question that they're overpromising, but that's part of the excitement," says Massachusetts Institute of Technology chemist John Deutch, undersecretary of energy during the Carter Administration. Deutch says success will hinge on the Administration's ability to sustain generous support over many years, along with regulations that allow new technologies to flourish.

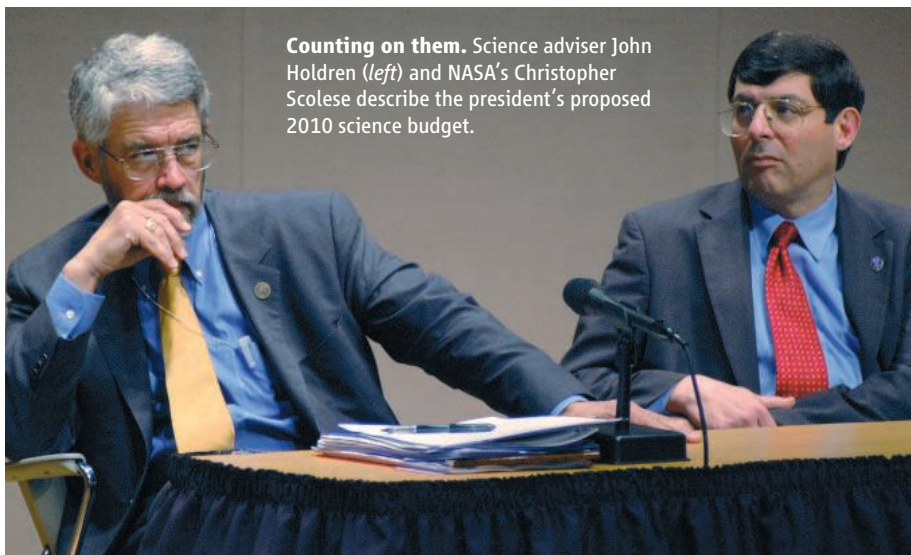


Succumbing to
disease politics

3 Obama's 2010 budget to make cancer research the top priority for the National Institutes of Health (NIH) has dismayed biomedical research advocates, who say such set-asides are harmful to science. Varmus, a former NIH director, has written that it's a bad idea to set aside funding

for a specific disease because discoveries in one area often turn out to benefit another. Richard Marchase, president of the biology association FASEB, is also concerned that other disease groups will follow suit and that a coalition of patient and research groups that have pushed for increasing the NIH budget "will begin to unravel."

Advocates take heart in the fact that the increase is spread over all 27 NIH entities, not just the National Cancer Institute. Research on cancer covers basic studies of cell growth and genetics that could have broad implications for other diseases, says David Moore of the Association of American Medical Colleges. Still, there will be a push for Congress to embrace a broader approach.



Counting on them. Science adviser John Holdren (left) and NASA's Christopher Scolese describe the president's proposed 2010 science budget.

Bush favorite, from \$169 million to \$68 million. As Chu explained during a budget briefing, "Is it likely in the next 10 or 15 or even 20 years that we will convert to a hydrogen car economy? The answer, we felt, was no."

Old and new

Obama provided few specifics about science when he previewed his 2010 budget in late February. But the details released last week contain more than a passing resemblance to those of his Republican predecessor, says Bush science adviser John Marburger. "It is certainly the sort of budget I would have expected under the previous administration, and indeed it carries forward the priorities of that administration, as the Bush administration carried forward science priorities of the Clinton administra-

tion," Marburger wrote in an e-mail to *Science*.

The promised budget doubling for DOE science, NSF, and the National Institute of Standards and Technology, for example, was a cornerstone of Bush's last three requests and had been embraced—but not always followed—by a bipartisan majority in Congress. The meager NIH increase, after the huge bulge from stimulus funding, also continues a tradition going back to 2004 after the agency's budget finished a 5-year doubling course. The competitive research program at the U.S. Department of Agriculture would remain at about \$200 million. Similarly, most of NASA's vastly overcommitted science programs (*Science*, 3 April, p. 34) would get no more assistance from Obama than they received from Bush. But whereas astrophysics would drop by 7% in 2010,

earth sciences, already buoyed by \$325 million in stimulus funding, would receive boosts in each of the next 4 years, growing from \$1.4 billion in 2009 to \$1.6 billion in 2013.

The biggest question mark for NASA is the fate of its human exploration program following the planned retirement of the space shuttle next year. On budget day, presidential science adviser John Holdren announced that Norman Augustine, former CEO of space and defense giant Lockheed Martin, has agreed to head a panel to do a quick review of the new rocket and space capsule that NASA has promised will be ready by 2015. "I anticipate they are going to ... assess the status of where we are at and the progress that we are making," explained acting NASA Administrator Christopher Scolese. "Clearly, if we are on the wrong path, we should change."

At the budget briefing, Holdren talked about how much the president "gets it" when discussing science and how he lights up when the topic turns to science education. But this year's budget request may not be the best metric to measure progress toward the president's goals. Standing alongside Holdren at the briefing—and singled out for praise—was National Oceanic and Atmospheric Administration Administrator Jane Lubchenco, a much-decorated marine ecologist to whom Holdren kidded he was "joined at the hip," having been nominated the same day, appeared together before the Senate, and sworn in at the same ceremony. But despite that close kinship, NOAA's proposed 2010 research budget of \$568 million is actually \$8 million less than the Bush Administration requested last year.

—JEFFREY MERVIS



4

Many people are watching nervously as NIH, still without a permanent director, doles out its \$10.4 billion stimulus windfall. On the one hand, acting NIH Director Raynard Kington is

doing a fine job, they say, and delays in appointing an NIH director aren't unusual—the institute had no designated director for more than 2 years after Varmus left in December 1999, for example.

Still, advocates believe that a fresh vision is needed for 2011 and beyond to avoid the same sort of crash that occurred in 2004 when NIH ended a 5-year budget doubling. In the meantime, Congress will need to be convinced that the stimulus money was spent in innovative ways and not just to let researchers extend current projects. "We're going to need big, glamorous things to hang our hats on," says one lobbyist.



5

Public health scientists and environmental advocates are still seething from the previous Administration's approach to regulating air pollution. Stephen Johnson, EPA head under President George W. Bush, endured scathing criticism when he picked standards for ozone and soot that were looser than those his experts advised (*Science*, 21 March 2008, p. 1602).

The Clean Air Act requires EPA to base standards for these and four other common air pollutants only on what the science says will adequately protect human health. In 2005 and 2008, Johnson disregarded the advice of science advisers on portions of those standards. Advocacy groups sued, and now the soot and ozone standards are back at EPA for a second look.

Lisa Jackson, EPA's new administrator, has promised to follow the science in deciding whether to tighten regulations on power plants, the auto industry, and other sources of air pollution. But will a recession erode that commitment? In her Senate confirmation hearing, Jackson left herself some breathing room: "I understand that the laws leave room for policymakers to make policy judgments."

—DAN CHARLES, JOCELYN KAISER, ELI KINTISCH, AND ERIK STOKSTAD

BIOMEDICAL RESEARCH

Stimulus Funding Elicits a Tidal Wave of 'Challenge Grants'

A frantic grant-writing effort that has consumed biomedical research scientists this spring came to an end last week, resulting in a huge pile of new applications—more than 10 times larger than expected—to be reviewed by the National Institutes of Health (NIH). After this enthusiastic response, there will be many disappointed applicants: The rejection rate could run as high as 98%.

The flurry of activity was sparked by the recent economic stimulus bill, which enabled NIH to expand ongoing grants and offer so-called Challenge Grants, described as an opportunity to jump-start research on certain topics. The NIH director's office announced the competition for these 2-year grants, worth \$1 million each, in early March. This was just 2 weeks after President Barack Obama signed the bill that gave NIH \$8.2 billion to spend on extramural research by October 2010 (*Science*, 17 April, p. 318). By 12 May, NIH had logged about 20,000 applications for the Challenge awards. That total surpasses anyone's expectations and tops what NIH normally receives in its regular three-times-a-year grant cycle. By contrast, NIH received only 1600 applications from researchers seeking to expand existing grants—fewer than anticipated.

Initially, NIH expected to receive perhaps 1500 Challenge Grant applications and make 200 or more awards, says Anthony Scarpa, director of the NIH Center for Scientific Review (CSR). But as NIH officials spoke with university administrators, Scarpa says, NIH kept revising its estimate upward.

Even after the 27 April deadline had passed, it took a while to pin down the total numbers. Some applications got clogged in the federal grants-submission portal, Grants.gov. Although researchers worried that the Web site would collapse, that did not happen—the system just took longer than usual to process applications, so NIH gave investigators an 11-day extension. The 20,000 total is surprising, says one NIH official, but NIH has seen a similar disproportionate spike in first-year applications for some other new programs, such as the Pioneer Awards.

Although some scientists grumble that the Challenge Grant award success rate will be so low that decisions cannot be made

rationally, others are buoyed by the outpouring of ideas: "This is our march on Washington. Now policymakers need to step up to the plate," says cancer researcher Peter Bitterman of the University of Minnesota, Twin Cities, which submitted about 240 applications.

To review the applications, CSR has called on 15,000 people, largely previous reviewers but also new ones found with help from scientific societies. Each application will be sent electronically to three experts, then some 30 study sections will meet in person to assign overall scores, using a new



Swamped. NIH is calling in reinforcements to help review roughly 20,000 proposals for 2-year research projects.

"editorial board" model, Scarpa says. CSR staff members, who are also organizing a regular round of reviews this spring, have been working overtime, he adds: "It's a heroic effort. They're really overworked." But Scarpa says he is confident that "it will be an excellent level of review."

Scientists should expect that "substantially more" than 200 awards will be made, because many institutes and centers will decide to fund some on their own, says acting NIH Director Raynard Kington. NIH expects at least 400 overall. Still, the success rate will be low. But Kington says the effort won't be wasted because many investigators will resubmit their ideas in the bread-and-butter R01 category starting next fall.

—JOCELYN KAISER

ScienceInsider

From the Science Policy Blog



ScienceInsider went all over town last week to hear federal agency officials present details of President Barack Obama's 2010 budget request to Congress. Here is a sampling of what we learned.

At **NASA**, the **earth sciences program** was the favored child within space science, adding to its \$325 million haul from the recent stimulus package. The budget offers little help for other heavily mortgaged science programs. However, the president threw a wild card into the NASA deck by announcing a review of the Bush Administration's plans for human exploration of the moon and Mars.

The **intramural labs at NIST** fared well, as did external industrial support programs such as the Technology Innovation Program, a perennial target for the Bush Administration. Look for a boost in efforts to build a smart grid, advance solar energy, and revamp information technology in health care.

Problems with the Advanced Spectroscopic Portal program, which was started in 2004 to screen cargo at land and sea borders for signatures of nuclear material, have led to a proposed elimination of acquisition funds for the **Domestic Nuclear Detection Office** within the Department of Homeland Security. Administration officials say they plan to use stimulus money to buy the detectors if and when they are proven effective.

While most institutes and the director's Common Fund would receive tiny raises, **cancer research at the National Institutes of Health** would take off on an 8-year doubling path. "It's a presidential priority," explained acting NIH Director Raynard Kington. "I don't think it's inconsistent with the broad mission of the agency in any way." Another Obama campaign pledge would boost autism research by 16%, to \$141 million. Reversing a Bush policy, the president's budget also requests funding, totaling \$194 million, for the longitudinal National Children's Study.

For the full postings and more, go to blogs.sciencemag.org/scienceinsider.

NEWSMAKER INTERVIEW

Texas Transplant Alfred Gilman Guides \$3 Billion Cancer Project

Texas biomedical researchers were elated 2 years ago when voters approved spending \$3 billion over 10 years for cancer research and prevention in the state. But they also worried about keeping funding decisions free of politics (*Science*, 31 August 2007, p. 1154). Dealing with such concerns is a top priority, says the Cancer Prevention and Research Institute of Texas's (CPRIT's) scientific director, biochemist Alfred Gilman, named last month.

Gilman, 67, won a Nobel Prize in 1994 for work on G proteins and their role in cell signaling. A Connecticut native, he has spent nearly 3 decades at the University of Texas (UT) Southwestern Medical Center at Dallas, where he is now an executive vice president, provost, and medical school dean. In June, he will step down to join the new venture. As *Science* went to press, the Texas House of Representatives and Senate were expected to approve the full \$300 million from bond sales for each of CPRIT's first 2 years, and Gilman hopes to make the first awards late this year. Gilman's comments have been edited for brevity.

—JOCELYN KAISER

Q: Why were you interested in this job? You're not a cancer biologist.

A.G.: No, but the basic research I did was applicable to most cellular functions. I actually was funded by the American Cancer Society for several years. So I'm not without cancer connections.

This is an exciting thing for Texas to do. It's real money, it's a real opportunity to accomplish some novel things in cancer research. I'm at a perfect point in my career to do something like this. I don't want to be dean anymore.

Q: What is CPRIT going to do that will be different from what the National Cancer Institute does?

A.G.: First of all, the biggest part of my job is going to be to put together the best darn scientific review committees you've ever seen,



headed by superb cancer scientists. They will all be non-Texans. The first question that will be asked [of grant proposals] is, "How important and innovative is this research?" Not, "Can it be done?"

I'm very much looking forward to having a high-impact, high-risk grant program that will give out, say, \$100,000 for a year or 18 months to get preliminary data. We'll be putting forth RFAs [requests for applications] to encourage recruitment to Texas of both senior and junior scientists. We definitely want to recruit some stars. There will be some big consortium grants. I'll be surprised if there aren't big infrastructure projects, say, high-throughput screening or tumor-sample repositories. Certainly we'll support training.

Q: Do you have any idea how much will go to basic versus clinical research and treatment versus prevention?

A.G.: Some people have written down those numbers, and I've said, I don't want to see 'em. I want the judgment of quality to determine the distribution of money.

My plan is that I would have the chairs of the study sections in essence constitute the equivalent of a [National Institutes of Health] council. They will get together in a meeting and merge their study sections' lists into a final funding list. I think that will be a very interesting meeting.

Q: Is there going to be any attempt at geographic diversity?

A.G.: Not much. (Laughs.) I've said a pretty consistent line here that I'm going to take the politics out of this. But if you look at the data, roughly half of NCI [National Cancer Institute] funding in Texas goes to M. D. Anderson [Cancer Center]. All of the UT components account for about 75% of NCI funding in the state. Now add Baylor [College of Medicine], and you are at about 90%. So that's not evenly distributed geographically. It's based on peer review. And so I think it will shake out roughly that way.

But I think the high-risk, high-impact program will provide opportunities for people in smaller schools to compete. A great idea can come from anywhere.

Q: Are Texans going to expect cures?

A.G.: Every time everyone uses the "C" word, I say, "Please, we will not overpromise." And what I've said to one of the sponsors of the legislation [is], we'll work hard but we're not going to promise that we're going to cure anything. I'm saying that we're going to make a lot of progress.

Q: You will remain on the boards of two drug companies [Eli Lilly and Regeneron]. Why don't you see that as a conflict of interest?

A.G.: Because I don't see either Eli Lilly or Regeneron coming to CPRIT for funding or being involved in projects with CPRIT investigators, but if they do, it's just as big a conflict of interest that I've been at UT Southwestern for 28 years. I've recused myself from here to eternity. I'm setting up the review system, I'm organizing it, I'm facilitating it. And I'm not voting.

Q: Is there anything else to know about how CPRIT will work?

A.G.: I said to the oversight committee, "You give me the tools I need, I will give you the world's best peer-review system." I want to call up these folks and invite them to participate. I'll say, "You're going to help give away \$300 million a year for cancer research, and your advice will be taken." And I said, "If you ignore the advice of review groups, then they'll walk and I'll walk with them."

CREDIT: UT SOUTHWESTERN MEDICAL CENTER

PARTICLE PHYSICS

Austria's Possible CERN Withdrawal Rattles Physicists

Physicists across the globe are looking forward to exciting discoveries once the world's most powerful particle accelerator, the Large Hadron Collider, fires up in September at the CERN particle physics lab near Geneva, Switzerland. But researchers in Austria, one of the lab's 20 European member states, were shocked to hear last week that they may have to leave the party early. Austrian science minister Johannes Hahn announced on 7 May that he intends to withdraw the country from CERN membership by the end of 2010 because his ministry thinks its €16 million annual contribution would be better spent on smaller research projects. Christian Fabjan, director of the Institute of High Energy Physics in the Austrian Academy of Sciences, calls the decision "devastating," adding: "It degrades the position of Austria to a backseat in fundamental research."

The matter has attracted huge public interest in Austria. "We were surprised by the amount of reaction," says physicist Daniel Grumiller of the Institute for Theoretical Physics at the Vienna University of Technology. Researchers have been quick to gather support for reversing the decision, setting up Web sites for letters and an online petition that attracted 5500 signatures in its first 24 hours. "It would be a great loss for Austria, and a blow to Europe and the scientific world, if short-term thinking and lack of vision caused Austria—birthplace of Ludwig Boltzmann, Erwin Schrödinger, Wolfgang Pauli, Victor Franz Hess, and Lise Meitner—to pull out of CERN now," posted physics Nobel laureate Frank Wilczek of the Massachusetts Institute of Technology in Cambridge.

Hahn said in his statement that Austria wants to participate in new research facilities that will soon be starting up in Europe. And facing a flat budget, the science ministry (BMWf) decided to review current interna-

tional memberships. CERN, he noted, takes up 70% of the ministry's fund for international research, and a small nation such as Austria has a low visibility in such a large endeavor.

Fabjan counters that the ministry received a modest increase in its budget for 2009, although he acknowledges that BMWf still has more commitments than it can afford. "Having too many projects is a good situation. It promotes healthy competition," he says. But the ministry should have been more open in the way it decided between CERN and other efforts, he contends: "The choice was made internally, without consulting the scientific community." Fabjan also points out that Austria's contribution to CERN, which is calculated according to its size and national wealth, is just 0.47% of the ministry's annual budget.

Austria has been a member of CERN for 50 years. Because membership is governed by an international treaty, Austria's withdrawal must be approved by the council of ministers and Parliament, and the order signed by the president. Physicists are hoping that a sustained media campaign will reverse the decision.

CERN, too, is hoping for a different outcome. The lab's director general, Rolf Heuer, visited Vienna to speak with Hahn on 11 May. They agreed to continue discussions and seek an outcome satisfactory to both sides. CERN spokesperson James Gillies says that a number of member states have in the past had trouble paying their fees, but something was usually worked out, such as a temporary rebate. However, Yugoslavia did secede from CERN in 1961 as did Spain in 1969, although Spain rejoined in 1983. Austria accounts for only 2.2% of CERN's budget, but the lab's greater concern, during the financial crisis, is a domino effect. Says Grumiller: "If a relatively rich country like Austria pulls out, it could set other members thinking."

—DANIEL CLERY



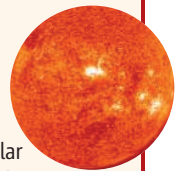
Vanishing point. As CERN makes final repairs to the LHC, its managers look for a way to stop Austria from jumping ship.

ScienceNOW.org

From *Science's* Online Daily News Site

Nice Guys Finish First. In tribal societies, one might expect that the fiercest warriors get the most women and father the most children. But that's not necessarily the case, says a new study of the brutal Waorani tribe of Ecuador, published in the *Proceedings of the National Academy of Sciences*. The most aggressive Wao warriors have about the same number of wives and children as milder-mannered men have, and their children are less likely to survive beyond the age of 15, largely due to an endless cycle of revenge killings. <http://tinyurl.com/r9zbwv>

Unpredictable Sun. Fans of solar storms and power failures are in for some bad news. A panel of the world's solar scientists announced that the next solar maximum—when the sun's irradiance, solar wind, and sunspots are most volatile—is not coming as soon and will not be as strong as predicted. That means fewer solar storms, which can cause power outages here on Earth. <http://tinyurl.com/r4753z>



How Do You Hide a 5-Ton Shark? Every summer, hundreds of basking sharks emerge off the northeast coast of the United States, jaws agape to capture the tiny zooplankton that make up their diet. But by winter, the world's second-largest fish seems to vanish. Now, researchers have used satellites to solve the mystery of the basking sharks' winter home, they report in *Current Biology*. The findings could help conservationists better protect the 10-meter-long sharks, which may number fewer than 10,000 worldwide. <http://tinyurl.com/r9gvrz>

Stronger Than Steel. New supercomputer simulations of the crusts of neutron stars—the rapidly spinning ashes left over from supernova explosions—reveal that they contain the densest and strongest material in the universe. So dense, in fact, that the gravity of the mountain-sized imperfections on the surfaces of these stars might actually jiggle spacetime itself. If so, researchers report in *Physical Review Letters*, neutron stars could offer new insights into gravitational waves. <http://tinyurl.com/on9nqn>

Read the full postings, comments, and more on sciencenow.sciencemag.org.

SWINE FLU OUTBREAK

Flu Researchers Train Sights On Novel Tricks of Novel H1N1

Shortly after receiving word on 23 April that the same odd strain of swine influenza had infected humans in both the United States and Mexico, researchers around the world pounced on this novel H1N1 virus. "I've never seen so many people mobilized for something like this so quickly," says molecular virologist Elodie Ghedin, who specializes in influenza genomics at the University of Pittsburgh School of Medicine in Pennsylvania. Indeed, several journals, including *Science*, have already published papers about the outbreak.

In contrast to the regimented organization of the public health effort, the research community has a free-for-all spirit, more Wikipedia than *Encyclopædia Britannica*. Questions include: Where does this virus come from, how does it do its dirty work, where is it heading, and how do we combat it?

"Everybody is trying to make sure we do the analysis quickly and get the human specimens we need to capitalize on this," says Richard Scheuermann, a molecular immunologist at the University of Texas (UT) Southwestern Medical Center at Dallas. "Even if this virus turns out not to be too virulent, it may help us be prepared to respond rapidly in the situation where the emerging outbreak strain is highly virulent." Another reason, experts say: This H1N1 has also made headway into the Southern Hemisphere, which is entering winter now, influenza's favorite season, putting billions of people at risk. And it may well return to the north in September.

One of the earliest research projects to go public was a wiki-style Web site called "Human/Swine A/H1N1 Influenza Origins and Evolution" created by two evolutionary biologists in the United Kingdom: Andrew Rambaut of the University of Edinburgh and Oliver

Pybus of the University of Oxford. Rambaut and Pybus began pulling sequences of the new virus off public databases on 27 April; by 30 April they had posted the wiki with phylogenetic analyses of the strain's origins. "Researchers were making the sequence data publicly available, so we decided, let's make our analyses publicly available even though they might be provisional," says Pybus. Many others quickly joined in, too.

Their most provocative finding is that the sequences available so far have a common ancestor that dates back to "Septemberish" 2008, says Pybus. "So there were a few good months of transmission of this virus before anyone noticed it," he says. Pybus is also co-author of a paper *Science* published online on 11 May that analyzes the Mexican outbreak, estimating that it infected 23,000 people by the end of April with a case fatality rate similar to an epidemic in 1957 but not as deadly as the infamous 1918 Spanish flu.

Probing origins is tricky because the virus disappears within a week or so of a person becoming infected, but antibodies to the infection last much longer. "It's very important for us to go back and do retrospective serosurveys in Mexico in humans and perhaps pigs," says Jeffrey Taubenberger, a virologist at the U.S.

National Institute of Allergy and Infectious Diseases (NIAID) in Bethesda, Maryland, who has studied the 1918 Spanish flu.

Finding more of the virus's pig ancestors could be key. The current virus, a "triple reassortant," is a hodgepodge of North American swine (30.6%) and avian (34.4%) and Eurasian swine (17.5%) and human (17.5%) flus. It's possible that the Eurasian swine flu virus may have gone undetected in North American swine for many years, says Taubenberger. "We've

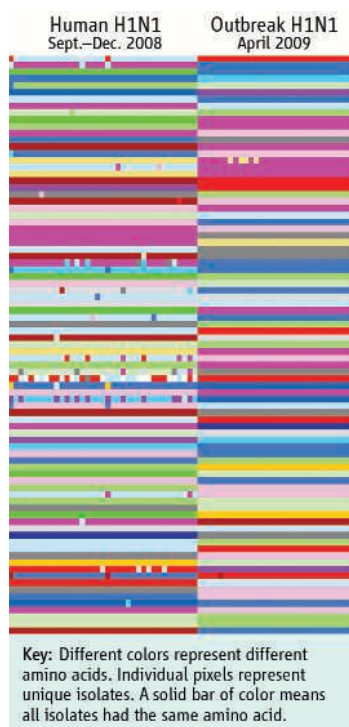
done a great job of getting thousands of human influenza virus sequences, and hundreds, at least, of the bird virus sequences, but very few pig viruses," he says.

So far, the only pigs found to harbor this novel H1N1 are in an isolated herd in Alberta, Canada, but scientists there doubt those animals are the source of the new virus. The Canadian Food Inspection Agency suspects that a carpenter working on the farm who had recently returned from Mexicali, Mexico, with flulike symptoms infected the pigs. Researchers did not isolate virus from the man, probably because they tested him after he recovered, and now are studying his antibodies to see if he had the swine H1N1. They are also sequencing the pig virus, which should clarify its place in the family tree.

Scheuermann has scoured databases to see how each of the eight genes in the current strain compares with previously isolated genes from several species. His group has found similar genes in Southeast Asian and Hong Kong swine from the 1990s that were also in North American birds in 2000. "It could be that the virus in Southeast Asia got transferred from pigs to wild birds in the 1990s, and through migratory patterns went up the northeast coast of Asia and mixed with the wild bird population coming down to North America," he says.

Several groups are attempting to unravel just how virulent the virus is and what genetic changes enabled it to expand its host range from pigs to humans. Sequences from hundreds of isolates have shown that the virus does not have the virulence signatures of the deadly avian influenza that surfaced in humans in 1997 or the catastrophic 1918 strain. As to its efficient transmission, virologist David Spiro, who heads a large flu-sequencing project at the J. Craig Venter Institute (JCVI) in Rockville, Maryland, says the sequence of the most common recent ancestor might reveal the genetic changes that enabled the virus to adapt to humans. "That answer must be out there," says Spiro. But NIAID's Taubenberger says phylogenetics "is just the beginning"; hypotheses must then be studied in test tubes and lab animals. "Looking at where the differences are is interesting, but the key thing is to actually do transmission studies with these parent viruses and the new reassortant virus," he says.

One reason the new strain alarms flu experts is because it differs so radically from other human influenza viruses that our immune systems have little preexisting defense against it. Antibodies to the hemagglutinin glycoprotein—the "H" in H1 that studs the viral surface—play a central role in thwarting infection. A study done by the Uni-



No gray zone. Each row compares an amino acid from the hemagglutinin protein in the seasonal H1N1 (l) with the outbreak virus (r). The two viruses have markedly different amino acids, which means antibodies against one protein likely won't work against the other.

versity of Pittsburgh's Ghedin compared the amino acids in the current isolate's hemagglutinin glycoprotein to the one in the seasonal H1N1 and found little overlap (see diagram).

At the same time, the virus has caused severe disease in otherwise healthy young adults—the group usually least vulnerable to flu—prompting some to speculate that other influenzas or vaccines may provide some protection. And the elderly, the most vulnerable, have largely been spared. Virologist Nancy

Cox, who heads the influenza division at the U.S. Centers for Disease Control and Prevention, says CDC is analyzing antibodies from different age groups to see if the elderly population has some protection from previous flu seasons. No clear answers have surfaced yet. “These are very early days,” says Cox.

Inevitably, the new virus will reassort with existing ones and pick up new bad habits, such as increased drug resistance. Ghedin, who previously worked at JCVI, showed that at least

3% of humans who develop symptomatic seasonal flu are coinfecting by two different influenza viruses. Right now, the swine-origin H1N1 is susceptible to the anti-influenza drugs oseltamivir (Tamiflu) and zanamivir (Relenza), but the seasonal H1N1 has mutations in its neuraminidase gene that render the drugs worthless. If a person becomes coinfecting with both, the genes could swap, and then, JCVI's Spiro warns, “out the window goes the drug treatment regimen we have.”

—JON COHEN

SWINE FLU OUTBREAK

Swine Flu Names Evolving Faster Than Swine Flu Itself

The Germans call it *Schweinegrippe*; French newspapers talk about *la Grippe A*. The World Health Organization (WHO) now calls it “influenza A (H1N1),” and so do government officials in many countries—but not the Dutch, who are sticking with “Mexican flu.” The Mexican ministry of health, meanwhile, often calls it simply *la epidemia*.

Three weeks after the world woke up to the threat of an influenza pandemic, a Babylonian confusion has arisen about what the virus—and the pandemic, if it happens—should be called. Some virologists say WHO's new name, A(H1N1), although politically correct, isn't very clear and is not going to stick.

The U.S. team that first reported two cases of the new virus in the *Morbidity and Mortality Weekly Report* on 21 April called it “swine influenza A (H1N1),” because its genes matched those of viruses previously found in pigs. WHO adopted that name as well; during a 27 April press briefing, WHO flu expert Keiji Fukuda used the word “swine” 22 times. When asked the next day whether that name was appropriate, Fukuda said, “the virus that is identified is a swine influenza virus,” and “we do not have any plans to try to introduce any new names for this disease.”

But protests from the pork industry and the senseless slaughter of all pigs in Egypt announced on 29 April appear to have changed the agency's position. Since 30 April, the word “swine” has not appeared in any of WHO's official statements. Calling it the “Mexican flu” is problematic as well, says WHO spokesperson Dick Thompson: “We're very aware of the potential for stigmatization,” and besides, it's not certain that the virus originated in Mexico.

Health officials in many countries avoid the porcine and Mexican connections as well. Within days after the first report, U.S. Department of Agriculture officials started pointing

out that the new virus had never been found in pigs, says Anthony Fauci, director of the National Institute of Allergy and Infectious Diseases, and government officials started “veering away” from the term swine flu.

In *MMWR*, researchers from the U.S. Centers for Disease Control and Prevention (CDC) came up with several creative alternatives, including, on 28 April, “swine-origin influenza A (H1N1) virus,” or S-OIV for short. In the 6 May update of *MMWR*, CDC coined the name “novel influenza A (H1N1) virus.” “It's clearly a name that is evolving fast,” says Derek Smith, who studies flu evolution at the University of Cambridge in the United Kingdom.

The problem with WHO's name, A(H1N1), is that it isn't specific, says virologist Albert Osterhaus of Erasmus Medical Center in Rotterdam, the Netherlands. One of the three subtypes that make up seasonal influenza every year is also an A(H1N1), and so is the virus

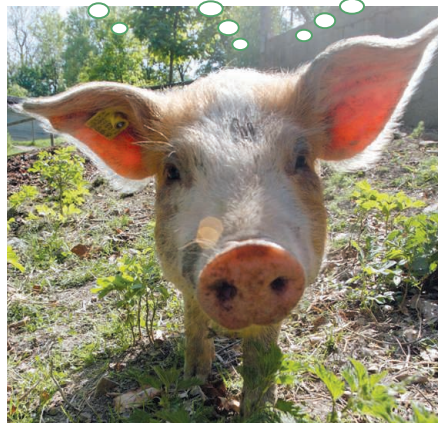
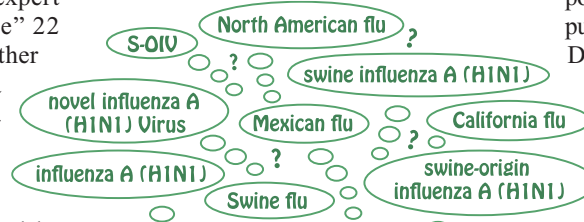
that caused the 1918–19 pandemic, widely known as the Spanish flu.

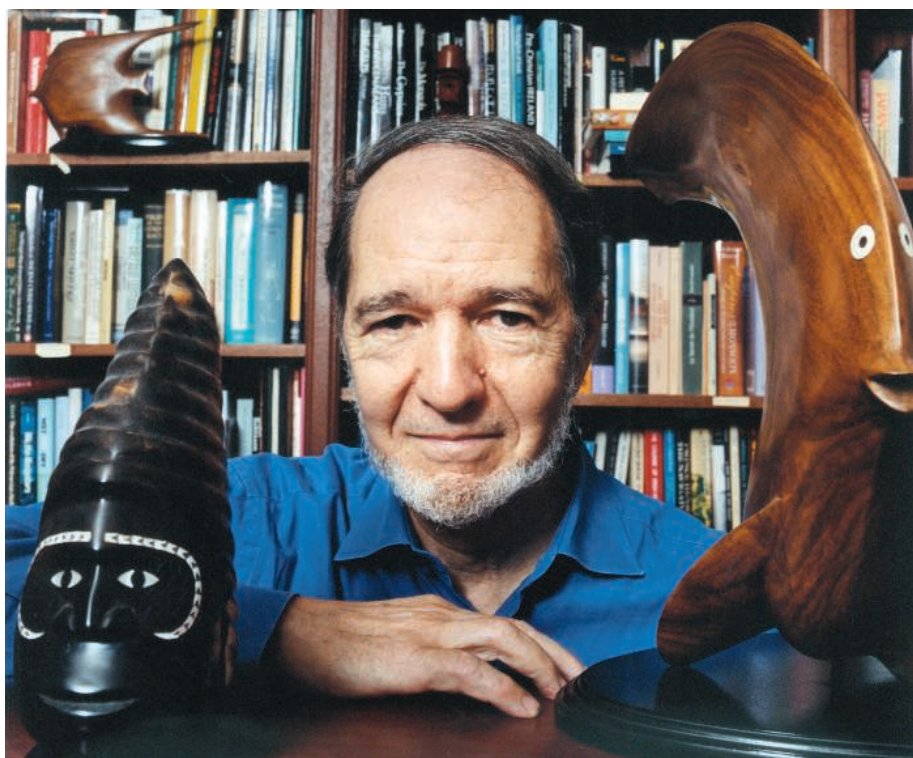
The International Committee on Taxonomy of Viruses, the official custodian of virus names, deals only with newly discovered viruses, says Australian virologist John Mackenzie, ICTV's vice-president. It has no official opinion on what particular flu strains should be called.

Nobody is in charge of naming pandemics either. The Spanish flu didn't originate in Spain; it got its name because of the mistaken idea that that country was hit first. The 1957–58 pandemic, first seen in China and caused by H2N2, came to be known as the Asian flu. The pandemic of 1968–69, an H3N2 strain, went down in history as the Hong Kong flu, because that's where the first known outbreak occurred. Calling the new outbreak the “Mexican flu” fits nicely with that tradition, says Osterhaus, who believes that it will be the popular name for the pandemic no matter what public health officials say. That's also why the Dutch Outbreak Management team, an expert group of which he is a member, continues using the term “Mexican flu,” as does the Dutch government. (Their insistence has triggered a fiery letter from the Mexican embassy in The Hague.)

Thompson says there are “ongoing discussions” at WHO about other names. Ideas abound: Some have suggested the “North American flu” in an effort to continue the geographic tradition without singling out any country. Others have suggested the “California flu” because the two patients described in the first *MMWR* were children from southern California. Influenza vaccine expert David Fedson likes the California connotation but has a better idea. “I favor calling it the ‘Schwarzenegger virus,’” Fedson says. “If it leads to a terrible pandemic, we'll call it ‘the Terminator.’ Then everyone will know what we're talking about.”

—MARTIN ENSERINK





'Vengeance' Bites Back At Jared Diamond

Two tribesmen from Papua New Guinea sue the prominent biologist over a popular magazine article about the human thirst for retribution

IN APRIL 2008, WELL-KNOWN BIOLOGIST and author Jared Diamond penned a dramatic story in *The New Yorker* magazine, a violent tale of revenge and warfare in Papua New Guinea (PNG). Titled "Vengeance is Ours" and published under the banner "Annals of Anthropology," the 8000-word article tells the story of a clan war organized by a young Papua New Guinean named Daniel Wemp to avenge the death of Wemp's uncle, Soll. In Diamond's telling, the war started in the 1990s over a pig digging up someone's garden, went on for 3 years, and resulted in the deaths of 29 people. In the end, Diamond wrote, Wemp won: His primary target, a man Diamond referred to as "Isum," had his spine cut by an arrow and was confined to a wheelchair. Diamond juxtaposed Wemp's story with that of his own father-in-law, a Holocaust survivor who never exacted retribution for the loss of his family, to draw an overall lesson about the human need for vengeance.

In recent weeks, Diamond's article itself seems to have come back with a vengeance. On 20 April, Diamond, 71, was sued in the Supreme Court of the State of New York for allegedly defaming both Daniel Wemp and Isum Mandingo, the alleged target of Wemp's revenge war. The lawsuit, which also names as a defendant Advance Publications Inc., the owner of *The New Yorker*, demands at least \$10 million in damages. It follows a yearlong investigation led by Rhonda Roland Shearer, an artist and the widow of evolutionary biologist Stephen Jay Gould. Shearer directs the Art Science Research Laboratory, a non-profit organization based in New York City that she and Gould founded before Gould's death in 2002. Among its activities is a journalism ethics program and a Web site called Stinkyjournalism.org, which published the Shearer team's 10,000-word report, "Jared Diamond's Factual Collapse," the day after the lawsuit was filed.

In the report, Shearer and her colleagues,

Face-off. Jared Diamond is being sued for allegedly defaming Papua New Guinea tribesmen in an article in *The New Yorker*.

who included three researchers in PNG, claim that Diamond and *The New Yorker* got many important facts wrong in the original article, including the contentions that Wemp had personally organized the warfare, that Soll was his uncle, and that Mandingo had been paralyzed by an arrow. Indeed, the Stinkyjournalism.org report includes a recent photograph said to be of Mandingo standing and looking strong and healthy. The report maintains that neither Wemp, Mandingo, nor any other of several New Guineans named in *The New Yorker* were told about the article beforehand. It also claims that Wemp's life is now in danger from other clans that might want to avenge Mandingo's alleged injuries, or even from members of his own clan for portraying them as ruthless killers.

Diamond stands by his story, arguing that it was based on detailed notes that he took during a 2006 interview with Wemp as well as earlier conversations the two men had in 2001 when Wemp served as his driver in PNG. "The complaint has no merit at all," Diamond told *Science* in an interview in his office at the University of California, Los Angeles, where he is a professor of geography. Diamond adds that he still considers Wemp's original account to be the most reliable source for what happened. David Remnick, editor of *The New Yorker*, also defends the magazine's story: "It appears that *The New Yorker* and Jared Diamond are the subject of an unfair and, frankly, mystifying barrage of accusations."

The affair has raised concerns among anthropologists familiar with PNG, who worry that *The New Yorker's* "Annals of Anthropology" banner has tarnished the field's reputation. Anthropologist Pauline Wiessner of the University of Utah in Salt Lake City, a leading expert on tribal warfare in PNG, thinks Diamond was naïve if he accepted Wemp's stories at face value, because young men in PNG often exaggerate their tribal warfare exploits or make them up entirely. "I could have told him immediately that it was a tall tale, an embellished story. I hear lots of them but don't publish them because they are not true."

Different worlds

Three worlds collide in this case. First is the world of science, specifically anthropology, which uses fieldwork and scientific methodology to study human cultures. Next is the craft of journalism, with its own set of ethics

CREDIT: 2005 TOM JOHNSON/BLACK STAR/NEWS.COM

and practices aimed at reaching the general public. Finally, there is Papua New Guinea, a young nation still struggling to integrate many hundreds of tribes and clans into a modern state. For many years, Diamond, a physiologist by training, has worked in all three domains: He is a member of the U.S. National Academy of Sciences and a winner of the National Medal of Science, as well as a highly successful writer. In 1998, he won a Pulitzer Prize for his bestseller *Guns, Germs, and Steel*, on the geographic factors that made some societies rich and some poor. His most recent book, *Collapse*, about the environmental forces that brought some societies down, has also sold well. And he has regularly visited PNG for nearly 50 years, although primarily to study the island's birds rather than its people.

Although Diamond's frequent merging of these worlds has brought him both success and some criticism, this time it may have landed him in legal trouble. When Diamond's article appeared in *The New Yorker*, it drew the attention of Shearer, a fierce media critic who in recent years has gone after numerous reporters for alleged transgressions of journalistic ethics. (One of her most celebrated campaigns was against journalist William Langewiesche, who asserted in a book that firefighters had looted blue jeans from stores in the World Trade Center after the 9/11 attacks.) Shearer says that after reading Diamond's article, which appeared in the 21 April 2008 issue of *The New Yorker*, she immediately was "very skeptical" at the suggestion that Mandingo could have continued to live in the remote, rugged PNG Highlands while confined to a wheelchair and perhaps needing special medical care. She e-mailed Diamond and *The New Yorker* asking if they had verified this and other details; Shearer says that she received no response from Diamond and that the magazine's initial reaction was to say that it stood by its story.

Shearer already had contacts in PNG from an earlier investigation during which she chased down rumors that a Komodo dragon was running amok in the country. (It turned out to be a hoax.) She asked her contacts to try to find Wemp. One, biologist Michael Kigl of the PNG Institute of Biological Research in Goroka, explained to *Science* that he was able to contact one of his own relatives in Wemp's province, who in turn managed to help locate one of Wemp's relatives. Thus Kigl found Wemp in his Highlands village in July 2008 and tape recorded an interview with him. According to Shearer and the 10,000-word report, Wemp denied organizing the revenge warfare attributed to him in Diamond's story.

The report says that Wemp expressed surprise at *The New Yorker* article and claimed that Diamond had never told him about it. (Wemp's attorneys in New York City and PNG declined to make him available for an interview for this story, saying that their clients preferred to tell their stories in court and not in the press.) According to the report, the following month Kigl also located Isum Mandingo and took several photographs of him standing and walking.

At least one other Papua New Guinean supports the account of Shearer's team. "Diamond's article is a confused story that names real places and persons but mixes up false, wrong, and defamatory allegations that bring into disrepute the good name of the named clans and their members," said Mako Kuwimb, a member of Wemp's Handa



Annals of unease. Some anthropologists thought *The New Yorker* banner reflected poorly on their discipline.

clan and a PNG attorney now doing graduate work at James Cook University in Queensland, Australia. In an e-mail to *Science*, Kuwimb added that PNG Highlanders are accustomed to having anthropologists among them, "and we know what [they] do and how they gather information." Diamond, Kuwimb says, "converted a simple, casual conversation [with Wemp] into an article that looks and sounds like an anthropological piece" but "never followed [anthropological] procedures and protocols." On 21 April of this year, Kuwimb sent *The New Yorker's* publisher, Lisa Hughes, a detailed, 30-page refutation of

the Diamond article. Among Diamond's biggest errors, Kuwimb told Hughes, were his statements that the war he described had begun with the "pig in the garden" episode and had lasted 3 years. Kuwimb contends that the war was sparked by a gambling dispute and lasted only a few months.

Some anthropologists have their own concerns with Diamond's article. For starters, many think that the "Annals of Anthropology" banner was misleading. "*The New Yorker* was wrong to imply that Diamond was an anthropologist or that what he wrote was anthropology," says Dan Jorgensen of the University of Western Ontario in London, Canada, who has worked in PNG since the 1970s. Cultural anthropologist Alex Golub of the University of Hawaii, Manoa, who says *The New Yorker* fact checker spoke with him for about 10 minutes while the story was being prepared, agrees. "This affects our discipline's brand management," he wrote on an anthropology blog he participates in called *Savage Minds*. "It's important for people to know that if they meet an anthropologist, they are not going to be written up in *The New Yorker* without being told about it." *Savage Minds* has now teamed up with *Stinkyjournalism.org* to produce a series of invited essays on the case.

A number of researchers say that Diamond should not have used the names of real people and real clans; cultural anthropologists

often use pseudonyms for the people they write up and follow strict ethical guidelines for informed consent when they do name people. Wiessner thinks Diamond should have refrained from naming even the tribes involved. "That was a very big mistake," she says.

Journalism versus science

But both Diamond and Remnick insist that such anthropological criticisms are irrelevant, because Diamond was working as a journalist for a popular magazine, not as an anthropologist writing a scholarly article. Although Diamond says he did not find out about the "Annals of Anthropology" line until shortly before publication and now regrets it, Remnick points out that the magazine routinely uses the "Annals" logo for stories not written by trained experts in the field at hand. Says Diamond, "Everyone knows that *The New Yorker* is not a scientific publication; it's journalism." That's why he used the names Wemp gave him, he says. "In journalism, you do name names so that people can check out what you write." Remnick agrees: "Journalistic practice differs from scientific practice in a number of ways," he says, "and this seems to

be one of them. Using real names is the default practice in journalism.”

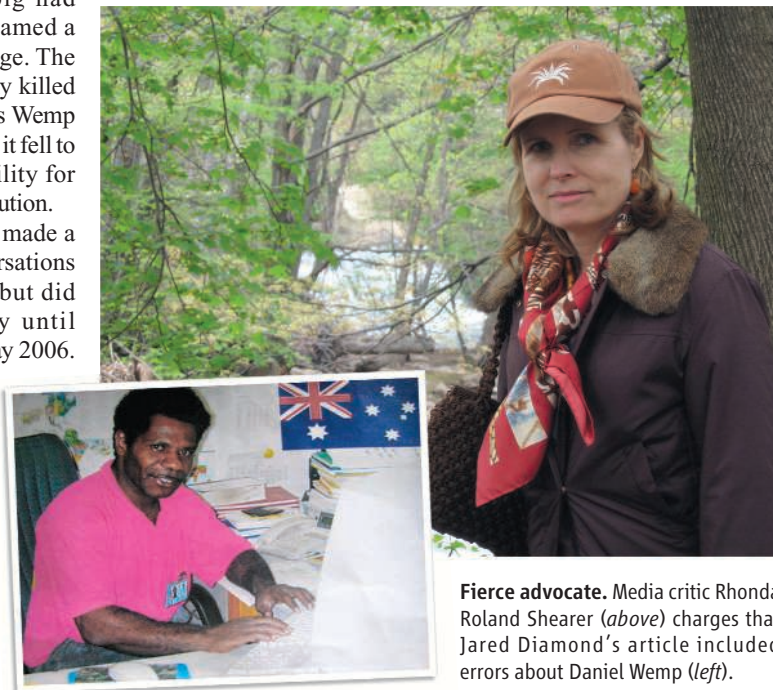
Diamond insists that he followed good journalistic practice and that his article was based on detailed notes he took of the stories that Wemp told him. In 2001, Diamond says, Wemp drove him and Australia-based ornithologist David Bishop around the oil fields of Highland PNG as they conducted a survey of local birds. During several long drives, Diamond says, Wemp told them stories about the Highlands war that had supposedly begun when a man from Mandingo’s clan, the Ombal, found that a pig had ruined his garden and blamed a Handa man for the damage. The ensuing warfare eventually killed Soll, whom Diamond says Wemp identified as his uncle, and it fell to Wemp to take responsibility for organizing a war for retribution.

Diamond says that he made a few notes of these conversations when back in his room but did nothing with the story until another trip to PNG in May 2006. By then he had begun work on a new book about tribal societies and contacted Wemp to get a more detailed account of the war Wemp had described 5 years earlier. Diamond says that in 2006, he told Wemp explicitly that the story would go into the book. But he was unable to find Wemp again in 2007 when he decided to excerpt one of the book’s chapters for *The New Yorker*; Wemp had left his job without leaving contact information, Diamond says.

In 2006, “I said to Daniel, ‘Would you be willing to tell the whole story in one piece and I will take notes?’” Diamond says. He pulled out a large, red notebook and took “sentence by sentence” shorthand notes of the conversation, Diamond says, adding that Wemp spelled out the names of the warriors and other individuals who would later be named in *The New Yorker* piece. (Both Diamond and Shearer agree that Bishop was present during some of the May 2006 conversation; reached by telephone, Bishop declined to comment.) The Shearer account agrees that Diamond took notes in shorthand in a red notebook but differs markedly about what Wemp said.

Diamond says that although Wemp clearly understood that he would be named in the book, he did not try to get permission from Mandingo and the others: “I trusted Daniel’s

judgment about what was appropriate to discuss.” Diamond says he did double-check Wemp’s story with some younger members of his tribe, who confirmed that some of the people Wemp named had been involved in a tribal war. Diamond also told *Science* that he heard conflicting accounts about how serious Mandingo’s injuries were and that Mandingo now may have recovered from his wounds. In regard to *The New Yorker*’s fact checking, Remnick says that the fact checker was unable to find Wemp before the story was published. After Shearer’s team found Wemp,



Fierce advocate. Media critic Rhonda Roland Shearer (*above*) charges that Jared Diamond’s article included errors about Daniel Wemp (*left*).

however, the fact checker did speak with him by telephone, on 21 August 2008. Soon afterward, Shearer, who had kept in regular touch with the magazine, scored her first victory: In a 12 September 2008 letter to a London attorney, *The New Yorker* general counsel Lynn Oberlander agreed, “as a sign of good will,” that the magazine would remove Diamond’s article from the freely accessible part of its Web site, although it is still available online to registered subscribers.

Remnick nevertheless defends the magazine’s efforts to verify Diamond’s story. He says that this particular fact checker “is one of the best I have ever had the privilege of working with.” And he adds that “we had Jared Diamond’s meticulous, detailed notes from the 2006 interview with Daniel Wemp, ... and we consulted with people with expertise in the Southern Highlands, who confirmed that Daniel Wemp’s description of the revenge battle was consistent with known practice.” Remnick also insists that in the August 2008

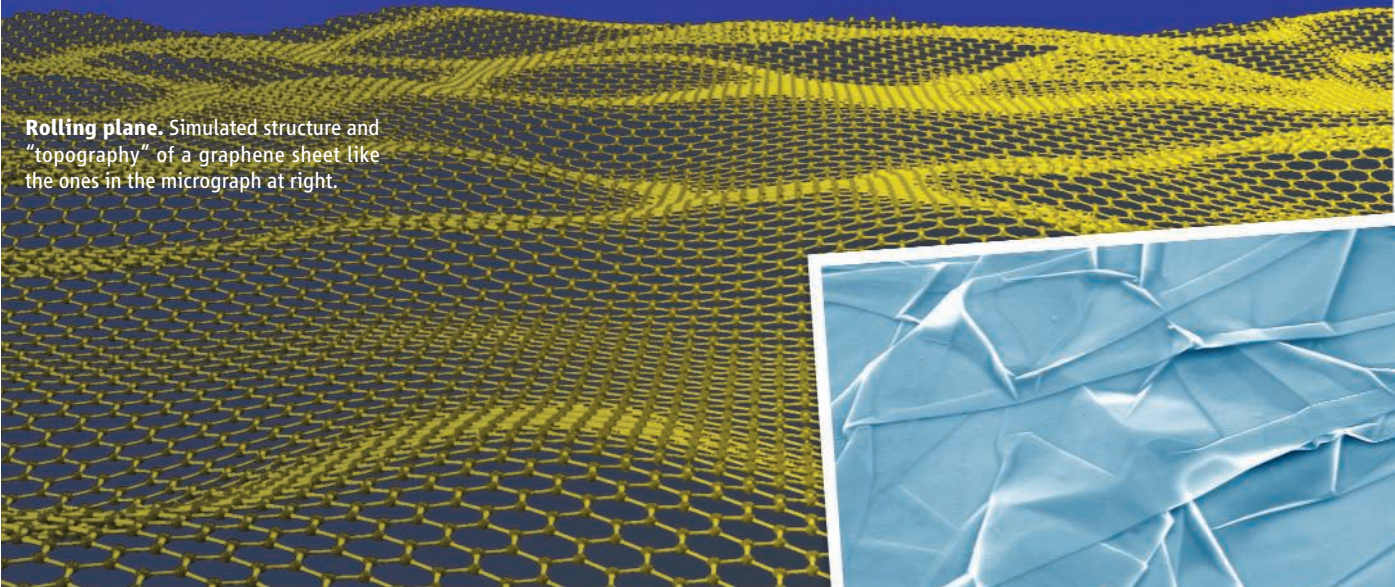
conversation between Wemp and the fact checker—which was tape recorded by mutual consent—Wemp raised only relatively minor factual objections to Diamond’s account and asserted that the stories were basically true. In Diamond’s view, the case is really about scientists coming under fire for popular writing.

Whether or not Diamond got the facts of Wemp’s case right, it is true that the tribes of PNG do practice revenge warfare, says Wiessner, who has studied war in PNG’s Enga Province, just north of the region where Wemp and Mandingo live. In Enga, more than 300 tribal wars have taken the lives of nearly 4000 people since 1991. That’s one reason Wiessner, who is active in local efforts to bring peace to PNG clans, is worried about the outcome of the case if it results in a large monetary award: She fears that the money could eventually go to buy weapons that would make the wars even more deadly. “When these wars first started, they were fought with bows and arrows, but now they have M-16s,” she says. And although Wiessner faults Diamond for apparently taking Wemp’s stories at face value, she also believes Wemp himself violated clan ethics by telling them in the first place. “For him to have given the names of tribes and implicate[d] other people than himself,” as Diamond reported, “that was wrong,” she says. “He should have sought approval of the clan elders beforehand.”

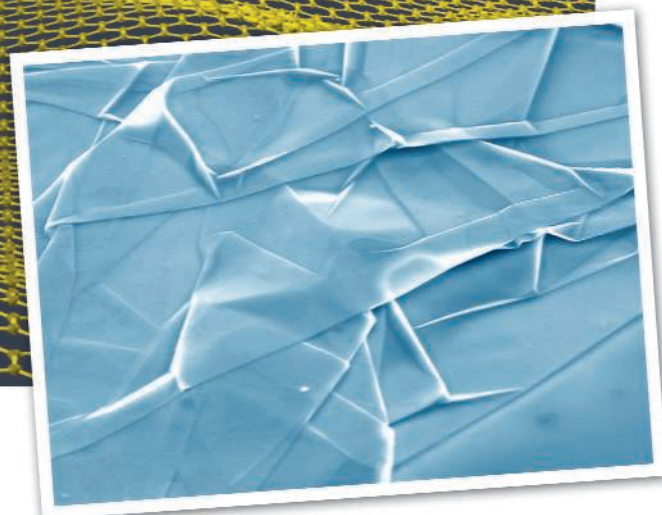
In Wiessner’s view, *The New Yorker* article gave a one-sided view of tribal warfare. Although the death toll often seems high, she says Highlanders are expert practitioners of what anthropologists call “restorative justice”: the mediation of disputes in which aggrieved parties receive compensation from those who have wronged them, thus avoiding warfare. “Diamond did not put it into that context,” Wiessner says. She thinks that Diamond should travel to PNG and engage in some restorative justice of his own. “Diamond has been wonderfully respectful of PNG and has done so much to raise the image of the country in the world, until that story,” Wiessner says. “He should be taken to a village court; he should apologize; he should say that he was told this story and he should have checked it; and in compensation, he should give some money to each tribe, for their schools, a health center, or some community project.”

—MICHAEL BALTER

CREDITS: RONALD R. SPADAFORA; (INSET) STINKYJOURNALISM.ORG/DANIEL WEMP



Rolling plane. Simulated structure and "topography" of a graphene sheet like the ones in the micrograph at right.



MATERIALS SCIENCE

Carbon Sheets an Atom Thick Give Rise to Graphene Dreams

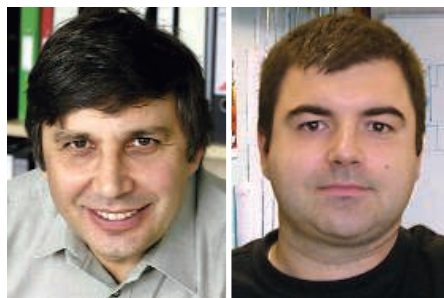
Interest in a novel material with amazing properties continues to sweep through physics and chemistry labs worldwide. Will graphene's promise pay off?

The lab-coat realm of science may seem worlds away from the fashion-crazed frenzy of New York City's Garment District. Yet science is not immune to fashion trends. Take the science of new materials: High-temperature superconductors, organic electronic materials, even cold fusion have all been trendy topics—some for longer than others. Scientists flock to new areas that show unique promise and offer knotty riddles, but careers can depend on which fashions have staying power and which are mere fads.

When a material called graphene, which consists of single-atom-thick sheets of carbon, came along 5 years ago and caught a spark, it was hard to tell which way it would go. Researchers quickly discovered that these sheets are very strong yet flexible and highly conductive. So interest spiked. But would graphene be a flash in the pan?

Half a decade after its arrival on the scene, graphene is showing staying power. Last year, researchers churned out some 1500 papers on graphene. The number of Google searches on the topic rivals the number for carbon nanotubes, another hot topic with a 20-year head start. "It's gone from zero to infinity," says George Flynn, a chemical physicist at Columbia University. And the torrent shows no sign of abating. "I don't see it saturating anytime soon," says Andre Geim, a physicist at the University of Manchester in the United Kingdom, who led the team that first isolated flecks of graphene back in 2004.

It's easy to see why. Graphene's carbon atoms, which are arranged in a chicken-wire pattern of hexagons, give it a perfect crystalline order. This order makes graphene the strongest material ever made when yanked along the sheets, yet it flexes like plastic wrap. It's also an outstanding heat conductor. Electrons whiz through the sheets at rates far beyond those achieved in other materials. All these characteristics have made graphene a playground for researchers including theoretical and high-energy physicists, chemists, and computer-chip-device makers looking to lend graphene's exceptional properties to tomorrow's ultrasmall gadgetry. "Graphene is amazing in basically every perspective," Vitor Pereira, a physicist at Boston University, told attendees at the recent American Physical Society (APS) meeting in Pittsburgh, Pennsylvania, which featured 23 packed sessions on graphene.



Instigators. Andre Geim (left) and Konstantin Novoselov first isolated graphene in 2004.

Uncertain beginnings

It was never obvious that graphene could exist as a freestanding sheet. Throughout the 1980s and 1990s, a variety of research groups worked to extract single layers of graphene from graphite, the "lead" in pencils, which is made up from stacks of graphene sheets. The sheets in graphite are only loosely bound together, which is why scraping a pencil along a piece of paper leaves them behind. Early on, researchers tried to cleave ever-thinner slices from those three-dimensional flecks of graphite. That worked to a point but typically left scientists with thin stacks of about 100 layers of graphene. So groups tried other approaches, such as chemically wedging other atoms between the stacks to exfoliate single sheets or using an atomic-force microscope tip to drag a graphite fleck over a surface in hopes of dislodging a single sheet.

In 2004, Geim and his Manchester colleague Konstantin Novoselov, together with others in Manchester and at the Institute of Microelectronics Technology and High Purity Materials in Chernogolovka, Russia, reported that they had found a simple way to do the job. In a technique that left a lot of people slapping their foreheads and wishing they had thought of it first, Novoselov simply placed a fleck of graphite between two layers of cellophane tape, peeled them apart, and repeated the process multiple times. Eventually, they whittled the graphite down to single layers (*Science*, 22 October 2004, p. 666).

Once graphene was isolated, the race was on to see what it could do. Even in their first *Science* paper, Geim and his colleagues saw some alluring properties. For starters, electrons traveling over microscopic distances raced through graphene with little of

the electrical resistance common to other materials, likely because graphene is so atomically pristine that it contains few defects to scatter electrons. The researchers also patterned electrodes atop it to create a transistor. By applying different voltages to their electrodes, they could control the numbers of negatively charged electrons and positively charged electron vacancies (also known as “holes”) left behind when a conducting electron surfs from one atom to another. The achievement marked the first time such a “field effect” had been seen in a single-layer conductor.

Those early studies revealed that graphene was a semimetal, a versatile charge carrier that conducts both electrons and holes. The Manchester team’s original study found that charges moved through the group’s devices at up to 10,000 centimeters squared per volt second (cm^2/Vs), the standard unit of current velocity. By contrast, electrons zip through silicon, the workhorse

of electronics, at a mere $1500 \text{ cm}^2/\text{Vs}$ and through high-speed gallium arsenide (GaAs) at $8500 \text{ cm}^2/\text{Vs}$. That initial electron speed record didn’t last for long: In 2008, Geim and his colleagues reported that electrons could fly through graphene at an unheard-of $200,000 \text{ cm}^2/\text{Vs}$. At the recent APS meeting, Columbia University postdoctoral assistant Kirill Bolotin reported that he and colleagues had increased the speed to $250,000 \text{ cm}^2/\text{Vs}$ by chilling a sheet of graphene to 5 kelvin and suspending it between a pair of tiny pillars.

Lending a hand

Graphene’s high speed for electrons and other remarkable properties are promising practical payoffs in applications as diverse as energy-storing capacitors and sensors. Most of the excitement right now focuses on using graphene to improve silicon-based computer chips, which form the backbone of a \$260-billion-a-year industry. Chipmakers

have thrived over the past 4 decades by continually shrinking the dimensions of transistors and other devices and packing more of them into a tighter area, thereby steadily increasing computing power. But researchers are nearing the limits of conventional transistors, which rely on silicon as the semiconductor to ferry electrical charges in a channel between electrodes. One strategy for further boosting the performance of transistors is to replace the silicon channel with a better conductor.

For use in conventional transistors, however, graphene is too good a conductor. A key property of a semiconductor is that its conductivity can be switched on and off: Digital circuits differentiate between binary “0s” and “1s” by whether a semiconductor transmits an electrical current. But graphene’s conductivity never turns off.

That shortcoming doesn’t automatically count graphene out for use in chips. It could prove handy in mobile phones, for example. Cell phones use analog-based radiofrequency

RELATIVISTIC PHYSICS IN THE LAB

Graphene holds enormous promise for transistors and other electronic devices. But it is already making an impact in the arcane world of high-energy physics.

That’s because electrons in graphene don’t behave like electrons in a standard metal. In the lattice of a typical metal, electrons feel the push and pull of surrounding charges as they move. As a result, moving electrons behave as if they have a different mass from their less mobile partners. When electrons move through graphene, however, they act as if their mass is zero—behavior that makes them look more like neutrinos streaking through space near the speed of light.

At such “relativistic” speeds, particles don’t follow the usual rules of quantum mechanics. Instead, physicists must invoke the mathematical language of quantum electrodynamics, which combines quantum mechanics with Albert Einstein’s relativity theory. Even though electrons course through graphene at only $1/300$ the speed of neutrinos, physicists realized several years ago that the novel material might provide a test bed for studying relativistic physics in the lab.

Andre Geim and his team at the University of Manchester in the United Kingdom pounced on the idea. In the September 2006 issue of *Nature Physics*, they suggested that by tracking the way charges move in graphene, scientists might be able to demonstrate a 90-year-old quantum mechanical oddity called the Klein paradox. In 1929, Swedish physicist Oskar Klein came up with a thought experiment: What would happen if a relativistic particle—one traveling near the speed of light—tried to cross a high-energy barrier? Quantum mechanics states that subatomic particles behave not like tiny billiard balls, which exist in one definite place at a given time, but like waves in which the probability of their being in any one place is spread out. Such ephemeral behavior suggests that a low-speed particle has a small chance of “tunneling” through a modest energetic

barrier, because the particle’s wavelike nature gives it some probability of appearing on the other side. Electron tunneling is commonly seen in modern materials and even vexes computer-chip designers by enabling electrons to stray to where they are not wanted. To keep the electrons on course, computer makers raise energy barriers around electrical conductors by surrounding them with strong insulators.

Klein realized that when electrons travel at relativistic speeds, the likelihood that they will tunnel through a barrier can skyrocket. That’s because in the spooky world of quantum mechanics, within which particles can wink in and out of existence, a relativistic particle that hits a barrier can generate its

own antiparticle, in this case a positron. The electron and positron can then pair up and travel through the barrier as if it weren’t even there.

Experimental physicists love a good challenge, and several groups sought to use graphene to turn Klein’s thought experiment into reality. After some initial progress by others, Columbia University physicist Philip Kim and his graduate student Andrea Young recently confirmed that Klein tunneling occurs in graphene. Young and Kim patterned a trio of electrodes atop a graphene sheet, allowing

them to raise a narrow energetic barrier to charges moving through the graphene. The quantum mechanical waves of charges moving through this barrier create an interference pattern. In the March 2009 issue of *Nature Physics*, the pair reported that when they turned a magnetic field on these charges, it shifted their interference pattern—the expected signature of Klein tunneling (see figure).

“It’s the first step in realizing quantum field effects in graphene,” Young says. Kim adds that the insights that can be gleaned using graphene are just beginning. Most materials, he notes, are complex, dirty mixtures of atoms, impurities, and defects, which make calculating their expected behavior nearly impossible. But that problem goes away with graphene. “For the theorists, it’s one of the simplest systems. But it has very rich physics,” Kim says.

—R.F.S.



Klein’s fingerprint. Wiggles in this interference pattern verified a 90-year-old paradox.

(RF) circuitry. Instead of digital circuitry's simple on/off states, RF devices differentiate signals by their relative strength. RF circuits are traditionally made from high-priced semiconductors such as GaAs and indium phosphide (InP). Because charges move more quickly in graphene, it has a shot at beating out conventional devices.

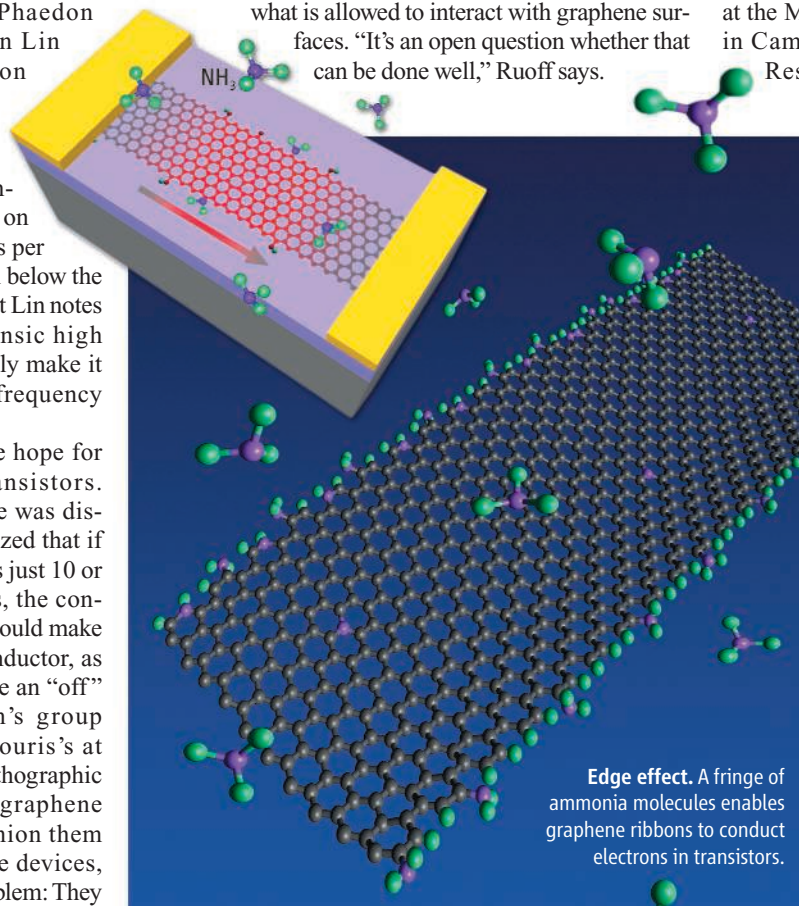
Progress is already beginning. In the 14 January issue of *Nano Letters*, for example, researchers led by Phaedon Avouris and Yu-Min Lin at IBM's T. J. Watson Research Center in Yorktown Heights, New York, reported making graphene transistors that can switch on and off 26 billion times per second. That's still well below the performance of InP. But Lin notes that graphene's intrinsic high speed should eventually make it possible to push the frequency much higher.

There may even be hope for digital graphene transistors. Even before graphene was discovered, theorists realized that if it were cut into ribbons just 10 or 20 nanometers across, the confinement of electrons could make the material a semiconductor, as crowding would enable an "off" state. In 2007, Kim's group at Columbia and Avouris's at IBM reported using lithographic patterning to create graphene nanoribbons and fashion them into transistors. Those devices, however, still had a problem: They didn't show as large a difference in the conductivity between the off and on states as chipmakers would like for reliable circuits.

A team led by Hongjie Dai, a chemist at Stanford University in Palo Alto, California, improved matters with a scheme for making nanoribbons chemically, which produced much larger on/off ratios (*Science*, 29 February 2008, p. 1229). Those devices turned out to be good at ferrying positive charges, making them positive, or p-type, transistors. To make modern circuitry, however, chipmakers need negative-charge-conducting, or n-type, transistors as well. In the 8 May issue of *Science* (p. 768), Dai's group reported that by adding ammonia groups to the edges of the graphene nanoribbons, they can "dope" the material and use it to make n-type transistors. Rodney Ruoff, a chemical engineer at the University of Texas (UT),

Austin, calls the progress "encouraging."

Even so, graphene transistors remain a long way from finding their way into your next computer. Numerous groups have recently shown that atoms and surfaces that sit next to graphene can dramatically influence its conductivity, among other properties. So making millions of devices that all work the same way—an essential property for computer chips—will require controlling exactly what is allowed to interact with graphene surfaces. "It's an open question whether that can be done well," Ruoff says.



Edge effect. A fringe of ammonia molecules enables graphene ribbons to conduct electrons in transistors.

Growing prospects

Up to this point, an even bigger hurdle has been manufacturing large-area graphene films, say Ruoff, Geim, and others. Geim acknowledges that his team's original cellophane-tape approach to making graphene flakes has little chance of being scaled up into an industrial operation capable of covering the 300-millimeter-wide silicon wafers that are the industry's standard substrate. So researchers around the globe have been racing to come up with other ways to grow large-area graphene films at low cost.

Several groups have made steady progress in growing graphene atop wafers made from silicon carbide. The technique uses high temperatures to boil off silicon from the outer surface of the wafer, leaving

graphene behind. Researchers have created large graphene sheets with this approach. But because there is no easy way to peel those graphene layers off the expensive silicon carbide wafer, many groups are looking for answers elsewhere.

They've been finding them. "There has been spectacular progress in the last 2 or 3 months," Geim says. In 2008, for example, a team led by Jing Kong, an electrical engineer at the Massachusetts Institute of Technology in Cambridge, reported at the Materials Research Society meeting in Boston that they had used a technique known as chemical-vapor deposition to grow large graphene sheets atop thin nickel films sitting on silicon wafers (*Science*, 19 December 2008, p. 1785). They also showed that they could pattern the graphene films using a simple stamping procedure. In the 5 February issue of *Nature*, researchers at Sungkyunkwan University and the Samsung Advanced Institute of Technology, both in South Korea, reported that they had extended the technique to transfer high-quality nickel-grown films onto sheets of transparent plastics for use as transparent electrodes in light-emitting diodes and other devices.

Researchers are growing large graphene sheets on other metals as well. In a paper posted online in *Science* on 7 May (www.sciencemag.org/cgi/content/abstract/1171245), Ruoff's team at UT, working with researchers at Texas Instruments in Dallas, reports using a similar technique to grow large-area graphene films on thin copper foils. Both the nickel and the copper growth techniques form highly pure graphene. But because copper normally forms larger grains that network themselves together in sheets, it makes larger regions of pristine graphene, Ruoff says.

Will larger area graphene sheets ensure that the ultrathin carbon membrane will be a scientific or commercial success? Not necessarily, Ruoff and others say. But materials science, physics, and chemistry are crowded, highly competitive fields. "People are desperately looking for a new idea," Avouris says. So far, graphene is offering them in bunches. As long as that continues, graphene will remain firmly in fashion.

—ROBERT F. SERVICE



Termination. Both the Shepherd Spacecraft (foreground) and Atlas upper stage will hit the moon.

LUNAR RESOURCES

Two Missions Go in Search of A Watery Lunar Bonanza

Frustrated by long-controversial hints of water ice on the moon, researchers-turned-miners are going to blast for the mother lode in hopes that astronauts can use water to fuel a permanent moon base

Almost half a century ago, theoreticians began arguing that the moon—despite blistering midday temperatures—harbors cons-old permanent ice. Orbiting spacecraft eventually found hints of ice near the lunar poles, but the remote observations weren't convincing. Now, scientists are going for broke in their search for lunar water that could fuel and water a long-duration presence on the moon.

Early next month, NASA plans to launch an Atlas 5 rocket to the moon. It will carry a rather conventional spacecraft, Lunar Reconnaissance Orbiter (LRO), designed primarily to peer down in search of safe landing sites for future astronauts. But piggy-backing on the Atlas launch will be the Lunar CRater Observation and Sensing Satellite (LCROSS) mission. Actually, most of LCROSS *is* the Atlas, as the one mission

involves two craft bound for the moon. The Shepherd Spacecraft bearing LCROSS's brains, eyes, and maneuvering jets will send the spent Atlas upper stage to a 7200-kilometer-per-hour impact on the moon this fall. Minutes later, the shepherd will crash as well. The terminal encounters are intended to blast lunar water—if any—high above the surface for all the world to see.

No one is sure that the water is there, where exactly it would be, or how well the \$80 million LCROSS will excavate it, but scientists are looking forward to the big splat. "I think it's highly likely that there's ice," says lunar scientist Paul Spudis of the Lunar and Planetary Institute (LPI) in Houston, Texas. "If there is no ice there, I don't really care. But I want to know." That urge to know—and the lure of a resource easily convertible to a high-energy fuel of oxygen and

hydrogen—have driven the decades-long and often exasperating search for lunar ice.

Hints but no pay dirt

Apollo moon rocks are drier than bone dry, yet ice on the moon makes abundant sense. Icy comets and water-rich asteroids have been bombarding the moon since its formation, Spudis notes, and there are places on the moon where the explosively delivered water would be stable indefinitely. Thanks to the moon's tiny tilt on its axis, its polar regions barely lean toward the sun in "summer." As a result, the kilometers-high walls of some near-pole impact craters cast eternal shadows across adjacent crater floors. Although the lunar surface can reach 120°C in sunny spots, temperatures in permanent shadow hover at about 50 degrees above absolute zero by most calculations, cold enough to freeze nitrogen and to lock up water ice forever.

Before finding signs of polar ice on the moon, astronomers stumbled across them on hellishly hot Mercury. Bouncing radar signals off the innermost planet to image its rocky geology in the early 1990s, radar astronomers received reflections from permanently shadowed craters near the poles. The reflections behaved electromagnetically as if they had bounced around within thick ice layers on the planet.

Inspired by the apparent discovery, in 1994 planetary physicist Stewart Nozette of LPI and colleagues jury-rigged a last-minute radar experiment that bounced signals from the Clementine lunar orbiter off the lunar surface. On the radar's one pass over the moon's south pole, the reflected signal was "suggestive of" ice, the Clementine team reported, although other planetary radar specialists remained doubtful.

Follow-up using ground-based radars, principally by planetary scientist Donald Campbell of Cornell University and his colleagues, failed to support the Clementine observations, Campbell says. Some parts of the moon did return the distinctive reflections, but they come from rough terrain, Campbell says, not permanently shadowed areas. "I'm skeptical about significant water deposits at the lunar poles," he says, although he adds that there could be grains of water ice too small for radar to pick up.

The next moon mission after Clementine could look for just such grains. In 1998, the neutron spectrometer aboard the orbiting Lunar Prospector spacecraft gauged the energy of neutrons that cosmic rays create on hitting the moon's surface. Such neutrons slow dramatically if they collide with hydrogen atoms in the upper meter of lunar soil

CREDIT: NASA/NORTHROP GRUMMAN

before flying off to the spacecraft. By measuring the proportion of fast neutrons to slow ones, Lunar Prospector proved to everyone's satisfaction that the moon's polar regions are enriched with hydrogen—possibly from traces of ice mixed in with the soil.

Lunar Prospector's principal investigator, Alan Binder of the Lunar Research Institute in Tucson, Arizona, immediately hailed the result as proof of water in lunar polar regions at an abundance of about 1 weight percent, enough to mine (*Science*, 13 March 1998, p. 1628). Subsequent studies have tended to narrow the hydrogen signal to permanently shadowed regions. But “that doesn't mean it's water,” says the instrument's principal investigator, William Feldman of the Planetary Science Institute in Tucson. The hydrogen could have been beamed in on the solar wind, for example.

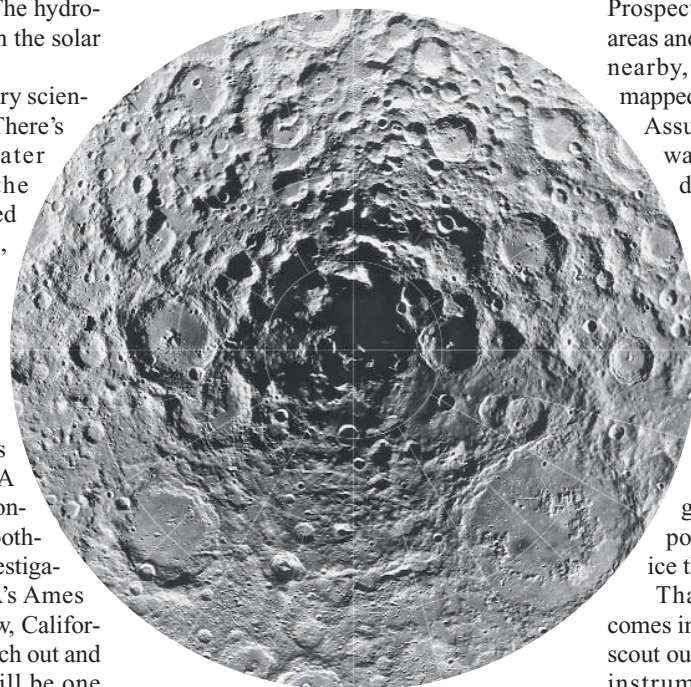
All in all, a majority of planetary scientists remain guardedly hopeful. “There's a good probability there's water there,” says Dana Hurley of the Johns Hopkins University Applied Physics Laboratory in Laurel, Maryland, who has modeled the preservation of cometary water on the moon. “The issue is that none of the data is conclusive.”

Fire in the hole

When space on board LRO's launch vehicle opened up, NASA selected LCROSS as a means of conclusively testing the icy-moon hypothesis, or, as LCROSS principal investigator Anthony Colaprete of NASA's Ames Research Center in Mountain View, California, puts it, as a way to finally “reach out and touch the lunar hydrogen.” It will be one bang-up experiment. Separating from LRO, the still-coupled upper stage and Shepherd-ing Spacecraft will swing by the moon and enter two long, looping orbits around Earth before separating just before impact.

The 10-meter-long, 2-ton upper stage will lead the way, crashing at a steep angle at 7200 kilometers per hour into the likeliest permanently shadowed region available. A flash, an upward jet of debris, and excavation of a 3-meter-deep, 20-meter-wide crater will follow. The instrument-laden shepherd and LRO, as well as Earth-based telescopes, will probe the rising debris plume for signs of ice, water vapor, hydroxyl from water, and hydrated minerals. Then the trailing 700-kilogram shepherd will fly through the plume—sending back data all the while—before blasting its own, smaller crater near the first.

At least, that's the plan. Whether the basic physics of impact probing will cooperate remains to be seen. “It's a very unproven and highly unpredictable science, impact cratering,” Colaprete told an audience at the Lunar and Planetary Science Conference (LPSC) in March. Erik Asphaug agrees. Asphaug, an impact modeler at the University of California (UC), Santa Cruz, calls LCROSS “the most challenging impact modeling I've ever done.” If too little of the right stuff rises into view above the crater rim, observations will be compromised or impossible. But calculating the depth of excavation and the amount, speed, and direction of ejecta is fraught with uncertainty, Asphaug notes.



Inky targets. LCROSS will target permanently shadowed crater floors near the pole (center).

The uncertainties start with the LCROSS impactor. “By planetary standards, it's pretty slow,” says Asphaug. Making assumptions that work in simulations of faster comet and asteroid impacts may give a misleading idea of what to expect in slower impacts. And the upper stage is a far cry from models' usual solid spheres. “A good model of it would be a soda can,” says Asphaug, a hollow shape that's tough to model. In laboratory experiments reported at LPSC by impact specialist Peter Schultz of Brown University, hollow projectiles fired into targets similar to lunar soil splash out high-speed ejecta at lower angles than solid projectiles do. As a result, models may underestimate the chances that ejecta will

hit the crater rim instead of rising into view, Schultz says.

Then there's the target, the dirt and rubble of the upper few meters of the moon. As much empty space as rock, this “regolith” will be highly compressible, another challenge for modeling. All things considered, “it's going to be interesting,” Schultz says.

Even if there's ice on the moon and LCROSS kicks up plenty of debris high into the sky, it could still miss striking it rich. Clementine radar and Lunar Prospector neutrons painted broad-brush pictures of where ice might be, including sunlit areas surely too hot to harbor ice. Planetary scientist Richard Elphic of Ames Research Center and colleagues have recently sharpened the Lunar Prospector picture by discarding the sunlit areas and confining the detected hydrogen to nearby, permanently shadowed areas as mapped recently by Japan's Kaguya orbiter.

Assuming the hydrogen is bound up in water, the analysis boosts its abundance well above 1% in some craters, Elphic says. “But some permanently shadowed features still do not appear to have any hydrogen.”

LCROSS will avoid apparently dry places, of course, but the absence of hydrogen in locations where simple theory would call for it suggests to some that any lunar ice could be patchy. “I didn't like LCROSS from the get-go,” says Spudis. “It is highly possible that it will miss a deposit of ice that is there.”

That's where the \$550 million LRO comes in. Although its primary mission is to scout out safe landing sites, four of its seven instruments are dominantly or entirely devoted to the search for water ice. It carries another neutron detector to map hydrogen at higher spatial resolution. Radar will get the best view yet inside permanently shadowed craters. (A similar instrument is already flying on board the Indian Chandrayaan-1 orbiter.) A laser altimeter will map topography. And a radiometer will gauge actual temperatures in permanent shadow.

“We have hope, but that's not the same as data,” says David Paige of UC Los Angeles, the principal investigator of LRO's radiometer. “Is the LCROSS approach going to work? We don't know. Even LCROSS, LRO, and the international effort combined may in fact not be enough to solve this problem. There's no guarantee the moon will cooperate.” And no country has a mission in the works to land in eternal darkness to force the issue.

—RICHARD A. KERR



LETTERS

edited by Jennifer Sills

Politics Still in Play

TAKEN TOGETHER, THREE ARTICLES IN THE 20 MARCH ISSUE PRESENT A JARRING CONTRAST. In the Editorial “The Enlightenment returns” (p. 1538), K. Gottfried and H. Varmus rejoice in the fact that the White House has rejoined the community of scientific integrity and is “listening to what [scientists] tell us...especially when it’s inconvenient.” They celebrate this new policy, which ensures “that scientific data is never distorted or concealed to serve a political agenda.” Then, on page 1548, we read the News of the Week story by J. Mervis: “Senate majority leader hands NSF a gift to serve the exceptionally gifted.” This clearly meritorious gift, however, is also an earmark, and a substantial part of the money would be spent in the majority leader’s state. Finally, in the News Focus story “A lifetime of work gone to waste?” (p. 1557), D. Charles profiles the rejection and waste of hundreds of millions of dollars of highly reputable (albeit disputable) scientific effort by the Senate majority leader and the White House because the conclusion—it would be safe to build a nuclear waste repository at Yucca Mountain in Nevada—was politically inconvenient. If the second and third articles are true, maybe the first article should have been titled “Some parts of the Enlightenment have returned.” Political convenience remains.

LOUIS S. THOMPSON

TGA LLC, 14684 Stoneridge Drive, Saratoga, CA 95070–5745, USA. E-mail: lthompson@alum.mit.edu

Yucca Mountain. Politics has permeated the reaction to recent results about Yucca Mountain.

Invest in Postdocs

I AM WRITING REGARDING THE ROLE OF THE NIH in the American Recovery and Reinvestment Act of 2009 (ARRA). Given the short period of time the NIH has been allowed to disperse its funds, it seems that extending the duration of grants that are nearing completion or raising the payline of currently funded grants are two of the most straightforward options. Along these lines, allocating a subset of this money to extend the funding of NIH F32 grants by 12 months for postdoctoral scholars nearing the end of their fellowship would both serve the NIH commitment to fostering young scientists and meet the goals of the ARRA to infuse money into the economy.

The current economic climate has created a scarcity of positions for highly trained scientists seeking employment in both academic and industrial research settings. In these uncertain times, many universities have closed their advertised faculty searches or have instituted a complete hiring freeze (1, 2). In addition, many large biotechnology companies have implemented layoffs, while small start-up companies are being forced out of business, making the prospect of moving from academia to industry equally daunting. This frozen job market—coupled with the difficulty principal investigators have in obtaining funding from national sources (3) and the plummeting endowments for research universities (2) and

private granting agencies—is creating a situation in which postdoctoral fellows will find no safe port. To stave off a flight of promising young scientists to other fields, it is imperative that funding be extended for postdoctoral fellows so that they can weather this economic perfect storm.

In addition to accomplishing the NIH goal to foster talented young scientists, directly funding postdoctoral fellows will meet goals of the ARRA. Under the current NIH pay scale for postdoctoral fellows, a 4th-year fellow makes about \$45,000. This level of pay necessitates that the majority of a fellow’s income is ploughed directly back into the economy through payments for food, shelter, and clothing, not simply placed in savings (4). Securing National Research Service Award (NRSA) fellowships for an additional 12 months should provide for a high return in terms of the percentage of dollars that will be directly contributed into the economy.

KEVIN G. HOFF

Division of Chemistry and Chemical Engineering, California Institute of Technology, Pasadena, CA 91125, USA. E-mail: khoff@caltech.edu

References

1. G. Bjorn, *Nat. Biotech.* **27**, 206 (2009).
2. E. Hand, *Nature* **457**, 11 (2009).
3. “A broken pipeline? Flat funding of the NIH puts a generation of science at risk” (2008); www.brokenpipeline.org.
4. S. Jashick, “Raising the bar on postdoc pay and benefits,” *Inside Higher Ed* (January 2008); www.insidehighered.com/news/2008/01/21/postdoc.

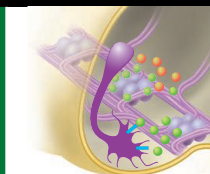
Mining the Data on Coal

R. A. KERR’S NEWS FOCUS STORY “HOW MUCH coal remains?” (13 March, p. 1420) gave welcome attention to the results of curve-fitting according to the methods of M. King Hubbert to predict future coal utilization. Gratifyingly, it also mentioned the technique known as Hubbert linearization (HL), where annual production as a fraction of cumulative production is plotted against the cumulative production, allowing simple but powerful predictions of the ultimately recoverable reserves of resources. As an example, the article mentioned the HL analysis for UK coal production performed by David Rutledge. The actual analysis shows an



Releasing the egg

890



Axon accuracy

893

almost perfect linear fit spanning about 150 years of UK coal production. This should make us very skeptical of claims reported in Kerr's article that the decline in UK coal production is the result of diversification into other energy sources that began only in the last 100 years.

Although energy economists might see price as the only barrier to utilization of a resource, scientists (including geologists) should place greater trust in the predictive value of the laws of thermodynamics. When the energy required for mining coal becomes greater than the energy obtained by subsequently burning it, then the mining will not occur—no matter how high the coal price or how much coal remains in the ground.

The true power of HL analysis is that it uses the past behavior of a system to indicate possible future performance rather than relying on the usually overoptimistic opinions of resource "experts." Using the past to predict future behavior always carries uncertainty. However, on large scales spanning decades of time, humans' energy-dependent behaviors (such as growth of the population or the use of fossil energy) appear to follow curves resembling the growth and decline of populations of other organisms temporarily released from resource constraints.

Another worrisome example of resource reserve optimism that conflicts with HL analysis is mining of rock phosphate, upon which world agriculture currently depends.

HL analysis suggests that rock phosphate reserves are 75% depleted and that production will soon collapse (1), whereas authorities such as the United States Geological Survey (whose past predictions of recoverable world oil reserves now appear overly optimistic) see no such problem (2).

MICHAEL LARDELLI

School of Molecular and Biomedical Science, University of Adelaide, SA 5005, Australia. E-mail: michael.lardelli@adelaide.edu.au

References

1. P. Déry, B. Anderson, "Peak phosphorus," *Energy Bull.* (13 August 2007); www.energybulletin.net/node/33164.
2. R. W. Bentley, S. A. Mannan, S. J. Wheeler, *Energy Pol.* **35**, 6364 (2007).

Conference Covered Climate from All Angles

THE COVERAGE BY E. KINTISCH OF THE Copenhagen Climate Conference ("Projections of climate change go from bad to worse, scientists report," 20 March, p. 1546) follows the dominant mode of media reporting that has emerged in the weeks following the conference—that of impending doom.

As chairs of some of the 57 sessions held during the 3-day meeting, we would like to highlight the enormous breadth of new research presented at Copenhagen about the interactions between climate and human society. Of the 593 research papers orally presented, only about 25% dealt with observed or modeled behavior of the Earth system. Nearly 50% of the papers were from scholars from the social sciences and humanities—geographers, philosophers, political scientists, anthropologists, economists, sociologists, and environmental historians—offering new insights about governance, adaptation, communication, behavior, resilience, innovation, and

culture. These insights suggest that it is possible to avoid the catastrophic outcomes foreseen by biogeophysical scientists, particularly if climate change is addressed as part of the much larger societal transformations that are necessary to foster both equity and sustainability. However, little of this new research on climate change from the social sciences and humanities has been reported or recognized in mainstream media reporting from the event.

The key messages of the conference were not, and could not be, the “consistent” message of some 2000 scientists. The conference messages indeed constitute an important call to action. They would have been more inspiring, however, if they had taken note of the depth of insight that emerged from the research about the motives, forms, scales, and processes of possible actions.

There is a large and growing body of research about climate change from the social sciences and humanities, which offers new ways of framing the phenomenon, of opening up discourses between peoples and political actors, of elaborating potential solutions that can be sustainable, and of linking such solutions to other key social, economic, and envi-

ronmental phenomena. These are all insights that are more engaging, empowering, and fruitful than a discourse of catastrophe, and it is important that they are given much more prominence in climate change science-policy interactions and in media reporting.

**MIKE HULME,^{1*} MAX BOYKOFF,² JOYEETA GUPTA,³
THOMAS HEYD,⁴ JILL JAEGER,⁵ DALE JAMIESON,⁶
MARIA CARMEN LEMOS,⁷ KAREN O'BRIEN,⁸
TIMMONS ROBERTS,⁹ JOHAN ROCKSTRÖM,¹⁰
COLEEN VOGEL¹¹**

¹School of Environmental Sciences, University of East Anglia, Norwich NR4 7TJ, UK. ²School of Geography, University of Oxford, Oxford OX1 3QY, UK. ³Institute of Environmental Studies, Vrije Universiteit, Amsterdam 1081 HV, Netherlands. ⁴Department of Philosophy, University of Victoria, Victoria, BC V8W 3P4, Canada. ⁵Vienna, Austria; jill.jaeger@seri.at. ⁶Environmental Studies Program, New York University, New York, NY 10003, USA. ⁷School of Natural Resources and Environment, University of Michigan, Ann Arbor, MI 48209, USA. ⁸Department of Sociology and Human Geography, University of Oslo, Oslo NO-0317, Norway. ⁹Department of Sociology, The College of William and Mary, Williamsburg, VA 23185, USA. ¹⁰Stockholm Environmental Institute, Stockholm SE 103 14, Sweden. ¹¹Department of Geography and Environmental Studies, University of Witwatersrand, Johannesburg, Private Bag 3, Wits 2050, South Africa.

*To whom correspondence should be addressed. E-mail: m.hulme@uea.ac.uk

Letters to the Editor

Letters (~300 words) discuss material published in *Science* in the previous 3 months or issues of general interest. They can be submitted through the Web (www.submit2science.org) or by regular mail (1200 New York Ave., NW, Washington, DC 20005, USA). Letters are not acknowledged upon receipt, nor are authors generally consulted before publication. Whether published in full or in part, letters are subject to editing for clarity and space.

ECONOMICS

Far from a Rational Crowd

Michelle Baddeley

Between November 1636 and February 1637, the demand for tulip bulbs in the Netherlands spiraled out of control. Explosive price increases of up to 6000% were recorded for the rarer tulip bulbs, and folklore claims that at the height of Tulipmania a single bulb from the exotic, beautiful *Semper Augustus* plant cost more than a three-story house in central Amsterdam. The bust following this short craze was just as dramatic. Within three months, most bulbs became impossible to sell—at any price—and tulip speculators lost fortunes. Standard economic theory cannot easily explain this speculative frenzy or any of the many other similar episodes that litter history. In *Animal Spirits*, George Akerlof and Robert Shiller argue that this is because it neglects noneconomic motivations, irrationality, and the animal spirits central to human decision-making. “You pick the time. You pick the country. And you

future is not easily quantifiable. In the absence of a basis for rational calculation, people’s decisions (to invest, to intervene, etc.) are the result of animal spirits, “a spontaneous urge to action” (1).

On opening *Animal Spirits*, you might expect an analysis with roots in either Galen or Keynes. Although Akerlof (a Nobel laureate in economics at the University of California, Berkeley) and Shiller (an economist at Yale University) hail Keynes as their hero, their animal spirits are a broader and more diffuse phenomenon than his. They define five animal spirits: confidence,

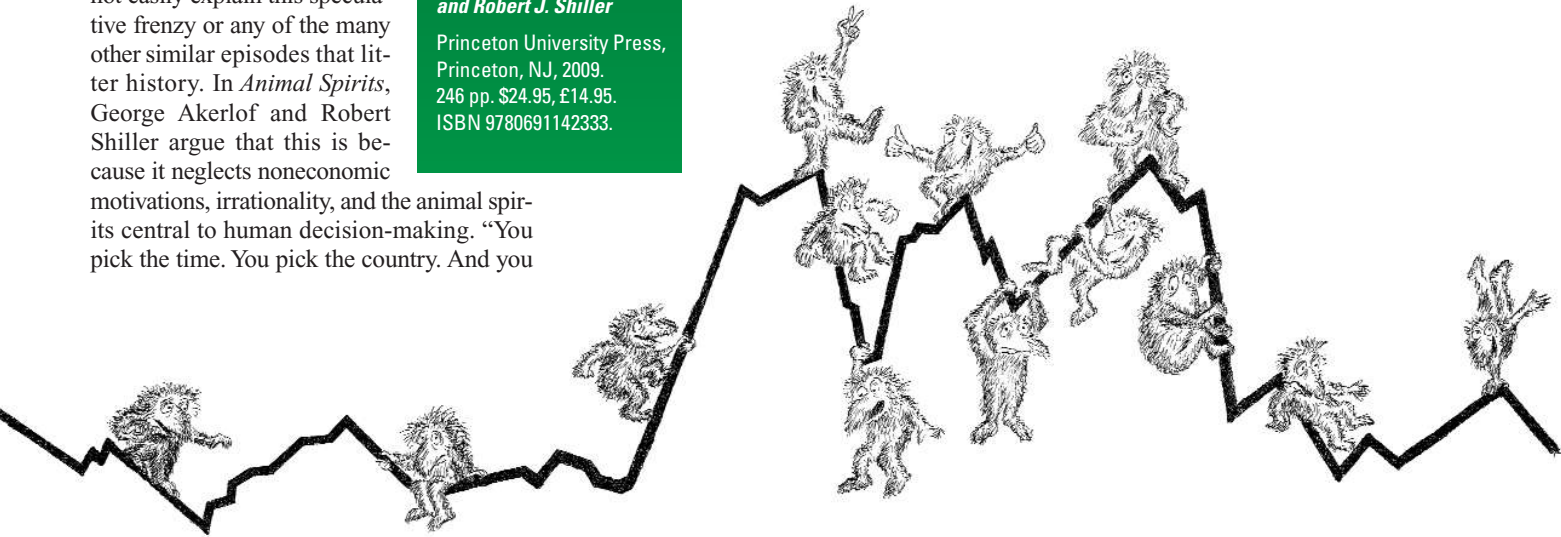
Animal Spirits
How Human Psychology
Drives the Economy,
and Why It Matters for
Global Capitalism

by George A. Akerlof
and Robert J. Shiller

Princeton University Press,
Princeton, NJ, 2009.
246 pp. \$24.95, £14.95.
ISBN 9780691142333.

market in which supply exceeds demand. But labor markets function differently. In most markets, the goods being sold are inanimate and emotionless, whereas in labor markets, workers can adapt and change with repercussions for work effort. Psychological and sociological factors prove central: Workers worry about a fair wage; they suffer money illusion and may resent a lower take-home wage even when falling prices have increased its value. Workers respond to good treatment by trusting their employers. But when wages fall, they then feel anger and resentment; their morale drops and their sense of duty is offended. Work effort declines and, because worker productivity is eroded, even as wage costs decrease, employers’ profits also fall.

People’s savings decisions offer another puzzle. Why do people accumulate credit card debt at high interest rates while simultaneously holding assets that earn low interest rates? Their actions are affected by environ-



can be fairly well guaranteed that you will see at play in the macroeconomy the *animal spirits* that are the subject of this book.”

Galen asserted that *spiritus animalis* had origins in the brain and mediated nerve function—perhaps he envisaged them functioning as neurotransmitters do. Linking Galen’s animal spirits with economics would fit well with behavioral economics and with economists’ increasing interest in neuroscience and experimental psychology. John Maynard Keynes introduced animal spirits in his analysis of entrepreneurship: entrepreneurs cannot properly calculate the future benefits of investments because the

fairness, corruption (bad-faith behavior), money illusion (confusion about the effects of inflation and deflation), and storytelling (narratives that shape our sense of who we and others are). So while their analysis does not always fit neatly with a fundamentalist interpretation of Keynes, it does resonate with the growing field of behavioral economics. Moreover, they use animal spirits to take behavioral economics from the microeconomy to the macroeconomy to explain a range of macroeconomic phenomena, including financial crisis, depression, and involuntary unemployment.

One of the puzzles on which they focus is workers’ resistance to wage cuts. Most versions of mainstream economic theory predict that rising unemployment will precipitate falling wages, just as prices will fall in any

mental cues and framing effects. For example, the authors cite Hershey Shefrin and Richard Thaler’s experiment in which people who experienced a \$2400 windfall saved different proportions depending on the circumstance of the windfall and the context in which it was received: They spent \$1200 if the windfall was spread over a series of monthly payments, \$785 if it was a single lump sum, and nothing if it was an inheritance placed in a five-year-term interest-bearing account (2). Rather than treating economic decisions together as one, gigantic maximization problem, people assign different events to separate “mental” accounts. People’s behavior may also be inconsistent over time: Plans to do something constructive (e.g., giving up smoking) in the future change as the future becomes the present—people lack self-control.

The reviewer is at the Faculty of Economics and Gonville and Caius College, Cambridge CB2 1TA, UK. E-mail: mb150@cam.ac.uk

CREDIT: © EDWARD KOREN/COURTESY PRINCETON UNIVERSITY PRESS

In their explanation of financial instability, Akerlof and Shiller argue against models that assume efficient processing of information in financial markets. Instead, animal spirits, including confidence and storytelling, determine market trends. Markets fluctuate erratically, reflecting social mood. Waves of euphoria, optimism, and overconfidence are followed by slumps of pessimism and crises of confidence. All spread through the economy via herding and contagion, fed by word of mouth and false intuitions (e.g., that prices don't fall) and perturbed by anything from dramatic news stories to sporting events.

This instability propagates through the "beauty contest" game—first described by Keynes, who used it as a metaphor for the iterated reasoning that characterizes financial speculation. In the newspaper contests Keynes referred to, competitors were asked to select from a series of photos not who they thought were the prettiest but who they thought others would think were prettiest. Similarly, people will purchase a tulip bulb (or a dotcom share or a house) at a seemingly exorbitant price not because they independently believe that the object is worth the cost but because they believe that other people think that it is.

Akerlof and Shiller claim that all these factors make asset prices susceptible to feedback loops, with instability further magnified by leverage (the use of borrowings to

fund asset purchases). The feedback has knock-on effects for the real economy: growing (and bursting) asset price bubbles affect wealth, investment, and the availability of finance. Such instability is exacerbated by the corruption that increases during boom phases. The authors note the repeated roles of corruption in determining the severity of downturns in the U.S. economy: Prohibition and the Roaring Twenties were followed by the Great Depression of the 1930s, the Savings and Loan crisis contributed to the 1991 recession, the Enron scandal was associated with the 2001 recession, and the subprime mortgage crisis precipitated the present recession.

Akerlof and Shiller suggest some policy solutions for the current global financial meltdown. They hold that governments have an important role to play in complementing capitalism and that "capitalism must live within certain rules." Given the overwhelming influence of animal spirits on our economic behavior, "the government must set those rules." They see our old financial system as a Humpty Dumpty: it's broken, cannot be fixed, and so must be replaced. To moderate the present slump, Akerlof and Shiller recommend that governments adopt a dual-target approach in which fiscal and monetary stimuli are complemented by targeting financial flows (e.g., through lending and capital injections)

to ensure that the stimuli are consistent with full employment.

Economists typically avoid psychological and sociological models because they find them too arbitrary and too difficult to quantify. Overall, Akerlof and Shiller advocate a move away from this antipathy. *Animal Spirits* "is a book about macroeconomics," but this is its principal problem. It is built on a foundation of findings from a behavioral microeconomics. Although behavioral economics can capture individual decision-making in an experimental context, at an aggregate level the interactions among people are too complex to provide the evidence needed to properly verify theories of behavioral macroeconomics. The authors therefore emphasize the importance of history and stories and of qualitative alongside quantitative analyses. However, the problem remains that their theory is difficult to falsify. That said, economics is often criticized for its practically misleading emphasis on theoretical precision. So it is refreshing to see two such influential economists advocating a shift toward a broader, more intuitive, interdisciplinary approach.

References

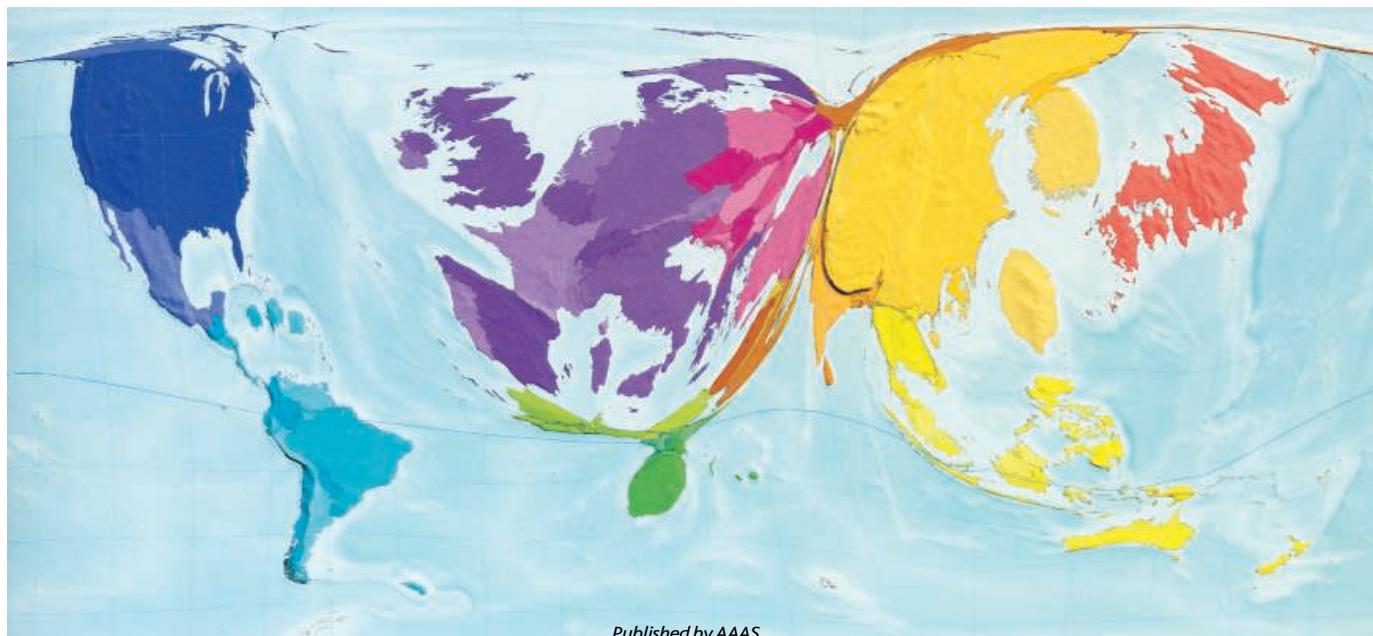
1. J. M. Keynes, *The General Theory of Employment, Interest, and Money* (Macmillan, London, 1936).
2. H. Shefrin, R. H. Thaler, *Econ. Inquiry* 24, 609 (1988).

10.1126/science.1174219

BROWSEINGS

The Atlas of the Real World: Mapping the Way We Live. Daniel Dorling, Mark Newman, and Anna Barford. Thames and Hudson, London, 2008. 400 pp. \$50, C\$55, £29.95. ISBN 9780500514252. Cartographers generally try to minimize the distortion introduced in projecting Earth's surface onto a flat sheet. Dorling and his colleagues instead opt to "make the most of it." They depict characteristics of our

world as cartograms, maps in which territories are resized according to the magnitude of the variable of interest (here by treating the data as a diffusing fluid). The book presents 366 environmental, economic, and social statistics—e.g., the number of cell phone subscribers in 2002 (below). Many additional cartograms can be seen at www.worldmapper.org.



PUBLIC HEALTH

The Cholera Crisis in Africa

S. Bhattacharya,¹ R. Black,² L. Bourgeois,³ J. Clemens,⁴ A. Cravioto,⁵ J. L. Deen,^{5*} Gordon Dougan,⁶ R. Glass,⁷ R. F. Grais,⁸ M. Greco,⁹ I. Gust,¹⁰ J. Holmgren,¹¹ S. Kariuki,¹² P.-H. Lambert,¹³ M. A. Liu,¹⁴ I. Longini,¹⁵ G. B. Nair,¹⁶ R. Norrby,¹⁷ G. J. V. Nossal,¹⁰ P. Ogra,¹⁸ P. Sansonetti,¹⁹ L. von Seidlein,⁵ F. Songane,²⁰ A.-M. Svennerholm,¹¹ D. Steele,³ R. Walker³

In July 1994, 500,000 to 800,000 Rwandans crossed the border into the North Kivu region of Zaire (now called the Democratic Republic of the Congo, DRC). During the first month after the influx, almost 50,000 refugees died; cholera was a major contributor (1).

From 1995 to 2005, the largest number of cholera cases and outbreaks in Africa continued to be reported from this area of the DRC (2). Renewed fighting has displaced at least 250,000 people, making an already difficult situation worse for more than a million people living without clean water, food, or access to health care. By December 2008, the most recent cholera outbreak had affected 10,332 persons and resulted in 201 deaths (3). Cholera is also in the headlines in Zimbabwe. From August 2008 to February 2009, the number of reported cases was 70,643 with 3467 deaths (4). Cholera is also spreading to the neighboring countries of South Africa, Mozambique, Zambia, and Angola (5–7).

The management of cholera outbreaks has changed little over the last decades. Oral rehydration solution (ORS) is accepted as the cornerstone for rehydration, although for those severely dehydrated, intravenous fluids are

life-saving. Provision of safe water and adequate sanitation can be established as emergency measures but are not guaranteed to remain once the outbreak ends.

The international community has responded vigorously within recommended guidelines. Physicians for Human Rights recently called on the United Nations to take responsibility for the Zimbabwean health system (6). The World Health Organization's (WHO's) Global Task Force on Cholera Control urged prioritization of prevention, preparedness, and response activities and an efficient surveillance system (8). The WHO's Disease Control in Humanitarian Emergencies program is helping with distributing ORS and chlorine tablets, finding funds to pay thousands of Zimbabwean health-care workers, and providing better services in remote areas (9). Although these efforts have saved many lives, the rising cases and deaths point to the limitations of the current strategy.

Is it time to consider other options? An oral cholera vaccine was evaluated in Mozambique 5 years ago and showed ~90% protection against cholera of life-threatening severity, even in a population in whom a high percentage was infected by HIV (10). Internationally licensed and available, the vaccine has also been shown to confer herd protection against cholera among unvaccinated neighbors of vaccinees (11). To date, the WHO has been reluctant to consider vaccination as a strategy to contain cholera in Zimbabwe “due to its two-dose regimen, short shelf-life, high cost, and need for cold chain distribution” (8). There are certainly logistical complexities to administering a two-dose regimen in a setting as desperate and chaotic as Zimbabwe, as well as strategic choices to be made for how to target high-risk groups for vaccination. Yet delivery of this vaccine was feasible in three WHO-sponsored community demonstration projects in rural and urban sub-Saharan Africa (10, 12, 13).

Further complicating a recommendation to vaccinate is the existing dogma that “with the currently available internationally prequalified vaccine, vaccination is not recommended in an area where an outbreak has already started” (14). However, this dogma is based on a single analysis (15) that assumed that outbreaks are self-limited and short-lived, in contrast to

Long-lasting cholera outbreaks in Africa suggest limitations in the current strategy of disease control.

cholera in Zimbabwe, which has been raging since mid-2008. If the blockade against potential use of oral cholera vaccines could be lifted, then public-health workers, ministries of health, international organizations, and donor groups could discuss how, when, and where the vaccine could be deployed. The cost of the only internationally licensed oral cholera vaccine (Dukoral, Crucell-SBL) is U.S. \$7 to \$12 (€5.25 to €9) per dose; a lower price is offered for WHO-supported programs. A potentially cheaper vaccine was developed in Vietnam; its technology was transferred to Shanta Biotechnics (India) and is in clinical trials (16, 17). In the short term, the vaccination costs may be borne by donor foundations and international organizations.

The size and expected duration of the outbreak would seem to justify the implementation of mass vaccinations. The lack of flexibility to adapt to the circumstances is regrettable; for the people at risk it is a disaster.

References and Notes

1. Goma Epidemiology Group, *Lancet* **345**, 339 (1995).
2. D. C. Griffith *et al.*, *Am. J. Trop. Med. Hyg.* **75**, 973 (2006).
3. F. Fleck, *Bull. World Health Organ.* **87**, 6 (2009).
4. “Zimbabwe: Daily cholera update and alerts, 09 Feb 2009” (Government of Zimbabwe and WHO, Geneva, 2009); <http://reliefweb.int/rw/rwb.nsf/db900SID/VDUX-7P4SU520OpenDocument>.
5. National Outbreak Committee, *Cholera Outbreak in South Africa, National Outbreak Committee Situational Report* (Government of South Africa, Pretoria, 5 February 2009).
6. C. Kapp, *Lancet* **373**, 447 (2009).
7. ProMED-mail, International Society for Infectious Diseases, Brookline, MA, 7 February 2009; www.promedmail.org.
8. “An old enemy returns,” *Bull. World Health Organ.* **87**, 85 (2009).
9. R. Koenig, *Science* **323**, 860 (2009).
10. M. E. S. Lucas *et al.*, *N. Engl. J. Med.* **352**, 757 (2005).
11. M. Ali *et al.*, *Lancet* **366**, 44(2005).
12. D. Legros *et al.*, *Bull. World Health Organ.* **77**, 837 (1999).
13. C.-L. Chaignat *et al.*, *Expert Rev. Vaccines* **7**, 431 (2008).
14. WHO Global Task Force on Cholera Control, Cairo, Egypt, 14 to 16 December 2005 (WHO/CDS/NTD/IDM/2006.2, WHO, Geneva, 2006).
15. A. Naficy *et al.*, *JAMA* **279**, 521 (1998).
16. D. Mahalanabis *et al.*, *PLoS One* **3**, e2323 (2008).
17. Clinical trials, <http://clinicaltrials.gov/ct2/show/NCT00289224>.
18. J.C., J.L.D., and L.v.S. received support from the Bill and Melinda Gates Foundation. R.B., J.C., G.D., R.G., M.G., I.G., J.H., M.A.L., I.L., R.N., G.J.V.N., P.O., F.S., P.H.L., and A.M.S. are/have been members of the Board of Trustees and/or Scientific Advisory Group of IVI, which is engaged in the development and technology transfer of the oral vaccine described (17).

¹Indian Council of Medical Research, Ansari Nagore, New Delhi, 110029, India. ²Department of International Health, Bloomberg School of Public Health, Johns Hopkins University, Baltimore, MD 21205, USA. ³Enteric Vaccine Initiative, PATH, Seattle, WA 98107, USA. ⁴International Vaccine Institute, Seoul, 151-600, Korea. ⁵Centre for Diarrhoeal Disease Research, Dhaka 1000, Bangladesh. ⁶The Wellcome Trust Sanger Institute, Wellcome Trust Genome Campus, Hinxton, Cambridge, CB10 1RQ, UK. ⁷Fogarty Institute, National Institutes of Health, Bethesda, MD 20892, USA. ⁸Epidemiology and Population Health, Epicentre, FR-75011 Paris, France. ⁹FR-69110 Lyon, France. ¹⁰The Department of Microbiology and Immunology and the Department of Pathology, University of Melbourne, Melbourne, VIC, 3010, Australia. ¹¹University of Gothenburg, SE-405 30 Gothenburg, Sweden. ¹²Centre for Microbiology Research, Kenya Medical Research Institute, Nairobi, Kenya. ¹³University of Geneva, CH-1211 Geneva 4, Switzerland. ¹⁴Karolinska Institute, SE-171 77 Stockholm, Sweden. ¹⁵Fred Hutchinson Cancer Research Center and the University of Washington, Seattle, WA 98109, USA. ¹⁶National Institute of Cholera and Infectious Disease, Kolkata, 700010, India. ¹⁷Swedish Institute for Infectious Disease Control, SE-171 82 Solna, Sweden. ¹⁸University at Buffalo, School of Medicine and Biomedical Sciences, Buffalo, NY 14214, USA. ¹⁹Unité de Pathogénie Microbienne Moléculaire, INSERM U786, Institut Pasteur, FR-75724 Paris Cedex 15, France. ²⁰Partnership for Maternal, Newborn and Child Health, 1211 Geneva, Switzerland.

*Author for correspondence. E-mail: jdeen@ivi.int

Seasons and Life Cycles

Heidi Steltzer¹ and Eric Post²

An apparent contradiction has arisen in studies of plant phenological response to climatic warming: Field and satellite data at the community and biome levels indicate a lengthening of the growing season across much of the Northern Hemisphere (1–6) and—where data exist—in the Southern Hemisphere (5, 7, 8), yet life history observations of individual species suggest that many species often shorten their life cycle in response to warming (9–12). Here, we pair evolutionary and ecological viewpoints to resolve this conundrum.

If a plant starts to green earlier, subsequent events in the plant's life cycle often occur earlier as well (9–12). Advancing the timing of early-season events in this way may increase plant fitness by ensuring that reproduction occurs before loss of reproductive tissues to, for example, herbivory or drought (13, 14). An extended life cycle can also improve fitness if it leads to more or larger offspring, but exposes plants to the risk of damage to flowers or fruits before maturation (13). The prevalence of these divergent strategies at the community level will depend on the responses of individual plant species to climatic trends and interannual variation in climatic conditions.

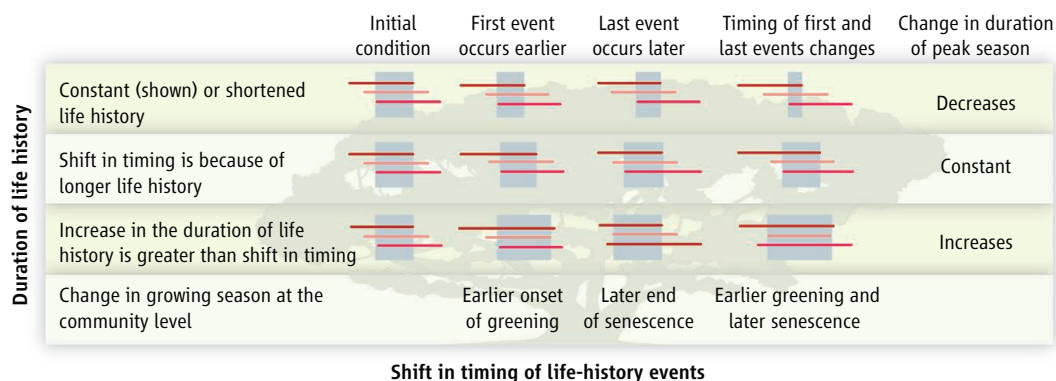
Within a community of several species, life history strategies typically vary, increasing the probability that the length of the growing season quantified at the community level will increase with climate warming. For example, the length of the community's growing season will rise even if early-season species green but also senesce earlier while the timing of events for late-season species remains stable or advances less in response to warming. Thus, ecological constraints on the length of the community's growing season

may be eased by climate warming, whereas evolutionary constraints on the life-cycle durations of individual species may limit their response and explain the diverse responses of different species to warming (9–12).

A longer growing season has been one of the most widely observed biological changes in response to climatic warming across temperate to polar latitudes during the 20th century (1–6). This change in growing season length has been occurring in regions where temperatures have increased (5) and in passive warming experiments that have been replicated across the Northern Hemisphere (15–17). A nearly universal advance in spring temperature indices of first leaf and bloom dates for cloned lilac and honeysuckle across temperate areas of the Northern Hemisphere has also been reported (18). In the Southern Hemisphere, a recent passive warming study in an Australian subalpine meadow showed an advance in spring events for 7 of 14 species (19). Predictions from phenological models that use temperature data to estimate the timing of spring events suggest that comparable changes in growing season length have not taken place over the past two centuries in boreal Eurasia (1) and that the expected warming in the 21st century will further lengthen the growing season by 5.0 to 9.2 days in North America (20).

Few studies on the effects of temperature on growing season length have been conducted in the tropics because of the expecta-

A conceptual framework explains how individual species' responses to climate warming affect the length of the growing season.



A conceptual framework. This table is a guide to determining how individual species are responding to an extended growing season by observing the duration of peak season. The life history of a species—from the onset of greening through the end of senescence—is illustrated by the length of the solid lines. Each case represents a shift in the timing (columns) and duration (rows) of one or more species in a hypothetical three-species community that includes an early-, mid-, and late-season species. The growing season begins when the first species greens and ends when the last species senesces. The peak season (gray shaded area) occurs when all species have started and none have completed their life history. Reproductive life history events likely begin before the peak season and are completed before its end. The final row and column list changes that can be observed through frequent observations of surface greenness.

tion that temperature does not constrain growing season length there, but the absence of data should not be considered a lack of response (5). In two of the three tropical regions studied in Africa, the growing season has lengthened since the early 1980s (7). However, earlier budburst in warmer urban areas relative to nearby rural areas was found only in one-third of tropical cities versus three-fourths of temperate cities (21).

In contrast to the observed changes in the overall length of the growing season, warming often shortens the duration of life histories of individual species. For many species, climate warming leads not only to earlier greening but also to earlier flowering and senescence (9–12). Although life histories of individual species may thus be shortened, a longer growing season could still result if the responses of different species in a community diverge, possibly as a result of seasonal niche divergence (see the table). Earlier springs could be caused by an advance in the life history of early-season species in response to warmer air temperatures. Later falls could result from a delay in the life history of late-season species because of extreme mid-season temperatures and low water availability.

These divergent responses by different species to gradual climate warming and to extreme warming events have been seen in forest, grassland, and tundra communities in North America (9, 11, 12), Europe (14), and

¹Natural Resource Ecology Laboratory, Colorado State University, Fort Collins, CO 80523, USA. ²Department of Biology, Pennsylvania State University, University Park, PA 16802, USA, and Department of Arctic Environment, National Environmental Research Institute, Aarhus University, 4000 Roskilde, Denmark. E-mail: steltzer@nrel.colostate.edu; esp10@psu.edu

Australia (19). Thus, the widespread increase in growing season length may be a result of shortened and more divergent life histories.

Monitoring of the peak season duration through observations of surface greenness can be used to determine how individual species respond to an extended growing season (see the table). Changes in the duration of species' life histories have consistent effects on the peak season duration. Constant or shortened life histories decrease the peak season duration. Alternatively, if the shift in timing occurs because of a longer life history, the duration of the peak season will remain constant. Finally, the peak season duration will only increase if species extend their life cycles by more days than the growing season is lengthened.

Daily measurements of surface greenness from ground-based platforms are increasingly used in phenological studies (22, 23), including those in the tropics (24). These data may be sufficient to characterize the duration of peak season in regions where canopy closure corresponds with the onset of peak leaf area. However, models that relate leaf density to greenness may be needed where this does not

occur. Piecewise linear models can be fit to the data to determine the duration of peak season via the onset of peak leaf area and senescence. Observations of surface greenness in phenological networks would create continental-scale data sets that could be compared to regional trends in climate and to satellite data.

Although an extended growing season may lead to increased plant production, this is less likely if individual species shorten their life histories. Shortened, more divergent life histories may lead to gaps in the availability of resources for pollinators and herbivores (11) and may facilitate the establishment of invasive species (12). Nutrient losses during the growing season could also increase through decreased species complementarity (9). Thus, the contrasting changes in the duration of the growing season and species' life cycles are consistent, but increase the likelihood that climate warming is altering the structure and function of ecological communities, perhaps adversely.

References

1. N. Delbart *et al.*, *Global Change Biol.* **14**, 603 (2008).
2. A. Menzel *et al.*, *Global Change Biol.* **12**, 1969 (2006).
3. R. B. Myneni, C. D. Keeling, C. J. Tucker, G. Asrar, R. R. Nemani, *Nature* **386**, 698 (1997).

4. C. Parmesan, *Global Change Biol.* **13**, 1860 (2007).
5. C. Rosenzweig *et al.*, *Nature* **453**, 353 (2008).
6. L. M. Zhou *et al.*, *J. Geophys. Res.* **106**, 20069 (2001).
7. B. W. Heumann, J. W. Seaquist, L. Eklundh, P. Jonsson, *Remote Sens. Environ.* **108**, 385 (2007).
8. P. R. Petrie, V. O. Sadras, *Aust. J. Grape Wine Res.* **14**, 33 (2008).
9. E. E. Cleland, N. R. Chiariello, S. R. Loarie, H. A. Mooney, C. B. Field, *Proc. Natl. Acad. Sci. U.S.A.* **103**, 13740 (2006).
10. R. D. Hollister, P. J. Webber, C. Bay, *Ecology* **86**, 1562 (2005).
11. E. S. Post, C. Pedersen, C. C. Wilms, M. C. Forchhammer, *Ecology* **89**, 363 (2008).
12. R. A. Sherry *et al.*, *Proc. Natl. Acad. Sci. U.S.A.* **104**, 198 (2007).
13. D. W. Inouye, *Ecology* **89**, 353 (2008).
14. A. Jentsch, J. Kreyling, J. Boettcher-Treschkow, C. Beierkuhnlein, *Global Change Biol.* **15**, 837 (2009).
15. A. M. Arft *et al.*, *Ecol. Monogr.* **69**, 491 (1999).
16. J. Penuelas *et al.*, *Ecosystems* **7**, 598 (2004).
17. L. E. Rustad *et al.*, *Oecologia* **126**, 543 (2001).
18. M. D. Schwartz, R. Ahas, A. Aasa, *Global Change Biol.* **12**, 343 (2006).
19. F. C. Jarrad, C. Wahren, R. J. Williams, M. A. Burgman, *Aust. J. Bot.* **56**, 617 (2008).
20. X. Morin *et al.*, *Global Change Biol.* **15**, 961 (2009).
21. R. Gazal *et al.*, *Global Change Biol.* **14**, 1568 (2008).
22. A. D. Richardson *et al.*, *Oecologia* **152**, 323 (2007).
23. K.-P. Wittich, M. Kraft, *Int. J. Biometeorol.* **52**, 167 (2008).
24. C. E. Doughty, M. L. Goulden, *J. Geophys. Res.* **113**, G00B06 (2008).

10.1126/science.1171542

ECOLOGY

Phenology Feedbacks on Climate Change

Josep Peñuelas, This Rutishauser, Iolanda Filella

Climate warming has advanced the biological spring and delayed the arrival of biological winter (1, 2). These changes in the annual cycle of plants and the lengthening of the green-cover season have many consequences for ecological processes, agriculture, forestry, human health, and the global economy (3). Studies on vegetation-atmosphere interactions (4) and particularly on the impact of leaf emergence on climate (5–9) suggest that the phenological shifts in turn affect climate. The magnitude and sign of this effect are unknown but depend on water availability and regional characteristics.

The earlier presence of green land cover and the delay in autumnal senescence and leaf fall of deciduous canopies may alter the seasonal climate through the effects of biogeo-

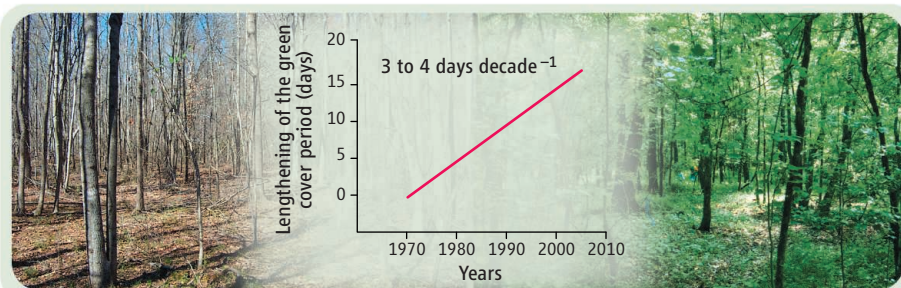
chemical processes (especially photosynthesis and carbon sequestration) and physical properties (mainly surface energy and water balance) of vegetated land surfaces.

CO₂ uptake is the main biogeochemical effect. An extended plant activity season increases biospheric CO₂ uptake (3) and thus decreases the current rise of atmospheric CO₂ concentration and its influence on the green-

A longer growing season as a result of climate change will in turn affect climate through biogeochemical and biophysical effects.

house effect (1). The extended plant activity also further increases the total annual emission of biogenic volatile organic compounds (BVOCs) (10). These increased emissions may also contribute to the complex processes associated with global warming (10).

Although the atmospheric lifetime of BVOCs is short, they have an important influence on climate through aerosol formation and



Phenology and climate. The change from a dormant winter to a biologically active spring landscape has numerous biogeochemical and biophysical effects on climate. Earlier leaf unfolding and delayed leaf fall as a result of global warming (graph) (3, 17) will thus affect climate change itself.

Global Ecology Unit, Center for Ecological Research and Forestry Applications (CREAF-CEAB-CSIC), Universitat Autònoma de Barcelona, 08193 Bellaterra (Barcelona), Spain. E-mail: josep.penuelas@uab.cat, this@creaf.uab.cat, i.filella@creaf.uab.cat

direct and indirect greenhouse effects. BVOCs generate large quantities of organic aerosols (11, 12) that could affect climate by forming cloud condensation nuclei. The result should be a net cooling of Earth's surface during the day because of radiation interception. Furthermore, the aerosols diffuse the light received by the canopy, increasing CO₂ fixation. However, BVOCs also increase ozone production and the atmospheric lifetime of methane, enhancing the greenhouse effect of these gases. Whether the increased BVOC emissions will cool or warm the climate depends on the relative weights of the negative (increased albedo and CO₂ fixation) and positive (increased greenhouse action) feedbacks (10).

A longer presence of the green cover in large areas should also alter physical processes such as albedo, latent and sensible heat, and turbulence. Observations in the Eastern United States show that springtime air temperatures are distinctly different after leaves emerge (5). Latent heat flux increases and the Bowen ratio (the ratio of sensible to latent heat) decreases after leaf emergence. As a result, the increased transpiration cools and moistens air, and the spring temperature rise drops abruptly (5, 6). The coupling between land and atmosphere also becomes more efficient, because an increase in surface roughness lowers aerodynamic resistance, generates more turbulence and higher sensible and latent heat fluxes, and leads to a wetter, cooler atmospheric boundary layer (7).

The longer presence of green cover thus generates a cooling that mitigates warming by sequestering more CO₂ and increasing evapotranspiration. However, this carbon fixation and evaporative cooling decline if droughts become more frequent or when less water is available later in the summer. In fact, an early onset of vegetation green-up and a prolonged period of increased evapotranspiration seem to have enhanced recent summer heat waves in Europe by lowering soil moisture (8, 9). The depletion of summer soil moisture strongly reduced latent cooling and thereby increased surface temperature (9) and likely reduced summer precipitation (13).

Furthermore, reduced albedo after leaf emergence may warm the land surfaces—especially those with high albedo, such as snow-covered areas—at spatial scales of hundreds and even thousands of kilometers. The lengthening of the green-cover presence can hence either dampen or amplify global warming, depending on water availability and regional characteristics. In wet regions and seasons, additional water vapor may form clouds that contribute to surface cooling and increased rainfall in nearby areas, whereas in

drier conditions, a longer presence of the green cover may warm regional climate by absorbing more sunlight without substantially increasing evapotranspiration.

There are many unknowns in the combined impacts of all these biogeochemical and biophysical processes on local, regional, and global climate. Phenology models used in global climate simulations are highly empirical and use a few local-scale findings that represent only a fraction of the global bioclimatic diversity, and that therefore preclude global coverage validation. As a result, the predicted timing of temperate and boreal maximum leaf area may be too late by up to 1 to 3 months, resulting in an underestimate of the net CO₂ uptake during the growing season (14). Satellite data assimilation can be of great help to minimize the large differences between observed and predicted spatiotemporal phenological patterns (15, 16).

Future studies should aim to quantify and understand the effects of earlier leaf unfolding and later leaf fall on temperature, soil moisture, and atmospheric composition and dynamics; this information will help to improve the representation of phenological changes in climate models and thus increase the accuracy of forecasts. Reinterpreting existing data sets (17) and advances in remote sensing techniques, in combination with con-

tinued long-term ground observations, will be crucial for this task.

References and Notes

1. IPCC, *The Physical Science Basis: Contribution of Working Group I to the Fourth Assessment of the Intergovernmental Panel on Climate Change* (Cambridge Univ. Press, Cambridge, 2007).
2. H. Steltzer, E. Post, *Science* **324**, 886 (2009).
3. J. Peñuelas, I. Filella, *Science* **294**, 793 (2001).
4. G. B. Bonan, *Science* **320**, 1444 (2008).
5. M. D. Schwartz, *J. Climate* **9**, 803 (1996).
6. D. R. Fitzjarrald, O. C. Acevedo, K. E. Moore, *J. Climate* **14**, 598 (2001).
7. G. B. Bonan, *Ecological Climatology: Concepts and Applications* (Cambridge Univ. Press, Cambridge, 2nd ed., 2008).
8. B. Zaitchik, A. K. Macalady, L. R. Bonneau, R. B. Smith, *Int. J. Climatol.* **26**, 743 (2006).
9. E. Fischer, S. Seneviratne, P. Vidale, D. Lüthi, C. Schär, *J. Climate* **20**, 5081 (2007).
10. J. Peñuelas, J. Llusà, *Trends Plant Sci.* **8**, 105 (2003).
11. M. Claeys *et al.*, *Science* **303**, 1173 (2004).
12. A. Laaksonen *et al.*, *Atmos. Chem. Phys.* **8**, 2657 (2008).
13. X. Jiang, G.-Y. Niu, Z.-L. Yang, *J. Geophys. Res.* **114**, D06109 (2009).
14. J. T. Randerson *et al.*, *Global Change Biol.*, 10.1111/j.1365-2486.2009.01912.x (2009).
15. R. Stöckli *et al.*, *J. Geophys. Res.* **113**, G04021 (2008).
16. M. F. Garbulsky, J. Peñuelas, D. Papale, I. Filella, *Global Change Biol.* **14**, 2860 (2008).
17. A. Menzel *et al.*, *Global Change Biol.* **12**, 1969 (2006).
18. Supported by the Spanish (Consolider Montes program) and Catalan (Agència de Gestió d'Ajuts Universitaris i de Recerca) governments and the Swiss National Science Foundation. We thank R. Stöckli for comments on the manuscript.

10.1126/science.1173004

OCEAN SCIENCE

Ice Sheet Stability and Sea Level

Erik R. Ivins

How much will sea levels rise if the West Antarctic Ice Sheet becomes unstable?

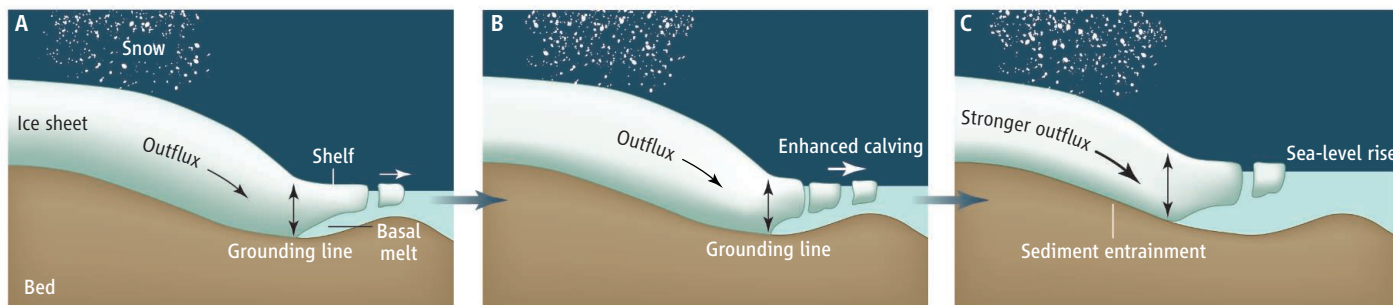
Volume changes in the Antarctic Ice Sheet are poorly understood, despite the importance of the ice sheet to sea-level and climate variability. Over both millennial and shorter time scales, net water influx to the ice sheet (mainly snow accumulation) nearly balances water loss through ice calving and basal ice shelf melting at the ice sheet margins (1). However, there may be times when parts of the West Antarctic Ice Sheet (WAIS) are lost to the oceans, thus raising sea levels. On page 901 of this issue, Bamber *et al.* (2) calculate the total ice volume lost to the oceans from an unstable retreat of WAIS, which may occur if the part of the ice sheet that overlies sub-marine basins is ungrounded and moves to

a new position down the negative slope (see the figure).

More than 90% of the ice delivered from Antarctica to the oceans comes from fast-moving ice streams and outlet glaciers, with velocities of tens to hundreds of meters per year (3). The outflux is controlled in part by the intrinsic resistance to flow provided by stresses at the bedrock or as internal shear. Also controlling the flow rate are gravitational driving forces and mechanical buttressing at the seaward margins provided by floating ice shelves (4).

How intrinsically stable is the ice sheet, given the marine-based bottom topography and geometry in much of the interior of West Antarctica and the potential loss of buttressing provided by ice shelves (5, 6)? Satellite data have shown dramatic changes in West Antarctica, as some important out-

Jet Propulsion Laboratory, California Institute of Technology, Pasadena, CA 91109, USA. E-mail: eri@jpl.nasa.gov



Runaway instability. Currently the grounding line sits to the right, upslope just outside the marine-based basin (A). Warm thermal ocean upwelling beneath the ice shelf (11) and lubrication by wet sediment at the base may exacerbate the potential instability and aid in accelerating the outward ice flow. As ice thickens

at the transition zone (near the vertical arrow at the grounding line), ice flow increases. The runaway instability (evolving from A to C) does not stop until a new stable position is found and ice that was once grounded to the floor of the submarine basin has been lost to the global oceans. [Adapted from (5)]

flux systems have increased their flow velocities during the past decade (7, 8). Data from the Gravity Recovery and Climate Experiment (GRACE) satellite pair since late 2002 strongly indicate ongoing losses caused by enhanced drainage into Pine Island Bay and the Amundsen Sea (9, 10) via glaciers that penetrate hundreds of kilometers upstream into the partially marine-based WAIS.

Numerical simulations suggest that positive feedback at the grounding line of the Pine Island Glacier exists between changes in ice shelf geometry and enhanced advection of warm ocean water (11). No numerical demonstration exists, however, that a runaway instability has already been triggered. A number of parameters, such as those controlling resistance at the bedrock, are too poorly constrained to decide whether runaway instability is occurring or will occur.

Once a runaway instability starts it cannot be stopped until a new stable position is found (see the figure). In the transition to this new stable state, sea levels will rise globally. Recent microfossil data from a 600-m-deep sedimentary core in the Ross Sea reveal many successions of waxing and waning ice cover and suggest that open marine conditions existed there 3 to 5 million years ago, a time when average terrestrial temperatures were about 3°C higher than they are today (12). A runaway scenario may have occurred then and may occur again in the future.

Bamber *et al.* have now used new data on surface elevation, bedrock topography, geoid, and current-flow configuration to calculate the total volume of ice that is susceptible to loss under a runaway instability scenario. The calculation is rooted in simple geometrical considerations, largely decoupled from the detailed flow instability mechanics. The time scale for the flux instabilities to be fully manifest is uncertain, but the calculated global consequences to sea level are important, considering that just 0.5 to 1.0 m of uniform sea-

level rise will cause catastrophic geopolitical and economic devastation in many urbanized coastal settings (13).

The good news is that the predicted globally uniform sea-level rise of 3.2 m is roughly half the predicted value quoted for the past 30 years. But the bad news is that some regions, including North America and the southern Indian Ocean, will experience enhanced inundation (by as much as ~0.4 m with respect to the global mean) due to changes in the gravity field and moments of inertia of Earth compared to present-day values. The latter cause the mean spin axis of Earth's rotation to move toward the region of discharging ice mass (14). Though smaller than past predictions, the scale of the fully manifested instability is enormous: The total mass gained by the oceans (1.8×10^6 gigatons; 1 gigaton = 10^9 tons) would be roughly equal to the mass showered to Earth by the impact of ~2000 Halley-sized comets.

As the gravity field adjusts to the changing distribution of mass between land and ocean, Earth's spin axis moves through the crust, changing the distribution of the centrifugal forces acting on the ocean. These two effects produce a global pattern of sea-level change similar to that computed recently by Mitrovica *et al.* (15). However, Bamber *et al.*'s calculation gives more precise predictions of sea-level change from a WAIS collapse, because they have better estimates of how much ice goes into the ocean from WAIS instability and at which geographical positions the mass shifts will occur; they can thus also better calculate the shifts in moments of inertia and gravitational field.

The situation in the near future could be complicated by the fact that Greenland, though lacking the unstable configuration of the WAIS, seems to be losing as much mass as, or more than, Antarctica (10, 16). Greenland needs only half the mass loss rate of Antarctica to have an equivalent effect on polar motion due to its less polar position

than that of WAIS (14). However, as termini of Greenland glaciers change from tidewater to land-based, the glaciers may become less susceptible to rapid flow and the rate of mass loss may diminish (17). The observed accelerations of ice outflux into the Amundsen Sea Embayment in Antarctica are potentially more ominous (18). Should the ice sheet grounding line migrate farther inland, ice resting on bedrock well below sea level could become unstable (see the figure). The time scale of the fully manifested instability cannot currently be predicted. Better predictions require both better in situ data and space monitoring coupled to a fully three-dimensional high-resolution (< 1 km) computational model.

References and Notes

1. A. Shepherd, D. Wingham, *Science* **315**, 1529 (2007).
2. J. L. Bamber, R. E. M. Riva, B. L. A. Vermeersen, A. M. LeBrocq, *Science* **324**, 901 (2009).
3. R. A. Bindaschadler, T. A. Scambos, *Science* **252**, 242 (1991).
4. T. J. Hughes, *Ice Sheets* (Oxford Univ. Press, New York, 1998).
5. C. Schoof, *J. Geophys. Res.* **112**, F03S28 (2007).
6. J. L. Bamber, R. B. Alley, I. Joughin, *Earth Planet. Sci. Lett.* **257**, 1 (2007).
7. R. Thomas *et al.*, *Science* **306**, 255 (2004).
8. E. Rignot *et al.*, *Nat. Geosci.* **1**, 106 (2008).
9. I. Velicogna, J. Wahr, *Science* **311**, 1754 (2006).
10. G. Ramillien *et al.*, *Global Planet. Change* **53**, 198 (2006).
11. A. J. Payne *et al.*, *J. Geophys. Res.* **112**, C10019 (2007).
12. T. Naish *et al.*, *Nature* **458**, 322 (2009).
13. D. M. Fitzgerald *et al.*, *Annu. Rev. Earth Planet. Sci.* **36**, 601 (2008).
14. T. S. James, E. R. Ivins, *J. Geophys. Res.* **102**, 605 (1997).
15. J. X. Mitrovica, N. Gomez, P. U. Clark, *Science* **323**, 753 (2009).
16. E. Rignot, J. E. Box, E. Burgess, E. Hanna, *Geophys. Res. Lett.* **35**, L20502 (2008).
17. F. M. Nick, A. Vieli, I. M. Howat, I. Joughin, *Nat. Geosci.* **2**, 110 (2009).
18. D. G. Vaughan, J. W. Holt, D. D. Blankenship, *Eos Trans. AGU* **88**, 10.1029/2007EO460001 (2007).
19. This work was performed at the Jet Propulsion Laboratory, California Institute of Technology, and funded by the Solid Earth and Surface Processes Focus Area within NASA's Earth Science Program.

10.1126/science.1173958

DEVELOPMENT

Ovulation Signals

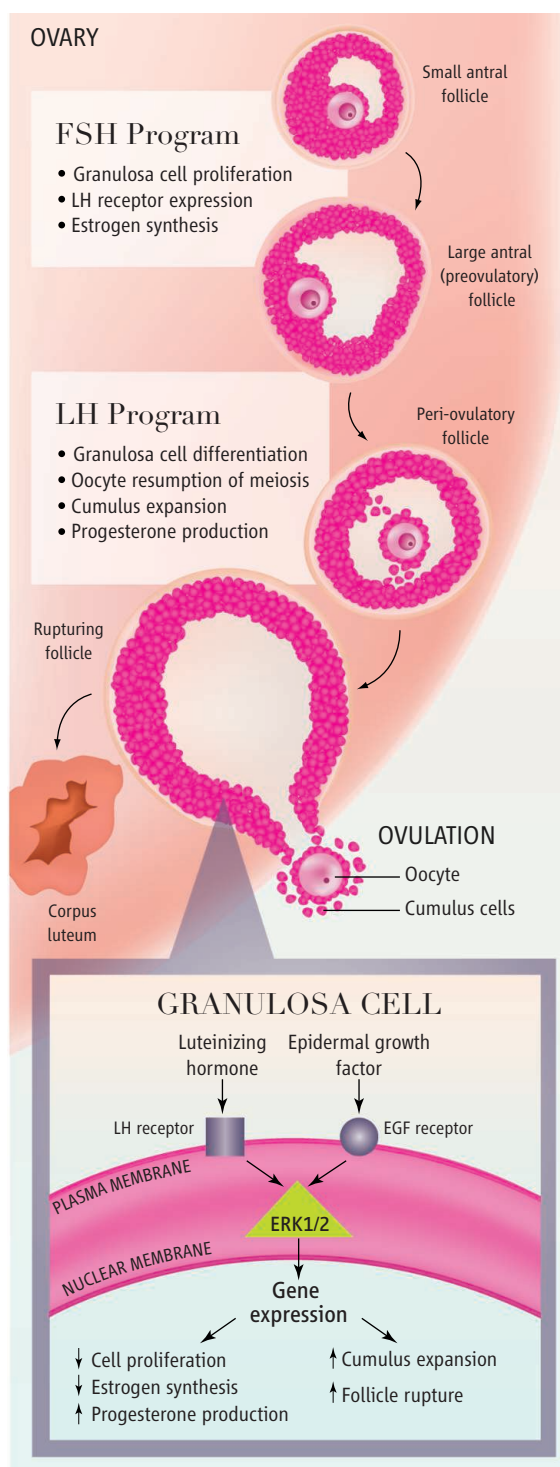
Rajesha Duggavathi¹ and Bruce D. Murphy²

Successful mammalian reproduction requires that the female gamete (oocyte or egg) acquires, within the growing ovarian follicle, the ability to be fertilized. Failure to initiate or complete follicle development, or defects in the oocyte (such as aneuploidy) result in infertility. On page 938 in this issue, Fan *et al.* (1) describe cellular signaling pathways in the mouse ovary that support follicle maturation and, ultimately, the discharge of a mature egg. The findings could help elucidate the underlying molecular nature of ovarian pathology and infertility-producing conditions in humans.

In the mammalian ovary, a specific number of follicles (for example, usually one in humans and up to 10 in mice) ovulate during each reproductive cycle. Follicle development and ovulation are controlled by two pituitary hormones, follicle-stimulating hormone (FSH) and luteinizing hormone (LH) (see the figure). Luteinizing hormone causes an orderly continuum of follicle remodeling, which includes expansion in overall size (through fluid uptake), and termination of cell division in granulosa cells, the somatic cells in the ovary that support the oocyte. Meiosis in the oocyte, arrested in the first meiotic division during embryogenesis, is reinitiated by luteinizing hormone. Luteinizing hormone also initiates the proteolysis of the follicular wall that allows the follicle to rupture and release the oocyte.

Signaling occurs in granulosa cells through nuclear receptors (2), cyclic adenosine monophosphate, and members of the epidermal growth factor family (3). Fan *et al.* developed a mouse model to examine how mitogen-activated protein kinase (MAPK) intracellular signaling pathways in granulosa cells provoke ovulation and, consequently, collapse of the follicle and development of the successor tissue, the corpus luteum.

¹Animal Science, McGill University, Ste-Anne-de-Bellevue, Quebec, H9X 3V9 Canada. ²Centre de recherche en reproduction animale, Université de Montréal, St-Hyacinthe, J2S 7C6 Canada. E-mail: raj.duggavathi@mcgill.ca; bruce.d.murphy@umontreal.ca



Mammalian ovulation. Follicle-stimulating hormone and luteinizing hormone control events that support follicle maturation. In granulosa cells, ERK1/2 is activated by different factors and can control cell functions through specific effectors.

Human infertility may be associated with aberrant cell signaling events within ovarian granulosa cells.

The MAPK pathways are widespread signaling routes in eukaryotic cells. There are six distinct groups of MAP kinases in mammals, stimulated by a variety of extracellular signals (4). Fan *et al.* focused on MAP kinases 3 and 1, also known as extracellular-regulated protein kinases 1 and 2 (ERK1/2). Germline deletion of ERK1 does not affect mouse fertility, whereas germline deletion of ERK2 is lethal early in embryogenesis (5). The authors thus developed a fertile mouse line in which ERK2 expression was deleted only in granulosa cells. However, crossing these mice with those engineered to lack ERK1 produced ERK1/2-deficient mice that were infertile. Females displayed multiple disrupted ovarian processes, including prolonged follicle development and failure of oocytes to mature.

The ERK1/2-deficient mice had a major defect in luteinizing hormone signaling, not unexpected because this hormone activates ERK1/2 in granulosa cells within 30 min (6). Follicle development induced by follicle-stimulating hormone normally arrests when luteinizing hormone triggers differentiation of granulosa cells (7). Consequently, in the ERK1/2-deficient mice, the sequence of events induced by follicle-stimulating hormone was prolonged. Likewise, the effects of luteinizing hormone were compromised, as events such as cessation of estrogen synthesis and the expression of genes required for cumulus oophorus (granulosa cells that surround the oocyte) expansion, failed to occur.

The intracellular targets of activated ERK1/2 signaling pathways in granulosa cells are only partially known, so it is not clear where the major lesions in signaling are located in the ERK1/2-deficient mice. Fan *et al.* propose that disrupted signaling occurs downstream of signals initiated at the cell surface by epidermal growth factorlike molecules that are produced by a granulosa cell itself. Reduced expression of one such factor, epiregulin, and the failure of another, amphiregulin, to induce cumulus oophorus expansion and oocyte maturation support this view. Nevertheless,

CREDIT: ADAPTED BY N. KEVITYAGALA/SCIENCE

abrogation of epidermal growth factor signaling reduces, but does not eliminate, activation of ERK1/2 (3) implicating targets elsewhere, including factors upstream of epidermal growth factor expression. Moreover, luteinizing hormone may activate steroidogenesis by interacting with ERK signaling pathways (8). Disruption of this interaction could account for the dysfunctional steroidogenesis observed in ERK1/2-deficient mice. Autocrine regulation of the late stages of follicle maturation is mediated by estrogens, produced by granulosa cells, which act through membrane-type estrogen receptors at the cell surface and activate ERK1/2 (9). Although this receptor alone cannot support ovulation (10), it may be that the ERK1/2 signal is essential for this process.

The phenotype of the ERK1/2-deficient mice is similar to that seen in mice engineered

to lack the transcription factor CCAAT/Enhancer-binding protein- β (C/EBP β), suggesting that C/EBP β is a major downstream effector of ERK signaling pathways. Additional potential targets were not explored, but candidates include the receptor-interacting protein 140 (Rip140), because this factor is a phosphorylation target of ERK2 (11) and mice lacking this factor cannot ovulate (12). ERK signals are not only induced by a number of extracellular stimuli but they are frequently pleiotropic. The absence of ERK1 and ERK2 in granulosa cells not only disrupted the action of epidermal growth factor-like molecules, but other ERK-generating systems are probably impaired as well as targets beyond C/EBP β -mediated transcription. The findings of Fan *et al.* should help elucidate ovarian pathology such as poly-

cystic ovarian disease, a common condition in which ERK1/2 activation is attenuated in follicle cells (13), and other anovulatory and infertility-producing conditions in humans.

References

1. H.-Y. Fan *et al.*, *Science* **324**, 938 (2009).
2. R. Duggavathi *et al.*, *Genes Dev* **22**, 1871 (2008).
3. S. Panigone *et al.*, *Mol. Endocrinol.* **22**, 924 (2008).
4. M. Krishna, H. Narang, *Cell. Mol. Life Sci.* **65**, 3525 (2008).
5. M. Aouadi *et al.*, *Biochimie* **88**, 1091 (2006).
6. H. Y. Fan *et al.*, *Development* **135**, 2127 (2008).
7. B. D. Murphy, *Biol. Reprod.* **63**, 2 (2000).
8. Y. Q. Su *et al.*, *Biol. Reprod.* **75**, 859 (2006).
9. M. Razandi *et al.*, *Mol. Endocrinol.* **18**, 2854 (2004).
10. A. Pedram *et al.*, *J. Biol. Chem.* **284**, 3488 (2009).
11. P. C. Ho *et al.*, *Cell Signal.* **20**, 1911 (2008).
12. J. M. A. Tullet *et al.*, *Endocrinology* **146**, 4127 (2005).
13. V. L. Nelson-Degrave *et al.*, *Mol. Endocrinol.* **19**, 379 (2005).

10.1126/science.1174130

APPLIED PHYSICS

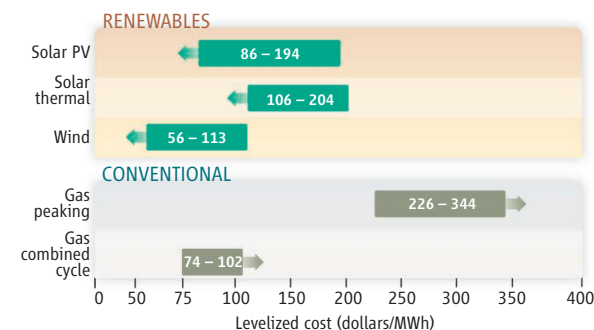
Photovoltaics Power Up

Richard M. Swanson

The global photovoltaic (PV) power industry is experiencing dramatic technology advances and market growth. Over the past 20 years, manufacturing output has grown by a factor of 200, reaching 5 gigawatts (GW) in 2008. The total accumulated installed capacity is now around 15 GW. This is quite small relative to the world's 4000 GW of installed electric generation capacity—just 0.375% to be precise. However, industry leaders expect similar rapid growth over the coming years, with PV generation a major contributor to power generation 20 years hence (1).

In this quickly evolving environment, investors must assess which technologies and companies are best positioned, policy-makers must assess what role PV generation should play in our energy mix, utility planners must assess the impacts this will have on the electric grid, government and industry must decide how to allocate research and development (R&D) funds, and citizens must sort through a barrage of conflicting messages. For example, a recent *Wall Street Journal* opinion editorial article states, "There's an unavoidable problem with renewable-energy technologies: From an economic standpoint, they're big losers" (2). Perhaps this was once true when the industry was so small that it didn't matter anyway.

SunPower Corporation, 3939 North First Street, San Jose, CA 95134, USA. E-mail: richard.swanson@sunpowercorp.com



Measuring up. Levelized cost of energy by resource for new generation constructed in the 2009 to 2012 time frame. Prices include the 30% U.S. federal investment tax credit for renewables. PV is a viable utility option, with its competitiveness only expected to increase as PV costs decrease and gas prices rise. [Source: Lazard Capital Markets, 1/9/09]

But in many cases it is no longer true today.

Driven by advances in technology and increases in manufacturing scale and sophistication, the cost of PV has declined at a steady rate since the first solar cells were manufactured (3). For example, in 2000, solar cells typically used 15 g of expensive, highly refined silicon to generate 1 W of power. By comparison, SunPower Corporation's modules currently use only 5.6 g/W. Today, the manufacturing cost of standard crystalline silicon modules produced in a state-of-the-art facility is around \$1.40/W (4). This cost includes the cost of refining silicon but not the added gross margin in sales price. Manufacturers foresee manufacturing cost to fall to

The power-generating capacity of solar cells, while currently small relative to other sources, is increasing exponentially.

\$1/W within 5 years. An upshot of these cost reductions is that the levelized cost of energy (LCOE) for PV plants (see the figure) is now in the range of conventional generation options when taking into account the impact of the U.S. federal 30% investment tax credit, and will be fully competitive without that incentive in 5 years. Perhaps surprisingly, PV electricity today costs less than that from a new natural gas peaking plant, and is rapidly encroaching on combined cycle base-load generation costs.

From the perspective of an electric utility, what counts in making new generation decisions is the cost of electricity from the new plant. That their customers might pay a lower cost due to older, lower-cost generation in the mix (such as from hydroelectric or coal plants) is irrelevant when more capacity is needed. This fact has contributed to the recent increase in interest in PV on the part of electric utilities. For example, the California utility Pacific Gas and Electric (PG&E) has recently contracted for the purchase of 800 MW of PV-generated power (5). When utilities consider adding PV, they take into account not only its cost effectiveness but also its lack of fuel price risk, lack of potential carbon emission costs, minimal

siting limitations, and lack of water use. Furthermore, construction times are short; for example, the PV industry installed more than 2 GW of PV power plants in Spain during 2008. Construction times for 2 GW of conventional generation would be 10 to 15 years. PV will thus not be insignificant much longer.

Conventional crystalline silicon modules compete with emerging thin-film technologies. Leading thin-film producers have lower cost, but at lower module energy conversion efficiency. The lower efficiency results in higher installation cost, with the result that there is near cost parity at the installed-system level. Indeed, there is a spectrum of technologies—from higher-performance, higher-cost modules to lower-performance, roll-on thin

films—all competing successfully. Crystalline silicon modules are capable of attaining the long-term cost targets. Therefore, one should not think of thin-film technologies as somehow disruptive or uniquely enabling for the emergence of large-scale PV. Thin films are rather new technologies that may, if successful, help drive costs lower over time. The competition from crystalline silicon, however, will remain formidable because of the vast R&D resources being deployed. New entrants to the PV industry need to be cognizant of this fact as they allocate their own capital to the field.

Our energy future is becoming clearer. PV will not be a panacea, but it will take its place as a major source of energy alongside energy efficiency, other renewables, nuclear, and improved

conventional generation, perhaps with carbon sequestration, as we transition to a carbon-free electric grid over the next half century.

References

1. P. Mints, "Sunny outlook: Predictions for growth in the PV industry," *Renewable Energy World*, September 2007 (www.renewableenergyworld.com/rea/news/article/2007/09/sunny-outlook-predictions-for-growth-in-the-pv-industry-51464).
2. M. Schulz, "Don't count on 'countless' green jobs," *Wall Street Journal*, 20 February 2009, p. A15.
3. R. M. Swanson, *Prog. Photovolt. Res. Appl.* **14**, 443 (2006).
4. *Photon International*, December 2008, pp. 84–92.
5. PG&E press release, "PG&E signs historic 800 MW photovoltaic solar power agreements with Optisolar and SunPower," August 2008 (www.pge.com/about/news/mediarelations/newsreleases/q3_2008/080814.shtml).

10.1126/science.1169616

APPLIED PHYSICS

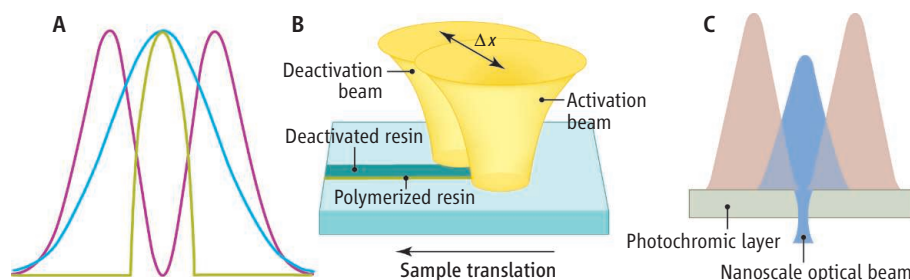
Two Beams Squeeze Feature Sizes in Optical Lithography

Joseph W. Perry

The fabrication of electronic circuits on chips relies on the patterning of surfaces by optical lithography, which is used to control where different components—metal wires, semiconductor gates, and oxide insulators—form (1). Three papers in this issue (2–4) report a new approach to optical lithography that allows small feature sizes to be created more easily than with traditional approaches.

In optical lithography, a light-sensitive film, called a photoresist, is exposed in selected areas by using a patterned mask. The light triggers chemical reactions that change the film's solubility. Solvents are then used to remove the exposed or unexposed areas, so that only selected areas on the chip undergo the next processing step. For example, after selective removal of photoresist, protected parts of a semiconductor layer become separated gate regions, whereas exposed regions are open for doping or deposition of electrodes.

Feature sizes as small as 45 nm can now be achieved in device fabrication, beating the diffraction limit set by the wavelength of the far-ultraviolet (FUV) light used for exposure (193 nm) through clever optical tricks (5). However, the light sources and the masks that create the patterns are costly; even higher costs



Two beams create smaller features. (A and B) The polymerization reactions initiated by a beam of light exciting a photoresist, which changes its solubility, can be inhibited by a second light source. (A) In the exposure scheme used by Scott *et al.*, the second coincident beam (whose profile is shown in purple) surrounds the first beam (shown in blue), which has a different wavelength and activates a reaction inhibitor. The net activation profile is shown in green. (B) In the work of Li *et al.*, an intense initiator beam is followed by a second, longer-duration beam of the same wavelength that inhibits the reaction. The beams can be coincident or offset, as shown by a distance Δx . (C) Two light sources can be used to create grating lines much smaller than the wavelength of either source. Andrew *et al.* place a photochromic film over the photoresist. A grating of UV light (325 nm, shown in blue), which makes the film transparent, is offset from a grating created by red light (633 nm) that makes the film opaque. The UV light penetrates a nanoscale region as small as ~40 nm, which is much smaller than its wavelength.

can be anticipated for the shorter wavelengths needed for even smaller feature sizes. A simpler and less costly way to achieve smaller features is to use light to control the kinetics of the reactions that occur within the film. The three studies in this issue [Scott *et al.* (2), page 913; Li *et al.* (3), page 910; and Andrew *et al.* (4), page 917] make use of comparatively longer-wavelength light (UV to near infrared) that beats diffraction limits in optical lithography and creates features on the scale of tens of nanometers. In these approaches, one optical

beam controls the spatial distribution of exposure while another beam induces chemical activation.

The classical resolution limit imposed by diffraction (about half the wavelength of light) applies to any light source focused by a lens. When coherent laser sources are used, destructive interference effects can restrict the actual area being illuminated through a mask. In this way, quarter-wavelength (45 nm) features can be created with 193-nm light from an argon fluoride excimer laser with phase-shift masks.

School of Chemistry and Biochemistry and Center for Organic Photonics and Electronics, Georgia Institute of Technology, Atlanta, GA 30332, USA. E-mail: joe.perry@gatech.edu

Some of the light passing through a phase-shifted part of the mask destructively interferes with light traveling through adjoining unmodified parts of the mask. Despite important advances in shorter-wavelength exposure systems, sophisticated mask technologies, and more sensitive photoresists (6), there is considerable interest in alternative lithography approaches that can achieve nanoscale resolution with longer-wavelength optical sources, which have much lower maintenance and cost.

The main concept behind the “subdiffraction” resolution approaches reported in this issue is the use of dual exposures to create a spatial exposure pattern. These beams can have a donutlike pattern—the beam that activates the patterning chemistry is surrounded by a ring of intensity of another beam that suppresses the activation while maintaining a valley (or node) at the center of the activating beam. The product of the activation peak and “deactivation” donut pattern gives a spatial dosing pattern that is substantially finer than the far-field diffraction pattern of a tightly focused optical beam.

Subdiffraction resolution is achieved in optical microscopy by using a pair of beams as described above and taking advantage of stimulated emission depletion of chromophores (7). One beam is used for excitation of fluorescence with a peaked spatial distribution, and one with a donutlike pattern is used for rapid de-excitation via stimulated emission. The net

spatial distribution of the excitation provides subdiffraction (nanoscale) imaging resolution.

The studies reported in this issue adapt these ideas for subdiffraction lithography by using photoinhibition or photoinduced absorption, rather than stimulated emission, to narrow the exposure profiles. Scott *et al.* report an optical lithography method based on the use of two wavelengths: One, at 473 nm, excites a photoinitiator that activates free-radical polymerization and gelation of a dimethacrylate monomer and renders the exposed area insoluble (see the figure, panel A). The second beam, with a wavelength of 365 nm, excites a photoinhibitor, which then scavenges free radicals and stops the reaction. Li *et al.* used a different initiator molecule that allowed both beams to share the same wavelength (800 nm). Activation is achieved with an intense initial beam (200 fs) that proceeds through a two-photon process, while long-duration 50-ps or continuous-wave light deactivates the reaction through a one-photon process (see the figure, panel B). This approach created features 1/20 the size of the wavelength of light along the beam direction through beam shaping.

Andrew *et al.* used exposure of a photochromic film at two wavelengths (see the figure, panel C). Ultraviolet light at 325 nm caused the film to become more transparent at that wavelength, whereas red light at 633 nm caused it to become strongly absorbing at the

UV wavelength. By setting up a simple grating interference pattern with peaks of the 325-nm light occurring in the valleys of the 633-nm light and controlling the relative intensities of the beams, nanoscale regions are obtained at the nodes of the red light where the UV light is transmitted. Features as small as 40 nm in width were created in an underlying photoresist layer.

How and when these lithographic schemes will enter into chip fabrication is hard to predict. However, these methods should already offer alternatives to the methods now in use, such as electron-beam lithography and micro-contact printing, for creating nanoscale features in a lab setting. It may well be possible to harness these ideas to create lithographic schemes that will shrink the feature sizes obtainable with shorter-wavelength ultraviolet sources.

References

1. K. Suzuki, B. W. Smith, Eds. (CRC Press, Boca Raton, FL, ed. 2, 2007).
2. T. F. Scott *et al.*, *Science* **324**, 913 (2009); published online 9 April 2009 (10.1126/science.1167610).
3. L. Li *et al.*, *Science* **324**, 910 (2009); published online 9 April 2009 (10.1126/science.1168996).
4. T. L. Andrew *et al.*, *Science* **324**, 917 (2009); published online 9 April 2009 (10.1126/science.1167704).
5. M. Totzeck, W. Ulrich, A. Goehnermeier, W. Kaiser, *Nature Photonics* **1**, 629 (2007).
6. D. Bratton, D. Yang, J. Dai, C. K. Ober, *Polym. Adv. Technol.* **17**, 94 (2006).
7. S. W. Hell, *Science* **316**, 1153 (2007).

10.1126/science.1174224

NEUROSCIENCE

Crossing the Line

Thomas Kidd

A key process in animal evolution was the development of a nerve-rich, bilaterally symmetric longitudinal structure, the central nervous system. Without such a symmetric body axis, Earth might still be populated by just sea anemones, sponges, and similar organisms (1). The switch from radial to bilateral symmetry created a distinct left- and right-hand side to the animal and its nervous system. The dividing line, or axis of symmetry, is known as the midline. One of the earliest decisions a developing neuron must make is whether to extend its long cellular process (the axon) across the midline. On page 944 of this issue, Yang *et al.* (2) uncover an unexpected level of complexity in how this initial decision is made.

Commissural axons connect the two sides of the nervous system and are attracted to grow toward the midline by netrin proteins. In the fruit fly *Drosophila melanogaster*, Netrins are secreted by specialized glial cells at the midline and are detected by Frazzled/DCC (Fra) receptors on commissural axons (3) (see the figure). As they cross the midline, axons increase expression of Robo-family receptors. These receptors detect Slit, a protein that repels axons. Slit is also secreted by midline glial cells, thereby causing axons to continue growing to the other side of the nervous system (4).

Mutations in the gene *commis sureless* (*comm*) that disrupt expression of the encoded protein Comm abolish all left-right connections in the ventral nerve cord, the fly homolog of the spinal cord (5). Comm promotes midline crossing by silencing axon responses to the midline repellent Slit (6, 7). In the absence

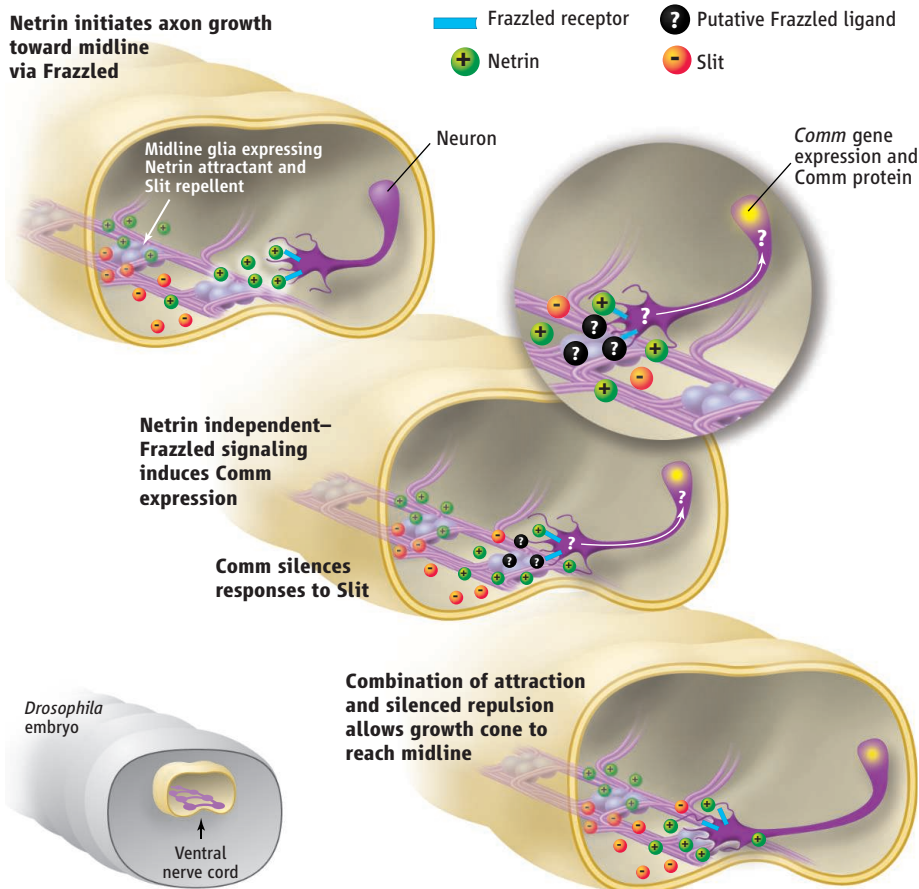
An axon guidance receptor generates a transcriptional response independent of its known ligand.

of Comm, Robo receptors are expressed at the cell surface of commissural axons prematurely, thus allowing Slit-Robo interactions and preventing midline crossing. It appears that commissural neurons begin to express Comm as they approach the midline, and then decrease Comm expression after crossing to allow continued axon growth (7).

A Fra receptor that lacks its cytoplasmic domain (FraΔC) also inhibits midline crossing, producing a phenotype far more severe than the *fra* mutant (which lacks Fra receptors), and identical to the phenotype of the *comm* mutant (8). Genetic evidence suggested that FraΔC and Comm could act in the same intracellular signaling pathway. This prompted Yang *et al.* to determine that expression of *comm* mRNA in individual neurons is reduced when *fra* is absent. In a complementary experiment, overexpression of *fra* induced *comm* mRNA

Department of Biology, University of Nevada, Reno, NV 89557, USA. E-mail: tkidd@unr.edu

Netrin initiates axon growth toward midline via Frazzled



Midline crossing. A schematic of a *Drosophila* ventral nerve cord, in which longitudinal tracts of nerves (axons) are connected in a repeated fashion by midline-crossing (commissural) axons. A commissural axon is shown at successive stages of development. Molecular events in the actively moving tip of the axon are depicted with Fra binding Netrin and a putative unidentified ligand.

expression. Furthermore, neuronal expression of *comm* partially rescued *fra* mutants, showing that Fra induces *comm* expression. Remarkably, however, *comm* expression does not require Fra's ligand Netrin.

What is the signaling pathway that connects Fra to Comm? If the absence of Fra was simply preventing growing axons from contacting the midline and detecting a signal that induces *comm* expression, then expression of *comm* should also be reduced in *netrin* mutants, but Yang *et al.* did not observe this. Furthermore, many axons still cross the midline in *fra* mutants, so they must have been exposed to a candidate midline signal, yet the axons show reduced *comm* expression. The presence of reduced *comm* expression in *fra* mutants indicates that it is not necessary to induce *comm* expression to the level seen in wild-type fly commissural axons to allow midline crossing, and that an additional mechanism also induces *comm* expression.

Why is the FraΔC phenotype so much stronger than that of the *fra* mutant? The likely explanation is that FraΔC interferes with the functions of other proteins. One candidate is

the Down syndrome cell adhesion molecule (Dscam), another receptor expressed by commissural axons. Dscam forms a complex at the cell surface with a protein called Deleted in Colorectal Cancer (9). Dscam responds to an unidentified midline cue as well as to Netrins (10), but Dscam alone cannot account for the severity of the FraΔC phenotype, so other components remain to be discovered.

Although we know some of the transcription factors that specify the complement of receptors expressed in the growing axon tip (growth cone) (11), the study by Yang *et al.* may be the first to show that neuronal gene expression is altered by an external signal encountered during navigation of the growth cone toward the midline. The nature of this external signal is unknown; however, the strong correlation between proximity to the midline and ability to induce *comm* expression suggests a membrane-anchored or short-range midline cue as the most likely explanation.

Identification of a Netrin-independent function for Fra opens up possibilities for identifying novel axon guidance mechanisms. Fra is large enough to accommodate a binding site

for an additional ligand, and the number of external signals that control axon guidance is relatively limited. The Netrin-independent intracellular signaling mechanism does not require any of the previously identified cytoplasmic motifs (sites of interaction with other proteins) in Fra, suggesting a yet unknown signaling pathway. The Fra homolog Neogenin can be cleaved by γ -secretase to produce an intracellular fragment that can regulate gene transcription (12), and such a mechanism might be evolutionarily conserved.

In vertebrates, initial midline crossing appears to be achieved by a different mechanism. A splice variant of Robo3/Rig-1 inhibits Slit repulsion in axons as they approach and cross the midline (13). However, concentrations of Robo1 and Robo2 increase after axons cross the midline (14), suggesting that a mechanism similar to that of Comm could be operating. No *comm* homolog has been found in vertebrates, but even within insects, *comm* sequences are highly divergent.

The next questions include determining the nature of Netrin independent-Fra activation, how this activation transduces a signal to the nucleus, and what signal turns *comm* expression off after midline crossing. Amazingly, Robo proteins engineered to be insensitive to regulation by Comm do not prevent midline crossing (7), suggesting that Comm targets other components required for responding to Slit. In *netrin* mutants, many axons still cross the midline, indicating the existence of a yet unknown midline attractant. This is likely to be a diffusible cue, because in the absence of Netrins, growth cones still orient toward the midline even when at a distance (15). Clearly, the midline still guards many secrets as to how multiple overlapping systems ensure that the decision to cross the midline is made with a high degree of accuracy.

References

1. A. Ghysen, *Int. J. Dev. Biol.* **36**, 47 (1992).
2. L. Yang, D. S. Garbe, G. J. Bashaw, *Science* **324**, 944 (2009); published online 26 March 2009 (10.1126/science.1171320).
3. S. W. Moore *et al.*, *Adv. Exp. Med. Biol.* **621**, 17 (2007).
4. B. J. Dickson, G. F. Gilestro, *Annu. Rev. Cell Dev. Biol.* **22**, 651 (2006).
5. G. Tear *et al.*, *Neuron* **16**, 501 (1996).
6. K. Keleman *et al.*, *Cell* **110**, 415 (2002).
7. G. F. Gilestro, *PLoS One* **3**, e3798 (2008).
8. D. S. Garbe *et al.*, *Development* **134**, 4325 (2007).
9. A. Ly *et al.*, *Cell* **133**, 1241 (2008).
10. G. L. Andrews *et al.*, *Development* **135**, 3839 (2008).
11. S. J. Butler, G. Tear, *Development* **134**, 439 (2007).
12. D. Goldschneider *et al.*, *Mol. Cell. Biol.* **28**, 4068 (2008).
13. Z. Chen *et al.*, *Neuron* **58**, 325 (2008).
14. C. Sabatier *et al.*, *Cell* **117**, 157 (2004).
15. M. Brankatschk, B. J. Dickson, *Nat. Neurosci.* **9**, 188 (2006).

10.1126/science.1174216

CREDIT: K. SUTLUFF/SCIENCE

The Tail of Integrins, Talin, and Kindlins

Markus Moser,^{1*} Kyle R. Legate,^{1*} Roy Zent,² Reinhard Fässler¹

Integrins are transmembrane cell–adhesion molecules that carry signals from the outside to the inside of the cell and vice versa. Like other cell surface receptors, integrins signal in response to ligand binding; however, events within the cell can also regulate the affinity of integrins for ligands. This feature is important in physiological situations such as those in blood, in which cells are always in close proximity to their ligands, yet cell–ligand interactions occur only after integrin activation in response to specific external cues. This review focuses on the mechanisms whereby two key proteins, talin and the kindlins, regulate integrin activation by binding the tails of integrin- β subunits.

Integrins are members of a large family of functionally conserved cell–adhesion receptors. They have a critical role in anchoring cells to extracellular matrices and alter cell function by activating intracellular signaling pathways after ligand binding (“outside-in” signaling). Integrins can shift between high- and low-affinity conformations for ligand binding (“inside-out” signaling). This property of integrins is regulated by external cues that are transduced intracellularly and ultimately result in the direct binding of regulatory proteins to the short cytoplasmic domains of integrins. A shift from a low- to a high-affinity state is termed “integrin activation” (1, 2).

Regulation of the affinity with which integrins bind ligands is fundamental for various cellular functions. For example, during development migrating cells require activated integrins at their leading edge to attach newly protruded plasma membrane to the surface on which they are moving and inactivate integrins at their rear. In response to injury, the fibrinogen receptors on platelets, integrin α IIb β 3, are swiftly activated to mediate platelet adhesion and aggregation in order to stop bleeding. Because α IIb β 3 integrins are constantly exposed to fibrinogen, it is vital to keep them inactive so as to prevent pathological platelet aggregation and thrombus formation. Similarly, during inflammation leukocytes require integrin activation in order to adhere to and migrate across the endothelium on their way to affected tissues. Abnormal function of highly modulatable integrins or mutations in integrin-binding proteins required for integrin activation can result in aberrant development or diseases such as bleeding disorders, leukocyte–adhesion deficiencies, and skin blistering. In this review, we discuss recent structural and biochemical studies and data from genetic manipulations in animals that shed new light on how

two integrin tail-binding proteins, talin and kindlins, regulate integrin activation.

Integrin Structure

Integrins are formed by noncovalently bound α and β subunits. In mammals, 18 α and 8 β subunits combine in a restricted manner to form 24 specific dimers, which exhibit different ligand-binding properties. Integrin subunits have large

extracellular domains (approximately 800 amino acids) that contribute to ligand binding, single transmembrane (TM) domains (approximately 20 amino acids), and short cytoplasmic tails (13 to 70 amino acids, except that of β 4). All three domains are required to regulate the affinity of integrins. β 2 and β 3 integrins can change affinity on a subsecond time scale, and many of the paradigms of integrin structure and function were deduced from studies of these integrins; however, it is not clear whether they can be generalized to all integrins (1).

The extracellular domain of the heterodimer consists of a ligand-binding head domain standing on two long legs (Fig. 1A). α integrin subunits contain a seven-bladed β -propeller domain that forms the head, a thigh domain, and calf-1 and calf-2 domains. Half of the α subunits contain an I domain (also referred to as a von Willebrand factor A domain), which when present is nearly always the ligand-binding site. The I domain possesses a conserved metal ion-dependent adhesion site (MIDAS), which binds divalent cations required for ligand binding by integrins. The β subunit is composed of a hybrid domain that connects to the β I domain, which is

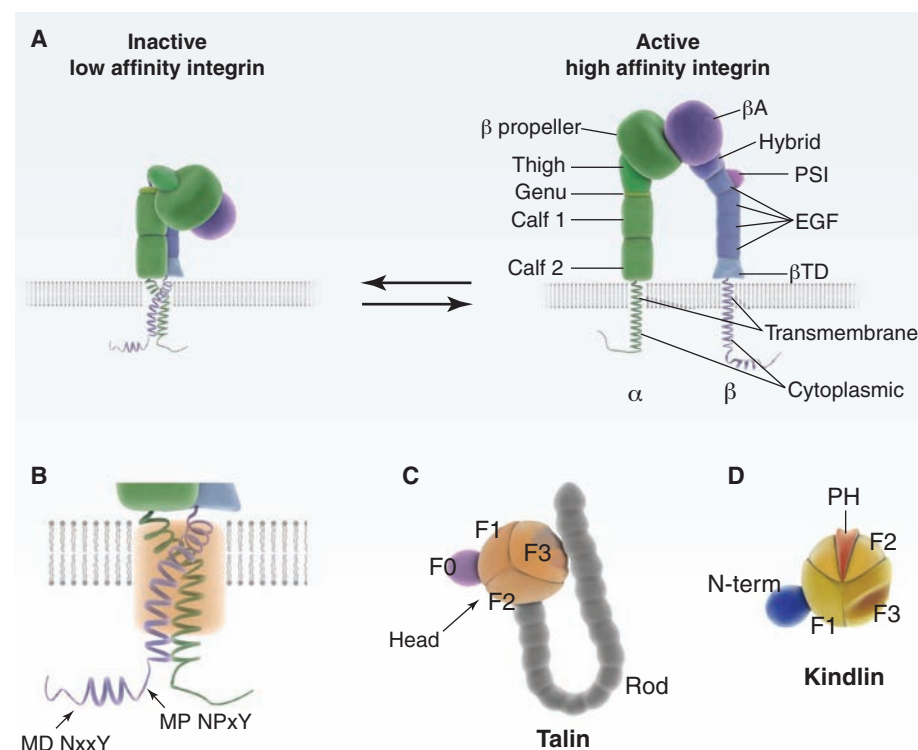


Fig. 1. (A) Integrin architecture and schematic representation of integrin activation. Specific contacts between the ectodomains, the TM, and cytoplasmic domains keep the integrin in its bent conformation. Separation of the integrin legs, TM, and cytoplasmic domains occurs during integrin activation, resulting in an extended integrin conformation. The α subunit is shown in green and the β subunit in violet. **(B)** A closer look at the interacting site (orange rectangle) between the TM and membrane proximal cytoplasmic domains of the α and β subunits. The membrane proximal (MP) and distal (MD) NPxY/NxxY motifs within the β tail are indicated. **(C and D)** Schematic drawings of the integrin-activating proteins talin (C) and kindlin (D). The FERM domains are depicted as balls subdivided into three subdomains, F1 to F3. Kindlins contain a PH domain inserted into the F2 subdomain. Domain sizes are not to scale, and talin is shown as a monomer for simplicity.

¹Max Planck Institute of Biochemistry, 82152 Martinsried, Germany. ²Division of Nephrology, Department of Medicine, Vanderbilt Medical Center and Veterans Affairs Hospital, Nashville, TN 37232, USA.

*These authors contributed equally to this work.

analogous to the I domain of the α subunit, a PSI (plexin/semaphoring/integrin) domain, four epidermal growth factor (EGF) domains, and a membrane proximal β tail domain (β TD). In integrins without an I domain, ligands bind to a crevice between the $\alpha\beta$ subunit interface, where they interact with a metal ion-occupied MIDAS within the β subunit and the propeller domain of the α subunit.

The structure of the short TM domains is poorly defined because of the lack of high-resolution structures of heterodimeric TM domains in their proper context, and only the structures of the $\beta 3$ and the α IIb subunits are solved in their entirety (3–5). The $\beta 3$ TM domain is a 30-residue linear α helix that is longer than the width of a typical lipid bilayer, which implies a pronounced helix tilt within the plasma membrane (5). The α IIb TM domain is a 24-residue α helix followed by a backbone reversal and does not exhibit a helix tilt (4). This unusual motif is highly conserved in the 18 human integrin α subunits and probably has an important role in the transition from low- to high-affinity states.

A high degree of similarity is found in the short α and β cytoplasmic tails, especially in the membrane proximal region where the GFFKR and HDR(R/K)E sequences are conserved in the α and β subunits, respectively (6). Nuclear magnetic resonance (NMR) studies that used integrin-derived α II $\beta 3$ polypeptides proposed that integrins interact with each other through hydrophobic and electrostatic interactions and a salt bridge between the R residue within the GFFKR motif and the D residue within the HDRRE motif (7, 8). However, these interactions were not seen by others, suggesting that tail interactions are very weak at best (9). Almost all β tails have two well-defined motifs that are part of a canonical recognition sequence for phosphotyrosine-binding (PTB) domains (10), consisting of a membrane proximal NPxY (where x represents any amino acid) motif and a membrane distal NxxY motif (Fig. 1B). These NxxY motifs are binding sites for multiple integrin-binding proteins, including talin and the kindlins.

Integrins Can Exist in Multiple Affinity States for Ligands

Integrins exist in low-, intermediate-, and high-affinity states. On the basis of structural studies, it is thought that integrins are in a low-affinity state when their extracellular domains are bent and in a high-affinity state when those are extended (Fig. 1A). The exact changes that occur in the head domain when integrins move to the high-affinity state are still unclear. Two models have been proposed: The “switchblade” model (11) predicts that only extended integrins will bind ligand, and the “deadbolt” model (12) suggests that integrin extension occurs only after ligand binding has taken place. In both models, conformational changes within the head domain facilitate ligand binding (11, 13).

The TM domains have a key role in integrin activation. Inactive integrins are proposed to have a coiled-coil interaction between canonical GxxxG dimerization motifs within the TM domains that regulates integrin subunit packing (14). Separation of integrin TM domains has been suggested to be a requirement for integrins to adopt the high-affinity state. There are two possible ways by which TM domain interactions

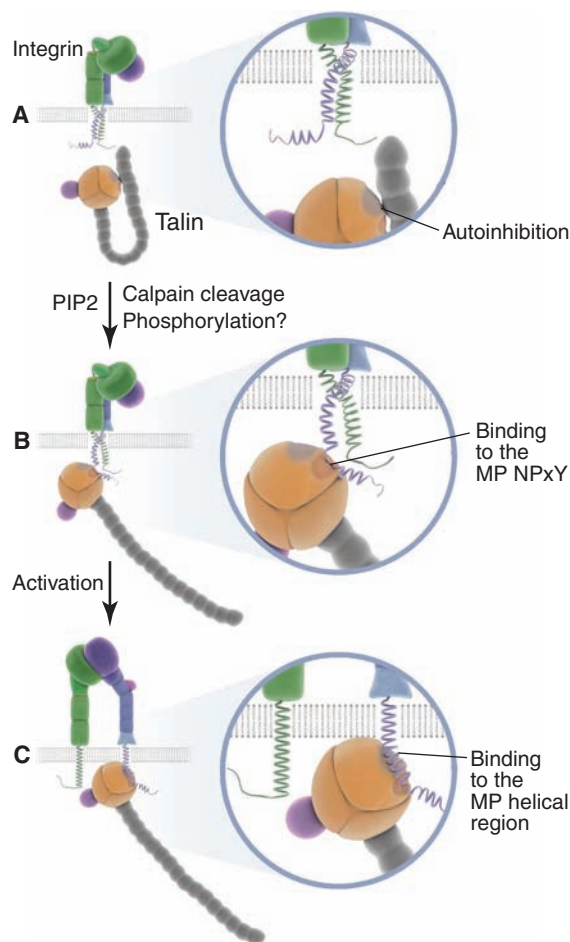


Fig. 2. Integrin activation by talin. (A) Cytoplasmic talin becomes activated upon binding phosphatidylinositol 4,5-bisphosphate (PIP₂), which abrogates an autoinhibitory interaction with the rod domain. In addition, calpain cleavage and phosphorylation events may activate talin. (B) The talin F3 subdomain engages the membrane proximal NPxY motif in β integrin tails. (C) In a second step, a talin-specific loop structure within the F3 subdomain interacts with the membrane-proximal α helix of the β integrin cytoplasmic tail, thereby disrupting the connection between cytoplasmic tails. Pulling forces at the β tail probably reorient the β integrin TM domain, thereby disrupting the packing of the $\alpha\beta$ TM domains.

can be disrupted. The number of residues of the β integrin TM domain buried within the lipid bilayer may be shortened upon activation, leading to a straightening of the TM domain within the membrane. Alternatively, pistonlike movement of integrin TM domains might cause the disruption of interactions within the membrane by changing the register of TM-domain side chains.

The role of integrin cytoplasmic tails in regulating integrin affinity, especially with respect to the binding of proteins such as talin and kindlins to the highly conserved NxxY motifs, has been extensively examined in the rapidly activated $\beta 2$ and $\beta 3$ integrins. Although mutational analysis suggests that the salt bridge is important for maintaining these integrins in a low-affinity state (15), this might not be the case for all integrins, especially the $\beta 1$ integrins (16). Despite the controversial role of the salt bridge in maintaining integrins in a low-affinity state, high integrin affinity is thought to be associated with separation of the α and β cytoplasmic tails. Many proteins bind directly to integrin tails, yet only talin and kindlins can regulate integrin affinity. The role of these NxxY motifs-binding proteins in integrin activation and function will now be discussed in detail.

Talin Is an Essential Mediator of Integrin Activation

Talin is a component of adhesion plaques and interacts with integrin cytoplasmic tails (17). Its role in altering integrin function was originally demonstrated by its ability to induce a shift in the affinity of a normally inactive integrin expressed in chinese hamster ovary (CHO) cells (18, 19). Knockout and knock-down experiments subsequently reinforced the notion that talin is a key regulator of integrin affinity for ligand, and many mutational and structural studies have described the mechanism by which it accomplishes this task. Talin orthologs have been identified in all multicellular eukaryotes studied; vertebrates encode two talin isoforms, termed talin1 and talin2, whereas lower eukaryotes encode only a single talin isoform corresponding to talin1 (20, 21).

Talins are ~270-kD proteins consisting of an N-terminal 47-kD head domain and a ~220-kD C-terminal flexible rod domain (Fig. 1C). The talin rod domain consists of a FERM (4.1, ezrin, radixin, moesin) domain composed of 3 subdomains (F1, F2, and F3) and an F0 subdomain with no homology to known domains. The F3 subdomain resembles a PTB domain and binds integrin tails, phosphatidylinositol 4-phosphate 5-kinase γ (PIP₂IK γ), and the hyaluronan receptor layilin (22–25). The talin rod domain is composed of a series of helical bundles that contain multiple binding sites for the F actin-binding protein vinculin and a second integrin-binding site (26). The C

terminus contains a THATCH (talin/HIP1R/Slp2p actin tethering C-terminal homology) domain (also known as an ILWEQ motif) that mediates dimerization and provides a direct linkage between talin and F actin (27, 28).

The integrin-binding site for the talin head was mapped to the membrane-proximal NPxY motif, a common binding motif for PTB domain-containing proteins (18, 19, 29). Mutations within the NPxY motif of both $\beta 1$ (30) and $\beta 3$ (31) integrins, as well as mutations in the talin PTB domain (32), abolish talin binding and decrease integrin affinity. Insights into how talin increases integrin affinity came from NMR experiments showing that the talin head effectively outcompetes the α IIb tail for binding to the $\beta 3$ tail (7). Fluorescence energy transfer (FRET) experiments in cells confirmed that the talin head induces separation of the integrin tails (in this case α L β 2), which is concomitant with increased basal integrin ligand binding (33). Cells depleted of talin1 by small interfering RNA (siRNA) cannot respond to common activation stimuli (31). Furthermore, genetic experiments in *Caenorhabditis elegans* (34), *Drosophila* (35), and mice (36–38) demonstrated that talin1 ablation universally leads to integrin-adhesion defects. These experiments led to the belief that talin was both necessary and sufficient to activate integrins. However, the claims of sufficiency were later shown to be an oversimplification.

A critical question is why talin can modulate integrin affinity, whereas other PTB domain-containing proteins that bind the same NPxY motif, such as Dok1 (18), tensin (39), and Numb (18), cannot. Mutational and structural studies suggest that this might be because the talin head has an additional binding site on the β integrin tail, in the membrane proximal region where the α and β integrin tails interact (8, 40), whereas Dok1 binds only to the region surrounding the NPxY motif (41). Crystallographic data has clarified that talin-dependent integrin activation involves binding of the talin F3 subdomain to the $\beta 3$ integrin tail at two locations in order to induce the displacement of the α integrin tail and facilitate tail separation (32). The talin F3 subdomain contains an extra loop of amino acids that binds to membrane-proximal sequences in the $\beta 3$ integrin tail. Thus, it was proposed that talin first encounters the β integrin tail by binding the NPxY motif through its PTB domain, and the loop sequence subsequently interacts with membrane proximal sequences within the β tail to displace the α integrin tail and separate the TM domains.

Although the talin head increases integrin affinity, full-length talin is required to cluster integrins into focal adhesions (FA) [reviewed in (2)], which are hubs that relay signals from integrins to different cellular compartments. Cells that do not express talin are unable to undergo sustained spreading, which indicates an adhesion defect (42). Expressing the talin1 head in these cells partially restored the spreading defect, but FAs were still absent, demonstrating that the clustering of integrins into larger adhesion struc-

tures and the PTB domain that blocks the integrin-binding pocket (45). Therefore, when talin function is not required it may be maintained in an autoinhibited state. How talin is activated is not clear, but it probably involves binding to the lipid second messenger phosphatidylinositol-4,5-bisphosphate [PtdIns(4,5)P₂] because this lipid elicits a conformational change that disrupts the autoinhibitory interaction and enhances integrin-talin binding (45, 46). Although phosphoinositide binding can enhance the affinity of many PTB domains for their substrates (29), this does not hold true for the isolated talin head (46). Talin binds to PIPK1 γ and directs it to focal adhesions (22, 24); thus, a feed-forward loop may exist to enhance talin recruitment to sites of adhesion formation.

In hematopoietic cells, the guanine triphosphatase (GTPase) Rap1 has been implicated in talin recruitment to integrin tails. Expression of constitutively active Rap1A in T cells increases integrin activation (47), and the deletion of Rap1B in platelets decreases α IIb $\beta 3$ activation (48). Association of the Rap1 effector Rap1-GTP-interacting adaptor molecule (RIAM) resulting in a Rap1-RIAM-talin ternary complex at the integrin tail has been shown to be required for this interaction (49, 50). A similar GTPase-mediated activation mechanism might also occur in nonhematopoietic cells, because a direct interaction between talin and lamellipodin, a member of the MRL (Mig-10/RIAM/Lamellipodin) family of adaptor proteins, also results in integrin activation (51).

Talin-integrin interactions are also controlled through phosphorylation of the β integrin tail. The Tyr within the $\beta 1$ and $\beta 3$ integrin NPxY motif can be phosphorylated by src family kinases (52, 53), and when mutated to Phe it reverses the integrin-dependent spreading and migration defects in viral-Rous sarcoma oncogene (v-src)-transformed fibroblasts (53). The interaction between talin and β integrin tails is regulated by a phosphorylation switch mechanism. Structural analysis showed that the talin PTB-integrin NPxY interaction occurs through acidic and hydrophobic interactions (23) and cannot accommodate the introduction of a phosphate group. Accordingly, the affinity of the talin F3 subdomain for a phosphorylated $\beta 3$ tail peptide is reduced compared with that of the unphosphorylated peptide (41). Therefore, phosphorylation could inhibit integrin activation by maintaining an inhibitory complex on inactive integrin tails or by blocking talin binding directly.

Mutations and truncations of the $\beta 3$ integrin tail C terminal to the talin-binding site decrease integrin affinity for ligands (54–57), which raises the possibility that additional factors also

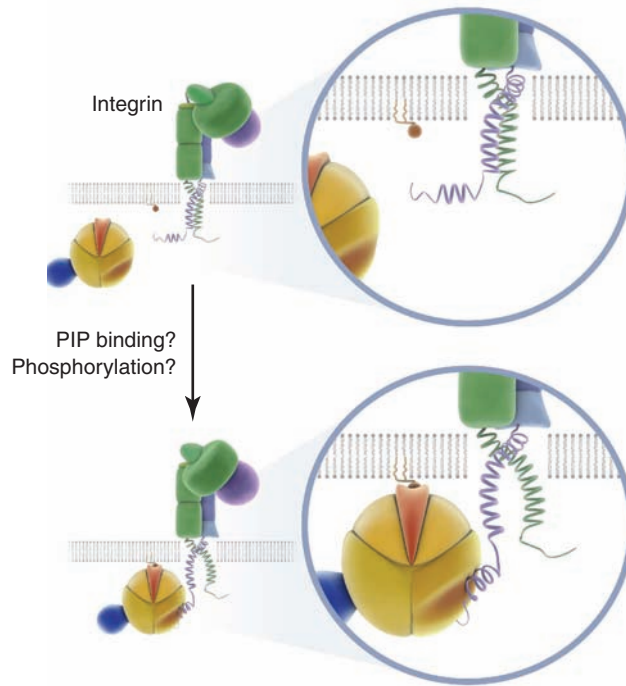


Fig. 3. Hypothetical model of kindlin recruitment and binding to the β integrin cytoplasmic tail. Phosphoinositide binding to the PH domain and/or phosphorylation might activate kindlin proteins and recruit them to the membrane, where they bind via their F3 subdomains to the membrane-distal NxY motif of β integrin cytoplasmic tails.

tures depends on both the head and rod of talin. These studies also showed that talin is essential for coupling the actin cytoskeleton to adhesion structures and established talin as a key adaptor linking the cytoskeleton to the extracellular matrix (42). Mutational analysis of talin indicates that a functional dimerization motif is both necessary and sufficient to localize talin to focal adhesions (28, 43). Because talin contains two β integrin-binding sites, one within the FERM and the other within the rod domain, the talin homodimer has up to four integrin-binding sites, which may enable talin to act as an integrin crosslinker in order to promote clustering. Consistent with this hypothesis, cleavage of the talin head from the rod domain by the protease calpain induces focal-adhesion disassembly (44).

Because integrin activation has to be strictly controlled, talin-integrin binding is tightly regulated (Fig. 2). NMR studies revealed an autoinhibitory interaction between the talin C terminus

alter integrin affinity status. Indeed, recent work shows that talin is not the only master regulator of integrin activation and that the kindlin family of proteins, which bind to this region of $\beta 1$, $\beta 2$, and $\beta 3$ integrins, are as important as talin in mediating this function (58–62).

Kindlins as Regulators of Integrin Activation

Kindlins belong to a family of evolutionarily conserved FERM domain-containing proteins named after the gene mutated in Kindler syndrome, a rare skin blistering disease. There are three kindlin family members in mammals: kindlin-1 [Unc-112 Related Protein 1 (URP1)], kindlin-2 (Mig2), and kindlin-3 (URP2) (63). Kindlin-1, which is predominantly expressed in epithelial cells, is found in tissues such as skin, intestine, and kidney; kindlin-2 is expressed in most tissues, with highest amounts in skeletal and smooth muscle cells; and kindlin-3 expression is restricted to cells of hematopoietic origin (63–65). All three proteins localize to integrin-dependent adhesion sites; kindlin-1 and -2 localize to focal adhesions, and kindlin-3 localizes to podosomes, which are integrin-dependent adhesion sites found in hematopoietic cells.

Kindlins are essential components of the integrin adhesion complex. The *C. elegans* ortholog of kindlin, Unc-112, localizes with integrins in dense bodies and M lines, and loss of its expression results in a muscle detachment phenotype that is similar to that seen in α or β integrin mutants (66). Two human diseases caused by kindlin gene mutations have characteristic features of defective integrin function. Kindler syndrome, which is caused by the loss of kindlin-1, is a rare genodermatosis characterized by an epithelial cell-adhesion defect followed by poikiloderma and cutaneous atrophy (63, 64). Mutations in kindlin-3 were implicated in a rare leukocyte-adhesion deficiency (LAD) type III (LAD-III), which results from severe defects in leukocyte and platelet integrin activation (67–70).

Genetic and siRNA depletion of kindlin-1, -2, and -3 in mice and cells provided definitive experimental proof that kindlins are essential regulators of integrin function because the conformational shift of integrins from the low- to high-affinity state does not occur in the absence of kindlins (56, 59, 61, 62). Kindlin-3 deletion causes severe bleeding that is reminiscent of Glanzmann thrombasthenia, a disorder arising from defects in αIIb or $\beta 3$ integrin subunits. The platelet integrins cannot bind ligands, and platelet aggregation is defective despite normal amounts of talin (61). The same phenotype occurs in talin-deficient platelets (37, 38), indicating that both proteins are required to regulate integrin affinity. Furthermore, leukocytes lacking kindlin-3 are unable to transmigrate across the vessel wall into inflamed tissues because of an integrin-mediated adhesion defect (60). The phenotypes of these mice resemble LAD-III patients, which led to the identification of mutations in kindlin-3 as a cause of this disease (67, 70). Mice lacking kindlin-1 have a phenotype similar to that of Kindler syndrome patients and exhibit skin atrophy and a detached colon epithelium because of

defective integrin function in intestinal epithelial cells (71). Kindlin-2 deletion results in death at implantation because of defective integrin function in cells of the endoderm and the epiblast, causing their detachment from the basement membrane (59, 72). This severe phenotype is consistent with the broad expression pattern of kindlin-2.

Kindlin-mediated integrin activation requires a direct interaction between kindlin and β integrin tails. The kindlin and talin FERM domains show high levels of sequence similarity (73); however,

intervening sequence between the two NxxY motifs in the $\beta 1$ and $\beta 3$ integrin cytoplasmic tails are dispensable for talin binding, mutation of a double Thr or Ser/Thr within this sequence impairs kindlin binding (61). Some Glanzmann patients carry a Ser-to-Pro mutation in $\beta 3$ integrins, and the same mutation abolishes kindlin-3 binding *in vitro*, which suggests that a lack of kindlin-3 binding might be responsible for the bleeding phenotype (61).

Because kindlins and talin bind distinct regions of the β integrin tail, they may cooperate to

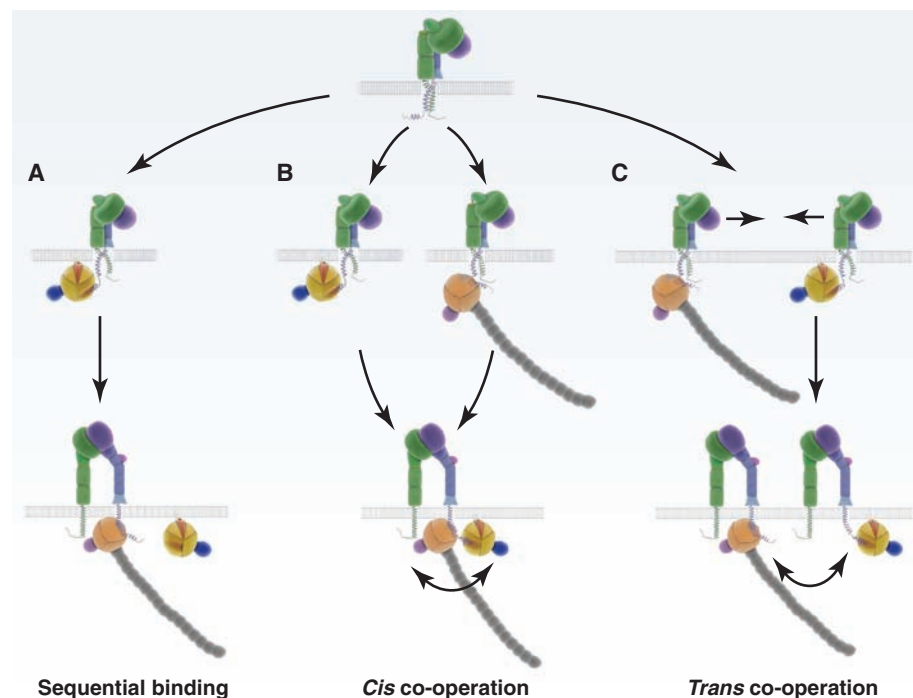


Fig. 4. Putative crosstalk mechanisms between talin and kindlin during integrin activation. **(A)** Model for the sequential binding of kindlin and talin to the integrin tail. Kindlin binding to the MD NxxY motif facilitates talin binding to the MP NPxY motif, which results in the displacement of kindlin from the β tail and final integrin activation. **(B)** Because of the distinct binding sites for talin and kindlin at the β integrin tail, simultaneous binding may be possible. The order in which each protein binds to the integrin tail is not known. **(C)** Communication between talin and kindlin in trans, where each protein is bound to a different integrin tail, can also be envisioned. In this model, talin and kindlin binding to integrin tails results in the formation of integrin nanoclusters and a subsequent talin-kindlin crosstalk (79).

the kindlin FERM domain exhibits the structural hallmark of being split into two halves by a pleckstrin homology (PH)-domain insertion in the F2 subdomain (Fig. 1D). Molecular modeling of the kindlin-2 F3 subdomain that uses the talin F3 subdomain as a structural template suggests that it also resembles a PTB domain capable of recognizing β integrin tails (74). Biochemical experiments confirmed the predicted interaction of kindlins with the cytoplasmic tails of $\beta 1$, $\beta 2$, and $\beta 3$ tails (58–61, 73, 74). Kindlin-1 and kindlin-2 PTB-domain mutations abolish their interaction with the $\beta 1$ integrin tail (62, 74) and impair the ability of kindlin-1 to activate integrins (61). Unlike talin, kindlins bind the distal NxxY motif on the $\beta 1$, $\beta 2$, and $\beta 3$ tails (Fig. 3) (58–62, 74); additional sequences may also be involved in kindlin binding. Although the

regulate integrin affinity (18, 19, 58–61). Although kindlins are not sufficient to shift integrins to a high-affinity state, they facilitate talin function. The amount of talin expressed in cells determines the efficacy of kindlins in promoting this function because overexpressing kindlin-2 in cells with relatively little talin (49) has little or no effect on integrin affinity modulation and co-expression of the talin-head domain with kindlin-1 or -2 results in a synergistic increase in $\alpha IIb\beta 3$ affinity. Conversely, talin depends on kindlins to promote integrin affinity because talin-head overexpression failed to increase $\alpha IIb\beta 3$ affinity in CHO cells in which kindlin expression was reduced by siRNA. Thus, kindlins require talin, and talin is not sufficient to increase integrin affinity.

Kindlins also function as cytoskeletal linker molecules in outside-in signaling. Kindlin-1 and -2 bind to integrin-linked kinase (ILK) and the filamin-binding protein migfilin, both of which link kindlins indirectly to the actin cytoskeleton (59, 75, 76). Both proteins localize to cell-matrix adhesions in a kindlin-dependent manner, demonstrating that kindlins are central linker proteins mediating the assembly of integrin-dependent adhesion complexes (59, 76, 77). Kindlin-3-deficient platelets exposed to divalent Mn^{2+} , which shifts integrins into the high-affinity state independent of intracellular cues, can adhere to fibrinogen- or collagen-coated surfaces; however, subsequent platelet spreading is impaired, which indicates that integrin-dependent cytoskeletal rearrangements do not occur in the absence of kindlin-3 (61). These observations suggest that kindlins remain associated with the adhesion complex and fulfill essential functions as bidirectional signaling molecules.

Perspectives

For years, talin was regarded as the sole regulator of integrin activation, but it now shares the spotlight with kindlins. Whether additional molecules regulate integrin affinity remains to be seen. Many unanswered questions on how kindlins and talin regulate integrin function remain. The binding modes that allow kindlins and talin to cooperatively regulate integrin affinity remain to be determined. Three possible scenarios are presented in Fig. 4. A direct interaction between kindlins and talin has not been detected, but low-affinity interactions cannot be excluded. Structural studies suggest that talin alone mediates the final step in integrin inside-out activation, but perhaps kindlin mediates integrin-talin binding. It is also unclear whether fast- and slow-activating integrins found on different cell types have the same mechanistic requirements for kindlin and talin. Lastly, the fate of kindlins and talin within the adhesion complex has not been determined. Because both talin and kindlins are involved in outside-in signaling, they must remain within the adhesion complex; but does their direct interaction with integrins persist, or does it become indirect through other binding partners? Answers to questions such as these will be essential to gain a full understanding of the mechanism behind inside-out integrin activation.

The activity of kindlin, like that of talin, is probably highly regulated; however, the nature of this control is unknown. Kindlins and talin might respond to the same or different activation signals. Because both kindlins and talin contain lipid-binding domains, they may both be controlled by phosphoinositide signals; however, no specific phosphoinositide is known that binds the kindlin PH domain, and lipid-mediated kindlin regulation has not been reported. Another mode of kindlin regulation may be phosphorylation. Kindlin-1 can be phosphorylated in keratinocytes (78), but its role is unidentified, and kindlin-2 and -3 phosphorylation *in vivo* has not been studied.

There are indications that kindlins have functions other than integrin activation. Kindlin-2

participates in outside-in signaling in FAs by binding to and recruiting ILK and migfilin, thus indirectly linking the integrin tail to the actin cytoskeleton and ILK-mediated signaling pathways. Both kindlin-1 and kindlin-2 also localize to cell-cell adhesion sites, but kindlin-2 cannot compensate for kindlin-1 loss, which suggests that these proteins have separate functions at this location, perhaps by binding distinct interaction partners. Lastly, kindlin-3 is required to maintain the proper architecture of the erythrocyte membrane skeleton (71), demonstrating an integrin-independent role for kindlin-3 because erythrocytes do not express integrins. Perhaps kindlins have similar roles in other cell types. Understanding these additional functions of kindlin is required to appreciate the biological importance of this class of proteins.

References and Notes

- R. O. Hynes, *Cell* **110**, 673 (2002).
- K. R. Legate, S. A. Wickstrom, R. Fassler, *Genes Dev.* **23**, 397 (2009).
- B. D. Adair, M. Yeager, *Proc. Natl. Acad. Sci. U.S.A.* **99**, 14059 (2002).
- T. L. Lau, V. Dua, T. S. Ulmer, *J. Biol. Chem.* **283**, 16162 (2008).
- T. L. Lau, A. W. Partridge, M. H. Ginsberg, T. S. Ulmer, *Biochemistry* **47**, 4008 (2008).
- Single-letter abbreviations for the amino acid residues are as follows: A, Ala; C, Cys; D, Asp; E, Glu; F, Phe; G, Gly; H, His; I, Ile; K, Lys; L, Leu; M, Met; N, Asn; P, Pro; Q, Gln; R, Arg; S, Ser; T, Thr; V, Val; W, Trp; and Y, Tyr.
- O. Vinogradova, T. Haas, E. F. Plow, J. Qin, *Proc. Natl. Acad. Sci. U.S.A.* **97**, 1450 (2000).
- O. Vinogradova et al., *Cell* **110**, 587 (2002).
- K. L. Wegener, I. D. Campbell, *Mol. Membr. Biol.* **25**, 376 (2008).
- D. A. Calderwood et al., *Proc. Natl. Acad. Sci. U.S.A.* **100**, 2272 (2003).
- B. H. Luo, C. V. Carman, T. A. Springer, *Annu. Rev. Immunol.* **25**, 619 (2007).
- J. P. Xiong, T. Stehle, S. L. Goodman, M. A. Arnaout, *Blood* **102**, 1155 (2003).
- M. A. Arnaout, S. L. Goodman, J. P. Xiong, *Curr. Opin. Cell Biol.* **19**, 495 (2007).
- K. E. Gottschalk, *Structure* **13**, 703 (2005).
- P. E. Hughes et al., *J. Biol. Chem.* **271**, 6571 (1996).
- A. Czuchra, H. Meyer, K. R. Legate, C. Brakebusch, R. Fassler, *J. Cell Biol.* **174**, 889 (2006).
- A. Horwitz, K. Duggan, C. Buck, M. C. Beckerle, K. Burridge, *Nature* **320**, 531 (1986).
- D. A. Calderwood et al., *J. Biol. Chem.* **277**, 21749 (2002).
- D. A. Calderwood et al., *J. Biol. Chem.* **274**, 28071 (1999).
- S. J. Monkley, C. A. Pritchard, D. R. Critchley, *Biochem. Biophys. Res. Commun.* **286**, 880 (2001).
- M. A. Senetar, C. L. Moncman, R. O. McCann, *Cell Motil. Cytoskeleton* **64**, 157 (2007).
- G. Di Paolo et al., *Nature* **420**, 85 (2002).
- B. Garcia-Alvarez et al., *Mol. Cell* **11**, 49 (2003).
- K. Ling, R. L. Doughman, A. J. Firestone, M. W. Bunce, R. A. Anderson, *Nature* **420**, 89 (2002).
- K. L. Wegener et al., *J. Mol. Biol.* **382**, 112 (2008).
- D. R. Critchley, A. R. Gingras, *J. Cell Sci.* **121**, 1345 (2008).
- M. A. Senetar, S. J. Foster, R. O. McCann, *Biochemistry* **43**, 15418 (2004).
- S. J. Smith, R. O. McCann, *Biochemistry* **46**, 10886 (2007).
- M. T. Uhlik et al., *J. Mol. Biol.* **345**, 1 (2005).
- M. Bouaouina, Y. Lad, D. A. Calderwood, *J. Biol. Chem.* **283**, 6118 (2008).
- S. Tadokoro et al., *Science* **302**, 103 (2003).
- K. L. Wegener et al., *Cell* **128**, 171 (2007).
- M. Kim, C. V. Carman, T. A. Springer, *Science* **301**, 1720 (2003).
- E. J. Cram, S. G. Clark, J. E. Schwarzbauer, *J. Cell Sci.* **116**, 3871 (2003).
- N. H. Brown et al., *Dev. Cell* **3**, 569 (2002).
- S. J. Monkley et al., *Dev. Dyn.* **219**, 560 (2000).
- B. Nieswandt et al., *J. Exp. Med.* **204**, 3113 (2007).
- B. G. Petrich et al., *J. Exp. Med.* **204**, 3103 (2007).
- C. J. McCleverty, D. C. Lin, R. C. Liddington, *Protein Sci.* **16**, 1223 (2007).
- S. Patil et al., *J. Biol. Chem.* **274**, 28575 (1999).
- C. L. Oxley et al., *J. Biol. Chem.* **283**, 5420 (2008).
- X. Zhang et al., *Nat. Cell Biol.* **10**, 1062 (2008).
- S. J. Franco, M. A. Senetar, W. T. Simonson, A. Huttenlocher, R. O. McCann, *Cell Motil. Cytoskeleton* **63**, 563 (2006).
- S. J. Franco et al., *Nat. Cell Biol.* **6**, 977 (2004).
- E. Goksoy et al., *Mol. Cell* **31**, 124 (2008).
- V. Martel et al., *J. Biol. Chem.* **276**, 21217 (2001).
- E. Sebzda, M. Bracke, T. Tugul, N. Hogg, D. A. Cantrell, *Nat. Immunol.* **3**, 251 (2002).
- M. Chrzanowska-Wodnicka, S. S. Smyth, S. M. Schoenwaelder, T. H. Fischer, G. C. White II, *J. Clin. Invest.* **115**, 680 (2005).
- J. Han et al., *Curr. Biol.* **16**, 1796 (2006).
- N. Watanabe et al., *J. Cell Biol.* **181**, 1211 (2008).
- H. S. Lee, C. J. Lim, W. Puzon-McLaughlin, S. J. Shattil, M. H. Ginsberg, *J. Biol. Chem.* **284**, 5119 (2009).
- D. A. Law, L. Nannizzi-Alaimo, D. R. Phillips, *J. Biol. Chem.* **271**, 10811 (1996).
- T. Sakai, J. Jove, R. Fassler, D. F. Mosher, *Proc. Natl. Acad. Sci. U.S.A.* **98**, 3808 (2001).
- Y. P. Chen et al., *Proc. Natl. Acad. Sci. U.S.A.* **89**, 10169 (1992).
- Y. P. Chen, T. E. O'Toole, J. Ylanne, J. P. Rosa, M. H. Ginsberg, *Blood* **84**, 1857 (1994).
- Y. Q. Ma et al., *Biochemistry* **45**, 6656 (2006).
- X. Xi, R. J. Bodnar, Z. Li, S. C. Lam, X. Du, *J. Cell Biol.* **162**, 329 (2003).
- Y. Q. Ma, J. Qin, C. Wu, E. F. Plow, *J. Cell Biol.* **181**, 439 (2008).
- E. Montanez et al., *Genes Dev.* **22**, 1325 (2008).
- M. Moser et al., *Nat. Med.* **15**, 300 (2009).
- M. Moser, B. Nieswandt, S. Ussar, M. Pozgajova, R. Fassler, *Nat. Med.* **14**, 325 (2008).
- S. Ussar et al., *PLoS Genet.* **4**, e1000289 (2008).
- D. H. Siegel et al., *Am. J. Hum. Genet.* **73**, 174 (2003).
- F. Jobard et al., *Hum. Mol. Genet.* **12**, 925 (2003).
- S. Ussar, H. V. Wang, S. Linder, R. Fassler, M. Moser, *Exp. Cell Res.* **312**, 3142 (2006).
- T. W. Kuijpers et al., *Blood*, 8 December 2008 (<http://bloodjournal.hematologylibrary.org/cgi/reprint/blood-2008-10-182154v1>).
- N. L. Malinin et al., *Nat. Med.* **15**, 313 (2009).
- A. Mory et al., *Blood* **112**, 2591 (2008).
- L. Svensson et al., *Nat. Med.* **15**, 306 (2009).
- M. Kruger et al., *Cell* **134**, 353 (2008).
- J. J. Dowling et al., *Circ. Res.* **102**, 423 (2008).
- S. Kloecker et al., *J. Biol. Chem.* **279**, 6824 (2004).
- X. Shi et al., *J. Biol. Chem.* **282**, 20455 (2007).
- J. E. Lai-Cheong, S. Ussar, K. Arita, I. R. Hart, J. A. McGrath, *J. Invest. Dermatol.* **128**, 2156 (2008).
- Y. Tu, S. Wu, X. Shi, K. Chen, C. Wu, *Cell* **113**, 37 (2003).
- Y. Zhang, Y. Tu, V. Gkretsi, C. Wu, *J. Biol. Chem.* **281**, 12397 (2006).
- C. Herz et al., *J. Biol. Chem.* **281**, 36082 (2006).
- H. Shroff et al., *Proc. Natl. Acad. Sci. U.S.A.* **104**, 20308 (2007).
- We thank M. Ginsberg, M. Costell, and S. Wickström for reading and commenting on the manuscript and M. Iglesias for artwork. We apologize to all whose papers have not been cited because of space constraints. K.R.L. is the recipient of a Marie Curie Incoming International Fellowship under the 6th Framework Programme. R.Z. is funded by a Merit Award from the Department of Veterans Affairs, DK65138, DK 69921, DK075594, and is an Established Investigator of the American Heart Association. M.M. and R.F. are supported by the Deutsche Forschungsgemeinschaft and the Max Planck Society.

10.1126/science.1163865

A Key Role for Similarity in Vicarious Reward

Dean Mobbs,^{1*} Rongjun Yu,^{1†} Marcel Meyer,^{1,2†} Luca Passamonti,^{1,3} Ben Seymour,^{4,5} Andrew J. Calder,¹ Susanne Schweizer,¹ Chris D. Frith,^{4,6} Tim Dalgleish¹

Game shows are one of the most popular and enduring genres in television culture. Yet why we possess an inherent tendency to enjoy seeing unrelated strangers win in the absence of personal economic gain is unclear (1). One explanation is that game show organizers use contestants who have similarities to the viewing population, thereby kindling their likeability, familiarity, and kin-motivated responses [e.g., prosocial behavior (1, 2)]. Social-cognitive accounts posit that, to simulate another's internal states successfully, we must deem ourselves as similar to the target person (3). We tested two predictions: Seeing a socially desirable contestant win will modulate neural systems associated with reward, and this rewarding experience is further influenced by perceived similarity to a contestant (i.e., similar attitudes and values).

Volunteers first viewed films of two confederate contestants answering questions about personal, social, and ethical issues. These contestants expressed themselves in either a socially desirable [SD (i.e., empathetic)] or socially undesirable [SU (i.e., inappropriate values)] manner (4). To check that this social judgment manipulation worked, volunteers performed a likeableness trait rating task (5). Positive trait scores were higher for the SD contestant, whereas negative traits were significantly higher for the SU contestant ($F = 107.9$, $P < 0.0005$) (Fig. 1A). Next, volunteers underwent functional magnetic resonance imaging scanning while they viewed SD and SU contestants playing a game where the contestants made decisions as to whether an unseen card would be higher or lower than a second unseen card (6). A correct decision resulted in the contestant winning £5 (4). The number of wins and probabilities of winning were identical across contestants. After volunteers watched the contestants play, they played the game for themselves (4).

Subjective ratings acquired after the experiment showed that volunteers perceived themselves to be more similar to, and in agreement with, the SD contestant (Fig. 1B), as well as found it more rewarding to see her win (Fig. 1C) (all t tests: $P < 0.05$) (4). Likewise, correlations were found between similarity and agreeableness and between positive likeableness scores and how rewarding it was to see

the SD contestant win. Both empathy and perspective-taking scores (4) correlated with similarity to the SD contestant (all Pearson's: $P < 0.05$) (4). No sex differences were found for similarity to SD and SU contestants [see (4) for additional results].

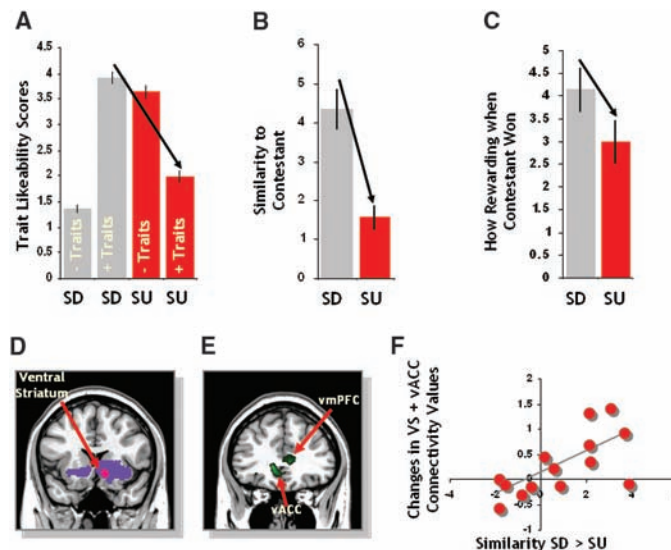


Fig. 1. (A) Results from the trait likeability ratings showing SD and SU contestant scores for positive and negative trait attributions. Volunteers (B) perceived themselves as significantly more similar to the SD contestant and (C) found it more rewarding to see the SD contestant win. Error bars indicate SEM. (D) Significant activity associated with self-win (purple) and correlation between how rewarding it was to see the SD versus the SU win (pink). (E) Correlation between similarity, vACC and vmPFC activity, and (F) psychophysiological interaction showing connectivity values (i.e., connectivity during SD winning minus connectivity during SU winning) and individual scores of similarity (4).

For the brain-imaging data, we first examined the correlation between how rewarding the volunteers found it when observing the SD versus the SU contestant winning (4). We found a significant increase in ventral striatum (VS) activity, a region also active when the volunteers themselves won while playing the game [Fig. 1D; see (4) for additional analysis] and known to be involved in the experience of reward and elation (7). We next correlated perceived similarity scores for the SD versus the SU contestant win, which resulted in elevated ventromedial prefrontal cortex (vmPFC) and ventral anterior cingulate cortex (vACC) activity (Fig. 1E). Although social psychological research shows that likeability and similarity are closely correlated, subtraction of the likeability ratings from the similarity ratings also resulted in significantly more vACC activity (Fig. 1F), supporting this region's putative role in self-other similarity (4, 8).

We next tested whether the relationship between the VS and vACC was influenced by perceived similarity. We used psychophysiological interaction to examine connectivity between the VS and the vACC (using an independent VS seed from the self-play condition). We saw a significant positive relationship between similarity and connectivity between these two regions for the SD-versus-SU contestant win contrast (Fig. 1F). No such modulation was found for likeability ratings (4). Given the vACC's unidirectional projections to the VS, the vACC may modulate positive feelings in situations relevant to the self (8).

Until now, studies of the neural representation of others' mental states have been concerned with negative emotions (e.g., empathy for pain). Here, we show that similar mechanisms transfer to positive experiences such that observing a SD contestant win increases both subjective and neural responses in vicarious reward. Such vicarious reward increases with perceived similarity and vACC activity, a region implicated in emotion and relevance to self (3, 9). Although other social preferences (e.g., fairness) (10) are likely to play a role in vicarious reward, our results support a proximate neurobiological mechanism, possibly linked to kin-selection mechanisms, where prosocial behavior extends to unrelated strangers (2).

References and Notes

1. E. Fehr, U. Fischbacher, *Nature* **425**, 785 (2003).
2. J. H. Park, M. Schaller, *Evol. Hum. Behav.* **26**, 158 (2005).
3. J. P. Mitchell, C. N. Macrae, M. R. Banaji, *Neuron* **50**, 655 (2006).
4. Materials and methods are available as supporting material on Science Online.
5. N. H. Anderson, *J. Pers. Soc. Psychol.* **9**, 272 (1968).
6. K. Preusschoff, P. Bossaerts, S. R. Quartz, *Neuron* **51**, 381 (2006).
7. D. Mobbs et al., *Neuron* **40**, 1041 (2003).
8. J. M. Moran et al., *J. Cogn. Neurosci.* **18**, 1586 (2006).
9. B. A. Völlm et al., *Neuroimage* **29**, 90 (2006).
10. T. Singer et al., *Nature* **439**, 466 (2006).
11. We thank M. Ewbank, R. Henson, and E. Hill for their help. This work was conducted at the Cognition and Brain Sciences Unit and supported by the MRC.

Supporting Online Material

www.sciencemag.org/cgi/content/full/324/5929/900/DC1
Materials and Methods
Figs. S1 to S5
References

6 January 2009; accepted 13 March 2009
10.1126/science.1170539

¹Cognition and Brain Sciences Unit, Medical Research Council (MRC), Cambridge CB2 7EF, UK. ²Department of Psychology, University of Birmingham, Birmingham B15 2TT, UK. ³Consiglio Nazionale delle Ricerche, ISN, Cosenza 87050, Italy. ⁴Wellcome Trust Centre for Neuroimaging, University College London (UCL), London WC1N 3BG, UK. ⁵The ESRC Centre for Economic Learning and Social Evolution (UCL), Drayton House, Gordon Street, London WC1H 0AN, UK. ⁶Centre for Functional Integrative Neuroscience, Aarhus University, DK-800 Aarhus, Denmark.

*To whom correspondence should be addressed. E-mail: dean.mobbs@mrc-cbu.cam.ac.uk

†These authors contributed equally to this work.

Reassessment of the Potential Sea-Level Rise from a Collapse of the West Antarctic Ice Sheet

Jonathan L. Bamber,^{1*} Riccardo E. M. Riva,² Bert L. A. Vermeersen,² Anne M. LeBrocq³

Theory has suggested that the West Antarctic Ice Sheet may be inherently unstable. Recent observations lend weight to this hypothesis. We reassess the potential contribution to eustatic and regional sea level from a rapid collapse of the ice sheet and find that previous assessments have substantially overestimated its likely primary contribution. We obtain a value for the global, eustatic sea-level rise contribution of about 3.3 meters, with important regional variations. The maximum increase is concentrated along the Pacific and Atlantic seaboard of the United States, where the value is about 25% greater than the global mean, even for the case of a partial collapse.

Glaciologists have proposed that the marine portion of the West Antarctic Ice Sheet (WAIS) is potentially unstable and that, as a consequence, it may be susceptible to a rapid disintegration as a result of a relatively modest change in climatic boundary conditions (1–4). There is compelling evidence that the WAIS has undergone partial collapse in the past, possibly as recently as 400 thousand years before the present (kyr B.P.) (5, 6) as a consequence of moderate warming. The proposed instability of the WAIS is a consequence of the marine ice sheet instability (MISI) hypothesis, which has its basis in the idea that removal of fringing ice shelves will result in the rapid and irreversible inland migration of the grounding line where the bedrock is below sea level and slopes downward from the margins toward the interior (4, 7). First suggested in the 1970s, the hypothesis is supported by recent theoretical analysis of grounding line stability (8). The WAIS is unique in possessing a large proportion of its mass where these conditions hold (Fig. 1). Collapse is considered to be a low-probability, high-impact event with, for example, a 5% probability of the WAIS contributing 10 mm year⁻¹ within 200 years (9). Risk and mitigation assessments have, in general, used a single, historic sea-level rise (SLR) value or range resulting from a collapse. The most often quoted range in the literature for a complete collapse of the WAIS is 5 to 6 m with no regional variations (10).

The first estimate of the potential eustatic (11) SLR from a collapse of the WAIS was about 5 m (2) and remains the generally accepted lower

value quoted (12). As is the case here and in paleoreconstructions (6), it was assumed, presumably on the basis of glaciological theory, that ice grounded above sea level would survive, but no details have been provided about how the calculation was made (Fig. 2).

More recently, with the benefit of improved bedrock and surface topography, the total volume of the WAIS, including the Antarctic Peninsula, and ice grounded above sea level was estimated and found to be equivalent to 5 m of eustatic SLR (13). This calculation was not, however, attempting to assess the volume of ice that met the MISI hypothesis criteria or any other glaciological or geophysical constraints, such as the response of East Antarctic glaciers or glacio-isostatic adjustment. Previous estimates have not defined the region susceptible to a collapse, the extent of the marine portion of the continent that they assume will contribute, or any assumptions made. The Antarctic Peninsula, for example, is both topographically and glaciologically distinct from the WAIS, lies almost entirely above sea level (Fig. 1 and 2), and was included in the most recent estimate of the sea level equivalent volume of the WAIS (13). Further, although much of the WAIS is grounded on bedrock below sea level (BSL), there are extensive areas around the Transantarctic and Ellsworth mountains and the Executive Committee Range that are not and/or that do not have negative bed slopes (i.e., where the bed elevation deepens inland in the opposite direction to ice motion) (Fig. 1 and figs. S1 and S2). Of equal importance is the fact that the impact on SLR of a collapse of the WAIS would not be uniformly distributed across the oceans. Although this was identified at an early stage, the estimation of the regional impact (14) assumed a uniform loss across the WAIS and did not include important effects, such as Earth rotational changes (polar wander) and shoreline migration (15). Here, we perform a detailed assessment of

the potential contribution of the WAIS, taking into account relevant glaciological constraints along with the solid earth and geoid response. To do this, we used recent estimates of the geoid, bedrock, and ice surface elevation, combined with a viscoelastic Earth model, to estimate the regional SLR from a glaciologically consistent collapse of the marine portion of the WAIS. We stress, however, that we are not attempting to assess the validity of the MISI hypothesis, the likely rate of mass loss, or the probability of a complete or partial collapse.

Data sets. We have taken new bedrock elevation data sets for the Amundsen Sea sector of West Antarctica (16, 17) and combined these with an older bed elevation data set for the rest of the continent (13), a new ice surface digital elevation model (18), and a new geoid derived from Gravity Recovery and Climate Experiment (GRACE) satellite mission data (www.gfz-potsdam.de/pb1/op/grace/results/index_RESULTS.html). We apply these data to two scenarios of steady wasting based on earlier estimates of the rate of wastage of the WAIS (19).

To determine the volume of ice resting on bedrock BSL, we merged new bedrock data for the Amundsen Sea Embayment sector with the older BEDMAP data set (13). We then identified grid cells that (i) were BSL and (ii) have negative bed slopes. This condition was applied loosely to provide an upper limit for the area susceptible to collapse (20). For convenience, this area will henceforth be referred to as the region of interest (ROI). The ROI is shown in Fig. 1 and includes the Antarctic Peninsula, although it is only its most southerly limit and margins that are BSL and nowhere does it satisfy the MISI conditions discussed earlier (Fig. 1).

The volume of ice in the ROI above sea level was summed, excluding floating ice shelves, by using the ice surface digital elevation model with respect to the geoid. We used the EIGEN-GLO4C gravity model, derived from data provided by the GRACE satellite mission, which has a stated accuracy of 0.18 to 0.44 m on the basis of comparison with Global Positioning System data across Europe and North America (www.gfz-potsdam.de/pb1/op/grace/results/index_RESULTS.html). The ice volume above sea level was corrected for the density difference between ice and seawater, assuming a value of 918 kg m⁻³ for the former and 1028 kg m⁻³ for the latter. The same densities were used to calculate the change in volume of submerged ice that is replaced by seawater. An additional term was calculated to take account of the drawdown of newly formed ice margins adjacent to the unstable areas. Where ice has been removed, rather than a nonphysical vertical boundary, the ice surface will, over time, relax to a new equilibrium profile. We estimated the impact of the surface drawdown by imposing a flotation criterion at the new ice margins and then using a thermomechanical ice sheet model to estimate the postcollapse equilibrium profiles, in

¹Bristol Glaciology Centre, School of Geographical Sciences, University of Bristol, Bristol BS8 1SS, UK. ²Delft Institute of Earth Observation and Space Systems, Delft University of Technology, NL-2629 HS Delft, Netherlands. ³Department of Geography, University of Durham, Durham DH1 3LE, UK.

*To whom correspondence should be addressed. E-mail: j.bamber@bristol.ac.uk

the absence of the collapsed ice (20). We also considered the impact of an acceleration in ice motion for the outlet glaciers in East Antarctica that flow into the ice shelves that have been removed (20). This defines the total volume of ice in the region that satisfies the MISI conditions plus the response of the extant ice to its removal. Instantaneous melting of the ice satisfying the MISI conditions would produce a eustatic SLR of 2.46 m with an error of 0.2 m resulting from uncertainties in the input data used. Drawdown of extant ice areas is responsible for a subsequent 0.74 m, and a further 0.06 m should be added because of the elastic response of the lithosphere, which gives a total of 3.26 m (table S1). This compares with a value of 4.8 m for the removal of the whole of the WAIS including the Peninsula. We consider two disintegration scenarios based on previous work (8, 19). These scenarios are used solely to calculate the glacial isostatic adjustment and polar wander response. They are not meant to indicate a probable decay behavior, which is likely to be nonlinear and asymptotic. They are equivalent to a eustatic SLR of 6.4 and 1.9 mm year⁻¹ and a freshwater flux of 0.07 and 0.02 sverdrup, respectively, assuming a linear loss over the time taken for collapse. These values are considerably smaller than, for example, melt-water pulse 1A at around 14 kyr B.P., which was responsible for a ~20-m rise in sea level in ~500 years and which may have partly originated from Antarctica (21, 22). They are also less than the estimate of 10 mm year⁻¹ mentioned earlier and derived from a risk assessment study (9).

Results. The extant ice and sectors removed are shown in Figs. 1 and 2. After taking into account the drawdown estimate, the volume left is equivalent to 1.8 m eustatic SLR (table S1). This comprises a fairly contiguous and sizable ice cap over the Executive Committee/Flood ranges [Marie Byrd Land Ice Cap (MBLIC) in Fig. 1], which is about 600 km in length and 300 km in width. A smaller (~200 km length) ice cap is centered just east of the Amundsen Sea Embayment. The Antarctic Peninsula makes only a small contribution to eustatic SLR out of a potential total of 24 cm because it is grounded on bedrock substantially above sea level. The other area that lies within the WAIS but which is considered stable is centered over the Ellsworth, Whitmoor, and Thiel mountain ranges and is connected to the East Antarctic Ice Sheet (EAIS) plateau [Ellsworth Mountain Ice Cap (EMIC) in Fig. 1]. The spatial distribution of extant ice is broadly similar to the early reconstruction by Mercer (Fig. 2) but with markedly different estimates of the eustatic SLR (2). We believe this discrepancy may be due to the dearth of reliable bed and surface elevation data available at the time of the earlier study (fig. S6). Removal of the sectors in the WAIS that are BSL but with positive bed slopes (i.e., relaxing the MISI condition to cover the entire marine portion) would contribute an additional 49 cm and cannot, therefore, explain the difference (table S1).

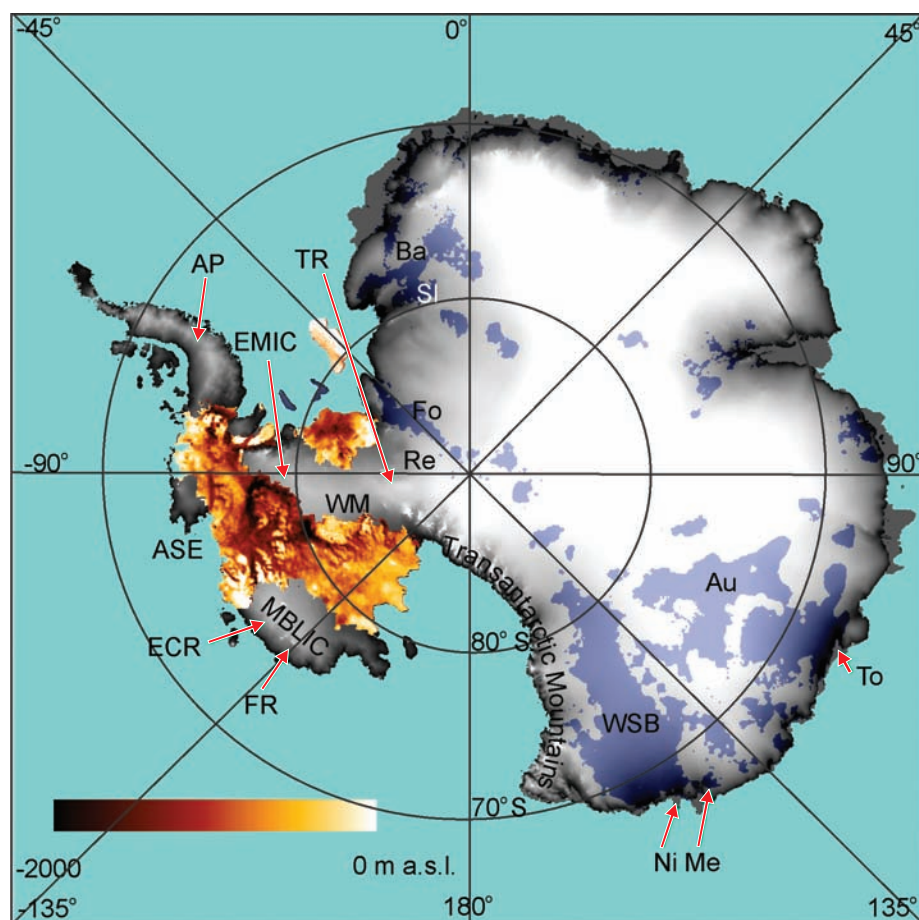


Fig. 1. Antarctic surface topography (gray shading) and bed topography (brown) defining the region of interest. For clarity, the ice shelves in West Antarctica are not shown. Areas more than 200 m BSL in East Antarctica are indicated by blue shading. AP, Antarctic Peninsula; EMIC, Ellsworth Mountain Ice Cap; ECR, Executive Committee Range; MBLIC, Marie Byrd Land Ice Cap; WM, Whitmoor Mountains; TR, Thiel Range; Ba, Bailey Glacier; SL, Slessor Ice Stream; Fo, Foundation Ice Stream; Re, Recovery Glacier; To, Totten Glacier; Au, Aurora Basin; Me, Mertz Glacier; Ni, Ninnis Glacier; WSB, Wilkes Subglacial Basin; FR, Flood Range; a.s.l., above sea level.



Fig. 2. A comparison of the area of ice sheet calculated to survive after a collapse of the WAIS in (A) this study and (B) the historic study by Mercer (2).

Global sea-level changes are not uniform because of regional variations in Earth's gravity field caused by (i) ice mass change in the WAIS, (ii) deformation of solid Earth, and (iii) changes in Earth's rotation vector as a result of mass redistribution. The combination of these effects,

all self-consistently included in our solution of the sea-level equation, leads to a complex regional pattern, as already recognized in early studies [e.g., (23, 24)]. We solved the sea-level equation by means of a pseudospectral algorithm (25, 26) for a self-gravitating, spherically

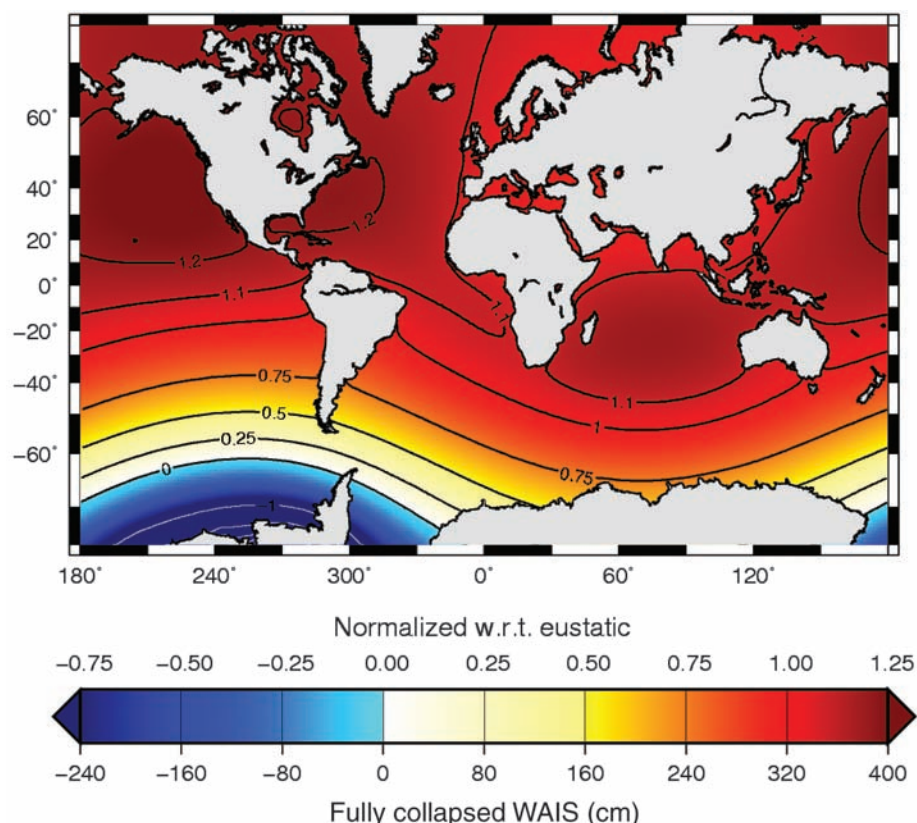


Fig. 3. Regional SLR after instantaneous removal of ice from the ROI, including the effects of self-gravitation, elastic rebound of the lithosphere, and Earth rotation perturbations but excluding the effects of ocean circulation (29) and other sources of ocean mass. w.r.t., with respect to.

layered, incompressible, viscoelastic Earth with Maxwell rheology. Our Earth model includes a 100-km-thick elastic lithosphere, a stratified viscoelastic mantle, and an inviscid core, where elastic parameters and densities are average preliminary reference Earth model values (27). The effect of WAIS melt on global sea level was computed by taking into account induced variations in ocean-continent geometry (shoreline migration) and perturbations in Earth's rotation vector (polar wander) (28). The initial ice load was uniformly distributed over the ROI, and a subsequent ice retreat history was constructed following bed-rock elevation curves (at each time, the grounding line is everywhere at the same elevation). We have limited our computations, solely, to the effect of a WAIS collapse. Our sea-level results are, therefore, variations with respect to present-day sea level from this source only.

Figure 3 shows the regional pattern of global sea-level change after complete collapse of the WAIS, considering only the quasi-instantaneous (elastic) response of solid Earth and ignoring ocean circulation effects that are important on a decadal time scale (29). In addition, we do not include here mass losses from other sources such as Greenland, glaciers, and ice caps. The peak increase lies in the Indian Ocean and in a latitudinal band centered at $\sim 40^\circ\text{N}$, along the Pacific and Atlantic coasts of the United States. We

provide two scales for sea-level changes: The first is normalized with respect to the eustatic value, and the second, in centimeters, is for the case of complete removal of the ROI. The normalized scale is applicable in the case of partial collapse: for example, in the fast melt scenario (6.4 mm year^{-1}), the maximum SLR at 100 years after present would amount to 81 cm (1.27 times the global eustatic value). The eustatic SLR resulting from the elastic response of the lithosphere within the ROI amounts to about 6 cm (included in the absolute scale in Fig. 3) and subsequently increases because of viscoelastic relaxation up to about 46 cm after 10,000 years (fig. S9).

We conclude that previous estimates of the impact on eustatic SLR of the rapid collapse of the WAIS have been overestimated. Our estimate of the likely limit to the contribution to eustatic SLR for that portion of the WAIS that loosely satisfies the MISI hypothesis conditions is no more than 3.20 m, with the addition of about 6 cm resulting from elastic rebound of the lithosphere. After 10,000 years, viscous glacio-isostatic adjustment and additional inland ice drawdown from the EAIS contribute a further 40 and 20 cm, respectively. Over this time scale, however, other dynamic and surface ice sheet processes may also contribute further mass to the oceans. As noted elsewhere, SLR is not uniformly

distributed (24), and we find the peak increases lie along the Pacific and Atlantic seabords of the United States.

References and Notes

1. T. Hughes, *J. Geophys. Res.* **78**, 7884 (1973).
2. J. H. Mercer, *Nature* **271**, 321 (1978).
3. T. Hughes, *Rev. Geophys.* **13**, 502 (1975).
4. R. H. Thomas, *J. Glaciol.* **24**, 167 (1979).
5. D. Fox, *Science* **320**, 1152 (2008).
6. R. P. Scherer *et al.*, *Science* **281**, 82 (1998).
7. J. Weertman, *J. Glaciol.* **13**, 3 (1974).
8. R. H. Thomas, T. J. O. Sanderson, K. E. Rose, *Nature* **277**, 355 (1979).
9. D. G. Vaughan, J. R. Spouge, *Clim. Change* **52**, 65 (2002).
10. R. S. J. Tol *et al.*, *J. Risk Res.* **9**, 467 (2006).
11. Here, we refer to eustatic SLR as the uniform global SLR resulting from a change in mass of the oceans and/or a change in the capacity of ocean basins.
12. R. B. Alley, R. A. Bindshadler, in *The West Antarctic Ice Sheet: Behavior and Environment*, R. B. Alley, R. A. Bindshadler, Eds. (American Geophysical Union, Washington, DC, 2001), vol. 77, pp. 1–12.
13. M. B. Lythe, D. G. Vaughan, *J. Geophys. Res.* **106**, 11335 (2001).
14. J. A. Clark, C. S. Lingle, *Nature* **269**, 206 (1977).
15. J. X. Mitrovica, G. A. Milne, *Geophys. J. Int.* **154**, 253 (2003).
16. J. W. Holt *et al.*, *Geophys. Res. Lett.* **33**, L09502 (2006).
17. D. G. Vaughan *et al.*, *Geophys. Res. Lett.* **33**, L09501 (2006).
18. J. L. Bamber, J. L. Gomez Dans, J. A. Griggs, *Cryosphere* **3**, 101 (2009).
19. The lower limit for a collapse of the WAIS was estimated to be 400 years, but several factors were identified that would likely reduce the rate of mass loss; we, therefore, have considered two scenarios. The first is a constant mass loss over 500 years, and the second is where ice discharge doubles, because of a doubling in velocities, and that this rate of mass loss is maintained until the ROI is completely removed. This occurs in 1735 years. In the first scenario, there is only an elastic response of Earth, so the result at 500 years is identical to a quasi-instantaneous removal. Here, the rate of mass loss is only relevant to how it affects the modeled glacio-isostatic adjustment and polar wander.
20. Materials and methods are available as supporting material on Science Online.
21. P. U. Clark, J. X. Mitrovica, G. A. Milne, M. E. Tamisiea, *Science* **295**, 2438 (2002).
22. A. J. Weaver, O. A. Saenko, P. U. Clark, J. X. Mitrovica, *Science* **299**, 1709 (2003).
23. W. E. Farrell, J. A. Clark, *Geophys. J. R. Astron. Soc.* **46**, 647 (1976).
24. J. X. Mitrovica, N. Gomez, P. U. Clark, *Science* **323**, 753 (2009).
25. J. X. Mitrovica, W. R. Peltier, *J. Geophys. Res.* **139**, 20053 (1991).
26. G. Di Donato, L. L. A. Vermeersen, R. Sabadini, *Tectonophysics* **320**, 409 (2000).
27. A. M. Dziewonsky, D. L. Anderson, *Phys. Earth Planet. Inter.* **25**, 297 (1981).
28. G. A. Milne, J. X. Mitrovica, *Geophys. J. Int.* **133**, 1 (1998).
29. D. Stammer, *J. Geophys. Res.* **113**, 16 (2008).
30. The authors thank R. Bindshadler, R. Thomas, D. Vaughan, and four anonymous referees for helpful and constructive comments on a draft of the paper. J.L.B. was supported by UK Natural Environment Research Council grant NE/E004032/1 and a Colorado University Cooperative Institute for Research in Environmental Sciences (CIRES) fellowship.

Supporting Online Material

www.sciencemag.org/cgi/content/full/324/5929/901/DC1
Materials and Methods
Figs. S1 to S9
Table S1
References

3 December 2008; accepted 18 March 2009
10.1126/science.1169335

Input-Specific Spine Entry of Soma-Derived Vesl-1S Protein Conforms to Synaptic Tagging

Daisuke Okada,* Fumiko Ozawa, Kaoru Inokuchi*

Late-phase synaptic plasticity depends on the synthesis of new proteins that must function only in the activated synapses. The synaptic tag hypothesis requires input-specific functioning of these proteins after undirected transport. Confirmation of this hypothesis requires specification of a biochemical tagging activity and an example protein that behaves as the hypothesis predicts. We found that in rat neurons, soma-derived Vesl-1S (Homer-1a) protein, a late-phase plasticity-related synaptic protein, prevailed in every dendrite and did not enter spines. *N*-methyl-D-aspartate receptor activation triggered input-specific spine entry of Vesl-1S proteins, which met many criteria for synaptic tagging. These results suggest that Vesl-1S supports the hypothesis and that the activity-dependent regulation of spine entry functions as a synaptic tag.

Synaptic plasticity is central for higher brain functions, including memory. Persistent late-phase synaptic plasticity depends on transcription and translation of new gene products, namely plasticity-related proteins (PRPs) or plasticity factors (1). Although the mechanisms underlying input-specific functioning of PRPs in the synapses expressing early-phase plasticity are critical for input-specific late-phase plasticity and consistent maintenance of network functions, they are not yet fully understood.

A synaptic tag is a hypothetical mark present in synapses expressing early-phase plasticity; it allows PRPs to function only in the tagged synapses (2, 3), although its molecular identity remains elusive. Three characteristics of a synaptic tag have been pointed out (4): A synaptic tag is locally activated, persists with a lifetime of 1 to 4 hours, and interacts with cell-wide molecular events that occur after strong stimulation evokes late plasticity. However, these characteristics are insufficient to define the biochemical activity required for synaptic tagging. It is also critical to specify the cell-wide molecular events that interact with the synaptic tag.

Local synthesis—the activity-dependent translation of some PRPs from mRNAs that reside in nearby dendrites—is a possible mechanism for synaptic tagging (4). Local synthesis is involved in long-term facilitation in *Aplysia* (3) and supplies several proteins that play important roles in synaptic plasticity in rodents, such as Arc/Arg3.1, PKM ζ , and GluR1 (5–8). However, this mechanism neither happens in a cell-wide manner nor considers the contribution of soma-derived PRPs. On the other hand, although contribution of soma-derived PRPs was suggested in synaptic tagging in the rodent hippocampus (2), no soma-

derived protein has so far been identified as a PRP consistent with the synaptic tag hypothesis. We sought to identify such a PRP as an example of the synaptic tagging mechanism and to specify cell-wide events that interact with the synaptic tag for soma-derived PRPs.

Previous synaptic tagging studies have primarily been conducted with two-pathway experiments to detect associative late-phase plasticity (2). Late-phase plasticity involves several elementary steps: a preceding early phase, induction of PRP synthesis, transport, integration, and synaptic function of PRPs. Identifying a synaptic tagging process among these steps by only measuring the eventual consequence [e.g., changes in transmission (2) or synaptic GluR1 accumulation (9)] would be difficult. However, these experiments suggest that new PRPs are transported from the soma along dendrites without a predetermined destination (2, 10). Enhanced PRP synthesis facilitated associative late-phase plasticity (11), whereas reduced PRP synthesis resulted in competitive maintenance of late-phase plasticity (12). These observations suggest that PRP delivery to synapses plays a key role in synaptic tagging.

It is reasonable to assume that a PRP can affect synaptic transmission only after it is delivered to and integrated into the active postsynaptic loci. Material transport across the spine neck is restricted (13) and is regulated in an activity-dependent manner for several proteins (14–17). Thus, we hypothesized that activity-dependent regulation of spine entry of the soma-derived PRPs serves as a synaptic tag (fig. S1), and we tested whether the spine entry has the following features of synaptic tagging: (i) The entry is activity-regulated; namely, PRPs stay in dendrites unless proper activity is provided. (ii) Inputs that activate early-phase plasticity evoke the entry (2). (iii) The entry is input-specific (4). (iv) PRPs during the dendritic transport from soma are subject to the entry (2). (v) The activation of spine entry is independent of protein synthesis (2). (vi) The entry activation has a persistent lifetime (18). We monitored the spine entry

of fluorescent protein–fused Vesl-1S (Homer-1a), a synaptic protein synthesized in the soma during late-phase long-term potentiation (19, 20) and required for long-term fear memory (21, 22).

Spine entry of Vesl-1S protein. Enhanced green fluorescent protein (EGFP)–tagged Vesl-1S (VE) or EGFP alone was exogenously expressed in dissociated primary culture of rat hippocampal neurons (fig. S2) (23). The replacement of extracellular medium with magnesium-free artificial cerebrospinal fluid (Mg-free ACSF) for 10 min led to the activation of synaptic *N*-methyl-D-aspartate (NMDA) receptors via glutamatergic transmission by spontaneous firing (24). VE fluorescence in mushroom-type spines was further observed in normal ACSF for 4 hours, and its increase relative to prestimulus intensity (F/F_{pre}) was calculated. VE fluorescence intensity increased gradually over time (Fig. 1A) in some but not all spines, which reflects heterogeneous inputs from spontaneous firing (Fig. 1B) (22), whereas changes in spine shape and size were more modest. To evaluate changes in a small portion of spines, we introduced a trap index: a numerical indication of VE increase in spines expressed as a rightward shift of cumulative frequency curves (Fig. 1C). Mg-free ACSF triggered a persistent and gradual increase in the trap index (Fig. 1D). The average trap index 240 min after the onset of stimulation (final trap index) was 2.08 ± 0.23 (SD) ($N = 7$ cells), which was significantly larger ($P = 2.1 \times 10^{-4}$, *t* test) than that measured in unstimulated neurons (1.41 ± 0.10 , $N = 5$ cells). Mg-free ACSF did not increase fluorescence in spines of neurons expressing only EGFP (final trap index = 1.42 ± 0.17 , $N = 4$ cells; $P = 0.001$ versus VE, *t* test).

To specify how spine fluorescence increased after stimulation, we estimated passive entry associated with size enlargement by line-scan analysis of individual spines. The analysis indicated that Mg-free stimulation largely increased the peak intensity [before stimulation: 8.8 ± 4.2 AU (arbitrary units); 4 hours after stimulation: 15.2 ± 7.1 AU; $N = 74$ spines from six cells, $P = 5.3 \times 10^{-10}$, *t* test] (Fig. 1E), whereas spine size (head half-width) was not affected (1.1 ± 0.4 μm versus 1.2 ± 0.4 μm , $P = 0.094$, *t* test) (Fig. 1F). Although the spine enlargement associated with long-term potentiation is greater in initially smaller spines (25), increases in the peak intensity and initial size were not correlated ($r = -0.14$), which suggests that the VE increase in spines is independent of morphological plasticity (Fig. 1G).

Incubation with a protein synthesis inhibitor, cycloheximide (CHX), did not affect the VE increase after Mg-free stimulation (final trap index = 2.00 ± 0.25 , $N = 5$; $P = 0.62$, *t* test) (Fig. 1H). VE content was not affected by incubation with 5 μM clasto-lactacystin β -lactone (LCL), a specific inhibitor of proteasomal activity involved in Vesl-1S protein degradation (26) (final trap index = 2.02 ± 0.10 , $N = 3$; $P = 0.42$, *t* test) (Fig. 1I). Together, these results indicate that the activity-dependent spine entry of the VE

Mitsubishi Kagaku Institute of Life Sciences (MITILS), 11 Minamiooya, Machida, Tokyo 194-8511, Japan, and Japan Science and Technology Agency (JST), Core Research for Evolutional Science and Technology (CREST), 4-1-8 Honcho, Kawaguchi 332-0012, Japan.

*To whom correspondence should be addressed. E-mail: kaoru@mitils.jp (K.I.); dada@mitils.jp (D.O.)

protein, but not synthesis or degradation, increases the VE content in spines. Henceforth, we call this activity VE trapping.

VE trapping is input-specific. Microperfusion was used to test the input specificity of VE trapping. Rhodamine was co-applied to estimate

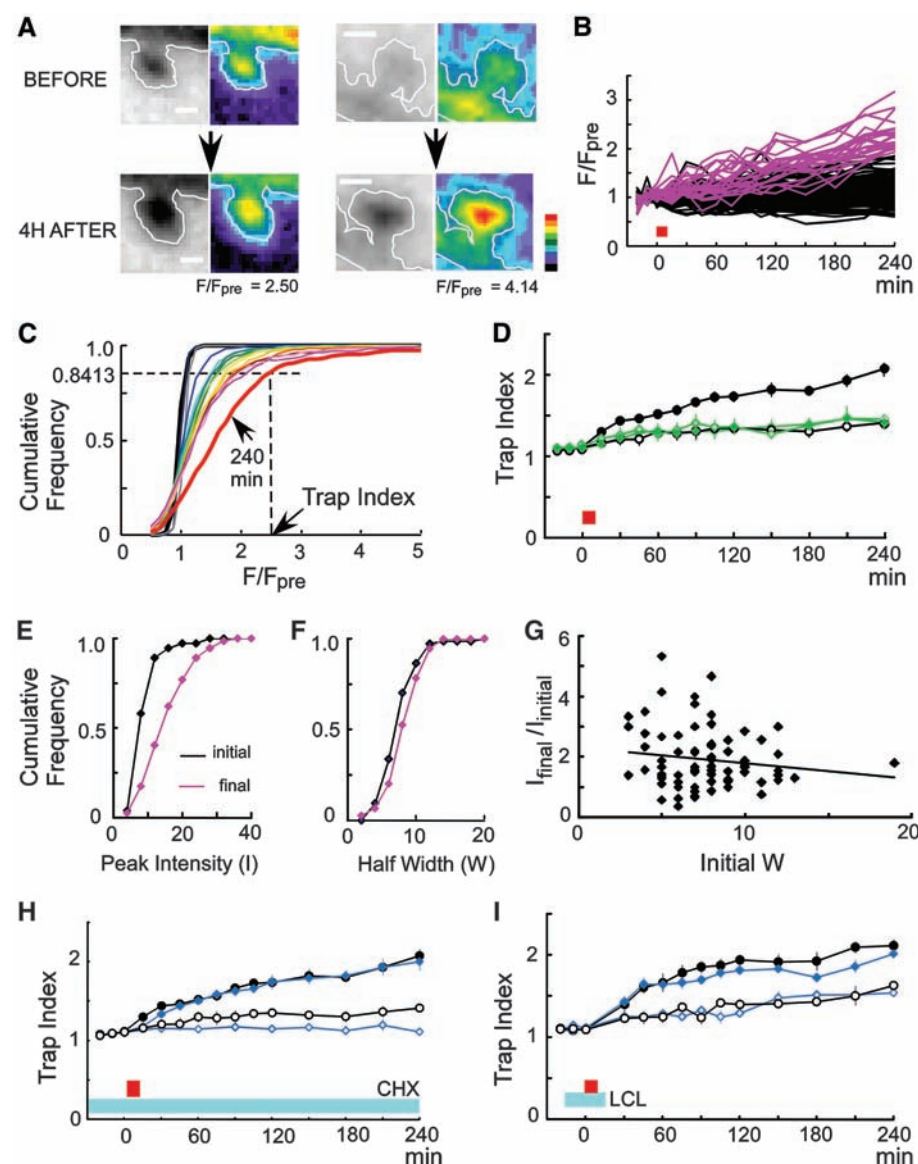


Fig. 1. VE trapping in spines. (A) VE fluorescence images in spines before and 4 hours after stimulation in both inverted black-and-white (black is higher) and pseudocolors (both scales apply to similar images in later figures). Scale bars, 1 μ m. (B) Changes by Mg-free ACSF stimulation (red rectangle) in fluorescence intensity (F) compared with prestimulus (F_{pre}) in 121 individual spines of a neuron. Magenta lines show 24 spines with F/F_{pre} values at 240 min that are greater than the average \pm SD ($1.39 \pm 0.53 = 1.92$). (C) Cumulative frequency curves of the pooled data of 652 spines in seven Mg-free stimulated neurons. Line colors indicate time (black, 20 min before; gray, 10 min before; dark blue, immediately before; blue, 15 min after; pale blue, 30 min after; dark green, 45 min after; green, 60 min after; yellow-green, 75 min after; yellow, 90 min after; dark yellow, 115 min after; orange, 120 min after; brown, 150 min after; pink, 180 min after; purple, 210 min after; red, 240 min after stimulation). The definition of trap index is indicated. (D) Trap index time courses. Values are averages \pm SEM (vertical bars). Solid circles, Mg-free ACSF on VE; solid green diamonds, Mg-free ACSF on EGFP; open circles, VE without stimulation; open green diamonds, EGFP without stimulation. (E and F) Line-scan analysis of 74 spines from six cells on peak intensity I (E) and half-width W (F) of spine fluorescence before and 4 hours after Mg-free stimulation. (G) Correlation between relative increase in I and initial value of W . (H) Trap index time courses. Solid circles, Mg-free; open circles, without stimulation; solid and open blue diamonds, Mg-free in the presence of 20 μ M CHX and CHX alone, respectively. (I) Trap index time courses. Solid circles, Mg-free + 0.05% dimethyl sulfoxide (DMSO); solid blue diamonds, Mg-free in the presence of 5 μ M LCL; open blue diamonds, LCL alone; open circles, 0.05% DMSO.

the affected area and to confirm whether the microperfusion reached the cell surface (Fig. 2, A and B). Microperfusion of normal ACSF did not affect VE fluorescence in spines, both inside and outside of the perfusion area (Fig. 2, C to E). Under these conditions, the increase in spine VE fluorescence followed a normal distribution in both areas as assessed by χ^2 analysis. This enabled comparison using a t test, which showed no significant difference between the areas (table S1); thus, microperfusion does not affect the spine fluorescence by nonspecific factors such as influx impact.

In contrast, local stimulation with Mg-free ACSF containing NMDA and glycine caused VE trapping exclusively inside the microperfusion area. The χ^2 analysis detected a significant deviation of VE increase from the normal distribution inside the perfusion area of three cells (Fig. 2, F to H, fig. S3, and cells 1 to 3 in table S1), but not outside the area. We applied a t test to the remaining five cells (cells 4 to 8 in table S1), for which spine fluorescence intensity was estimated as a normal distribution by χ^2 analysis, and found a significantly larger VE trapping inside the perfusion area than outside (Fig. 2, I to K).

When Mg-free ACSF containing NMDA, glycine, and 40 μ M MK801 (an irreversible open-channel blocker specific to NMDA receptors) was used for microperfusion, VE trapping was not detected either inside or outside the stimulated area (Fig. 2, L to N, and table S1), which indicates that VE trapping is NMDA receptor-dependent. Bath application of Mg-free ACSF after microperfusion with Mg-free ACSF containing NMDA, glycine, and MK801 led to VE trapping in spines outside of the microperfusion (Fig. 2, O to Q, and table S1), whereas spines treated with MK801 did not exhibit VE trapping.

VE stays in the dendrite unless NMDA receptors are activated. The promoter region of our VE plasmid is activated by 0.02 mM forskolin and 0.1 mM 3-isobutyl-1-methylxanthine (FI) (fig. S4) (27). VE fluorescence significantly increased in dendrites after bath perfusion of FI (Fig. 3, A to D). F/F_{pre} 240 min after FI application (1.10 ± 0.01 , $N = 6$ cells) was significantly larger than that without stimulation (0.98 ± 0.04 , $N = 6$ cells; $P = 0.011$, t test), whereas Mg-free ACSF did not increase dendritic VE fluorescence (F/F_{pre} 240 min after Mg-free ACSF application = 0.99 ± 0.04 , $N = 6$ cells; $P = 0.83$ versus ACSF, t test) (Fig. 3E). In contrast, VE fluorescence in spines was not significantly affected by FI treatment alone (trap index 240 min after FI = 1.63 ± 0.21 , $N = 5$; $P = 0.008$ versus Mg-free, $P = 0.071$ versus ACSF, t test) (Fig. 3, F to L). Sequential treatment of cells with FI followed by Mg-free ACSF enhanced VE trapping ($P = 0.029$ versus Mg-free, t test) (Fig. 3L). Similar results were obtained using BrG [8-bromo-cGMP (guanosine 3',5'-monophosphate)] instead of Mg-free ACSF

(F/F_{pre} 240 min after stimulus = 1.01 ± 0.02 , $N = 5$ cells; $P = 0.41$ versus ACSF, t test) (Fig. 3, E and L; see below).

Soma-derived Vesl-1S is subject to VE trapping. Vesl-1S mRNA was detected in the soma but not in the dendrites (fig. S5), which suggested that Vesl-1S proteins are synthesized in the soma and subsequently transported to dendrites. Vesl proteins are carried by transport vesicles via the interaction with metabotropic glutamate receptors (mGluRs 1 and 5) (28, 29); therefore, VE proteins during dendritic vesicular transport may be subject to VE trapping. We next examined this possibility with the use of photoactivatable GFP (PAGFP) fused with Vesl-1S

(VPA) (30). VPA proteins in the soma should be transported to the entire span of the cell along dendrites, and should be trapped in spines in an input-specific manner (Fig. 4A). Initially, cells expressing DsRed2, cotransfected as a morphological marker, showed only a slight fluorescence of VPA in the soma and a total absence of VPA fluorescence in dendrites. Brief photoactivation in the soma led to clear VPA fluorescence in the soma (Fig. 4B). The average photoactivation of VPA was smaller (factor of 5.4 ± 3.1 , $N = 13$) than that of PAGFP alone (factor of 34.1 ± 8.3 , $N = 4$), consistent with the instability of the Vesl-1S protein (26). VPA fluorescence moved along every dendritic branch

toward the distal ends, and this movement did not require local stimulation (Fig. 4C). Next, the dendritic region was viewed at higher magnification to acquire images before stimulation after somatic photoactivation; subsequently, neurons received microperfusion with normal ACSF 15 to 25 min after photoactivation and were observed for an additional 4 hours (Fig. 4D). VPA progressively increased in every dendrite, but it did not enter spines (Fig. 4, E to G, and table S2).

Local NMDA receptor activation caused VPA trapping inside, but not outside, the microperfusion area in all six cells tested after 4 hours (Fig. 5). A χ^2 analysis revealed significant deviation from normal distribution in two cells (Fig.

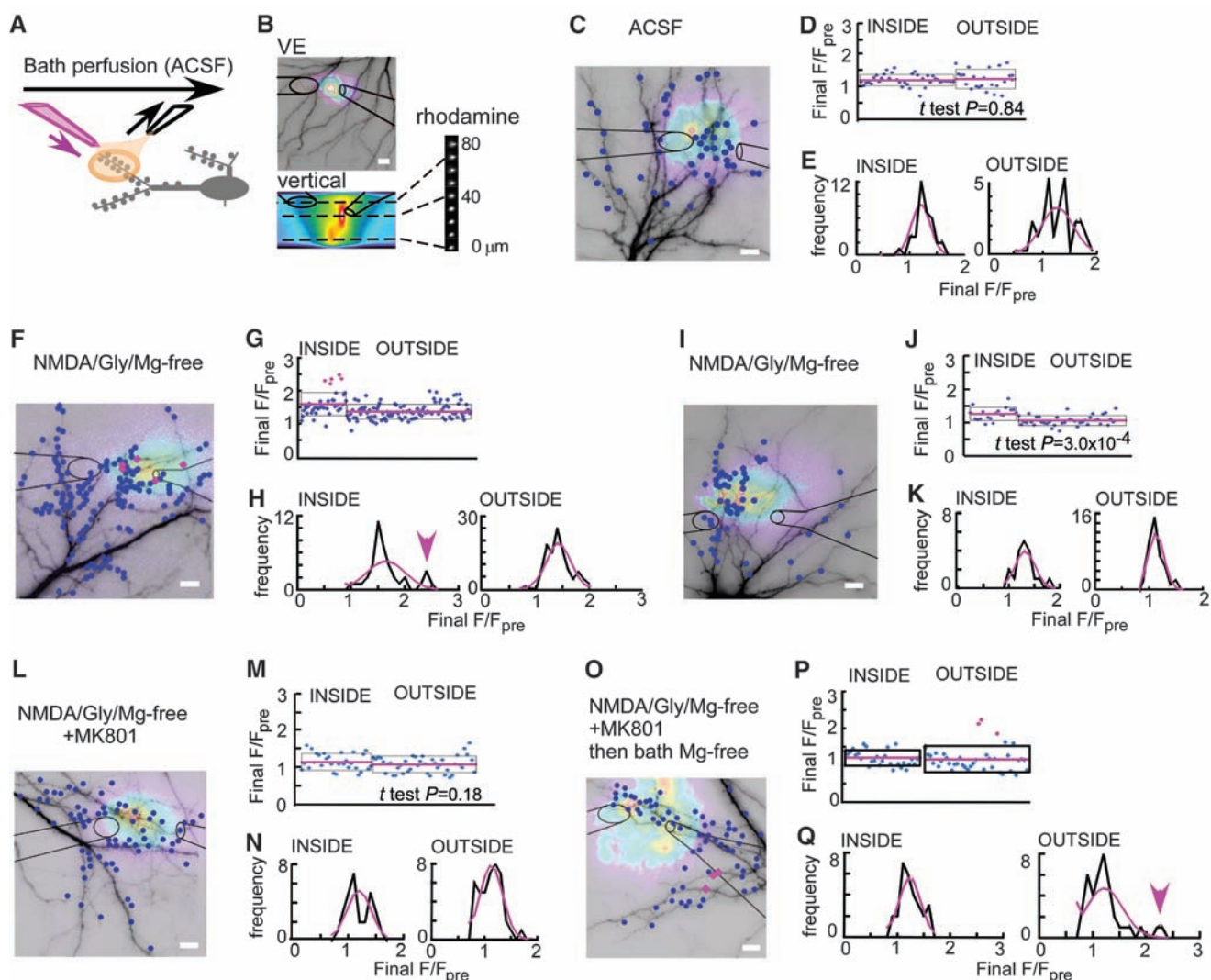


Fig. 2. Input-specific VE trapping. (A) Arrangement of injector (magenta) and suction (black) pipettes. (B) A vertical view of rhodamine fluorescence was reconstructed in three dimensions from images at different focal planes at 10- μ m intervals. A VE fluorescence image in dendrites is superimposed with rhodamine image (pseudocolors) at the height of the target dendrite and pipette positions (black lines). Scale bar, 10 μ m. (C to E) Microperfusion with normal ACSF for 10 min. (C) A representative VE image. Red and blue circles represent spines with significant and nonsignificant VE trapping by χ^2 test 240 min after microperfusion, respectively. Pipette positions and rhodamine distribution (pseudocolors) are superimposed. (D) F/F_{pre} of each spine 240 min

after microperfusion. Averages (red line) and average ± 1 SD levels (box) of the inside and outside spines are shown. (E) Frequency distribution of (D) (black) and the normal distribution calculated from the average and the SD (magenta). (F to H) Local NMDA receptor activation by microperfusion with Mg-free ACSF containing 0.15 mM NMDA and 10 μ M glycine for 10 min. Arrowhead in (H) indicates significant deviation in the frequency distribution detected by χ^2 test. (I to K) Local NMDA receptor activation by microperfusion. A t test showed significantly larger VE trapping in the inside area than outside. (L to N) Local NMDA receptor activation cocktail with 40 μ M MK801. (O to Q) Bath application of Mg-free ACSF 1 hour after MK801 microperfusion.

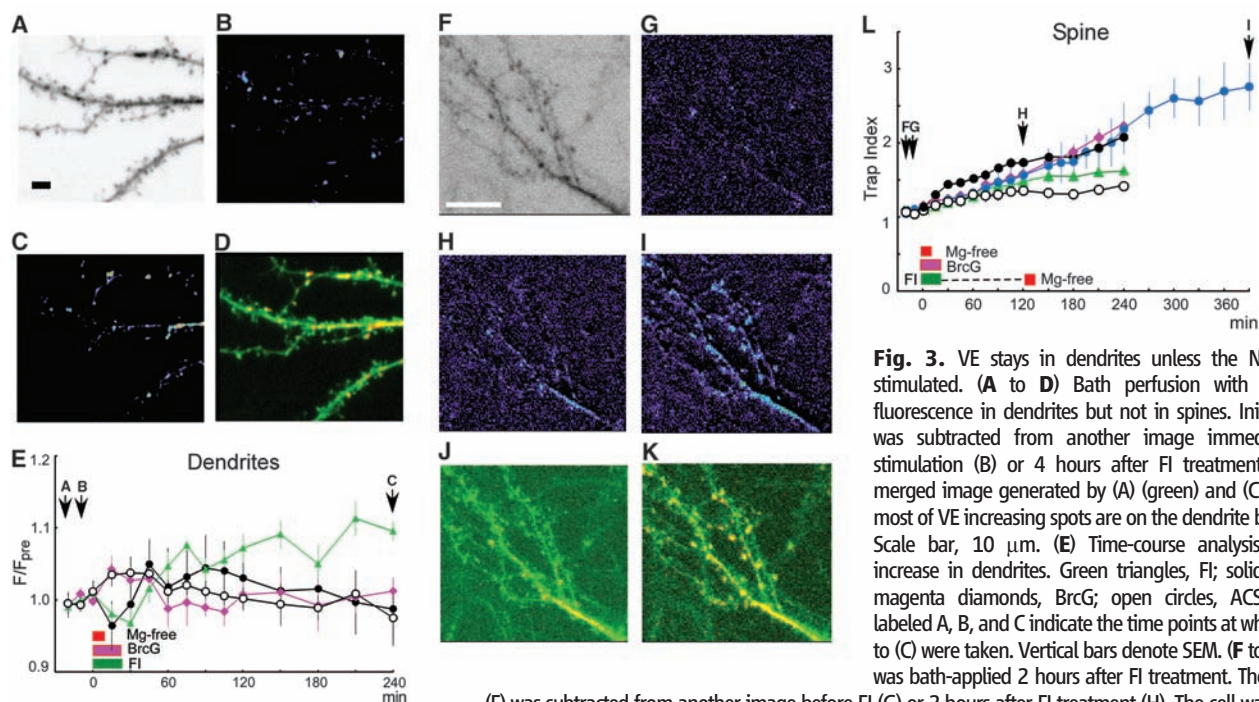


Fig. 3. VE stays in dendrites unless the NMDA receptor is stimulated. (A to D) Bath perfusion with FI increased VE fluorescence in dendrites but not in spines. Initial VE image (A) was subtracted from another image immediately before FI stimulation (B) or 4 hours after FI treatment (C). In (D), the merged image generated by (A) (green) and (C) (red) shows that most of VE increasing spots are on the dendrite but not the spines. Scale bar, 10 μ m. (E) Time-course analysis of fluorescence increase in dendrites. Green triangles, FI; solid circles, Mg-free; magenta diamonds, BrcG; open circles, ACSF alone. Arrows labeled A, B, and C indicate the time points at which pictures in (A) to (C) were taken. Vertical bars denote SEM. (F to K) Mg-free ACSF was bath-applied 2 hours after FI treatment. The initial VE image (F) was subtracted from another image before FI (G) or 2 hours after FI treatment (H). The cell was then stimulated by Mg-free ACSF. Subtraction image (4 hours after Mg-free stimulation minus initial VE image) (I) shows fluorescence increase in spines. (J) The merged image generated by (F) (green) and (H) (red). (K) The merged image generated by (F) (green) and (I) (red). Scale bar, 10 μ m. (L) Time-course analysis of trap index in spines. Solid blue circles, FI application before Mg-free stimulation; other symbols are as in (E). Arrows labeled F, G, H, and I indicate the time points at which pictures in (F) to (I) were taken.

Fig. 4. Somatic VPA spreads cell-wide but does not enter spines. (A) Experimental design. VPA in soma was photoactivated by laser illumination (blue arrowhead) and then carried along dendrites (green arrows). Distal dendrites with spines received microperfusion. AlexaFluor633 was used instead of rhodamine. VPA trapping should be exclusive to spines inside the microperfusion area. (B) Photoactivation of VPA. A cell expressing DsRed2 was selected (left) and its PAGFP image (middle) was taken. The entire soma was illuminated with a laser spot (red spot indicated by the arrow) by manual scanning. Both DsRed2 (not shown) and VPA (right) images were taken immediately after photoactivation. (C) VPA fluorescence gradually increased in entire dendrites without any stimulation. Scale bar, 10 μ m. (D) Experimental procedures defining “before” and “after” here and in Fig. 5. PA, photoactivation; stm, microperfusion. (E) Microperfusion with normal ACSF for 10 min. Images of DsRed2 (before) and VPA (before and after) are shown. The magenta line encloses the estimated area of stimulation. (F) DsRed2 image of dendrites with VE trapping significance (circles), estimated microperfusion area (pseudocolors), and pipette positions. Scale bar, 10 μ m. (G) The F/F_{pre} value of each spine measured 240 min after microperfusion (see Fig. 2).

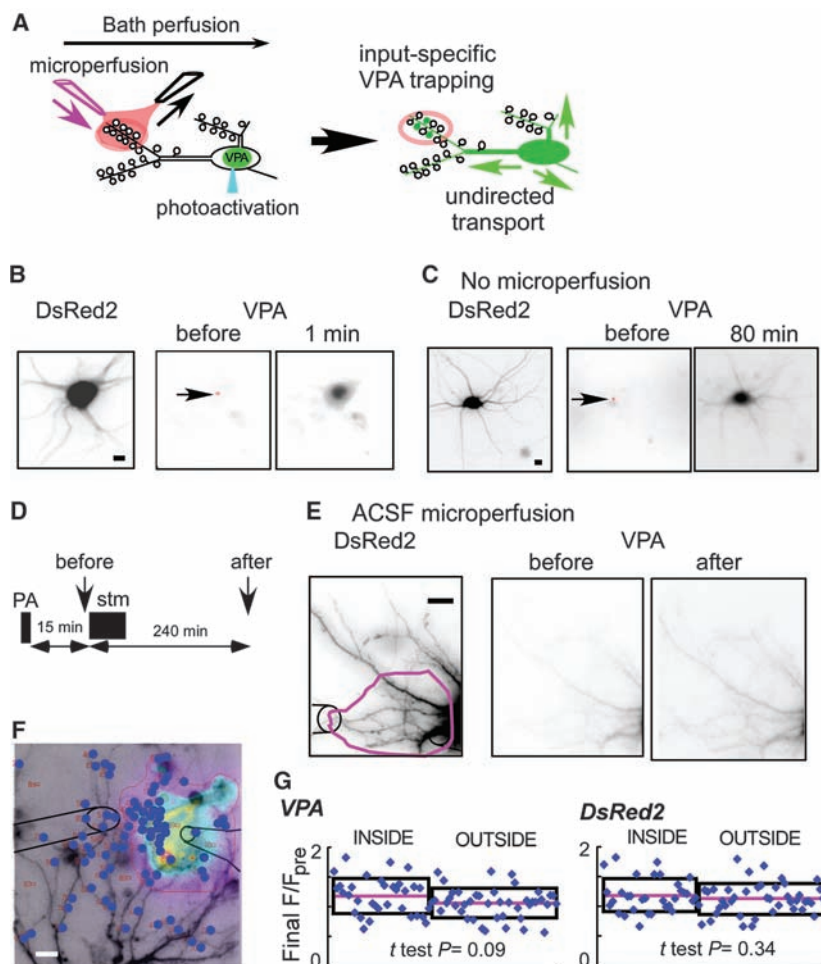
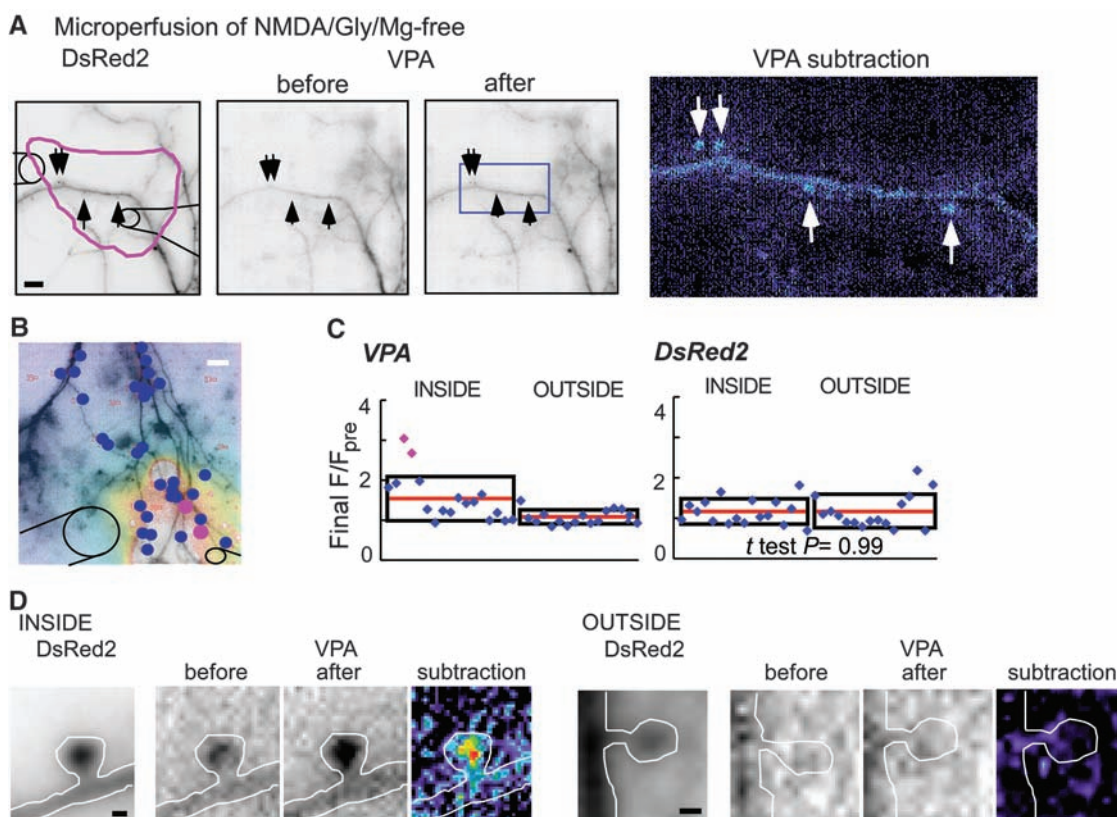


Fig. 5. VPA trapping by local NMDA receptor activation. (A) Microperfusion with Mg-free ACSF containing NMDA and glycine for 10 min in a limited area (magenta line) resulted in VPA trapping in some inside spines (arrows). The VPA subtraction image in pseudocolors ("after" minus "before") is shown to magnify the spines in the blue rectangle in the "after" image. Scale bar, 10 μ m. (B) DsRed2 image of dendrites (another cell) with VE trapping significance (circles), estimated microperfusion area (pseudocolors), and pipette positions. Scale bar, 10 μ m. (C) F/F_{pre} of each spine measured 240 min after microperfusion. (D) Representative images of VPA trapping inside (F/F_{pre} of VPA = 1.96) and outside (F/F_{pre} of VPA = 1.31) spines in a cell. Scale bar, 0.5 μ m.



5 and cells 1 and 2 in table S2); a *t* test performed for the remaining four cells (fig. S6 and cells 3 to 6 in table S2) showed that the VPA increase was always significantly greater inside the microperfusion area than outside. The final F/F_{pre} values of VPA and DsRed2 were not correlated (fig. S7). These movements were not observed for PAGFP alone (fig. S8 and table S2). DsRed2 fluorescence in spines was not affected in all experiments (table S2).

We also tested whether spine trapping is affected when dendritic transport of Vesl-1S protein is disrupted. Bath perfusion of Mg-free ACSF did not evoke VE trapping in cells expressing the W24A mutant of Vesl-1S, which does not interact with mGluRs 1 and 5 (31) (final trap index = 1.63 ± 0.12 , $N = 4$; $P = 0.008$, *t* test) (fig. S9A). VPA transport after local NMDA receptor activation was disrupted when the extracellular medium contained 1 μ M colchicine, a microtubule dissociation reagent (fig. S9B).

Signals for VE trapping. Calcium influx through NMDA receptor channels activates neuronal nitric oxide (NO) synthase (32). NO in turn increases cGMP, the intrinsic activator of protein kinase G (PKG) (33). Extracellular Ca^{2+} ions and the NO-PKG signaling pathway were required for NMDA receptor-dependent VE trapping (fig. S10). We also tested several inhibitors of other signals and found that activation of mGluRs 1 and 5 was not involved in VE trapping (table S3) (22).

A membrane-permeable analog of cGMP, BrcG, activated VE trapping (final trap index = 2.14 ± 0.25 , $N = 5$ cells; $P = 1.9 \times 10^{-5}$ versus

ACSF, *t* test) but did not alter the EGFP spine protein content (1.42 ± 0.21 , $N = 5$ cells; $P = 0.95$ versus ACSF, *t* test) (Fig. 6A). BrcG failed to evoke VE trapping in the presence of 1 μ M tetrodotoxin (TTX) throughout the experiment (final trap index = 1.24 ± 0.10 , $N = 5$; $P = 7.5 \times 10^{-5}$ versus BrcG, *t* test), whereas 50 nM TTX, which selectively suppresses Na^+ channels in dendrites where the channels are expressed sparsely (34, 35), did not affect VE trapping evoked by BrcG (final trap index = 1.95 ± 0.11 , $N = 6$; $P = 0.12$ versus BrcG, *t* test) (Fig. 6A). These results suggest that VE trapping requires a TTX-sensitive factor released by presynaptic activity in addition to NO-PKG signaling.

We used this synergy to estimate the lifetime of the PKG cascade. Cells were stimulated with BrcG in the presence of 1 μ M TTX. After further application of TTX for 2 hours, during which VE trapping was not observed, TTX was washed out and VE trapping was measured in normal ACSF for an additional 4 hours. VE fluorescence gradually increased in spines after TTX washout, and the trap index after 4 hours of washout was similar to that achieved without TTX (Fig. 6B). By changing the duration of TTX application, we found that the persistent activity lasted unchanged up to 3 hours, but TTX application for 4 hours abolished the VE trapping ability (Fig. 6, C and D). Interruption of TTX application for 1 hour led to a recovery of VE trapping activity after TTX washout, which was decreased by reapplication of TTX (Fig. 6E). Analysis of the average increase rates during initial TTX treatment ($0.001 \pm 0.010/\text{min}$), TTX washout ($0.0029 \pm$

$0.019/\text{min}$), and second application of TTX ($0.0006 \pm 0.007/\text{min}$) showed a significant activity increase during the washout period ($P = 0.04$ versus initial TTX, $P = 0.02$ versus second TTX; *t* test) (Fig. 6F).

Discussion. The present study revealed a mechanism of activity-dependent spine sorting for a PRP synthesized in the soma (Vesl-1S): VE trapping. We found that VE trapping meets the six criteria for synaptic tagging: (i) VE proteins did not enter the spines of hippocampal neurons in culture unless cells were properly activated (Fig. 3), which supports our central assumption that spine entry of Vesl-1S is activity-regulated. (ii) VE trapping required NMDA receptor activation, a known trigger of early-phase plasticity (Fig. 2) (2). (iii) VE trapping was input-specific (Fig. 2). (iv) VE trapping was independent of protein synthesis (Fig. 1) (2). (v) Soma-derived VE proteins were trapped into spines in a manner dependent on the dendritic vesicular transport (Fig. 5) without predetermined destination (Fig. 4), which is the most outstanding feature of synaptic tagging, discriminating it from the mail hypothesis (10). (vi) VE trapping was persistently permitted when PKG downstream signals were active (Fig. 6) (22).

On the basis of these results, we propose that Vesl-1S protein is a PRP that behaves in a manner consistent with the synaptic tag hypothesis. We conclude that activity-dependent PRP trapping in spines conforms to the synaptic tag hypothesis (Fig. 6G). The trapped PRPs should be further carried from the spine neck to synaptic membranes or other parts of the machinery that

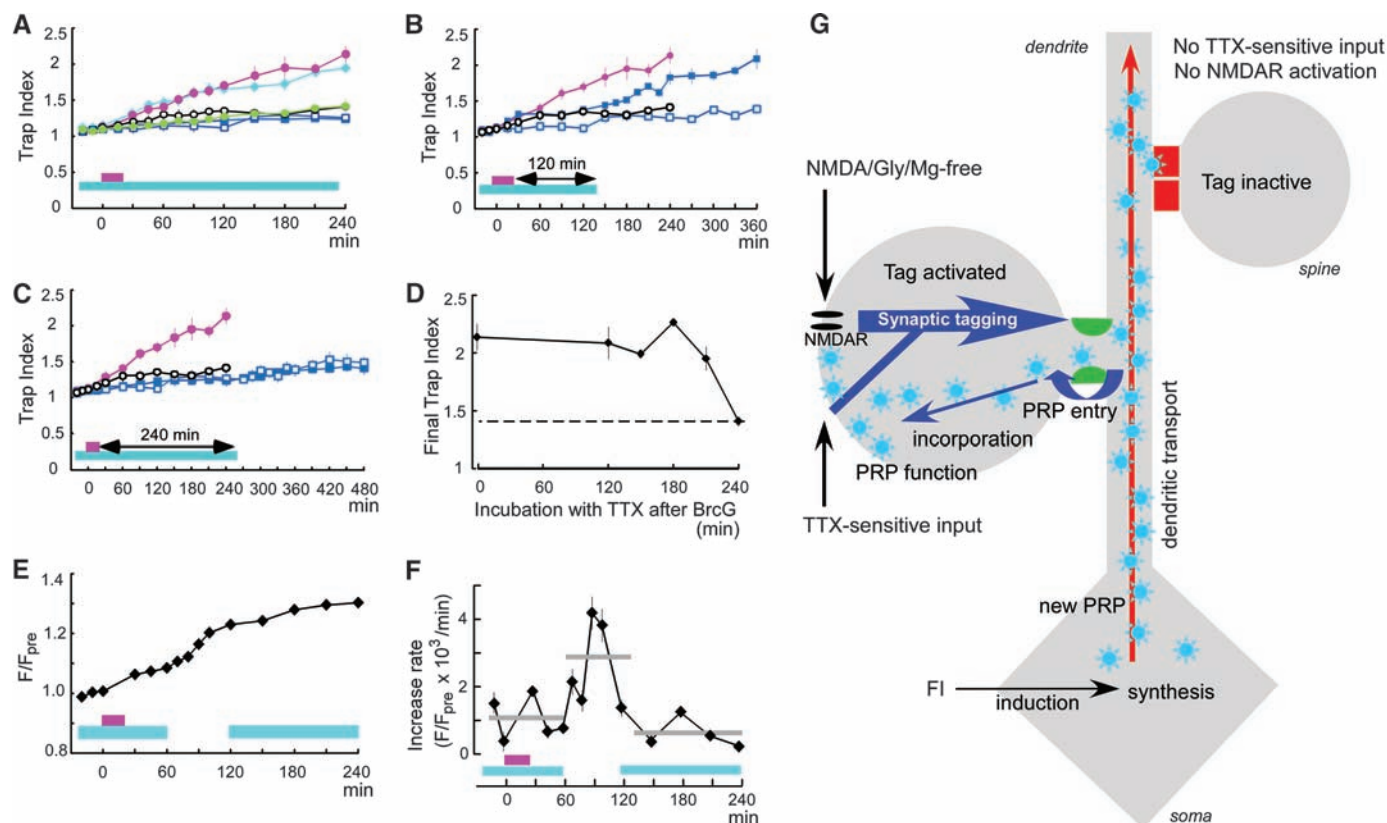


Fig. 6. Persistent activation of PKG signaling. **(A)** Trap index time courses. Solid magenta circles, BrcG on VE; solid green circles, BrcG on EGFP; solid cyan diamonds, BrcG + 50 nM TTX; solid blue squares, BrcG + 1 μ M TTX; open blue squares, 1 μ M TTX alone; open circles, ACSF alone. Vertical bars, SEM; horizontal bars, application of BrcG (magenta) and TTX (blue). **(B)** Neurons were stimulated with BrcG in the presence of 1 μ M TTX. TTX application was continued for an additional 2 hours, then TTX was washed out for 4 hours. Symbols are as in **(A)**. **(C)** Experiment with longer (4 hours) TTX incubation. Symbols are as in **(A)**. **(D)** Trap index 4 hours after TTX cessation versus TTX incubation time. **(E)** F/F_{pre} time-course analysis showing that TTX application blocked VE trapping, which was recovered during washout. **(F)** The time-course analysis of the

increase rates (F/F_{pre} change per time interval). Horizontal gray bars indicate the averages of increase rates during the different periods (first TTX incubation, washout, and second TTX incubation). **(E)** and **(F)** depict averages and SEM (vertical bars) from 2234 spines of eight cells. **(G)** Summary diagram showing somatically synthesized new PRPs (solar symbols), among which Vesl-15 is carried by microtubule-based vesicular transport along dendrites. Vesl-15 in the dendrites cannot enter spines without specific inputs (red closed gate in the distal spine neck). A synaptic tag successfully comes into operation exclusively in spines that receive both NMDA receptor activation and the TTX-sensitive input, which releases the blockade against Vesl-15 entry into spines (green open gate in the spine neck).

contribute to late-phase plasticity. The preferred mechanism for PRP trapping would thus involve transfer of the PRP from the kinesin-dependent dendritic transport to the myosin V-dependent intraspine transport. Interaction of myosin V with GluR1-containing recycling vesicles through rab11-FIP2 (36) has been reported, as well as direct interaction of myosin V with the C-terminal region of GluR1 (22, 37).

References and Notes

- K. G. Reymann, J. U. Frey, *Neuropharmacology* **52**, 24 (2007).
- U. Frey, R. G. M. Morris, *Nature* **385**, 533 (1997).
- K. C. Martin *et al.*, *Cell* **91**, 927 (1997).
- K. C. Martin, K. S. Kosik, *Nat. Rev. Neurosci.* **3**, 813 (2002).
- O. Steward, C. S. Wallace, G. L. Lyford, P. F. Worley, *Neuron* **21**, 741 (1998).
- I. A. Muslimov *et al.*, *J. Biol. Chem.* **279**, 52613 (2004).
- W. Ju *et al.*, *Nat. Neurosci.* **7**, 244 (2004).
- W. Smith, S. Starck, R. Roberts, E. Schuman, *Neuron* **45**, 765 (2005).
- N. Matsuo, L. Reijmers, M. Mayford, *Science* **319**, 1104 (2008).
- U. Frey, R. G. M. Morris, *Trends Neurosci.* **21**, 181 (1998).
- A. Barco, J. M. Alarcon, E. R. Kandel, *Cell* **108**, 689 (2002).
- R. Fonseca, U. V. Nägerl, R. G. M. Morris, T. Bonhoeffer, *Neuron* **44**, 1011 (2004).
- B. L. Bloodgood, B. L. Sabatini, *Science* **310**, 866 (2005).
- N. Honkura, M. Matsuzaki, J. Noguchi, G. C. R. Ellis-Davies, H. Kasai, *Neuron* **57**, 719 (2008).
- K. Shen, T. Meyer, *Science* **284**, 162 (1999).
- M. Ackermann, A. Matus, *Nat. Neurosci.* **6**, 1194 (2003).
- X. P. Ryan *et al.*, *Neuron* **47**, 85 (2005).
- U. Frey, R. G. M. Morris, *Neuropharmacology* **37**, 545 (1998).
- A. Kato, F. Ozawa, Y. Saitoh, K. Hirai, K. Inokuchi, *FEBS Lett.* **412**, 183 (1997).
- P. R. Brakeman *et al.*, *Nature* **386**, 284 (1997).
- N. Inoue *et al.*, *Mol. Brain* **2**, 10.1186/1756-6606-2-7 (2009).
- See supporting material on Science Online.
- R. Okubo-Suzuki, D. Okada, M. Sekiguchi, K. Inokuchi, *Mol. Cell. Neurosci.* **38**, 266 (2008).
- G. E. Hardingham, Y. Fukunaga, H. Bading, *Nat. Neurosci.* **5**, 405 (2002).
- M. Matsuzaki, N. Honkura, G. C. R. Ellis-Davies, H. Kasai, *Nature* **429**, 761 (2004).
- H. Ageta *et al.*, *J. Biol. Chem.* **276**, 15893 (2001).
- Y. Niibori, F. Hayashi, K. Hirai, M. Matsui, K. Inokuchi, *Neurosci. Res.* **57**, 399 (2007).
- F. Ango *et al.*, *J. Neurosci.* **20**, 8710 (2000).
- A. Kato *et al.*, *J. Biol. Chem.* **273**, 23969 (1998).
- G. H. Patterson, J. Lippincott-Schwartz, *Science* **297**, 1873 (2002).
- B. Xiao *et al.*, *Neuron* **21**, 707 (1998).
- K. S. Christopherson, B. J. Hillier, W. A. Lim, D. S. Bredt, *J. Biol. Chem.* **274**, 27467 (1999).
- H. G. Wang *et al.*, *Neuron* **45**, 389 (2005).
- P. J. Mackenzie, T. H. Murphy, *J. Neurophysiol.* **80**, 2089 (1998).
- J. C. Magee, M. Carruth, *J. Neurophysiol.* **82**, 1895 (1999).
- Z. Wang *et al.*, *Cell* **135**, 535 (2008).
- S. S. Correia *et al.*, *Nat. Neurosci.* **11**, 457 (2008).
- We thank A. Miyawaki (RIKEN, Japan) for the gift of PAGFP. Supported partly by grants from the Ministry of Education, Technology and Culture (K.I.), the Special Coordinate Funds for Promoting Science and Technology from MEXT of the Japanese Government (K.I.), and JST-CREST (K.I.).

Supporting Online Material

www.sciencemag.org/cgi/content/full/324/5929/904/DC1

Materials and Methods

SOM Text

Figs. S1 to S10

Tables S1 to S3

References and Notes

27 January 2009; accepted 2 April 2009

10.1126/science.1171498

Achieving $\lambda/20$ Resolution by One-Color Initiation and Deactivation of Polymerization

Linjie Li,¹ Rafael R. Gattass,¹ Erez Gershgoren,¹ Hana Hwang,² John T. Fourkas^{1,3,4,5*}

In conventional photolithography, diffraction limits the resolution to about one-quarter of the wavelength of the light used. We introduce an approach to photolithography in which multiphoton absorption of pulsed 800-nanometer (nm) light is used to initiate cross-linking in a polymer photoresist and one-photon absorption of continuous-wave 800-nm light is used simultaneously to deactivate the photopolymerization. By employing spatial phase-shaping of the deactivation beam, we demonstrate the fabrication of features with scalable resolution along the beam axis, down to a 40-nm minimum feature size. We anticipate application of this technique for the fabrication of diverse two- and three-dimensional structures with a feature size that is a small fraction of the wavelength of the light employed.

The demand for increasingly powerful integrated circuits has spurred remarkable progress in lithographic techniques in the past decades (1). However, progress toward higher resolution has proven to be increasingly difficult and expensive as feature sizes decrease. To improve resolution in photolithography, chemical nonlinearity can be employed to create a sharp intensity threshold for exposure (2). However, diffractive effects still limit feature sizes in conventional photolithography to about a quarter of a wavelength (λ) of the light used to expose the photoresist.

Nonlinear optical phenomena provide an alternative approach to photolithography (3–6). In multiphoton absorption polymerization (MAP), a photoinitiator in a prepolymer resin is excited by the simultaneous absorption of two or more photons of light. The absorption probability depends on the laser intensity to the power of the number of photons needed to cause an electronic transition, so an ultrafast laser is generally used to provide high peak intensity at low average power. The laser is focused through a microscope objective such that the intensity of the light is only high enough to drive multiphoton absorption in the small region defined by the focal volume of the beam. In the most common implementation of MAP, multiphoton absorption initiates cross-linking that hardens the prepolymer resin within the focal volume. By moving this focal volume relative to the sample, complex, three-

dimensional (3D) polymeric structures can be created.

Due to the optical nonlinearity of multiphoton absorption and the existence of an intensity threshold for polymerization, MAP can be used to create volume elements (voxels) with a resolution that is considerably smaller than the wavelength of the light used. For instance, 800 nm light has been used with MAP to create voxels with a transverse dimension of 80 nm (7), corresponding to $\lambda/10$ resolution. Even finer resolution has been reported for suspended lines, although based on the tapered nature of these lines at their attachment points, it is likely that shrinkage during the developing stage plays a role in this case (8). Using light of a shorter

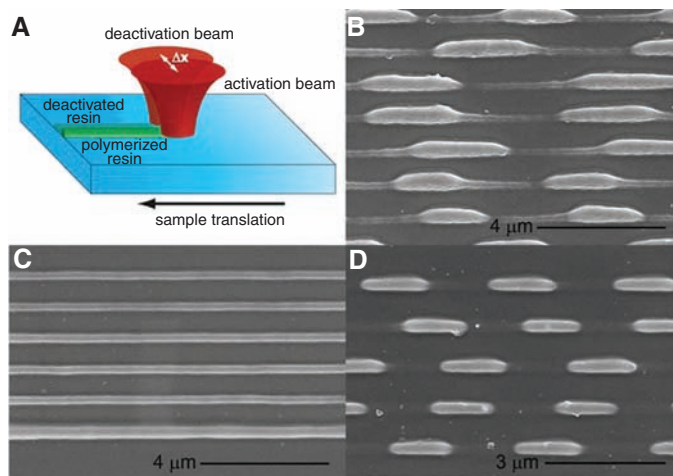
wavelength for MAP can also improve resolution (9). It should be noted that because of the shape of the focal region of the laser beam, the resolution of MAP along the beam axis is usually poorer by a factor of at least three than the transverse resolution (10).

We used a technique that we call resolution augmentation through photo-induced deactivation (RAPID) lithography. In RAPID lithography, one laser beam is used to initiate polymerization in a negative-tone photoresist. A second laser beam is used to deactivate the photoinitiator, preventing photopolymerization from occurring. By spatial shaping of the phase of the deactivation beam, features far smaller than the excitation wavelength can be fabricated.

The inspiration for RAPID lithography comes from stimulated emission depletion (STED) fluorescence microscopy (11–13). In STED, fluorescent molecules are excited by a short laser pulse. A second laser pulse, which is tuned to a substantially longer wavelength than the first pulse, is used to de-excite the molecules through stimulated emission. This depletion pulse must arrive after vibrational relaxation is complete in the excited electronic state but before significant fluorescence has occurred. Spatial phase shaping of the depletion beam causes de-excitation to occur everywhere except in a region at the center of the original focal volume (11–13). The size of this region depends on the intensity of the depletion beam and the corresponding degree of saturation of stimulated emission. Thus, fluorescence can be localized in a zone much smaller than the excitation wavelength.

In principle, STED should work equally well to deactivate polymerization in MAP or even

Fig. 1. (A) Schematic illustration of the experimental setup for demonstrating photoinduced deactivation of photopolymerization. The excitation and deactivation beams are focused in the prepolymer resin with a lateral separation of Δx . The substrate is translated perpendicular to the separation axis to fabricate polymer lines. **(B)** Top-view scanning electron micrograph of lines written with offset ($\Delta x > 0$), 200-fs excitation pulses and 50-ps deactivation pulses. The deactivation beam was chopped. The excitation power was 7 mW and the deactivation power 70 mW. **(C)** Top-view SEM of lines written with different timings between the excitation and deactivation pulses. The deactivation beam was at a low enough power to inhibit polymerization incompletely. The bottom line was written without a deactivation beam, and the remaining lines were written with delay times, from bottom to top, of 7 ns, 12 ns, 0 ns, 1 ns, and 6 ns; all delay uncertainties are <1 ps. The excitation power was 7 mW and the deactivation power 50 mW. **(D)** Top-view SEM of lines written with coincident ($\Delta x = 0$), 200-fs excitation pulses and a CW deactivation beam that was chopped to turn polymerization off and on. The excitation power was 5 mW and the deactivation power 34 mW.



¹Department of Chemistry and Biochemistry, University of Maryland, College Park, MD 20742, USA. ²Department of Physics, University of Maryland, College Park, MD 20742, USA. ³Institute for Physical Science and Technology, University of Maryland, College Park, MD 20742, USA. ⁴Maryland NanoCenter, University of Maryland, College Park, MD 20742, USA. ⁵Center for Nanophysics and Advanced Materials, University of Maryland, College Park, MD 20742, USA.

*To whom correspondence should be addressed. E-mail: fourkas@umd.edu

conventional photopolymerization. Typical radical photoinitiators undergo intersystem crossing to a triplet state on a time scale on the order of 100 ps (*14*). The radicals that lead to polymerization are formed in the triplet state, so de-excitation of molecules before intersystem crossing occurs will turn off photopolymerization. Furthermore, radical photopolymerization only occurs above a threshold concentration of radicals, so de-excitation of a small fraction of excited photoinitiator molecules could be sufficient to halt polymerization if the concentration of excited molecules is just above this threshold. In practice, to achieve efficient de-excitation, stimulated emission must dominate over absorption from the first excited electronic state to higher excited states, which will only happen when the oscillator strength between the ground and first excited electronic states is large (*15*). This oscillator strength condition is met for the strongly fluorescent molecules used for STED. However, radical photoinitiators generally have relatively small oscillator strengths between the ground and first excited states. As a result of excitation from the first excited state to higher-lying electronic states that have faster intersystem crossing times, in typical photoinitiators the deactivation beam would enhance polymerization as opposed to inhibiting it.

To solve the oscillator strength problem, we searched for molecules with large absorption cross sections that are not typically used as radical photoinitiators but that can still generate radicals upon photoexcitation. We focused our search on molecules with a low fluorescence quantum yield, on the premise that a nonradiative process might lead to radical generation. We identified a number of such dyes that could act as photoinitiators for MAP (*16*). We then investigated whether a second laser beam could be used to deactivate any of these molecules after the initial excitation. We employed two tunable, synchronized Ti:sapphire lasers for these experiments. The excitation laser produced pulses of 200-fs duration centered at 800 nm (*16*). Continuous-wave (CW) radiation from the same

laser did not lead to polymerization with any of the dyes tested, which verified that photoinitiation occurred through multiphoton absorption. The output of the second laser was stretched to a duration of ~50 ps to enhance the effectiveness of the stimulated emission process by allowing time for vibrational relaxation in the electronic ground state (*11*) and was tuned over a range of wavelengths to search for evidence of deactivation.

For one of the dye molecules tested, malachite green carbinol base, we were able to use the deactivation beam to reduce polymerization or, at high enough intensity, to inhibit polymerization completely (Fig. 1). We examined deactivation beam wavelengths ranging from 760 nm to 840 nm and in all cases were able to inhibit polymerization. The capacity to initiate polymerization with femtosecond pulses and inhibit polymerization with considerably longer pulses of the same wavelength confers the advantage that the entire process can be accomplished with the output of a single ultrafast laser if desired.

To demonstrate photoinduced deactivation of polymerization, we fabricated polymer lines with excitation and deactivation beams that were either offset or spatially coincident (Fig. 1A). Shown in Fig. 1B are lines drawn with an offset between the beams. The deactivation beam was blocked at regular periods with an optical chopper wheel. The resultant modulation of the polymer line demonstrates the effectiveness of the deactivation process.

In Fig. 1C, we show lines drawn by scanning the sample stage at constant velocity with no deactivation beam (lowest line) and with different timings between the excitation and deactivation pulses. The deactivation beam was set at an intensity that resulted in only partial inhibition of polymerization so that the dependence of the deactivation efficiency on timing could be determined. The efficiency of deactivation did not change noticeably for excitation/deactivation delays between 0 and 13 ns (*17*). This result implies that the photoinitiator goes through an intermediate state between optical excitation and the initiation of polymerization. The lifetime of this

intermediate state must be considerably longer than 13 ns, making it likely that the state is deactivated through a process other than stimulated emission. Once a structure was polymerized, it could not be erased by subsequent application of the deactivation beam, indicating that for deactivation to be effective it must occur while the dye molecule is in this intermediate state. However, a region in which deactivation was used to prevent polymerization can be polymerized subsequently by the excitation beam.

Given the high peak intensity of the short excitation pulses, two-photon initiation dominates over one-photon deactivation when they impinge on the prepolymer resin. In contrast, 50-ps deactivation pulses have considerably greater duration and correspondingly weaker peak intensity, so their overall energy can be much greater than that of the excitation beam without causing polymerization. Thus, for these longer pulses, deactivation can dominate over initiation. Even with 50 ps pulses, at high enough average power the deactivation beam caused increased polymerization, presumably through two-photon absorption. Based on the observation that delays as long as 13 ns did not affect the deactivation efficiency, we tested whether deactivation could be driven by CW radiation, for which considerably higher deactivation intensities would be feasible. As shown in Fig. 1D for spatially coincident excitation and deactivation beams (with the latter beam chopped), CW radiation is indeed effective for deactivation. This result is important because it allows RAPID to be performed without the need to establish any timing between the excitation and deactivation lasers and also implies that RAPID lithography should be feasible with single-photon absorption using CW excitation and deactivation beams.

Figure 1B gives a clear indication of how using different spatial intensity patterns for these two beams can improve resolution. We therefore next explored spatial phase shaping of the deactivation beam to alter its intensity distribution in the focal region. Our experimental setup for RAPID lithography with a pulsed excitation beam and a phase-shaped, CW deactivation beam is shown in Fig. 2. This setup employs two Ti:sapphire lasers tuned to 800 nm, one operating in pulsed mode for multiphoton excitation and one operating in CW mode for deactivation. The outputs of the two lasers were set to orthogonal polarizations and combined in a polarizing beam cube. The beams were focused into the sample with a high-numerical-aperture objective, the back aperture of which was overfilled by the excitation beam and filled completely by the deactivation beam.

We employed a spatial phase mask (*11*) that is designed to improve resolution along the optical axis of the fabrication system, which we will designate *z*. The mask consists of a flat substrate with a central circular region of an appropriate thickness to create a half-wave delay at 800 nm. The point-spread functions (PSFs) of the two beams (*18*) were measured, and proper overlap

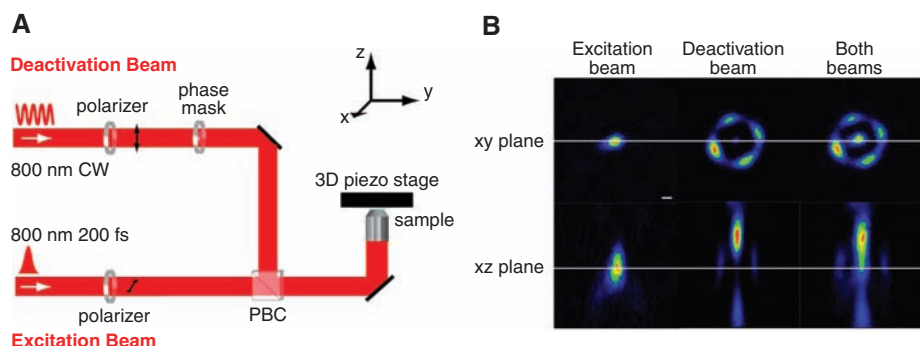


Fig. 2. (A) Schematic experimental setup for RAPID lithography with a pulsed excitation beam and a phase-shaped, CW deactivation beam. PBC, polarizing beam cube. (B) False-color, multiphoton-absorption-induced luminescence images of the cubes of the PSFs of the excitation beam, the deactivation beam, and both beams together. The long white lines indicate the approximate centers of the focal regions. The scale bar in the upper left image is 200 nm.

was ensured using multiphoton-absorption-induced luminescence (MAIL) (19) from a gold nanoparticle (Fig. 2B) (20). The majority of the intensity of the deactivation beam lies outside the center of the focal region. As can be seen from these images, there is no overlap between the excitation and deactivation PSFs in the xy plane, but there is considerable overlap along the z direction.

To assess the resolution enhancement of RAPID lithography with this phase mask, we studied the sizes and shapes of voxels created with different excitation and deactivation powers. To observe the voxel shapes, we employed an ascending-scan method in which identical, isolated voxels are created at different heights relative to the substrate (10). At some particular height, the voxel will barely be attached to the substrate. If the aspect ratio of the voxel is greater than unity it will fall over, allowing its dimensions to be determined readily with scanning electron microscopy (SEM) or atomic force microscopy (AFM).

Figure 3 shows SEM images from one such voxel study at a fixed excitation power (time averaged) of 10 mW (21) and different deactivation beam powers. As would be expected for the phase mask employed, deactivation did not have a substantial effect on the transverse dimensions of the voxels. However, with increasing deactivation power the z dimension of the voxel decreased by a factor of more than three. For a given excitation intensity, deac-

tivation intensity, and height relative to the substrate, voxels were either present at every exposed spot or were absent at every exposed spot. The variation in voxel dimensions for a fixed set of fabrication parameters was about $\pm 5\%$.

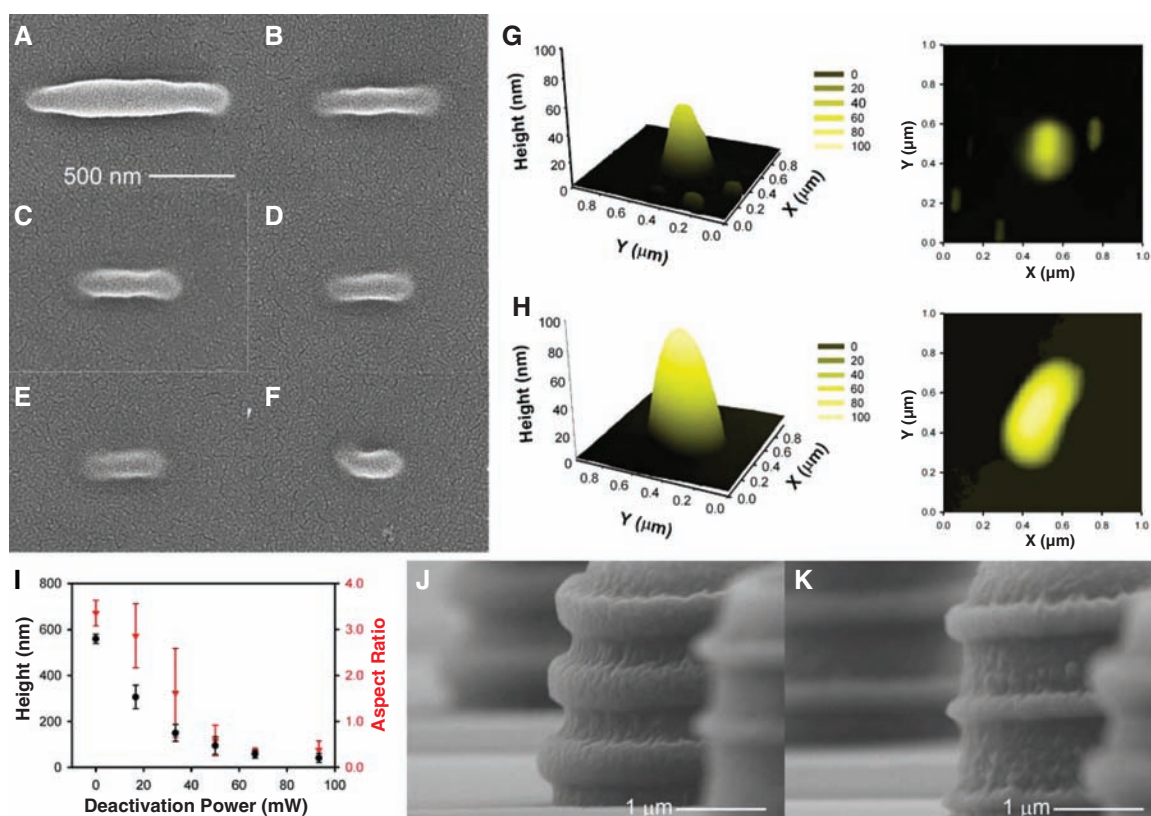
Because our voxel studies were performed on a glass cover slip (which is transparent but not electrically conductive), voxels had to be coated with metal for SEM imaging. Thus, to measure the smallest voxels that could be fabricated, we used AFM so that the metal coating step could be avoided. Shown in Fig. 3G is the smallest voxel that we were able to fabricate reproducibly with RAPID lithography using 800 nm light (22). For comparison, the corresponding smallest voxel that could be fabricated reproducibly without the deactivation beam is shown in Fig. 3H (23). Whereas the voxel in Fig. 3G is standing, the voxel in Fig. 3H has fallen over because of its high aspect ratio.

Resins used for MAP often exhibit shrinkage. The resin used here is composed of low-molecular-weight monomers that exhibit low shrinkage. To determine whether shrinkage takes on an increased importance at small feature sizes, we fabricated suspended polymer lines (fig. S1) with cross-sectional dimensions similar to those of the voxels in Fig. 3, G and H. The widths of the lines did not increase substantially at their attachment points to the supporting structures, and the lines are not always taut, which indicates that shrinkage is not responsible for the small voxel sizes observed here.

In Fig. 3I, we plot the height and aspect ratio of voxels measured in AFM experiments as a function of deactivation power. When the aspect ratio of a voxel is less than unity, it will not fall over even when barely attached to the substrate. For the excitation power used in Fig. 3I, we were able to reduce the voxel height from nearly 600 nm with no deactivation beam to 40 nm with a deactivation power of 93 mW, representing a resolution of $\lambda/20$. The aspect ratio was correspondingly reduced from more than 3 to 0.5. The rings on the towers shown in Fig. 3J (fabricated with conventional MAP) and Fig. 3K (fabricated with RAPID) demonstrate that enhancement of resolution and aspect ratio can also be achieved in 3D structures.

We have observed that above a certain excitation power, it becomes impossible to inhibit polymerization fully even at high deactivation beam power. This result implies that there are two different channels for photoinitiation, only one of which is deactivatable. If the concentration of radicals from the nondeactivatable channel is below the polymerization threshold, the deactivation beam can inhibit polymerization completely. We have further observed that the irreversible channel is weaker in more viscous resins. Although research into the nature of the photophysics of this system is ongoing, we believe that excitation of the photoinitiator leads to an electron transfer process that creates two relatively stable radicals. Due to their stability, these radicals initiate polymerization on a time scale

Fig. 3. (A to F) SEM images of voxels created with deactivation beam powers of 0 mW, 17 mW, 34 mW, 50 mW, 84 mW, and 100 mW, respectively. **(G)** Three-dimensional and contour AFM images of the smallest voxel that could be created with RAPID lithography. **(H)** Corresponding images of the smallest voxel that could be created with conventional MAP. The x and y dimensions of the voxels in **(G)** and **(H)** are exaggerated due to the width of the AFM tip, whereas the z dimension (height) is accurate. **(I)** Dependence of the height and aspect ratio of voxels on the power of the deactivation beam. The error bars represent ± 1 SD based on measurements of four voxels. **(J)** Tower with rings created with conventional MAP. **(K)** Tower with rings created with RAPID.



that is considerably longer than the 13-ns repetition time of our laser system. So long as the radicals do not diffuse apart, absorption of a photon from the deactivation beam can lead to back-transfer of the electron, depleting the radicals before they can react. If the radicals do diffuse apart, deactivation can no longer occur, accounting for the nondeactivatable channel.

With the phase mask used here, RAPID lithography can clearly produce features with heights as small as $\lambda/20$ along the optical axis. Analogous with results from STED microscopy, comparable transverse resolution should be attainable by employing a different phase mask, such as a spiral phase element (24). By using two phase-masked deactivation beams (25), it should further be possible to attain this resolution in all dimensions. The use of shorter excitation and deactivation wavelengths should improve resolution further. A current limiting factor in the resolution attainable is that even a CW deactivation beam can cause polymerization at high enough intensity. Because the resolution enhancement of RAPID lithography is based on an optical saturation effect, making the deactivation process more efficient should lead to finer features. In principle, the resolution of RAPID will ultimately be limited by material properties, particularly the minimum size of a self-supporting polymer voxel. With this limitation in mind, we believe that resolution on the order of 10 nm can be attained through full optimization of the photoresist properties and the

optical configuration. Resolution on this scale may be attractive for next-generation lithography, particularly considering that RAPID lithography can be implemented with a table-top instrument.

References and Notes

1. S. E. Thompson, S. Parthasarathy, *Mater. Today* **9**, 20 (2006).
2. H. Ito, in *Microlithography: Molecular Imprinting* (Springer-Verlag, Berlin, 2005), vol. 172, *Advances in Polymer Science*, pp. 37–245.
3. S. Kawata, H. B. Sun, T. Tanaka, K. Takada, *Nature* **412**, 697 (2001).
4. M. Rumi, S. Barlow, J. Wang, J. W. Perry, S. R. Marder, in *Photoreponsive Polymers I* (Springer-Verlag, Berlin, 2008), vol. 213, *Advances in Polymer Science*, pp. 1–95.
5. C. N. LaFratta, J. T. Fourkas, T. Baldacchini, R. A. Farrer, *Angew. Chem. Int. Ed.* **46**, 6238 (2007).
6. D. Yang, S. J. Jhaveri, C. K. Ober, *Mater. Res. Sci. Bull.* **30**, 976 (2005).
7. J.-F. Xing *et al.*, *Appl. Phys. Lett.* **90**, 131106 (2007).
8. D. Tan *et al.*, *Appl. Phys. Lett.* **90**, 071106 (2007).
9. W. Haske *et al.*, *Opt. Express* **15**, 3426 (2007).
10. H.-B. Sun, T. Tanaka, S. Kawata, *Appl. Phys. Lett.* **80**, 3673 (2002).
11. T. A. Klar, S. Jakobs, M. Dyba, A. Egner, S. W. Hell, *Proc. Natl. Acad. Sci. U.S.A.* **97**, 8206 (2000).
12. S. W. Hell, *Science* **316**, 1153 (2007).
13. S. W. Hell, *Nat. Methods* **6**, 24 (2009).
14. C. S. Colley *et al.*, *J. Am. Chem. Soc.* **124**, 14952 (2002).
15. J. O. Hirschfelder, C. F. Curtiss, R. B. Bird, *Molecular Theory of Gases and Liquids* (Wiley, New York, 1954).
16. Materials and methods are available as supporting material on Science Online.
17. The maximum delay time of 13 ns is determined by the 76 MHz laser repetition rate.
18. Because MAIL from gold nanoparticles is a three-photon process at 800 nm, the images show the cubes of the PSFs.
19. R. A. Farrer, F. L. Butterfield, V. W. Chen, J. T. Fourkas, *Nano Lett.* **5**, 1139 (2005).
20. The deactivation laser was operated in fs pulsed mode for the purpose of measuring its PSF using MAIL but was operated in CW mode for all other experiments. The beam profile and direction did not change measurably in going from pulsed to CW mode, so we expect the PSF to be nearly identical in both modes.
21. All powers were as measured at the sample position.
22. The slight asymmetry of the voxel is due to our use of linearly polarized light for fabrication. See (26).
23. AFM cannot measure reentrant (overhanging) features, so although the voxels appear to be tapered in these images, they are not.
24. M. W. Beijersbergen, R. P. C. Coerwinkel, M. Kristensen, J. P. Woerdman, *Opt. Commun.* **112**, 321 (1994).
25. B. Harke, C. K. Ullal, J. Keller, S. W. Hell, *Nano Lett.* **8**, 1309 (2008).
26. H. B. Sun *et al.*, *Appl. Phys. Lett.* **83**, 819 (2003).
27. We appreciate the support of the Maryland NanoCenter and its Nanoscale Imaging, Spectroscopy, and Properties Laboratory (NISPLab). NISPLab is supported in part by NSF as a *Materials Research Science and Engineering Center* (MRSEC) Shared Experimental Facility. This work was supported in part by the UMD-NSF-MRSEC under grant DMR 05-20471. We are grateful to E. Williams for the use of her AFM and to J. Goldhar, Y. Leng, and V. Yun for fabricating the phase mask used in this work. The University of Maryland has filed a provision patent based on the work presented in this paper.

Supporting Online Material

www.sciencemag.org/cgi/content/full/1168996/DC1
Materials and Methods
SOM Text
Fig. S1
References

25 November 2008; accepted 19 March 2009
Published online 9 April 2009;
10.1126/science.1168996
Include this information when citing this paper.

Two-Color Single-Photon Photoinitiation and Photoinhibition for Subdiffraction Photolithography

Timothy F. Scott,^{1*} Benjamin A. Kowalski,² Amy C. Sullivan,^{2†}
Christopher N. Bowman,¹ Robert R. McLeod^{2‡}

Controlling and reducing the developed region initiated by photoexposure is one of the fundamental goals of optical lithography. Here, we demonstrate a two-color irradiation scheme whereby initiating species are generated by single-photon absorption at one wavelength while inhibiting species are generated by single-photon absorption at a second, independent wavelength. Co-irradiation at the second wavelength thus reduces the polymerization rate, delaying gelation of the material and facilitating enhanced spatial control over the polymerization. Appropriate overlapping of the two beams produces structures with both feature sizes and monomer conversions otherwise unobtainable with use of single- or two-photon absorption photopolymerization. Additionally, the generated inhibiting species rapidly recombine when irradiation with the second wavelength ceases, allowing for fast sequential exposures not limited by memory effects in the material and thus enabling fabrication of complex two- or three-dimensional structures.

Photopolymerizations typically proceed when a chromophore absorbs a photon and subsequently generates active centers that initiate the polymerization reaction. This single-photon process exhibits high irradiation sensitivity, enabling the use of low-power lasers and high writing

speeds, which are critical for lithographic, stereolithographic, and data storage applications. However, feature size in depth is typically a multiple of the Rayleigh range of the focused beam (I), preventing the fabrication of micrometer-scale layers. Similarly, the transverse feature size is

constrained by the diffraction limit, a physical property associated with the focusing power of lenses that is dependent on the wavelength of the incident light and the numerical aperture of the lens. Finer feature sizes are achieved by reducing the irradiation intensity or time (2); however, this procedure unavoidably reduces the contrast between the conversion of the gelled, insoluble material and the ungelled, soluble material and results in the fabrication of loosely cross-linked, mechanically unsound structures unable to withstand the rigors of solvent processing that are necessary for device fabrication.

These limitations are partially addressed by two-photon photopolymerization, wherein a chromophore absorbs two photons to initiate polymerization. This approach has been exploited by a number of researchers to realize the fabrication of three-dimensional (3D) nanostructures (2–6) with

¹Department of Chemical and Biological Engineering, University of Colorado, Boulder, CO 80309-0424, USA. ²Department of Electrical and Computer Engineering, University of Colorado, Boulder, CO 80309-0425, USA.

*Present address: Center for Bioengineering, Department of Mechanical Engineering, University of Colorado, Boulder, CO 80309-0427, USA.

†Present address: Department of Physics and Astronomy, Agnes Scott College, Decatur, GA 30030, USA.

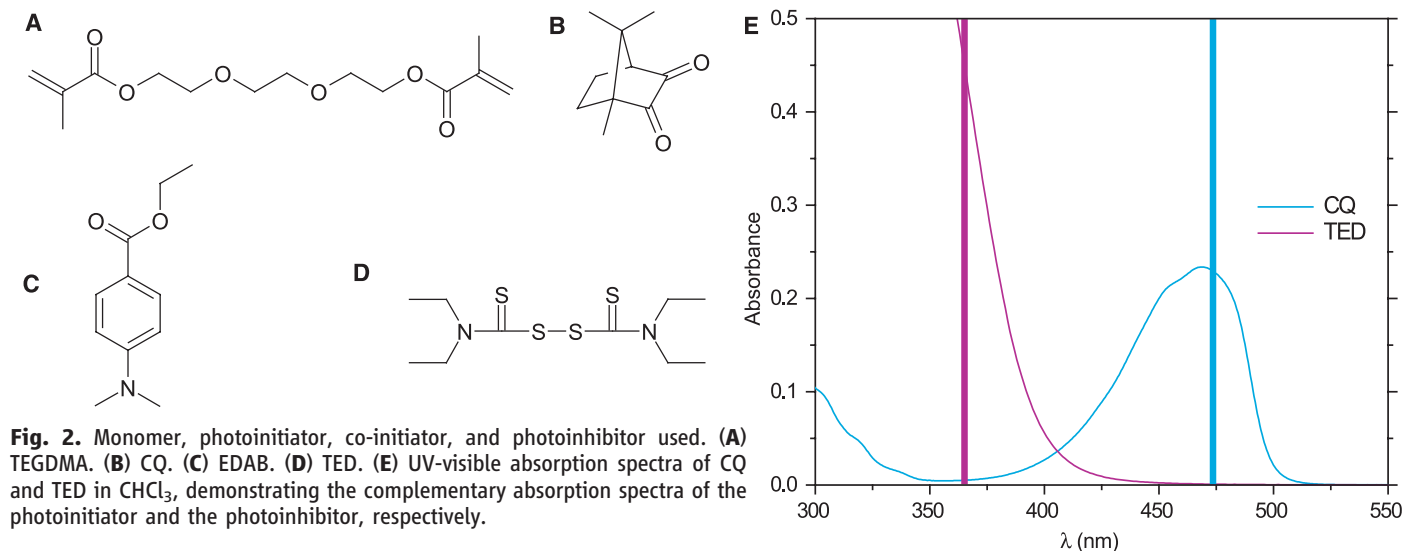
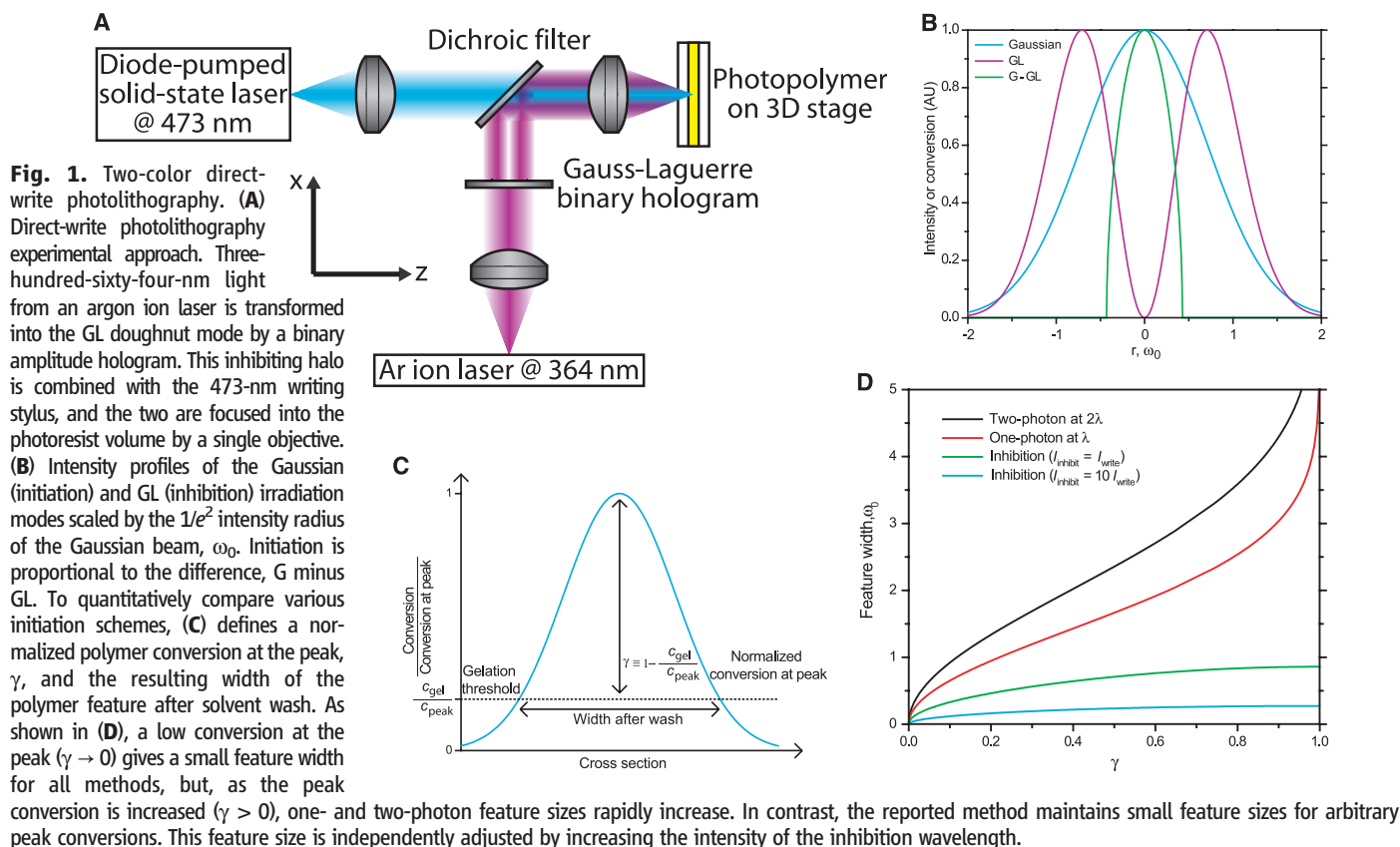
‡To whom correspondence should be addressed. E-mail: robert.mcleod@colorado.edu

feature sizes below the diffraction limit. The premise of these studies is that two-photon absorption (and hence polymerization) only occurs efficiently near the center of the focal volume, where photon density is highest. For many initiators, however, the two-photon absorption cross section is inherently small. Several approaches have been exploited to address this issue, such as application of π -conjugated donor-acceptor compounds (3) and quantum dots (7) or use of photochromic compounds as two-photon photosensitizers in free-radical photopolymerizations (8–11). Unfortunately, many of the confinement

benefits of two-photon processes are lost when the intermediate lifetime is greater than the exposure time. Moreover, high-power sources such as pulsed Ti:sapphire lasers focused in small areas are required for rapid exposures. Thus, only point exposures and low translation speeds are feasible. Ultimately, the combination of laser cost and extremely long fabrication times substantially decreases the scalability and impact of these processes.

An alternative means of confining polymerization would be to activate a localized inhibitor such as a radical trap transiently. Here, we de-

scribe a scheme whereby the initiation and the inhibition of a radical photopolymerization are uniquely correlated to two distinct irradiation wavelengths. Photoinduced inhibition is accomplished by noninitiating radicals produced via single-photon photolysis of an otherwise inert compound. These radicals are able to couple with the growing polymer chain, terminating polymerization and halting chain growth. Moreover, the inhibiting radicals are small molecular species that remain unbound to the polymer network and thus diffuse rapidly (12). As a result, they may be very short-lived, recombining with each other at



diffusion-controlled rates so that their concentration falls precipitously in the absence of photolysing irradiation. Assuming all species formed in the recombination reactions are also inert, there should be negligible residual inhibiting species after the photolysing irradiation has ceased.

To implement this technique, we focused the photoinhibiting beam into a Gauss-Laguerre (GL) “doughnut” mode surrounding the focal point of the primary beam used to initiate polymerization. An analogous irradiation scheme used in stimulated emission-depletion (STED) microscopy has been shown to resolve features on the order of 15 nm (13). In a similar vein, the final polymerized feature size in this irradiation scheme is a function of the difference between initiation and inhibition patterns. Uniquely, this difference is not governed by the conventional diffraction limit as in traditional photolithography: The limit now is determined by the contrast that is maintained between initiation and inhibition.

The small but finite initiation rate of the inhibiting radicals sets an upper limit on the ratio of inhibiting to initiating intensities, in turn limiting the confinement shown in Fig. 1D.

The layout of the optical system used to demonstrate this capability is shown in Fig. 1A (14). The initiating and inhibiting wavelengths are manipulated into complementary Gaussian and GL irradiation modes, respectively, where the GL mode is generated by a binary hologram. The GL mode is characterized by a central null, a high-contrast, topological feature of the electric field that is maintained throughout the entire focal volume. The two beams are combined with a dichroic filter and focused into the volume of the substrate material; the resulting diffraction-limited profiles at the coincident focal plane are shown in Fig. 1B. This two-color irradiation scheme produces a region of initiating species surrounded by a doughnut of inhibiting species.

The size of the resulting polymerized region is predicted by noting that, through application of the steady-state approximation (15), the polymerization rate (R_p) is predicted to scale with the square root of the initiation rate (R_i) for exclusively bimolecular termination. Thus, for single-photon absorption, R_i scales linearly with the irradiation intensity I and R_p is proportional to $I^{0.5}$. In the presence of photoinhibiting species, R_i is modified such that R_p scales as $(I_{\text{blue}} - \beta \times I_{\text{UV}})^{0.5}$, where I_{blue} and I_{UV} are the blue and ultraviolet (UV) irradiation intensities, respectively, and β is a constant encompassing the ratios of the inhibitor to the initiator absorption cross sections, quantum yields, and reaction rate constants. With this model, the predicted polymerization profile, shown in Fig. 1B for the case of $\max(I_{\text{blue}}) = \max(\beta \times I_{\text{UV}})$, is substantially smaller than the diffraction-limited spot size. Note that feature widths can be reduced by increasing the intensity of the UV beam; however, because the GL null is

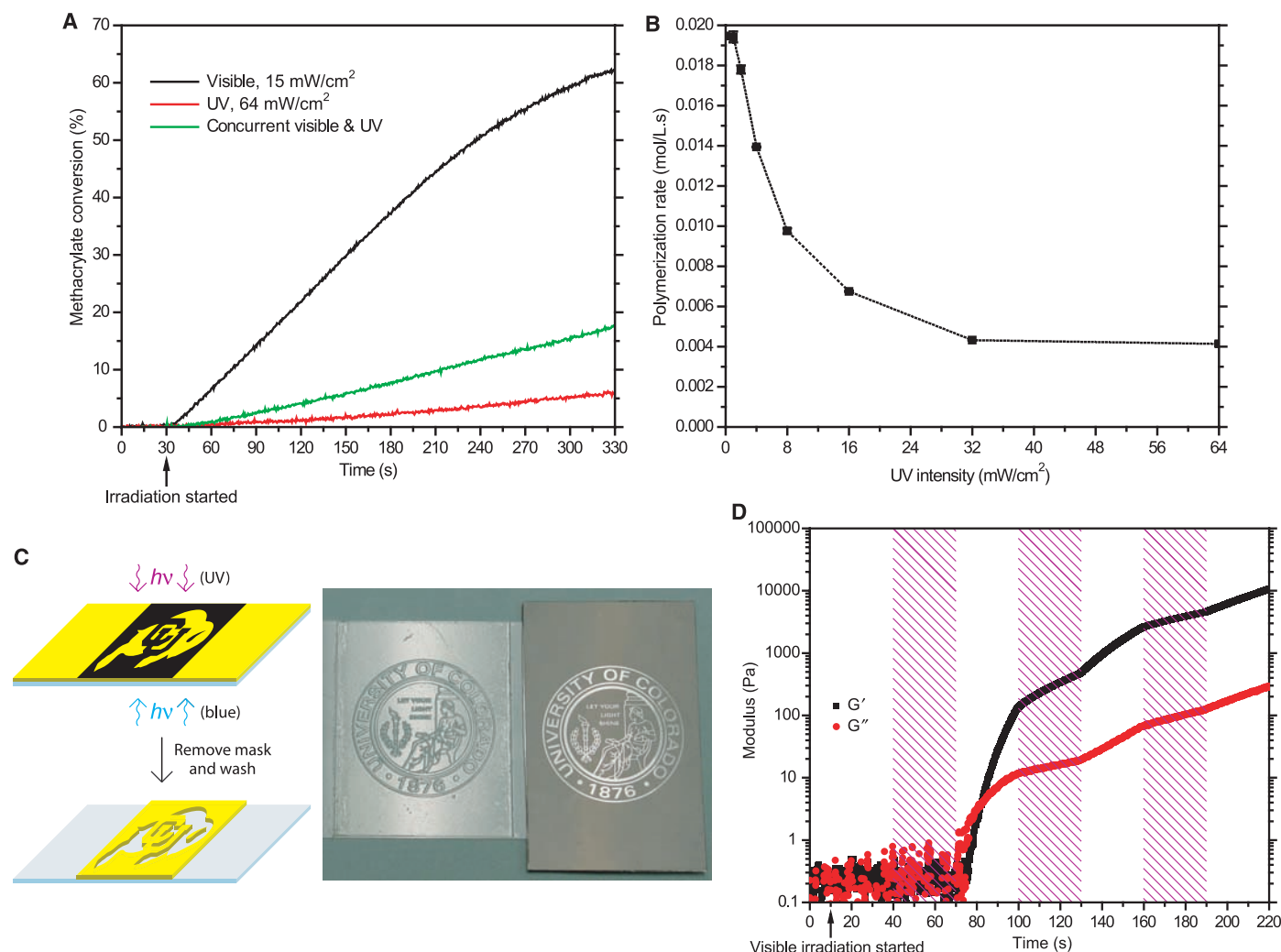


Fig. 3. Effect of photoinhibition on photopolymerization rate. **(A)** Methacrylate conversion profiles for formulated TEGDMA during irradiation. **(B)** Initial methacrylate polymerization rate versus UV irradiation intensity during visible irradiation (15 mW/cm²). **(C)** Schematic diagram of the photoinitiation-photoinhibition system using mask-based photolithography.

A sample produced by using the photoinitiation-photoinhibition system with the photomask used to pattern the photoinhibiting wavelength is also shown. **(D)** Elastic (G') and viscous (G'') moduli for formulated TEGDMA during constant visible (8 mW/cm²) and intermittent UV (64 mW/cm², indicated by the shaded regions) irradiation.

maintained regardless of intensity, the peak conversion occurring at the center of the focal point is independent of feature width.

The polymerized feature dimensions after removal of ungelled material via solvent wash depend on the degree of monomer conversion past the gelation threshold, as shown in Fig. 1C. Defining a normalized parameter, γ , which equals zero if the center of the feature is just at the conversion to reach gelation and conversely equals one if the entire intensity profile causes gelation, one can predict the polymer feature size for various initiation schemes as a function of peak conversion as shown in Fig. 1D. The one-photon curve defines the diffraction limit; note that this size limit is strongly dependent on the degree of conversion, as shown. The two-photon curve, shown at twice the one-photon wavelength because most two-photon photopolymerization studies are performed with Ti:sapphire lasers at about 800 nm that excite the third-order, nonlinear absorption of an ~ 400 -nm linear absorption, demonstrates that the feature size refinement resulting from two-photon absorption does not compensate for the longer irradiation wavelength. Both single- and two-photon absorption approaches suffer from an inherent trade-off between high conversion and feature size. Conversely, the two-color irradiation scheme used here maintains confinement even at extended irradiation times, enabling the fabrication of features possessing both small size and high, relatively uniform conversions through-

out the material; experimental confirmation of this confinement is presented in Materials and Methods.

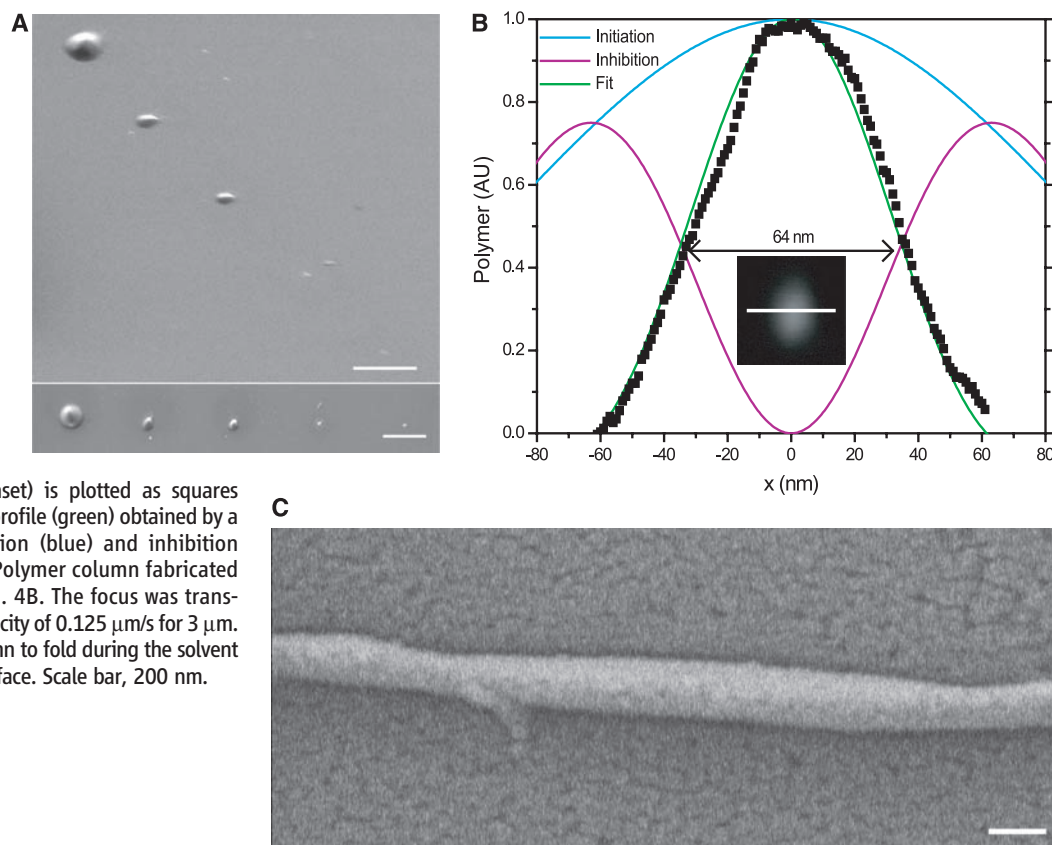
The monomer, photoinitiator, co-initiator, and photoinhibitor used in this study are shown in Fig. 2, A to D. The monomer, triethylene glycol dimethacrylate (TEGDMA), is readily polymerized to form a cross-linked, gelled polymer via a chain-growth, radical-mediated mechanism. Nonoverlapping absorption bands for the photoinitiator and photoinhibitor allow each of the two irradiating wavelengths to perform their role without encroaching on the role of the other wavelength. Thus, the camphorquinone (CQ)/ethyl 4-(dimethylamino)benzoate (EDAB) visible-light photoinitiation system was chosen in combination with the UV-active tetraethylthiuram disulfide photoinhibitor because camphorquinone does not absorb in the near-UV (Fig. 2E). Blue-light irradiation of TEGDMA formulated with CQ/EDAB and TED excites the photoinitiator (CQ) and initiates the polymerization via carbon-centered radicals, whereas irradiation with UV photocleaves the TED, producing sulfur-centered dithiocarbamyl (DTC) radicals (*16*) that recombine with propagating radicals, end-capping the polymer chain and terminating the polymerization.

Methacrylate conversion profiles during irradiation of the formulated TEGDMA were measured by using time-resolved Fourier transform infrared spectroscopy (Fig. 3A). Whereas the polymerization proceeds rapidly upon irradiation with visible light, UV irradiation generates a very

low polymerization rate, both in the presence and the absence of visible-light irradiation. Further, raising the UV intensity during co-irradiation of the resin with both visible and UV monotonically decreases the polymerization rate over the intensity range examined (Fig. 3, A and B), demonstrating effective photoinduced inhibition of the polymerization.

For this system to be translated to photolithography, the reduction in polymerization rate upon UV irradiation needs to be reflected in the time to gelation. The gel point occurs at a critical extent of reaction in a cross-linking system when a single macromolecule first spans the sample and the material transitions from a liquid to a cross-linked, insoluble gel (*17*). This point represents the conversion threshold where ungelled material is still soluble and is readily removed while gelled material remains. The time to gelation for the TEGDMA formulation, as determined by the $G'-G''$ crossover during parallel-plate rheometry of the material being cured in situ, increased from 50 s for visible irradiation (469 nm, 8 mW/cm²) to 255 s for simultaneous visible and UV co-irradiation (469 nm, 8 mW/cm² and 365 nm, 64 mW/cm², respectively). Delayed gelation occurred in regions simultaneously irradiated by visible and near-UV light, whereas gelation occurred more rapidly in regions irradiated exclusively with visible light, enabling facile discrimination between regions exposed to one or both wavelengths. A simple demonstration exploiting this contrast between gela-

Fig. 4. Scanning electron micrographs of polymerized features. **(A)** Voxels polymerized on a microscope slide using a 0.45-NA singlet lens and the coincident Gaussian blue/GL UV irradiation scheme, observed at 45° and normal to the slide surface. The blue power was held constant at 10 μ W while the UV was progressively increased. The UV power, from left to right, was 0, 1, 2.5, 10, and 100 μ W. The exposure time was 8 s for each dot. Scale bars, 10 μ m. **(B)** Profile of a voxel similarly fabricated but with 10 μ W of blue power and 110 μ W of UV focused at 1.3 NA, then imaged via SEM at normal incidence. The SEM intensity on the white line (inset) is plotted as squares against the expected polymerization profile (green) obtained by a double-parameter fit of the initiation (blue) and inhibition (violet) rate profiles, as shown. **(C)** Polymer column fabricated by using the same conditions as Fig. 4B. The focus was translated normal to the glass slide at a velocity of 0.125 μ m/s for 3 μ m. The high aspect ratio caused the column to fold during the solvent wash, leaving it lying on the glass surface. Scale bar, 200 nm.



tion times was performed by using a photo-mask lithographic approach as shown in Fig. 3C, where resin on a transparent substrate is irradiated uniformly through the substrate with the initiating wavelength while being irradiated by the inhibiting wavelength through a photo-mask. As a result, the masked region polymerizes and becomes insoluble, whereas the unmasked region remains liquid and is readily washed away.

The fabrication of complex, 3D microstructures requires that the doughnut of inhibiting radicals created spatially to refine the polymerization region be translated in conjunction with the writing spot without leaving a termination trail. This desired behavior in turn requires that the inhibiting species are rapidly eliminated in the absence of the photoinhibition irradiation wavelength. The rapid cessation of photoinhibition in the current system is demonstrated in Fig. 3D. During UV irradiation periods, the polymerization slowed dramatically, as evidenced by the reduced rate of increase in the storage and loss moduli; however, when the UV irradiation ceased, the polymerization rate underwent an immediate and marked increase.

To demonstrate that this polymerization rate control is useful to initiate polymerization below the optical diffraction limit, as predicted by Fig. 1D, we implemented the direct-write lithography scheme shown in Fig. 1A. Polymer voxels were created on a glass substrate and imaged by scanning electron microscopy (SEM) after solvent wash, as shown in Fig. 4A. As predicted in Fig. 1D, increasing the UV power, and therefore the photoinhibition rate, of the GL mode progressively reduces the voxel diameter in a controllable manner. In the sequence shown, the constant-power, 1.3- μm (full width to $1/e^2$) blue focus has written polymer voxels with diameter varying from 3.6 μm with no UV down to 200 nm for strong UV inhibition at 100 μW UV irradiation power. This resolution is typical of two-photon initiation using ~ 1.4 numerical aperture (NA) lenses (2, 5) with aberration-limited depth ranges of tens of μm ; the much lower NA demonstrated here enables mm-scale thicknesses. In Fig. 4B we show the ability to create 110-nm voxels full width and 65 nm full width at half maximum by using a 1.3-NA lens and measured by SEM, approaching the size of the smallest features produced with use of two-photon photopolymerization (6). Continuous writing under these conditions with the superimposed Gaussian/GL irradiation scheme is shown in Fig. 4C, resulting in lines of similar diameter. Reduction of voxel diameters using this irradiation scheme could be effected in other materials such as those containing reversibly photodimerizable functionalities, where dimers are created by irradiation at one wavelength and cleaved by irradiation at a different wavelength; however, photoreversibility precludes translation of a writing spot and disallows fabrication of dense, 3D structures.

Two-photon photopolymerization has been described as the only microprocessing approach

with intrinsic 3D fabrication capability (18). Although the optical approach demonstrated here produces confinement of the polymerized region along only two axes, manipulation of the photoinhibiting wavelength into a bottle beam profile (19) would induce confinement along the third axis, thus allowing fabrication of 3D structures with sub-100-nm isotropic resolution. Because single-photon absorption cross sections are often orders of magnitude larger than two-photon cross sections, this photoinitiation-photoinhibition system facilitates the use of inexpensive continuous wave (CW) diode lasers and very high write velocities. Thus, this single-photon approach to nanolithography uses dramatically cheaper hardware and scales to much higher throughput.

References and Notes

1. A. C. Sullivan, M. W. Grabowski, R. R. McLeod, *Appl. Opt.* **46**, 295 (2007).
2. S. Kawata, H.-B. Sun, T. Tanaka, K. Takada, *Nature* **412**, 697 (2001).
3. B. H. Cumpston *et al.*, *Nature* **398**, 51 (1999).
4. H.-B. Sun *et al.*, *Opt. Lett.* **25**, 1110 (2000).
5. T. Tanaka, H.-B. Sun, S. Kawata, *Appl. Phys. Lett.* **80**, 312 (2002).
6. W. Haske *et al.*, *Opt. Express* **15**, 3426 (2007).
7. N. C. Strandwitz *et al.*, *J. Am. Chem. Soc.* **130**, 8280 (2008).
8. K. Ichimura, M. Sakuragi, *J. Polym. Sci. Polym. Lett. Ed.* **26**, 185 (1988).
9. S.-K. Lee, D. C. Neckers, *Chem. Mater.* **3**, 852 (1991).

10. S.-K. Lee, D. C. Neckers, *Chem. Mater.* **3**, 858 (1991).
11. D. J. Lounnot, D. Ritzenthaler, C. Carre, J. P. Fouassier, *J. Appl. Phys.* **63**, 4841 (1988).
12. S. K. Soh, D. C. Sundberg, *J. Polym. Sci. Polym. Chem. Ed.* **20**, 1299 (1982).
13. G. Donnert *et al.*, *Proc. Natl. Acad. Sci. U.S.A.* **103**, 11440 (2006).
14. Materials and methods and a study examining the effect of exposure time on polymerized feature size are detailed in supporting material available on Science Online.
15. P. J. Flory, in *Principles of Polymer Chemistry* (Cornell Univ. Press, Ithaca, NY, 1953).
16. L. G. Lovell, B. J. Elliott, J. R. Brown, C. N. Bowman, *Polymer* **42**, 421 (2001).
17. F. Chambon, H. H. Winter, *J. Rheol.* **31**, 683 (1987).
18. H. B. Sun, S. Kawata, in *NMR - 3D Analysis - Photopolymerization* (Springer, Berlin, 2004), vol. 170, pp. 169–273.
19. J. Arit, M. J. Padgett, *Opt. Lett.* **25**, 191 (2000).
20. Supported by NSF programs IIP-0750506, IIP-0822695, and ECS-0636650, NIH grant DE10959, and the University of Colorado Innovative Seed Grant Program. A preliminary patent based on this technology has been filed by T.F.S., A.C.S., C.N.B., and R.R.M.

Supporting Online Material

www.sciencemag.org/cgi/content/full/1167610/DC1
Materials and Methods
Fig. S1
References

23 October 2008; accepted 24 March 2009
Published online 9 April 2009;
10.1126/science.1167610
Include this information when citing this paper.

Confining Light to Deep Subwavelength Dimensions to Enable Optical Nanopatterning

Trisha L. Andrew,¹ Hsin-Yu Tsai,^{2,3} Rajesh Menon^{3,4*}

In the past, the formation of microscale patterns in the far field by light has been diffractively limited in resolution to roughly half the wavelength of the radiation used. Here, we demonstrate lines with an average width of 36 nanometers (nm), about one-tenth the illuminating wavelength $\lambda_1 = 325$ nm, made by applying a film of thermally stable photochromic molecules above the photoresist. Simultaneous irradiation of a second wavelength, $\lambda_2 = 633$ nm, renders the film opaque to the writing beam except at nodal sites, which let through a spatially constrained segment of incident λ_1 light, allowing subdiffractional patterning. The same experiment also demonstrates a patterning of periodic lines whose widths are about one-tenth their period, which is far smaller than what has been thought to be lithographically possible.

Optical patterning is the primary enabler of microscale devices. However, the Achilles heel of optics is resolution. The far-field diffraction barrier limits the resolution of optical systems to approximately half

the wavelength (1) and therefore restricts nanoscale patterning at visible wavelengths. Scanning electron beam patterning has thus become the preferred method for fabricating nanostructures. However, electrons are affected by extraneous electromagnetic fields, limiting the accuracy with which patterns can be placed relative to one another (2). Furthermore, electron flux is limited by mutual repulsion effects, constraining the patterning speed (3). The vacuum environment and electron lenses increase system complexity and cost. Alternatively, the diffraction barrier can be overcome in the optical

¹Department of Chemistry, Massachusetts Institute of Technology (MIT), Cambridge, MA 02139, USA. ²Department of Electrical Engineering and Computer Science, MIT, Cambridge, MA 02139, USA. ³Research Laboratory of Electronics, MIT, Cambridge, MA 02139, USA. ⁴LumArray, Somerville, MA 02143, USA.

*To whom correspondence should be addressed. E-mail: rmenon@mit.edu

near field (4). The high spatial frequencies present in the optical near field are evanescent, and hence the recording medium needs to be placed at a precisely controlled nanometric distance from the source of the optical near field (5–7). By placing a prepatterned photomask in intimate contact with the photoresist, the optical near field may be recorded (8). In this case, high resolution is achieved at the expense of an inflexible and costly photomask and the high probability of contamination of the contacted surfaces. An alternative approach scans one or many nanoscale tips in close proximity to the sample (9). Precisely maintaining the gap between the tip (or tips) and the sample is problematic, especially when patterning over large areas or with multiple near-field probes (10). Plasmonic lenses can alleviate some of these problems (11), but they still require gaps of <100 nm and nanometric gap control (12, 13).

To overcome these limitations, we used a thin photochromic film on top of the recording photoresist layer. The molecules chosen to comprise the film adopt two isomeric forms that interconvert on respective absorptions of light at ultraviolet (λ_1) and visible (λ_2) wavelengths (14). We simultaneously applied both colors in an interference pattern that overlaps peaks at λ_1 with nodes at λ_2 . Absorption at λ_1 generates the isomer transparent at that wavelength, but regions exposed to λ_2 revert to the initial isomer and continue to absorb at λ_1 , protecting the photoresist. Only at the λ_2 nodes does a stable transparent aperture form (Fig. 1A) (15). Photons at λ_1 penetrate this aperture, forming a nanoscale writing beam that can pattern the underlying photoresist. The size of the aperture decreases as the ratio of the intensity at λ_2 with respect to that at λ_1 increases (15, 16). This technique, which we refer to as absorbance modulation, can therefore confine light to spatial dimensions far smaller than the wavelength.

Furthermore, because the photochromic molecules recover their initial opaque state, spatial periods smaller than the incident wavelengths can be achieved by repeated patterning (17). In Fig. 1B, we plot the simulated full width at half maximum (FWHM) of the transmitted light at λ_1 as a function of the ratio of intensities at the two wavelengths, illustrating that the transmitted light is spatially confined to dimensions far below the wavelength. In other words, optical near fields are generated without bringing a physical probe into close proximity with the sample. In the past, we used an interferometric setup to illuminate an azobenzene polymer-based photochromic film with a standing wave at λ_2 and uniform illumination at λ_1 (16). Although linewidths as small as $\lambda_1/4$ were demonstrated, the thermal instability of the azobenzene polymer as well as the nonnegligible sensitivity of the underlying photoresist to λ_2 prevented further scaling below 100 nm.

For optimum performance, it is essential that the photochromic molecules are thermally stable; otherwise, the size of the writing beam becomes dependent on the absolute intensities rather than their ratio alone. If the photochromic molecule in the transparent state is thermally unstable, then at low- λ_1 intensities the thermal back-reaction overwhelms the forward (opaque-to-transparent) reaction, essentially closing the aperture. The FWHM of the resulting

beam shows a minimum. This is illustrated in Fig. 1B, in which the photochromic parameters of 1,2-bis(5,5'-dimethyl-2,2'-bithiophen-yl)perfluorocyclopent-1-ene (compound **1**) (Fig. 1C) were assumed (18). A thermal rate constant of $5 \times 10^{-4} \text{ s}^{-1}$ was assumed for the dashed curve. The incident illumination is modeled as standing waves with a period of 350 nm ($\lambda_2 = 633 \text{ nm}$) and 170 nm ($\lambda_1 = 325 \text{ nm}$). Both curves were calculated by decreasing the peak

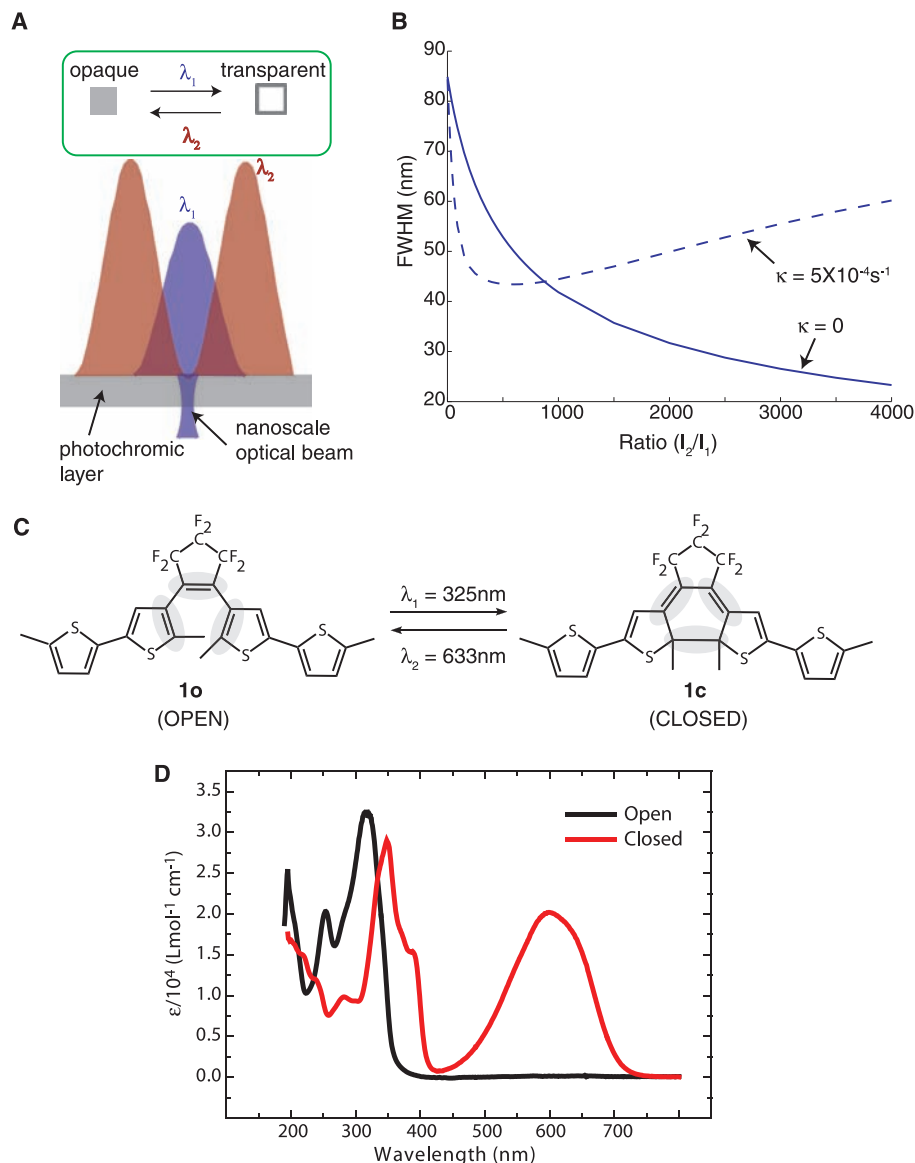


Fig. 1. The scheme of absorbance modulation. **(A)** The photochromic layer turns transparent upon exposure to λ_1 and opaque upon exposure to λ_2 . When illuminated with a node at λ_2 coincident with a peak at λ_1 , a subwavelength transparent region (or aperture) is formed through which photons at λ_1 penetrate, forming a nanoscale optical writing beam. **(B)** FWHM of the intensity distribution at λ_1 directly beneath the photochromic layer as a function of the ratio of the peak intensities at the two wavelengths. When the photochromic molecules are thermally stable [the thermal rate constant (κ) = 0], the size of the writing beam decreases monotonically, far below the wavelength. However, when a thermal instability is present ($\kappa = 5 \times 10^{-4} \text{ s}^{-1}$), the smallest beam size is limited, as shown by the dashed line. **(C)** Structures of the open- and closed-ring isomers of compound **1**. **(D)** Absorbance spectra of compound **1** in the open and closed forms in hexane. ϵ is the decadic molar absorptivity.

intensity of the λ_1 standing wave while maintaining the peak intensity of the λ_2 standing wave equal to 1 kW m^{-2} and repeating the numerical simulation for each intensity ratio. Although this deleterious effect can be overcome by using higher intensities at both wavelengths while maintaining the required intensity ratio, it is highly desirable to achieve nanoscale resolution at low intensities. For this reason, we turned our attention to thermally stable classes of photochromes, such as fulgides (19) and diarylethenes (20). In both of these classes of photochromes, photoinduced electrocyclic rearrangements transform a colorless (UV-absorbing) triene system into a highly colored cyclohexadiene photoproduct and vice versa. Because covalent bonds are either formed or broken during the photoisomerization process, conversion between the open-ring and closed-ring isomers is primarily photoinitiated, and the thermal contribution to this isomerization is negligible.

Initial investigations of furyl fulgide (21) as the active component in the absorbance-modulation layer (AML) revealed a susceptibility to photodegradation that significantly

reduced the concentration of this photochrome in the AML with prolonged irradiation. Cursory analysis of some fulgides reported in the chemical literature confirmed that many fulgides display a lack of fatigue resistance because of photooxidation of either their triene or heterocyclic moieties (19). Therefore, we explored a comparatively photostable class of thiophene-substituted fluorinated cyclopentenes as potential photochromes for absorbance modulation. The perfluorinated bridge in these systems prevents photooxidation of the active triene moiety and suppresses competing nonproductive isomerization pathways. Specifically, compound **1** (Fig. 1C) was chosen for use in the AML because it displayed an absorption band centered at 313 nm in the open state and one centered at 582 nm in the closed state (Fig. 1D). These spectral features allowed the use of the 325-nm line of the helium-cadmium laser and the 633-nm line of the helium-neon laser for the writing and the confining beams, respectively. High intensities could be applied at the nodal wavelength λ_2 because 633-nm light has no effect on most photoresists.

Pertinent photophysical constants, such as absorption coefficients and photoreaction quantum yields, were measured for compound **1** at room temperature in hexane solution [table S1 and supporting online material (SOM) text].

In order to spin-cast the photochromic layer, we used a 30 mg ml^{-1} solution of poly(methyl methacrylate) (PMMA) in anisole doped with 92 weight percent compound **1** (with respect to PMMA) (20). The photochromic layer was to be placed atop a photoresist layer in order to record the transmitted light at λ_1 . The solvent for the PMMA matrix, anisole, distorts the development rate of the photoresist. Therefore, a barrier layer of polyvinyl alcohol (PVA) was placed in between the two layers. The barrier layer also prevents any interdiffusion between the two layers. Because the high-spatial frequency content of the nanoscale writing beam is evanescent, it is important to keep the thickness of the PVA layer as small as possible.

In order to illustrate the effect of the thickness of the PVA layer on the linewidth of the pattern, we simulated the transmission of light through a subwavelength aperture in a metal

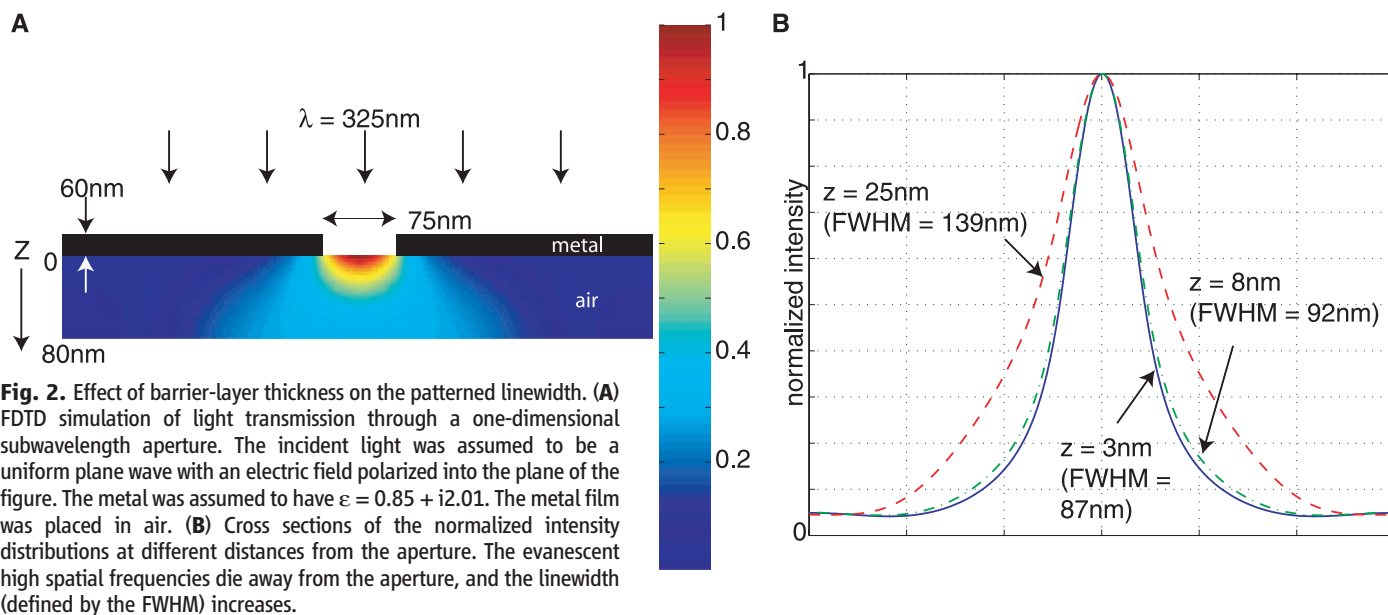
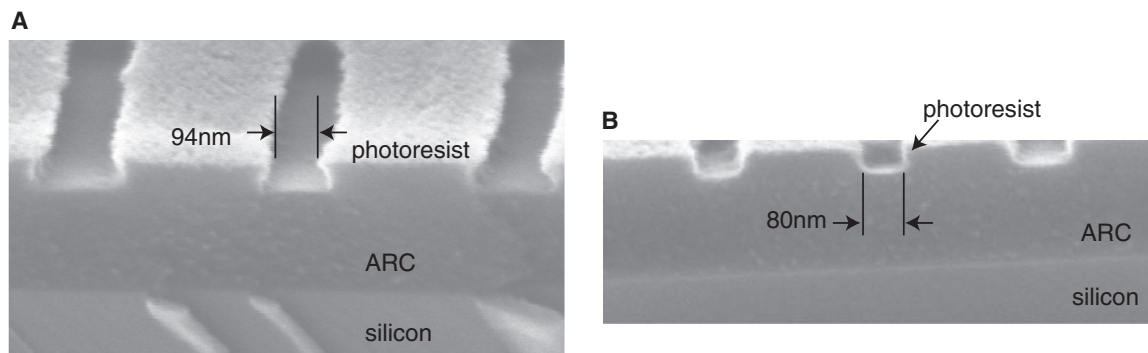


Fig. 3. Scanning electron micrographs of cross sections of exposed and developed lines in photoresist in which the PVA barrier layer thickness was (A) 25 nm and (B) 8 nm, respectively. The thinner the PVA layer is, the straighter is the resist sidewall and smaller is the exposed line. In both cases, the period of the lines is 350 nm, corresponding to the period of the λ_2 standing wave.



film using custom software that implements the finite-difference time-domain (FDTD) method (22). When a subwavelength aperture is illuminated, the transmitted light is primarily composed of evanescent high-spatial frequency components. These components decay exponentially away from the aperture, increasing the FWHM of the transmitted light. The illumination of a one-dimensional aperture with a width of 75 nm was simulated with a plane wave with a wavelength of 325 nm, as shown in the schematic in Fig. 2A. The electric field of the incident wave was polarized normal to the plane of the figure. The time-averaged intensity of the scattered light was calculated at steady state. Cross sections of the normalized intensity distribution in planes parallel to the aperture at varying distances from the aperture were computed and plotted in Fig. 2B. Clearly, the transmitted light is substantially broadened with distance from the aperture. Furthermore, the peak intensity at the center of the line also falls exponentially with distance from the aperture.

These theoretical predictions were qualitatively confirmed by our experimental results. Figure 3, A and B, shows scanning electron micrographs of the cross sections of exposed and developed photoresist with PVA barrier layer thicknesses of 25 nm and 8 nm, respectively. With the 25 nm layer, the exposed line exhibits considerable broadening with depth into the photoresist. The sidewall profile bears a qualitative resemblance to the intensity contours in Fig. 2A. With the thinner PVA, this linewidth broadening is noticeably curtailed, and the photoresist exhibits vertical sidewalls. This result also suggests that an ultrathin photoresist layer may be necessary to faithfully record the high spatial frequencies in the near field, which is in agreement with earlier work (23).

To minimize this effect of line broadening, we used a PVA film thickness of 8 nm, which was found to be sufficient to protect the photoresist from the solvent for the photochromic layer. Samples consisted of a silicon substrate spin-coated with 200 nm of anti-reflection coating, 200 nm of photoresist, 8 nm of PVA, and 410 nm of the photochromic layer. After exposure, the samples were rinsed in de-ionized water in a sonicator for about 5 min, which removed the PVA layer as well as the photochromic overlayer. The photoresist was baked on a hotplate at 120°C for 90 s and developed in 0.26 N tetramethyl ammonium hydroxide for 60 s. The resulting patterns were inspected in a scanning electron microscope after sputter-coating them with ~2 nm of a palladium/gold alloy.

The exposure system was a modified Lloyd's-mirror interferometer (fig. S5), consisting of a mirror at right angles to a vacuum chuck that held the sample. This configuration was illuminated at $\lambda_1 = 325$ nm and $\lambda_2 = 633$ nm. The angles of incidence of the two wavelengths were adjusted so that the resulting standing waves on the sample had periods of 350 nm at $\lambda_2 = 633$ nm and 170 nm at $\lambda_1 = 325$ nm (18). As illustrated in Fig. 4A, the nodes of the λ_2 standing wave approximately coincide with every other peak of the λ_1 standing wave. Photokinetic simulation using the extracted photochromic parameters reveal that the transmitted light at λ_1 is substantially narrower than the diffraction limit. The scanning electron micrograph in Fig. 4B shows that the average width of the lines recorded in the photoresist was 36 nm close to one tenth of λ_1 . Furthermore, the narrow lines were spaced by 350 nm, which corresponds to the period of the λ_2 standing wave. We separately confirmed that the photoresist is not sensitive to the λ_2 photons. Those λ_1 peaks that coincide with the

λ_2 peaks are suppressed beyond the photochromic layer. We confirmed this experimentally by recording lines at lower intensity ratios and examining their cross sections in the scanning electron microscope (fig. S6). In our current setup, in order to maintain high intensity in the λ_2 peaks, it was necessary to forgo spatial filtering of the λ_2 illumination. High-frequency noise therefore persisted in the λ_2 standing wave, causing line edge roughness as well as the line-width variation in the photoresist patterns. Nevertheless, these results clearly demonstrate the feasibility of deep subwavelength localization of light by using absorbance modulation.

Furthermore, these results also demonstrate the feasibility of patterning periodic lines far smaller than their spatial period. Because the absorbance of the AML is reversible, interspersed multiple exposures could pattern lines spaced apart by a distance far smaller than the far-field diffraction limit of the optical system. Although the current demonstration utilized one-dimensional standing waves, we anticipate straightforward extension to two-dimensional peaks and nodes, which can be generated with diffractive micro-optics (24, 25). Furthermore, such nanoscale optical beams may also be useful for optical nanoscopy (26).

References and Notes

1. E. Abbé, *Arch. Mikrosk. Anat. Entwicklungsmech.* **9**, 413 (1873).
2. K. Murooka, K. Hattori, O. Iizuka, *J. Vac. Sci. Technol. B* **21**, 2668 (2003).
3. R. F. W. Pease, *Microelectron. Eng.* **78**, 381 (2005).
4. E. A. Ash, G. Nichols, *Nature* **237**, 510 (1972).
5. E. Betzig, J. K. Trautman, T. D. Harris, J. S. Weiner, R. L. Kostelak, *Science* **251**, 1468 (1991).
6. L. Novotny, B. Hecht, D. Pohl, *Ultramicroscopy* **71**, 341 (1998).
7. H. G. Frey, F. Keilmann, A. Kriele, R. Guckenberger, *Appl. Phys. Lett.* **81**, 5030 (2002).
8. T. Ito et al., *Appl. Phys. Lett.* **89**, 033113 (2006).
9. X. Yin, N. Fang, X. Zhang, I. B. Martini, B. J. Schwartz, *Appl. Phys. Lett.* **81**, 3663 (2002).
10. A. Chovin, P. Garrigue, I. Manek-Höninger, N. Sojic, *Nano Lett.* **4**, 1965 (2004).
11. E. Ozbay, *Science* **311**, 189 (2006).
12. N. Fang, H. Lee, C. Sun, X. Zhang, *Science* **308**, 534 (2005).
13. Z. Jacob, L. V. Alekseyev, E. Narimanov, *Opt. Exp.* **14**, 8247 (2006).
14. J. C. Crano, R. J. Gugliemetti, Eds., *Organic Photochromic and Thermochromic Compounds* (Plenum, New York, 1999).
15. R. Menon, H. I. Smith, *J. Opt. Soc. Am. A* **23**, 2290 (2006).
16. R. Menon, R. H.-Y. Tsai, S. W. Thomas, *Phys. Rev. Lett.* **98**, 043905 (2007).
17. H.-Y. Tsai, G. M. Wallraff, R. Menon, *Appl. Phys. Lett.* **91**, 094103 (2007).
18. Materials and methods are available as supporting material on Science Online.
19. Y. Yokoyama, *Chem. Rev.* **100**, 1717 (2000).
20. M. Irie, *Chem. Rev.* **100**, 1685 (2000).
21. P. J. Darcy, H. G. Heller, P. J. Strydom, J. Whittall, *J. Chem. Soc. Perkin Trans. 1*, 202 (1981).
22. A. Taflov, S. C. Hagness, *Computational Electrodynamics: the Finite-Difference Time-Domain Method* (Artech House, Boston, 2000).
23. T. Ito et al., *Appl. Phys. Lett.* **89**, 033113 (2006).
24. R. Menon, H.-Y. Tsai, P. Rogge, *J. Opt. Soc. Am. A* **26**, 297 (2009).

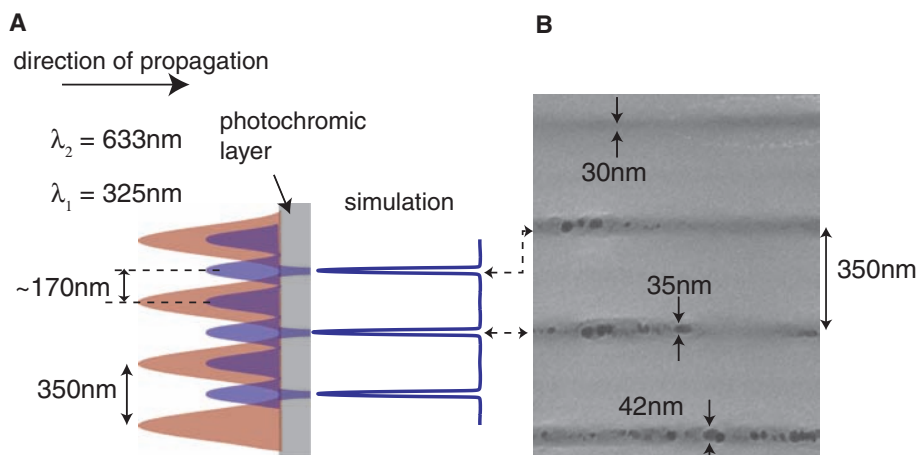


Fig. 4. Deep subwavelength patterning using absorbance modulation. (A) The photochromic layer is illuminated by two overlapping standing waves with periods of 350 nm ($\lambda_2 = 633$ nm) and 170 nm ($\lambda_1 = 325$ nm), respectively. Simulating the transmitted light at λ_1 supported narrow lines where the peaks of the λ_1 standing wave coincided with the nodes of the λ_2 standing wave. (B) Scanning electron micrograph of lines exposed in photoresist. Although the photoresist is underexposed, the lines represent a recording of the aerial image that is consistent with simulation.

25. H.-Y. Tsai, H. I. Smith, R. Menon, *Opt. Lett.* **33**, 2916 (2008).
26. S. W. Hell, *Nat. Biotechnol.* **21**, 1347 (2003).
27. We thank F. Stellacci and T. Swager for advice on synthesis of the photochromic molecules, H. Koh for the ellipsometric measurements, T. O'Reilly for assistance with the Lloyd's-mirror interferometer, and H. Smith for suggestions on the manuscript. T.L.A. was partially funded by a subcontract (6916866) from LumArray. H.-Y.T. was partially funded by an ignition grant from the MIT

Deshpande Center for Technological Innovation. R.M. was partially funded by a Defense Advanced Research Projects Agency Small Business Innovation Research award (W31P4Q-05-C-R156). Three patents have been filed through MIT based on the work presented herein.

Supporting Online Material

www.sciencemag.org/cgi/content/full/1167704/DC1
Materials and Methods

SOM Text
Figs. S1 to S6
Table S1
References

27 October 2008; accepted 24 February 2009
Published online 9 April 2009;
10.1126/science.1167704
Include this information when citing this paper.

Size and Shape of Saturn's Moon Titan

Howard A. Zebker,^{1*} Bryan Stiles,² Scott Hensley,² Ralph Lorenz,³
Randolph L. Kirk,⁴ Jonathan Lunine⁵

Cassini observations show that Saturn's moon Titan is slightly oblate. A fourth-order spherical harmonic expansion yields north polar, south polar, and mean equatorial radii of 2574.32 ± 0.05 kilometers (km), 2574.36 ± 0.03 km, and 2574.91 ± 0.11 km, respectively; its mean radius is 2574.73 ± 0.09 km. Titan's shape approximates a hydrostatic, synchronously rotating triaxial ellipsoid but is best fit by such a body orbiting closer to Saturn than Titan presently does. Titan's lack of high relief implies that most—but not all—of the surface features observed with the Cassini imaging subsystem and synthetic aperture radar are uncorrelated with topography and elevation. Titan's depressed polar radii suggest that a constant geopotential hydrocarbon table could explain the confinement of the hydrocarbon lakes to high latitudes.

The Cassini spacecraft has been orbiting Saturn for 4 years, observing Titan periodically. When close to Titan, it can return surface elevation data from a nadir-pointing radar altimeter (1) and a multiple-beam synthetic aperture radar (SAR) imaging system (2, 3). We have used these radar instrument modes to estimate the surface elevation by measuring the time delay of the altimeter echoes and the precise radar look angle to points on the surface by processing the multibeam SAR images with monopulse methods (Fig. 1) (4).

In the radar altimeter mode, the instrument transmits energy nearly vertically to the planetary surface below and records the received echo as a function of time; we corrected the data for biases due to mis-pointing errors (1). The Cassini altimetry data products record both the leading-edge location and the average delay of the return echo, but we used the mean return in order to estimate the mean surface height.

The SAR imaging system on Cassini comprises five parallel beams that produce a much wider ground swath than would have been possible with the use of a single beam. Each beam

is time-shared in order to maintain a contiguous swath on the ground (5, 6), so we sacrificed along-track resolution, averaging, and signal-to-noise ratio for the sake of the increased swath width. This is the burst-mode or ScanSAR imaging configuration, and it returns five overlapping obser-

vation swaths from the surface. The differencing of power images from the overlapped sections of adjacent beams forms an amplitude monopulse system to measure the precise angle to a given point on the ground (4, 7), which, combined with knowledge of the spacecraft imaging geometry, yields a surface height measurement. Hence, under this analysis, most of the SAR imaging passes also provide estimates of the elevation at the beam overlap regions. Although this method is more elaborate than altimetry, it provides wider coverage because SAR imaging is used more often. We used all possible beam overlaps containing pixels sufficiently bright that the intensity differences were meaningful. The effective footprint of each measurement is roughly the SAR resolution (0.5 km) in the range direction and 10 km in the along-track direction.

These techniques show that the poles of Titan lie at lower elevations than the equator and that the topography also varies longitudinally (Fig. 1). Measurements in the polar regions yield elevations of about -600 to -700 m, referenced to a 2575-km-radius sphere, whereas Titan's

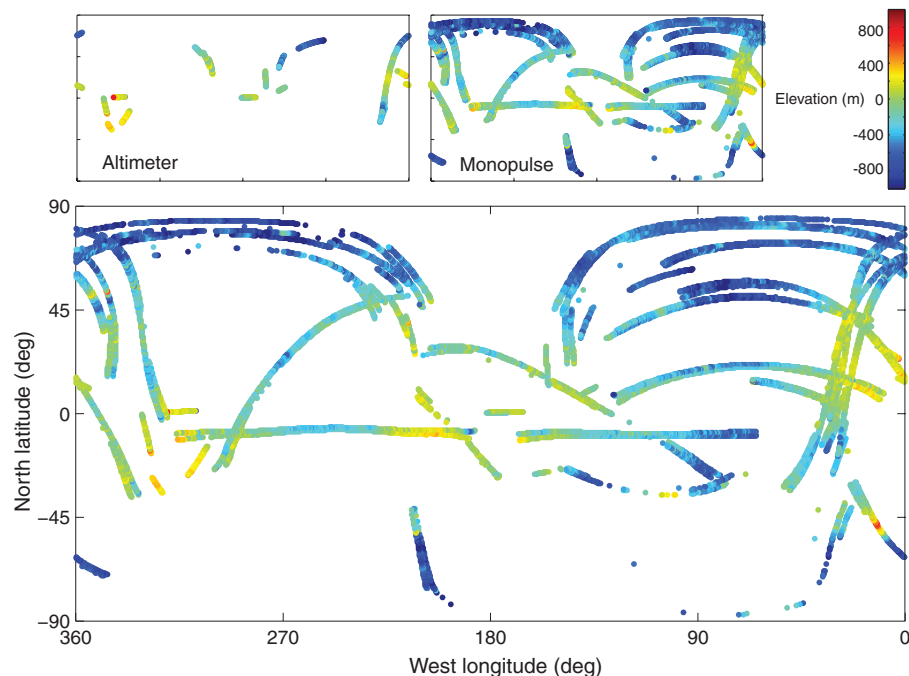


Fig. 1. Titan elevations observed with altimeter and SAR monopulse radar modes, cylindrical projection, displayed as deviation from an ideal 2575 km sphere located at Titan's barycenter. Locations on the figure give the latitude and west longitude of each measurement. Far more coverage is available from the monopulse mode than from altimetry, but these data are not as accurate as the altimeter measurements.

¹Departments of Geophysics and Electrical Engineering, Stanford University, Stanford, CA 94305, USA. ²Jet Propulsion Laboratory (JPL), California Institute of Technology, 4800 Oak Grove Drive, Pasadena, CA 91109, USA. ³Applied Physics Laboratory, Johns Hopkins University, 11100 Johns Hopkins Road, Laurel, MD 20723, USA. ⁴U.S. Geological Survey, 2255 North Gemini Drive, Flagstaff, AZ 86001, USA. ⁵Departments of Planetary Science and Physics, University of Arizona, Tucson, AZ 85721, USA.

*To whom correspondence should be addressed. E-mail: zebker@stanford.edu

highest areas approach +400 m. Errors in both the altimetry and monopulse data depend mainly on ephemeris accuracy and spacecraft pointing control (1, 7). The Cassini orbit reconstructions we used (8, 9) are accurate at the 10- to several-hundred-meter level, with the out-of-plane com-

Table 1. Best-fit surfaces to Titan elevation data. The ellipsoid axis *a* is the long axis pointing to Saturn, *c* is the polar axis, and *b* is the orthogonal equatorial axis. All results are in kilometers, except for rotations, which are in degrees.

	Ellipsoids			Spherical harmonics
	Sphere	Biaxial	Triaxial	Order 4
<i>a</i> axis	2574.97 ± 0.01	2575.06 ± 0.01	2575.15 ± 0.02	
<i>b</i> axis	2574.97 ± 0.01	2575.06 ± 0.01	2574.78 ± 0.06	
<i>c</i> axis	2574.97 ± 0.01	2574.51 ± 0.05	2574.47 ± 0.06	
<i>a</i> translation	0.03 ± 0.01	0.04 ± 0.02	0.06 ± 0.02	
<i>b</i> translation	0.30 ± 0.02	0.35 ± 0.02	0.39 ± 0.03	
<i>c</i> translation	−0.26 ± 0.02	−0.06 ± 0.03	−0.02 ± 0.03	
<i>a</i> axis rotation		−5.9° ± 2.6°	−16.2° ± 5.3°	
<i>b</i> axis rotation		0.9° ± 2.3°	4.6° ± 1.8°	
<i>c</i> axis rotation			0.9° ± 3.7°	
North polar radius	2574.71 ± 0.02	2574.46 ± 0.06	2574.47 ± 0.07	2574.32 ± 0.05
South polar radius	2575.23 ± 0.02	2574.58 ± 0.06	2574.52 ± 0.07	2574.36 ± 0.03
Mean equatorial radius	2574.97 ± 0.01	2575.05 ± 0.01	2574.95 ± 0.06	2574.91 ± 0.11
Mean radius				2574.73 ± 0.09
Data RMS misfit	0.32	0.28	0.26	0.19

Fig. 2. (A) Best-fit translated, rotated, triaxial ellipsoid. Measurements are plotted on top of the ellipsoid, exhibiting contrast where they differ from the solution. Color indicates elevation relative to a 2575 km reference sphere at Titan’s barycenter. Data plotted using a Mollweide projection to convey the areas associated with elevation features. (B) Fourth-order spherical harmonic fit to elevation data, using same conventions.

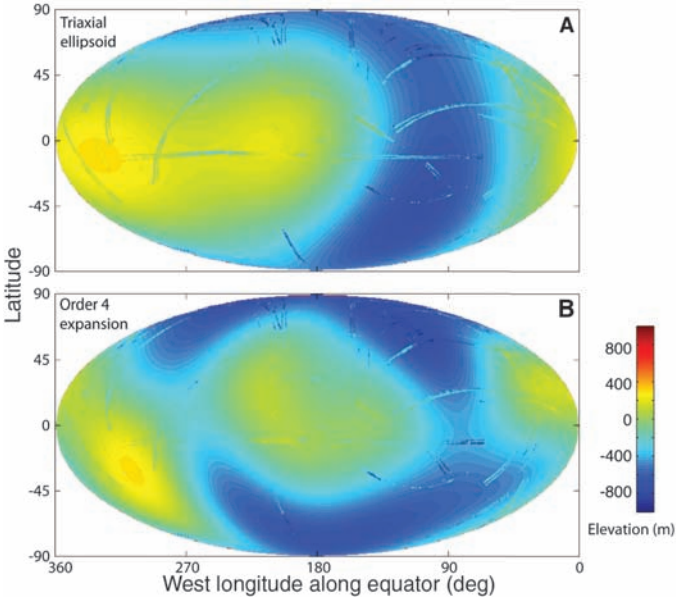


Table 2. Triaxial ellipsoid in synchronous rotation. The present value of q ($\omega^2 R^3/GM$) = 0.00003957. Calculated values are from first-order equations (23), with homogeneity parameter (H) = 1 for the homogeneous case and $H = 0.56$ for a layered Titan, assuming a mantle density of 0.9 g cm^{−3}.

Observed	Calculated, homogeneous Titan		Calculated, layered Titan	
	<i>q</i> (at present)	<i>q</i> ' = <i>q</i> × 1.25	<i>q</i> (at present)	<i>q</i> ' = <i>q</i> × 2.23
Equatorial radius toward Saturn (<i>a</i>)	2575.15 ± 0.02	2575.10	2575.17	2575.17
Orthogonal equatorial radius (<i>b</i>)	2574.78 ± 0.06	2574.72	2574.69	2574.69
Polar radius (<i>c</i>)	2574.47 ± 0.06	2574.59	2574.53	2574.53
RMS error (observed versus calculated)		0.08	0.06	0.16

ponent being most uncertain; pointing uncertainty leads to another 50 to 100 m for both data sets. Absolute errors up to 400 m are not uncommon on a point-by-point basis, because SAR monopulse measurements depend critically on pointing knowledge. We applied a network adjustment to reduce these raw errors by about a factor of 2 (7). We calculated formal errors in all of our solutions and found that for the low-order harmonic and ellipsoid solutions, errors ranged from 10 to 110 m (10), because we retrieved very few parameters in our inversion procedure, and we have 18 altimeter and 24 monopulse uncorrelated radar acquisition tracks. These uncertainties do not reflect systematic errors, such as any unknown degradation in the satellite ephemeris reconstruction on passes that diverge from the ecliptic plane, so that polar elevations may be systematically higher or lower because of errors in satellite position. A detailed description of the error analysis is given in the supporting online material (SOM).

We used the data described above to estimate the global shape of Titan. We fit the observations to ellipsoids and to low-order spherical harmonic series to examine the global properties of the inferred shape. Both sets of solutions gave similar estimates for polar and equatorial radii but differed in the exact body shape we inferred. Because the data are relatively sparse, and particularly lacking in the far southern hemisphere, harmonic expansions tend to be highly oscillatory and error-prone for this region. Therefore, we used constrained inversion methods to discard the unlikely solutions that yet fit the data at the measured locations (7). We required the solution to be nearly spherical and selected the degree of constraint by examining the error in the data-sparse south polar region, picking its least value that still allowed matching this subset of observations. To find the reference sphere size, we iterated the solution until its mean radius was equal to the constraint radius.

We determined the best-fitting, translated, and rotated sphere, biaxial ellipsoid, and triaxial ellipsoid by minimizing the root mean square (RMS) difference between the observations and each solution, weighted by the uncertainty in the observations (Table 1) (11). The misfit of the solution ranges from 190 to 360 m RMS, showing that more degrees of freedom in the model lead to a better fit. The ellipsoid parameters follow from combinations of all data points and thus exhibit far less uncertainty than an individual elevation measurement. We used a diagonal approximation to the data covariance matrix, justifiable because the data collected on different passes are generally uncorrelated. For the ellipsoid solutions, the poles are of lower elevation than the equator; in the triaxial case, a local maximum occurs at about 330°W longitude (Fig. 2A).

The spherical harmonic fits also show that the poles are low and the equator is high (Fig. 2B). The details of the solutions are different but the general shape is maintained. In this fourth-

order solution, a maximum occurs at 25°S, 305°W; other high-elevation regions can be found between ±45°N and 120° to 240°W. Spherical harmonics with other order expansions have a different elevation distribution but preserve the polar and mean equatorial values as seen above (Table 1; complete solutions up to the seventh order are given in the SOM).

The north and south polar radii are similar and agree within the formal errors for our solutions. The mean equatorial radius is very close to 2575 km. The ellipsoidal fits also show an offset between the center of figure and the center of mass, mainly in the along-orbit direction, of about 300 to 400 m. Although this could be a physical effect, it can also result from a non-ellipsoidal Titan figure or even systematic spacecraft ephemeris errors.

We compared our measurements of Titan to those predicted from a uniform, synchronously rotating, triaxial spheroid model in hydrostatic equilibrium (Table 2). Our fit yields an equatorial bulge $a-c$ of 0.68 km and an equatorial asymmetry $a-b$ of 0.37 km, approximating the expected shape of an ellipsoid in synchronous rotation (12). The RMS misfit of the three observed ellipsoid radii to the theoretical homogeneous planet case is 0.08 km, and the fit can be made even closer (0.06 km) if we increase the ratio of centrifugal to gravitational acceleration at the satellite surface (q) ($\omega^2 R^3/GM$) (12) by 25% (ω , rotation rate; R , radius; G , gravitational constant; M , mass of Titan).

On the basis of thermal modeling (13, 14) and measurements of changes in rotation rate, and by analogy with other large satellites, we expect Titan to have differentiated into a rock-rich, or possibly rock-iron, core with an outer ice/water mantle on the order of 100 km thick and crust that is less dense ($\sim 0.9 \text{ g cm}^{-3}$) than the global average density (1.88 g cm^{-3}). Under these conditions, q must be 2.23 times greater to minimize the misfit, implying that Titan's orbital radius was perhaps 77% of its present value when its shape was set. "Frozen-in" shapes from previous rotational states have been suggested for Earth, the Moon, Mars, and most recently for Iapetus (15). Although it may be unlikely

that tidal dissipation in Saturn is responsible for any migration of Titan's orbit, other mechanisms are possible, analogous perhaps to the proposed expansion of giant-planet orbits around the Sun by planetesimal scattering (16). Titan's observed shape is more consistent with a body orbiting closer to Saturn.

Despite the closeness of fit of our observations to the triaxial ellipsoid just described, the ratio $(b-c)/(a-c)$ for our data is 0.46 rather than the theoretical 0.25. Given our uncertainties, it is possible but not particularly likely that this ratio is 0.3 or even less, so that Titan may indeed be in hydrostatic equilibrium. Still, we cannot conclusively state that Titan is a synchronously rotating hydrostatic body.

Titan's geomorphology shows that substantial masses of surface material, in the form of polar lakes of liquid hydrocarbons or the equatorial dune sands, can be transported over global distance scales perhaps more quickly than the internal structure can adjust to changing loads (17, 18). Although both dunes and lakes appear to be active today, we cannot say whether enough mass can be moved on time scales sufficiently short to lead to a shape inconsistent with Titan's present orbit. It is also possible, as has been proposed for Europa (19), that topography can result from uneven heating of the icy shell. If heating is greater at the poles than the equator, an apparent equatorial bulge is produced.

We plotted the fifth-order global elevation solution over an image mosaic derived from the Cassini imaging subsystem (20) in order to examine relationships between observed image features and elevation (Fig. 3). Xanadu (21) is the most prominent surface region and was long speculated to be elevated. The optical and radar images indicate that it is a very rough, mountainous terrain, but its regional elevation is low. Other large-scale surface features do not appear to be correlated with elevation in our solutions.

These global elevation solutions may help in understanding the distribution of the Titan lakes. The lakes occur mainly in the polar regions (22), with a preference for the north polar area in the data collected to date by Cassini. If we posit that the lakes are surface expressions of a

more or less continuous liquid organic "water table," then the lower elevations of the poles could lead to the observed preponderance of lakes at high latitudes. However, whether the polar surface intersects a methane table depends on its distance from a constant gravity potential surface, and not on its elevation from the barycenter, because the equipotential may be depressed as well at the poles.

References and Notes

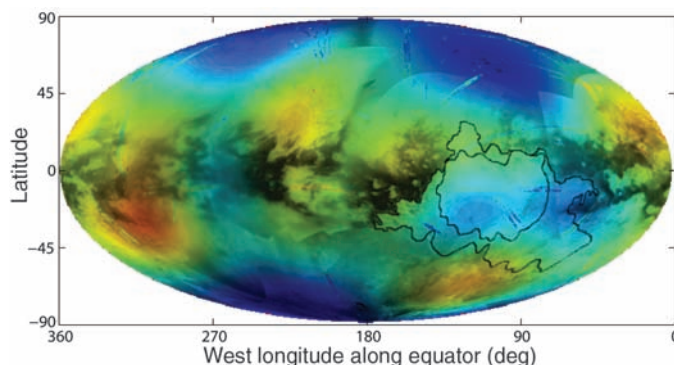
1. H. A. Zebker *et al.*, *Icarus* **200**, 240 (2009).
2. B. W. Stiles *et al.*, *Icarus*, 10.1016/j.icarus.2009.03.032 (2009).
3. C. Elachi *et al.*, *Science* **308**, 970 (2005).
4. D. R. Rhodes, *Introduction to Monopulse* (McGraw Hill, New York, 1959; reprinted by Artech House, Norwood, MA, 1980).
5. R. K. Moore, J. P. Claassen, Y. H. Lin, *IEEE Trans. Aero. Elec. Sys.* **AES-17**, 410 (1981).
6. C. Elachi *et al.*, *Proc. IEEE* **79**, 867 (1991).
7. See SOM on Science Online.
8. P. G. Antreasian *et al.*, American Astronomical Society (AAS) paper 2008-6747, presented at the American Institute of Aeronautics and Astronautics/AAS Astrodynamics Specialist Conference and Exhibit, Honolulu, HI, 18 to 21 August 2008.
9. The ephemeris we used was the JPL Cassini orbit solution as of October 2008.
10. The errors on each measurement are well known and range from tens of meters for the altimetry measurements to hundreds of meters for the SAR monopulse data (1, 8, 9) (SOM). The correlations in time for the spacecraft pointing and attitude knowledge errors, which dominate all of our observations, are less well known. We conservatively assumed that these errors are perfectly correlated along each pass (a constant attitude error) and uncorrelated between passes. We calculated formal errors using a diagonal approximation to the covariance matrix, subject to the assumption of correlated pointing errors for each acquisition.
11. The planetary radii given in Table 1 and elsewhere in the text are the distances from the specified location to the barycenter of Titan. The radii do not equal the corresponding ellipsoid axes if the best-fit ellipsoid is offset from the barycenter.
12. S. F. Dermott, *Icarus* **37**, 310 (1979).
13. A. D. Fortes *et al.*, *Icarus* **188**, 139 (2007).
14. G. Tobie, J. I. Lunine, C. Sotin, *Nature* **440**, 61 (2006).
15. J. C. Castillo-Rogez *et al.*, *Icarus* **190**, 179 (2007).
16. K. Tsiganis *et al.*, *Nature* **435**, 459 (2005).
17. G. Mitri *et al.*, *Icarus* **186**, 385 (2007).
18. J. W. Barnes *et al.*, *Icarus* **195**, 400 (2008).
19. G. W. Ojakangas, D. J. Stevenson, *Icarus* **81**, 220 (1989).
20. S. Albers, map of Titan derived from images at the Cassini Project Web site <http://saturn.jpl.nasa.gov>, available at <http://laps.noaa.gov/albers/sos/sos.html>.
21. C. C. Porco *et al.*, *Nature* **434**, 159 (2005).
22. E. R. Stofan *et al.*, *Nature* **445**, 61 (2007).
23. S. F. Dermott, *Icarus* **73**, 25 (1988).
24. We thank the Cassini Radar Team for detailed planning of these observations. This work was supported by the Cassini Project and by NASA as part of the Cassini Data Analysis Program. We also thank the reviewers for many constructive comments on our error analysis and data interpretation. The Cassini Project is a joint endeavor of NASA, the European Space Agency, and the Italian Space Agency. Cassini is managed by JPL, California Institute of Technology, under a contract with NASA.

Supporting Online Material

www.sciencemag.org/cgi/content/full/1168905/DC1
Materials and Methods
Figs. S1 to S4
Tables S1 to S3
References

24 November 2008; accepted 20 March 2009
Published online 2 April 2009;
10.1126/science.1168905
Include this information when citing this paper.

Fig. 3. Fifth-order solution (color) plotted over Cassini imaging mosaic of Titan surface. The outlined feature slightly south of the equator and west of 90° W is Xanadu, the largest identified region on Titan and believed to be a mountainous terrain. Two black outlines are shown. The inner region is the brightest portion of Xanadu, and the outer line denotes an extended Xanadu including less-dark but otherwise texturally similar material. Xanadu seems to be systematically lower than other parts of the equatorial belt, and not uplifted like most mountainous areas on Earth.



Observing the Quantization of Zero Mass Carriers in Graphene

David L. Miller,^{1*} Kevin D. Kubista,^{1*} Gregory M. Rutter,² Ming Ruan,¹ Walt A. de Heer,¹ Phillip N. First,^{1†} Joseph A. Stroscio^{2†}

Application of a magnetic field to conductors causes the charge carriers to circulate in cyclotron orbits with quantized energies called Landau levels (LLs). These are equally spaced in normal metals and two-dimensional electron gases. In graphene, however, the charge carrier velocity is independent of their energy (like massless photons). Consequently, the LL energies are not equally spaced and include a characteristic zero-energy state (the $n = 0$ LL). With the use of scanning tunneling spectroscopy of graphene grown on silicon carbide, we directly observed the discrete, non-equally-spaced energy-level spectrum of LLs, including the hallmark zero-energy state of graphene. We also detected characteristic magneto-oscillations in the tunneling conductance and mapped the electrostatic potential of graphene by measuring spatial variations in the energy of the $n = 0$ LL.

The two-dimensional (2D) form of carbon (i.e., graphene) is of interest not only because of its potential in nanoelectronics (1, 2), but also because it displays several intriguing fundamental properties. One of these, the half-integer quantum Hall effect (QHE) (3, 4), results from the symmetry of graphene's honeycomb crystal structure, which can be viewed as two equivalent hexagonal sublattices of carbon atoms. The same symmetry gives rise to unusual Landau levels (LLs) that are not equally spaced in energy but vary with both the square root of the magnetic field and the Landau index. This new LL spectrum, with its characteristic zero-

energy state (LL index $n = 0$) is emblematic of graphene and contains information unavailable in QHE measurements. Recent LL spectra acquired on the surface of graphite are complex and have been interpreted as being dominated by graphitic stacking through several layers (5) or as a mixture of a Dirac-fermion spectrum and the spectrum of bulk graphite (6). Similar measurements for single layer graphene samples have yet to be reported, in part because of the small sample sizes obtained in the exfoliation technique. Indirect measurement of the graphene LL structure have been obtained by measuring the transitions between LLs through the use of cyclotron resonance (7, 8).

In this report, we present scanning tunneling spectroscopy (STS) measurements of the graphene Landau quantization in samples grown on SiC. These experiments are free of the complications of previous studies because the graphene layers grown on SiC are electronically decoupled (9).

We demonstrate an innovative STS measurement technique with tunneling magneto-conductance oscillations (TMCOs). These magneto-oscillations are distinctly different from traditional Shubnikov-de Haas oscillations (SdHOs) in transport measurements, as they measure the band structure properties at a variable tunneling energy rather than a single energy at the Fermi surface. Using the TMCO measurements, we map the low-energy dispersion of graphene with an energy resolution of 2.8 meV, and we extend these measurements of energy versus momentum into the empty electronic states that are inaccessible to photoelectron spectroscopy. A fundamental characteristic of quantized cyclotron orbits in graphene is the $n = 0$ LL (LL_0) made up of both electron and hole carriers and located at exactly E_D , the energy of the Dirac (charge neutrality) point. We determined the local electrostatic potential of graphene on SiC with atomic scale resolution by spatially mapping the variation in LL_0 . We find the spatial variation of the local potential to be smoother than previously observed in exfoliated graphene on SiO_2 substrates (10, 11).

The experiments were performed at 4.3 K in a custom-built cryogenic ultrahigh vacuum scanning tunneling microscope (STM) with high-magnetic-field capability. Multiple layers of graphene were grown on the hydrogen-etched carbon-face of 4H-SiC(0001), via a low-vacuum induction furnace method (12), to a thickness of 10 ± 1 layers, as determined by ellipsometry (13). TMCO measurements, described below, were performed by sweeping the magnetic field at 0.04 T/min and measuring dI/dV with a lock-in amplifier at constant tunneling current and sample bias. dI/dV spectra as a function of tunneling bias were recorded in constant magnetic field with the tip-sample distance held fixed and using a root

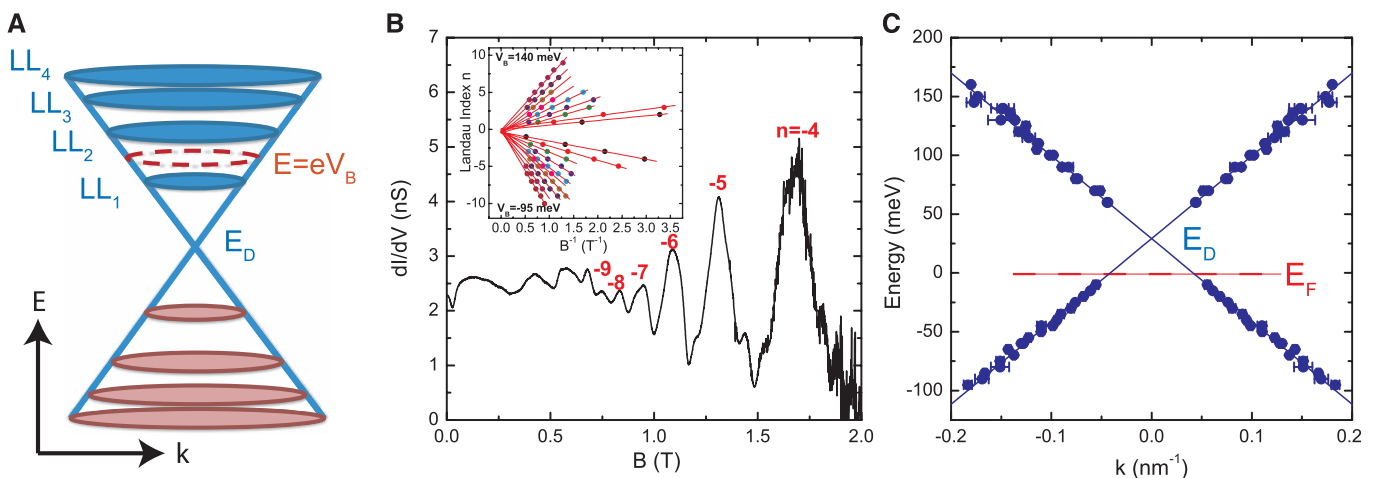


Fig. 1. TMCOs in epitaxial graphene. **(A)** Schematic of graphene low-energy dispersion with quantized LLs (LL_n) in a magnetic field. The Dirac point E_D locates the common apex of the electron and hole cones. The red dashed line indicates the k -space area A_E corresponding to a dI/dV measurement at the set-point energy $E = eV_B$. **(B)** TMCOs in dI/dV ($E = -65$ meV) as the magnetic field is swept perpendicular to the graphene plane. The largest oscillations originate from the LLs sweeping through the energy E . (Inset) Fan plot showing a linear

relation in the LL index n from the conductance oscillations versus $1/B$, yielding the TMCO frequencies B_E . The error in the peak positions is smaller than the symbol size, and each line corresponds to a separate TMCO measurement at different tunneling biases from -95 to 140 mV [see fig. S1 (13)]. **(C)** The energy-momentum dispersion (symmetrized about $k = 0$) obtained from the TMCO frequencies B_E . A linear fit yields a carrier velocity $c^* = (1.070 \pm 0.006) \times 10^6$ ms⁻¹ and a Dirac point location of $E_D = 29.7 \pm 0.5$ meV above E_F (20).

mean square modulation voltage of 1 mV superimposed on the sample bias at a frequency of 500 Hz. These two methods are complementary, as they each measure a dI/dV slice in the 2D magnetic field, energy (B , E) plane at either fixed E (TMCO spectra) or fixed B [conventional $dI/dV(E)$ spectra].

A schematic of the low-energy electronic structure for graphene (Fig. 1A) shows the two symmetric Dirac cones that meet at the Dirac point (E_D), where the density of carriers vanishes. Applying a perpendicular magnetic field causes the electron and hole states to condense into LLs, indicated by the projected circular cross sections intersecting the conical dispersion. Unlike conventional 2D systems with a parabolic dispersion, the LL energies E_n of graphene are not equally spaced: $E_n = \text{sgn}(n)c^*\sqrt{2e\hbar B|n|}$, $n = -2, -1, 0, 1, 2, \dots$ (Fig. 1A), where c^* is the characteristic carrier velocity, e is the elementary charge, and \hbar is Planck's constant h divided by 2π . In addition, the unique $n = 0$ LL at $E_0 = E_D$ is not present in a conventional 2D system and is at the heart of the half-integer QHE in graphene. The physics of the $n = 0$ LL itself is presently under active theoretical study due to expectations of unique topological and correlation phenomena and because of its effect on screening (14, 15).

Physical measurements of Landau-quantized systems exhibit characteristic oscillations in many properties as the LLs move through the Fermi level (E_F) with changing magnetic field. The most well-known magneto-oscillations in 2D electron systems are SdHOs in the magnetoresistance, which can be used to determine Fermi-surface properties. In Fig. 1B, we show TMCOs; a set of increasing oscillations were observed in the STS dI/dV signal from epitaxial graphene as

the magnetic field was swept from 0 to 2.0 T at a tunneling bias of -65 mV. These oscillations are analogous to SdHOs in conventional magneto-resistance measurements; however, TMCOs are not restricted to E_F . The oscillations vary as a function of energy E , with $E - E_F = eV_B$ determined by the tunneling bias and where E_F corresponds to $V_B = 0$ (Fig. 1A). (In what follows, we take E_F as the zero of energy for convenience.) As indicated in Fig. 1A, the dI/dV signal will oscillate with the density of states because the LLs move through the energy position $E = eV_B$; a maximum in dI/dV occurs at fields where $E_n = eV_B$ (Fig. 1B). For SdHOs, the frequency of oscillations in $1/B$ is given by $B_F = (\hbar/2\pi e)A_F$, where A_F is the cross-sectional area of the Fermi surface in a plane normal to the magnetic field (16–18). In our measurements, the TMCO frequency B_E is given by a similar expression, except that A_F is replaced by A_E , where A_E is the cross-sectional k -space area at energy $E = eV_B$ (Fig. 1A). This difference is crucial as it allows the TMCO measurements to determine the low-energy electronic band structure with very high resolution in both energy and crystal momentum as E is varied via the tunneling bias. This simple distinction makes the TMCO technique potentially applicable to a wide range of materials because no gate electrode is required.

For graphene, we assume circular constant-energy contours of area $A_E = \pi k_E^2$ to determine the graphene wave vector $k_E = [(4\pi e/h)B_E]^{1/2}$. The inset to Fig. 1B shows a “fan plot” of LL index measured from the TMCO peak maxima versus $1/B$ for different values of tunneling bias V_B . This analysis yielded a range of oscillation frequencies B_E corresponding to different constant energy contours A_E [see fig. S1 (13)]. The

zero inverse-field intercept of each line in the fan plot is sensitive to the chirality of the graphene wave function, which can be described by a pseudo-spinor. The fan plot intercepts all fall near zero, indicating a Berry phase of π (19); thus, the multilayer epitaxial graphene system exhibits the pseudo-spin of massless Dirac fermions. Figure 1C shows the linear energy-momentum dispersion determined from the TMCO measurements for energies within ± 125 meV of E_D . A linear fit to the TMCO dispersion data (solid lines in Fig. 1C) determines a velocity for this epitaxial graphene system of $c^* = (1.070 \pm 0.006) \times 10^6$ ms^{-1} for both electrons and holes (20), with the Dirac point energy 29.7 ± 0.5 meV above the Fermi level (the range of observed E_D values is discussed below). The TMCO measurement in Fig. 1C represents a high-accuracy determination of the graphene dispersion, with an energy resolution (2.8 meV) limited by the thermal and instrumental broadening at 4.3 K and a wave-vector resolution of ≤ 0.02 nm^{-1} . This high-resolution measurement also includes the unfilled electronic states, a regime that is not accessible by photoelectron measurements (21, 22).

The Landau quantization of the density of states was directly measured in the dI/dV spectra at fixed magnetic field. Figure 2A shows a direct measurement of the graphene quantization with over 20 LLs observed in the tunneling spectrum in an applied field of 5 T. The LL peaks are extremely sharp as compared with similar spectra from semiconductor 2D electron systems or bulk graphite (5, 6, 23). Evidence for massless Dirac fermions can be easily inferred by the observation of the LL_0 peak at 7 mV and the large energy gaps on either side of LL_0 with zero differential conductance. Small features in the spectrum near

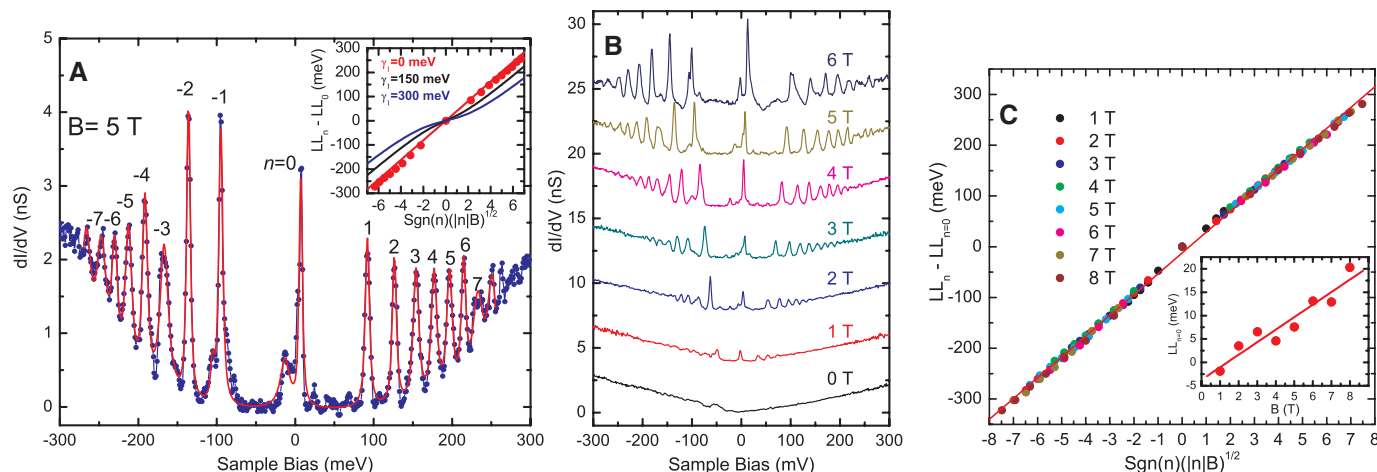


Fig. 2. Direct measurement of Landau quantization in epitaxial graphene. **(A)** Blue data points show the tunneling differential conductance spectra versus sample bias of LLs in multilayer graphene at $B = 5$ T. LL indices are marked. The red line shows a fit to a series of Voigt line shapes at the LL peak positions, which accounts for essentially all the density of states in the spectrum (tunneling set point, $V_B = 350$ mV, $I = 400$ pA). (Inset) LL peak position versus square root of LL index and applied field from the peak positions in (A). Errors in peak positions are smaller than the symbol size. Solid lines are fits to a bilayer model with interlayer coupling of zero (red),

150 meV (black), and 300 meV (blue). **(B)** LL spectra for various applied magnetic fields from 0 to 6 T. The curves are offset for clarity (tunneling set point, $V_B = 350$ mV, $I = 400$ pA). **(C)** LL peak energies for applied fields of 1 to 8 T, showing a collapse of the data when plotted versus square root of LL index and applied field. The solid line shows a linear fit yielding a characteristic velocity of $c^* = (1.128 \pm 0.004) \times 10^6$ ms^{-1} (20). (Inset) The shift in the LL_0 peak position as a function of applied field (symbols). The error is smaller than the symbol size. The solid line is a linear fit to the data points.

the $n = 0$ and $n = -1$ LLs remain unexplained; these may arise from defect scattering, as they vary somewhat with spatial position (Fig. 3), or they may be intrinsic fine structure of the LL states, particularly for the $n = 0$ LL, where electron correlations may lift the fourfold degeneracy (24). The LL spectrum in Fig. 2A fits well to a simple sum of Voigt line shapes; i.e., Lorentzians with variable energy widths convolved with a single Gaussian instrument function of 2.8-meV full width at half maximum. The Gaussian models both thermal and instrumental (bias modulation) contributions. As shown by the red line in Fig. 2A, the fit accounts for essentially all of the original spectral weight in the density of states. The rising background is dominated by the Lorentzian tails of each LL, which are determined by the carrier lifetimes, and all the density of states is quantized into the LLs. The observed linewidths of the LLs were very small. In particular, we measured a Lorentzian linewidth of 1.5 meV for LL_0 at $B = 5$ T (Fig. 2A). Associating this width with a characteristic scattering time $\tau = \hbar/\Delta E$ yields $\tau = 0.4$ ps. This scattering time is comparable to or larger than that observed in the highest mobility suspended graphene samples (25) and multilayer epitaxial graphene samples (26), with reported mobilities exceeding $200,000 \text{ cm}^2 \text{ V}^{-1} \text{ s}^{-1}$.

Previous tunneling spectroscopy measurements on graphite samples have shown quantization that varied linearly in magnetic field (5) instead of the square-root dependence expected for graphene or contained a complex mixture of spectral peaks that exhibited both equally and

non-equally-spaced LLs (6). The ability to observe pure graphene quantization in these results stems from the decoupled nature of the graphene layers grown on SiC (9). To investigate quantitatively the coupling between graphene layers in this multilayer sample, we fit the LL energies in Fig. 2A to a bilayer model for different values of the interlayer coupling γ_1 (Fig. 2A, inset) (27). An interlayer coupling of 300 to 400 meV has been measured for Bernal-stacked graphene bilayers (28, 29), yet the best fit to the spectrum in Fig. 2A clearly indicates zero-interlayer coupling ($\gamma_1 = 0$). We discuss the origin of these decoupled graphene layers on SiC below.

Figure 2B shows a series of dI/dV spectra for different magnetic fields. The LL peaks increased in intensity with increasing energy separation as the magnetic field is increased. A slight shift of LL_0 was also observed with increasing field. The Dirac point E_D lies below the Fermi level at low fields (-1.8 meV at 1 T) and shifts to a position of 13.1 meV above E_F at 6 T (Fig. 2C, inset). Extrapolating the LL_0 position to zero field yields a Dirac point $E_D = -3.7$ meV at $B = 0$, corresponding to an electron doping of $n = 8.8 \times 10^8 \text{ cm}^{-2}$. This low charge density in the top layer results from the decay in the charge profile through the multilayer stack from the highly doped interface layer and is similar to that seen in optical measurements (7). The shift of the Dirac point with field results from the redistribution of charge in the multilayer determined by the degeneracy of the available LLs and the effective screening perpendicular to the graphene planes.

The shift of LL_0 across the Fermi level is not completely understood at present and could be influenced by the electrostatic potential derived from the difference in the probe tip and graphene work functions. A more detailed theoretical analysis of the screening properties of Dirac carriers in the presence of a tip potential and a constant magnetic field would be required for a complete understanding of these results.

The spectrum of LLs in Fig. 2A demonstrates the direct measurement of the massless Dirac-fermion quantization in graphene. Further confirmation of graphene quantization and electronic structure comes from the scaling of LL energies E_n with magnetic field at high fields. For massless Dirac fermions in graphene, the spectrum E_n should scale as \sqrt{B} , whereas in all other forms (including bilayer graphene and graphite), the LLs scale linearly in B for energies near the Dirac point. Notably, a complete linear collapse of all of the LLs energies is obtained by plotting E_n versus $\sqrt{|n|B}$ (Fig. 2C), which is a distinct signature of graphene quantization. Fitting both electron and hole branches in Fig. 2C yields a common carrier velocity of $c^* = (1.128 \pm 0.004) \times 10^6 \text{ ms}^{-1}$, confirming massless Dirac fermions in this epitaxial graphene system and in good agreement with the range of values reported for graphene from other techniques (8).

Close inspection of Fig. 2C shows that the electron and hole states actually have slightly different velocities. Independent fits to the two branches give velocities $c^* = (1.189 \pm 0.007) \times 10^6 \text{ ms}^{-1}$ for the states below E_D and $c^* = (1.044 \pm 0.004) \times 10^6 \text{ ms}^{-1}$ for states above E_D . The 6%

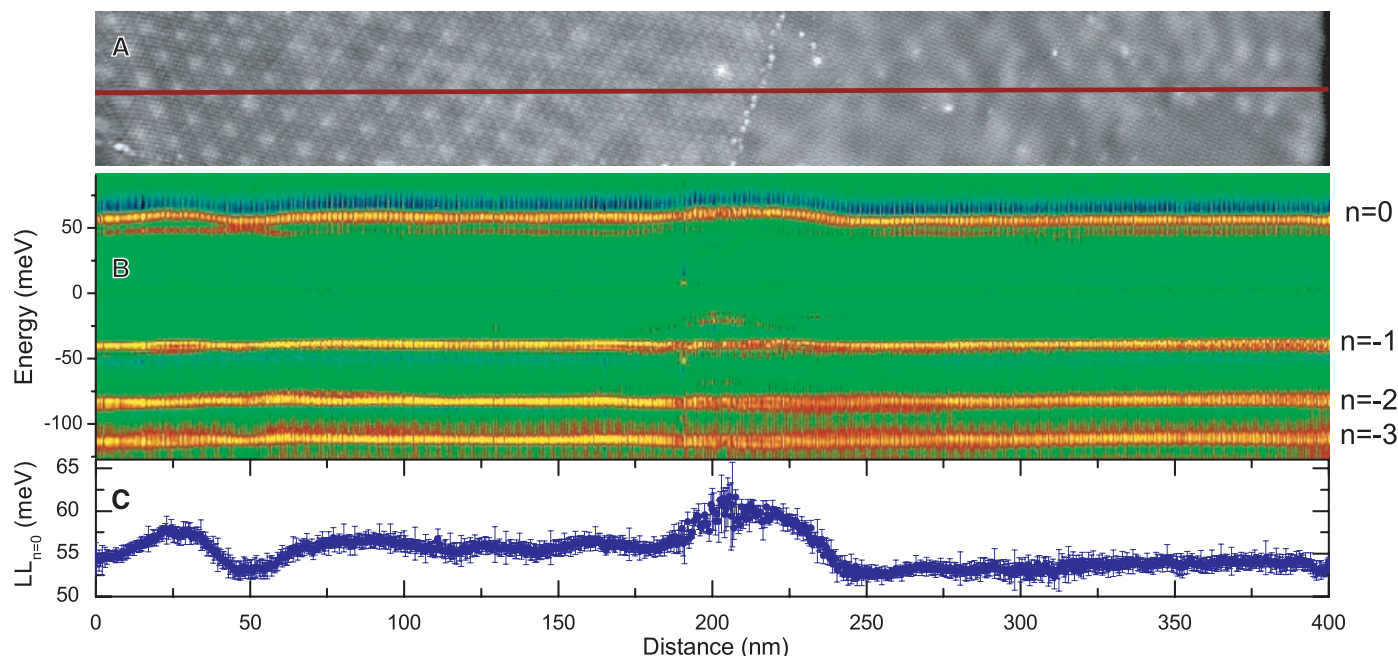


Fig. 3. Spatial variation of the surface potential in epitaxial graphene. (A) STM topograph (50 by 400 nm) showing a region containing a boundary between two different moiré regions. The gray scale range is 0.3 nm, and the periodic features correspond to the moiré [see fig. S2 (13)]. (B) A series of dI/dV spectra obtained along the center horizontal line in (A) showing

low-lying LLs. $B = 5$ T. Image color is the dI/dV intensity (blue: -1.5 nS to yellow: 2.5 nS), the horizontal axis is distance, and the vertical axis is energy. The LL indices are labeled to the right of the image. (C) Variation in the LL_0 peak position as a function of distance along the line indicated in (A). Error bars are 1σ error in fitting LL_0 peak positions in (B).

difference observed between these values may imply a breakdown of electron-hole symmetry because of many-body effects (8, 30). However, some contribution to the electron-hole asymmetry observed in Fig. 2C could also be caused by the screening of the tip electric field (band bending), requiring a small correction to the energy scale in Fig. 2C.

Spatial variation of the LL energies can be used to map fluctuations of the local potential (31), as we show for the $n = 0$ LL (Fig. 3). This level, composed of electron and hole carriers, occurs exactly at the Dirac point, as a direct consequence of the chiral solutions of the Dirac equation that describes graphene's low-energy electronic structure. Figure 3, A and B, shows a topographic image and corresponding spatial map of the lowest LL_n energies (vertical) and dI/dV intensities (color scale) for $n = 0, -1, -2$, and -3 along the line marked in Fig. 3A. The average position of E_D was 55.2 meV above E_F with a SD of ± 1.9 meV (Fig. 3C) (20). By far, the largest variation (in this image and generally in our measurements) corresponded to a subsurface rotational domain boundary that occurs in the center of the image [the top graphene layer is atomically continuous over the boundary (fig. S3)]. Away from such boundaries, the spatial fluctuations were much smaller: ~ 0.5 meV, as seen for the region from 250 to 400 nm in Fig. 3. The Dirac point energy map showed an extremely smooth potential (hence, small carrier density fluctuations) for this low-doped graphene sheet, in contrast to the electron and hole puddles observed for exfoliated graphene on SiO_2 substrates (10). In surveying the sample, a variation of $\sim \pm 25$ meV in E_D was observed over distances of many tens of micrometers (see E_D differences between Figs. 2 and 3). The larger density fluctuations on SiO_2 substrates apparently result from charged impurities in the SiO_2 substrate. The smooth charge/potential contour in epitaxial graphene could be the result of screening of the interface potential fluctuations by the graphene multilayer, and the crystalline SiC substrate may be more homogenous than the amorphous SiO_2 substrate with respect to trapped charges.

The dI/dV spectra in Fig. 2 show a direct measurement of graphene magnetic quantization expected for massless Dirac fermions. This result implies that the topmost layer of epitaxial graphene closely approximates an isolated sheet of graphene. We attribute this isolation to the presence of rotational stacking faults between the graphene layers in epitaxial graphene grown on the carbon face of SiC, which effectively decouples the electronic structure of the layers (9). A variety of rotational stacking angles were found in STM topographic images of the surface (fig. S2) (13). Slight rotations of one layer with respect to the next create moiré super periods superimposed on the atomic lattice (fig. S2) (9, 13). The ~ 0.02 -nm peak-to-peak height modulation originates from periodically varying the alignment of top-layer atoms with those below, but the exact source of image

contrast is still a subject of debate (32). Our survey of the carbon-face grown sample showed moiré patterns of various periods in almost every location examined, with spectra similar to those seen in Fig. 2. We expect this structure of multilayer epitaxial graphene to be important for future studies of Dirac point physics in graphene.

Note added in proof: A new publication reports the observation of graphene LLs in STS measurements over a graphene flake on graphite (33).

References and Notes

- C. Berger *et al.*, *J. Phys. Chem. B* **108**, 19912 (2004).
- C. Berger *et al.*, *Science* **312**, 1191 (2006); published online 12 April 2006 (10.1126/science.1125925).
- K. S. Novoselov *et al.*, *Nature* **438**, 197 (2005).
- Y. Zhang, Y. W. Tan, H. L. Stormer, P. Kim, *Nature* **438**, 201 (2005).
- T. Matsui *et al.*, *Phys. Rev. Lett.* **94**, 226403 (2005).
- G. Li, E. Y. Andrei, *Nat. Phys.* **3**, 623 (2007).
- M. L. Sadowski, G. Martinez, M. Potemski, C. Berger, W. A. de Heer, *Phys. Rev. Lett.* **97**, 266405 (2006).
- R. S. Deacon, K. C. Chuang, R. J. Nicholas, K. S. Novoselov, A. K. Geim, *Phys. Rev. B* **76**, 081406R (2007).
- J. Hass *et al.*, *Phys. Rev. Lett.* **100**, 125504 (2008).
- J. Martin *et al.*, *Nat. Phys.* **4**, 144 (2008).
- E. Rossi, S. Das Sarma, *Phys. Rev. Lett.* **101**, 166803 (2008).
- W. A. de Heer *et al.*, *Solid State Commun.* **143**, 92 (2007).
- Additional text and data are available on Science Online.
- C. Toke, P. E. Lammert, V. H. Crespi, J. K. Jain, *Phys. Rev. B* **74**, 235417 (2006).
- M. Arikawa, Y. Hatsugai, H. Aoki, *Phys. Rev. B* **78**, 205401 (2008).
- N. Ashcroft, N. Mermin, *Solid State Physics* (Brooks Cole, London, 1976).
- V. P. Gusynin, S. G. Sharapov, *Phys. Rev. B* **71**, 125124 (2005).
- S. G. Sharapov, V. P. Gusynin, H. Beck, *Phys. Rev. B* **69**, 075104 (2004).
- I. A. Luk'yanchuk, Y. Kopelevich, *Phys. Rev. Lett.* **93**, 166402 (2004).
- All uncertainties reported represent 1 SD in the measured quantity.
- E. Rollings *et al.*, *J. Phys. Chem. Solids* **67**, 2172 (2006).
- A. Bostwick, T. Ohta, T. Seyller, K. Horn, E. Rotenberg, *Nat. Phys.* **3**, 36 (2007).
- M. Morgenstern, J. Klijn, C. Meyer, R. Wiesendanger, *Phys. Rev. Lett.* **90**, 056804 (2003).
- Y. Zhang *et al.*, *Phys. Rev. Lett.* **96**, 136806 (2006).
- K. I. Bolotin *et al.*, *Solid State Commun.* **146**, 351 (2008).
- M. Orlita *et al.*, *Phys. Rev. Lett.* **101**, 267601 (2008).
- E. A. Henriksen *et al.*, *Phys. Rev. Lett.* **100**, 087403 (2008).
- G. M. Rutter, J. N. Crain, N. P. Guisinger, P. N. First, J. A. Stroscio, *J. Vac. Sci. Technol. A* **26**, 938 (2008).
- J. Yan, E. A. Henriksen, P. Kim, A. Pinczuk, *Phys. Rev. Lett.* **101**, 136804 (2008).
- P. E. Trevisanuto, C. Giorgetti, L. Reining, M. Ladisa, V. Olevano, *Phys. Rev. Lett.* **101**, 226405 (2008).
- M. Morgenstern, C. Witteven, R. Dombrowski, R. Wiesendanger, *Phys. Rev. Lett.* **84**, 5588 (2000).
- W. T. Pong, C. Durkan, *J. Phys. D Appl. Phys.* **38**, R329 (2005).
- G. Li, A. Luican, E. Y. Andrei, *Phys. Rev. Lett.* **102**, 176804 (2009).
- We thank A. MacDonald, H. Min, M. Stiles, and the NIST graphene team for valuable comments and discussions and C. Berger, N. Sharma, M. Sprinkle, S. Blankenship, A. Band, and F. Hess for their technical contributions to this work. Portions of this work were supported by NSF (grant ECCS-0804908), the Semiconductor Research Corporation Nanoelectronics Research Initiative (INDEX R329), and the W. M. Keck Foundation. Graphene production facilities were developed under NSF grant ECCS-0521041.

Supporting Online Material

www.sciencemag.org/cgi/content/full/324/5929/924/DC1
SOM Text
Figs. S1 to S3

3 February 2009; accepted 17 March 2009
10.1126/science.1171810

Direct Detection of Abortive RNA Transcripts in Vivo

Seth R. Goldman,¹ Richard H. Ebright,² Bryce E. Nickels^{1*}

During transcription initiation in vitro, prokaryotic and eukaryotic RNA polymerase (RNAP) can engage in abortive initiation—the synthesis and release of short (2 to 15 nucleotides) RNA transcripts—before productive initiation. It has not been known whether abortive initiation occurs in vivo. Using hybridization with locked nucleic acid probes, we directly detected abortive transcripts in bacteria. In addition, we show that in vivo abortive initiation shows characteristics of in vitro abortive initiation: Abortive initiation increases upon stabilizing interactions between RNAP and either promoter DNA or sigma factor, and also upon deleting elongation factor GreA. Abortive transcripts may have functional roles in regulating gene expression in vivo.

During transcription, RNA polymerase (RNAP) synthesizes the first ~ 8 to 15 nucleotides (nt) of RNA as an RNAP-promoter initial transcribing complex (1–3) [using a “scrunching” mechanism (4)]. Upon synthesis of an RNA transcript with a threshold length of ~ 8 to 15 nt, RNAP breaks its interactions with promoter

DNA, escapes the promoter, and enters into processive synthesis of RNA as an RNAP-DNA transcription elongation complex (1–3) [using a “stepping” mechanism (5)]. In transcription reactions in vitro, the RNAP-promoter initial transcribing complex can engage in tens to hundreds of cycles of synthesis and release of short RNA transcripts (abortive initiation) (1–3, 6–8). Abortive initiation competes with productive initiation in vitro and, as such, is a critical determinant of promoter strength and a target of transcription regulation in vitro (1–3, 7–13). It has been proposed that abortive initiation likewise occurs in vivo

¹Department of Genetics and Waksman Institute, Rutgers University, Piscataway, NJ 08854, USA. ²Department of Chemistry, Waksman Institute, and Howard Hughes Medical Institute, Rutgers University, Piscataway, NJ 08854, USA.

*To whom correspondence should be addressed. E-mail: bnicks@waksman.rutgers.edu

(6, 8). In support of this proposal, factors that affect yields of full-length transcripts in vitro through effects on abortive initiation likewise affect yields of full-length transcripts in vivo (9–14). However, no direct evidence that abortive initiation occurs in vivo has been presented.

The bacteriophage T5 N25 promoter and its derivative N25anti are classic model systems for the study of abortive initiation and promoter escape (9, 11–14). N25 and N25anti differ only in their initial transcribed sequences (positions +3 to +20) but exhibit radically different characteristics in vitro with respect to the abortive:productive ratio (APR) (40 for N25 and ~300 for N25anti), the maximum size of abortive transcripts (10 nt for N25 and 15 nt for N25anti), and the rate constant for promoter escape (k_{clear}) (~1.7 per min for N25 and ~0.06 per min for N25anti).

To determine whether abortive initiation occurs in vivo, we sought to detect abortive transcripts generated during transcription from a plasmid-borne copy of N25anti in *Escherichia coli* by using locked nucleic acid probes developed for the hybridization-based detection of microRNAs (15, 16). We reasoned that the relatively high APR of N25anti would facilitate the accumulation of detectable quantities of abortive transcripts and that the relatively high maximum size of abortive transcripts of N25anti would facilitate efficient hybridization of the locked nucleic acid probes.

To validate the method, we performed in vitro transcription reactions using *E. coli* RNAP and a DNA template carrying the N25anti promoter, a 100-nt transcription unit, and the tR2 terminator (N25anti-100-tR2). We performed parallel reac-

tions using radioactive nucleotide triphosphates (NTPs) with analysis by means of autoradiography (Fig. 1A, left) and using nonradioactive NTPs with analysis by means of hybridization (Fig. 1A, right). Hybridization was able to detect abortive transcripts having lengths of 11 to 15 nt.

To detect abortive transcripts in vivo, we introduced a plasmid carrying N25anti-100-tR2 into cells, isolated RNA, electrophoresed RNA on urea-polyacrylamide gels, and visualized transcripts by means of hybridization (Fig. 1B). RNA samples from cells with the plasmid carrying N25anti-100-tR2 (but not from cells with a control plasmid lacking N25anti-100-tR2) exhibited transcripts corresponding in mobility to the 11- to 15-nt abortive transcripts observed in vitro (Fig. 1B). The 11- to 15-nt transcripts generated in vivo were observed with both N25anti-100-tR2 carried on a multicopy plasmid (Fig. 1B) and N25anti-100-tR2 carried on a single-copy F-plasmid-derived plasmid (fig. S1).

To show that the 11- to 15-nt transcripts detected in vivo are abortive transcripts, we demonstrated that they exhibit three hallmarks of abortive transcripts as defined in vitro: (i) altering strengths of interactions between RNAP and promoter DNA alters yields of the 11- to 15-nt transcripts (figs. S2 and S3) (1, 3, 10, 13, 17); (ii) altering strengths of interactions between RNAP and transcription initiation factor σ alters yields of the 11- to 15-nt transcripts (figs. S4 and S5) (18, 19); and (iii) transcription elongation factor GreA alters yields of the 11- to 15-nt transcripts (fig. S6) (1, 3, 9).

We conclude that abortive initiation occurs in vivo (Fig. 1 and figs. S1 to S6). We further conclude that abortive initiation is a determinant

of promoter strength (figs. S2 and S3), a determinant of RNAP function (figs. S4 and S5), and a target of transcription regulation in vivo (fig. S6). The results were obtained with bacterial RNAP. However, because abortive initiation occurs in vitro with all characterized RNAPs—bacterial, archaeal, eukaryotic, and bacteriophage—we consider it likely that abortive initiation occurs in vivo with all RNAPs.

Analysis of initially transcribed region sequences of experimentally defined *E. coli* promoters indicates that as many as ~4000 different 2- to 10-nt abortive transcripts may be generated in vivo (table S1).

The finding that abortive transcripts are generated in vivo and accumulate to detectable levels in vivo raises the possibility that abortive transcripts may play functional roles. For example, an abortive transcript produced from a first promoter could function as a sequence-specific primer for transcription initiation at a second promoter or could function as an antisense effector against a specific RNA. Key priorities will be to define the full set of abortive transcripts produced in vivo (the “abortome”) and to define functional roles of abortive transcripts in vivo.

References and Notes

1. L. M. Hsu, *Biochim. Biophys. Acta* **1577**, 191 (2002).
2. K. S. Murakami, S. A. Darst, *Curr. Opin. Struct. Biol.* **13**, 31 (2003).
3. L. M. Hsu, *Methods* **47**, 25 (2009).
4. A. N. Kapanidis et al., *Science* **314**, 1144 (2006).
5. E. A. Abbondanzieri, W. J. Greenleaf, J. W. Shaevitz, R. Landick, S. M. Block, *Nature* **438**, 460 (2005).
6. W. R. McClure, C. L. Cech, *J. Biol. Chem.* **253**, 8949 (1978).
7. A. J. Carpousis, J. D. Gralla, *Biochemistry* **19**, 3245 (1980).
8. J. D. Gralla, A. J. Carpousis, J. E. Stefano, *Biochemistry* **19**, 5864 (1980).
9. L. M. Hsu, N. V. Vo, M. J. Chamberlin, *Proc. Natl. Acad. Sci. U.S.A.* **92**, 11588 (1995).
10. M. Monsalve, M. Mencia, F. Rojo, M. Salas, *EMBO J.* **15**, 383 (1996).
11. C. L. Chan, C. A. Gross, *J. Biol. Chem.* **276**, 38201 (2001).
12. L. M. Hsu, N. V. Vo, C. M. Kane, M. J. Chamberlin, *Biochemistry* **42**, 3777 (2003).
13. N. V. Vo, L. M. Hsu, C. M. Kane, M. J. Chamberlin, *Biochemistry* **42**, 3798 (2003).
14. W. Kammerer, U. Deuschle, R. Gentz, H. Bujard, *EMBO J.* **5**, 2995 (1986).
15. Materials and methods are available as supporting material on Science Online.
16. A. Valoczi et al., *Nucleic Acids Res.* **32**, e175 (2004).
17. T. Ellinger, D. Behnke, H. Bujard, J. D. Gralla, *J. Mol. Biol.* **239**, 455 (1994).
18. D. C. Ko, M. T. Marr, J. Guo, J. W. Roberts, *Genes Dev.* **12**, 3276 (1998).
19. M. Leibman, A. Hochschild, *EMBO J.* **26**, 1579 (2007).
20. We thank A. Hochschild, A. Revyakin, and J. Roberts for materials, and A. Gann, S. Garrity, A. Hochschild, L. Hsu, W. McAllister, E. McGlinn, and R. Sousa for discussion. Work was supported by NIH grant GM41376 and a Howard Hughes Medical Institute Investigatorship to R.H.E. and by a Pew Scholars Award to B.E.N.

Supporting Online Material

www.sciencemag.org/cgi/content/full/324/5929/927/DC1
Materials and Methods

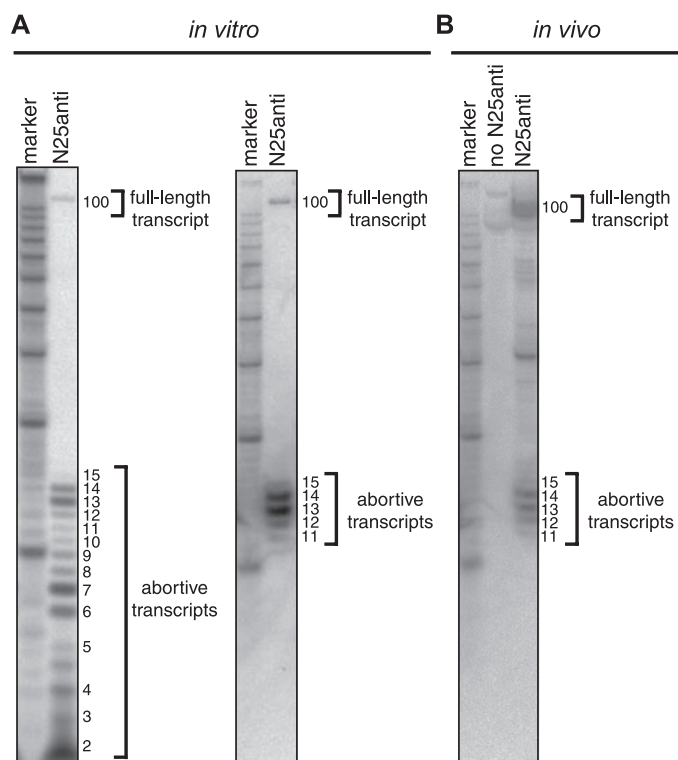
Figs. S1 to S6

Tables S1 to S3

References

2 December 2008; accepted 17 March 2009
10.1126/science.1169237

Fig. 1. Abortive initiation occurs in vivo. (A) Abortive initiation in vitro. (Left) Detection was performed by means of autoradiography of transcripts generated in “hot” (radioactive) reactions. (Right) Detection was performed by means of hybridization of transcripts generated in “cold” (nonradioactive) reactions. (B) Abortive initiation in vivo. Detection was performed by means of hybridization of transcripts generated in vivo.



The Nuclear DNA Base 5-Hydroxymethylcytosine Is Present in Purkinje Neurons and the Brain

Skirmantas Kriaucionis and Nathaniel Heintz*

Despite the importance of epigenetic regulation in neurological disorders, little is known about neuronal chromatin. Cerebellar Purkinje neurons have large and euchromatic nuclei, whereas granule cell nuclei are small and have a more typical heterochromatin distribution. While comparing the abundance of 5-methylcytosine in Purkinje and granule cell nuclei, we detected the presence of an unusual DNA nucleotide. Using thin-layer chromatography, high-pressure liquid chromatography, and mass spectrometry, we identified the nucleotide as 5-hydroxymethyl-2'-deoxycytidine (hmdC). hmdC constitutes 0.6% of total nucleotides in Purkinje cells, 0.2% in granule cells, and is not present in cancer cell lines. hmdC is a constituent of nuclear DNA that is highly abundant in the brain, suggesting a role in epigenetic control of neuronal function.

To investigate Purkinje and granule cell nuclei, we took advantage of the fact that ribosomal proteins are assembled in the nucleolus of all cells. Consequently, transgenic mice containing ribosomal protein L10a fused to enhanced green fluorescent protein (EGFP)—for example, the *Pcp2 bacTRAP* and *NeuroD1 bacTRAP* lines that express in cerebellar Purkinje and granule neurons, respectively—contain fluorescent nucleoli (1, 2) (figs. S1, D and E, and S2, C and D). This allowed us to obtain ~95% pure preparations of Purkinje or granule cell nuclei by fluorescence-activated cell sorting. While determining the total amount of cytosine methylation in CpG content in Purkinje and granule cell genomic DNA, we consistently observed a significantly smaller amount of 5-methylcytosine (mC) in Purkinje DNA (Fig. 1C) and the presence of an unidentified spot (“x”) on thin-layer chromatography (TLC) plates (Fig. 1A). Treatment of the DNA samples overnight with a mixture of ribonucleases (RNases) A and T1, followed by a 1-hour incubation with RNase H and V1 (hydrolyzing single-stranded RNA, RNA-DNA hybrids, and double-stranded RNA, respectively), did not remove spot “x” (fig. S3A). When the sample was treated with RNase-free deoxyribonuclease, spot “x” disappeared, together with most of the signal from other spots (fig. S3A). Using the same labeling procedure on total cerebellar RNA, we did not observe spot “x.” Spot “x” was not 2'-deoxyuridine monophosphate, which could appear after cytosine deamination, because a hydrolysate of uracil containing DNA generated a spot that migrated substantially below spot “x” (fig. S3B). Fragmenting DNA with Fok I restriction endonuclease and incorporating [α - 32 P]dATP (2'-deoxyadenosine 5'-triphosphate) into the resulting 3' end did not yield spot “x” on the resulting TLC plates, demonstrating that “x” is preferentially found in the context of xpG dinucleotides (fig. S3C). From the total number of nucleosides neighboring G, we estimated that “x” constitutes $0.59 \pm 0.05\%$ in

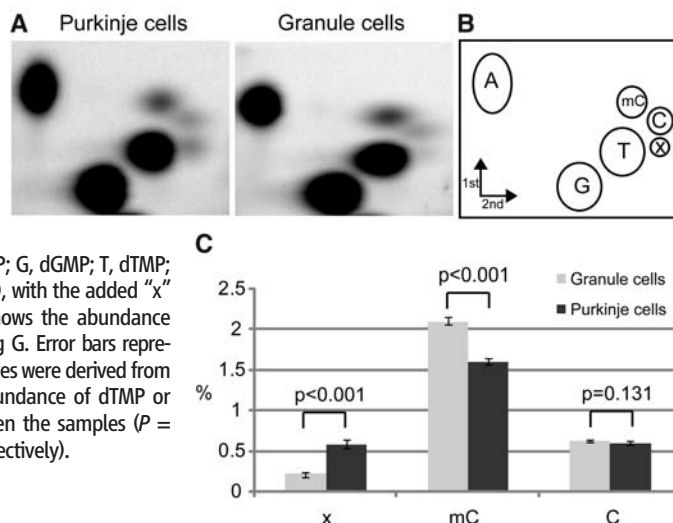
Purkinje cell DNA and $0.23 \pm 0.01\%$ in granule cell DNA. We noticed that the actual increase in the amount of xpG is proportional to the decrease in mCpG (Fig. 1C). Considering the quantitative “x” relation with mC and that the abundance of the other nucleosides was not different between these cell types (Fig. 1C and Fig. 1 legend), we tested the possibility that “x” is 5-hydroxymethyl-2'-deoxycytidine, which is found in T-even bacteriophage DNA (3). The results showed that hmdC monophosphate generated a spot that comigrated with the “x” spot on a TLC plate (Fig. 2A). When a synthetic DNA hydrolysate was separated with reverse-phase high-pressure liquid chromatography (HPLC), hmdC eluted just after the cytosine peak, consistent with the published observations (4) (Fig. 2B). HPLC analysis of cerebellar genomic DNA resulted in a small, but reproducible, peak on the HPLC chromatogram in the same position (Fig. 2B). To provide definitive proof that “x” is hmdC, we analyzed the corresponding fraction with high-precision mass spectrometry (MS). Mass spectra identified the presence of two ions, with a mass/charge ratio (m/z) of 142.06 ± 0.01 and 280.11 ± 0.02 , which matched the theoretical isotopic molecular weights of ions derived from hmdC— m/z 142.06 and 280.09, respectively (Fig.

2C). MS collision-induced fragmentation of the hmdC corresponding fraction from synthetic DNA produced the same ions (fig. S4). Together, these data demonstrate the presence of hmC in mouse cerebellar DNA. We were unable to detect hmC in four different cell lines of mouse and human origin (fig. S5A). The distribution of hmC in mouse tissues displays the enrichment exclusively in the brain, with higher abundance in the cortex and brainstem (fig. S5B).

It is unlikely that the hmC that we observed in vivo is a product of DNA damage (5, 6). We did not observe any other DNA damage products such as 8-oxoguanine, a preferential target for oxidants (7), or thymidine glycol, which is produced in vitro by the oxidation of mC (6). In addition, hmC is more abundant in brain, but not in other metabolically active nonproliferating tissues (fig. S5B). Finally, contrary to what one would expect for oxidative DNA damage, we found no correlation between the age of adult mice and the amount of hmC in Purkinje and granule cells (fig. S6).

An early publication suggesting the presence of hmC in mammalian genomes (8) has not been reproduced by others (9, 10). It has been suggested that hmC, if treated with bisulfite, will produce cytosine 5-methylsulfonate, which would be deaminated even at a slower rate than mC (11), leading to the interpretation of hmC as mC after bisulfite sequencing. Although active DNA demethylation is considered to occur, no enzyme has been found that can remove the methyl group from 5-methylcytosine (12). The presence of a hydroxylated methyl group could indicate either an intermediate for oxidative demethylation or a stable end-product, which eliminates the need for removal of the methyl group, by modulating the affinity of proteins that bind to the mC signal in nondividing neuronal cell types. The finding that the methyl-CpG binding domain of MeCP2 protein has a lower affinity toward sequences containing hmC supports this notion (13). It is notable that hmC is nearly 40% as abundant as mC in Purkinje cell DNA. Given the critical role of mC in epigenetic regulation of the genome, we believe that hmC has an important biological role in vivo.

Fig. 1. Quantification of mC and “x” abundance in Purkinje and granule neurons. (A) Two-dimensional (2D) TLC separation of nucleoside monophosphates from genomic DNA in Purkinje and granule cells. (B) Reference map of the TLC spots (A, dAMP; C, dCMP; G, dGMP; T, dTMP; mC, 5-methylcytosine) (14), with the added “x” position. (C) Percentage shows the abundance of a nucleotide neighboring G. Error bars represent the SEM ($n = 11$); P values were derived from Matt-Whitney statistics. Abundance of dTMP or dAMP did not differ between the samples ($P = 0.743$ and $P = 0.793$, respectively).



Laboratory of Molecular Biology, Howard Hughes Medical Institute, The Rockefeller University, New York, NY 10065, USA.

*To whom correspondence should be addressed. E-mail: heintz@mail.rockefeller.edu

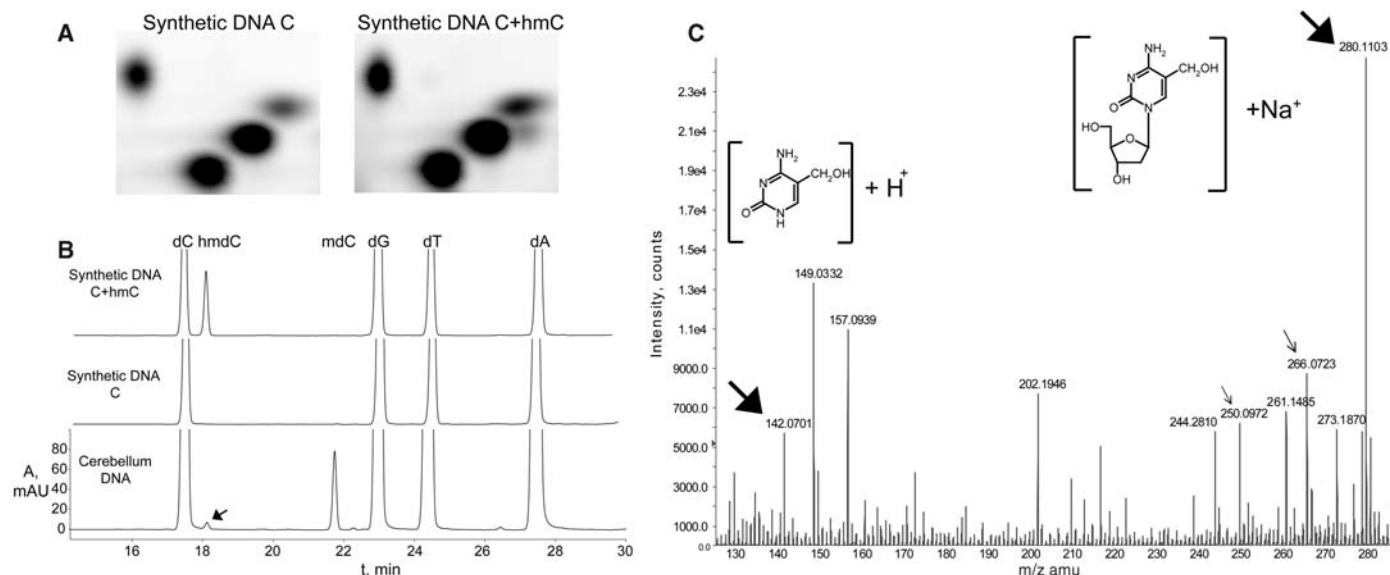


Fig. 2. Two-dimensional TLC, HPLC, and MS identification of hmC. **(A)** Two-dimensional TLC analysis of synthetic DNA templates indicates that hmC comigrates with the “x” spot (Fig. 1). **(B)** HPLC chromatograms (A, 254 nm) of the nucleosides derived from synthetic and cerebellum DNA. The peaks were identified by MS. The arrow points to the peak, which elutes at the same time

as hmdC. **(C)** MS of the fraction corresponding to the HPLC peak indicated above. Closed arrows indicate the masses of 5-hydroxymethylcytosine and 5-hydroxymethyl-2'-deoxycytidine sodium ions (structures are shown in the insets). Open arrows indicate the ions generated by 2'-deoxycytidine, which elutes in a large nearby peak and spills over into the analyzed fraction.

References and Notes

1. J. P. Doyle *et al.*, *Cell* **135**, 749 (2008).
2. M. Heiman *et al.*, *Cell* **135**, 738 (2008).
3. G. R. Wyatt, S. S. Cohen, *Biochem. J.* **55**, 774 (1953).
4. S. Tardy-Planechaud, J. Fujimoto, S. S. Lin, L. C. Sowers, *Nucleic Acids Res.* **25**, 553 (1997).
5. A. Burdzy, K. T. Noyes, V. Valinluck, L. C. Sowers, *Nucleic Acids Res.* **30**, 4068 (2002).
6. S. Zuo, R. J. Boorstein, G. W. Teebor, *Nucleic Acids Res.* **23**, 3239 (1995).
7. J. Cadet, T. Douki, J. L. Ravanat, *Nat. Chem. Biol.* **2**, 348 (2006).
8. N. W. Penn, R. Suwalski, C. O'Riley, K. Bojanowski, R. Yura, *Biochem. J.* **126**, 781 (1972).
9. R. M. Kothari, V. Shankar, *J. Mol. Evol.* **7**, 325 (1976).
10. J. H. Gommers-Ampt, P. Borst, *FASEB J.* **9**, 1034 (1995).
11. H. Hayatsu, M. Shiragami, *Biochemistry* **18**, 632 (1979).
12. S. K. Ooi, T. H. Bestor, *Cell* **133**, 1145 (2008).
13. V. Valinluck *et al.*, *Nucleic Acids Res.* **32**, 4100 (2004).
14. B. H. Ramsahoye, *Methods Mol. Biol.* **200**, 9 (2002).
15. We thank B. Gauthier for technical assistance; S. Mazel, C. Bare, and X. Fan for flow cytometry advice and nuclei sorts; and H. Deng and J. Fernandez for acquisition of MS data and help with HPLC. We are grateful to members of the Heintz laboratory for discussions and support. This

work was supported by the Howard Hughes Medical Institute and the Simons Foundation Autism Research Initiative.

Supporting Online Material

www.sciencemag.org/cgi/content/full/1169786/DC1
Materials and Methods
Figs. S1 to S6
References

15 December 2008; accepted 18 March 2009
Published online 16 April 2009;
10.1126/science.1169786
Include this information when citing this paper.

Conversion of 5-Methylcytosine to 5-Hydroxymethylcytosine in Mammalian DNA by MLL Partner TET1

Mamta Tahiliani,¹ Kian Peng Koh,¹ Yinghua Shen,² William A. Pastor,¹ Hozefa Bandukwala,¹ Yevgeny Brudno,² Suneet Agarwal,³ Lakshminarayan M. Iyer,⁴ David R. Liu,^{2*} L. Aravind,^{4*} Anjana Rao^{1*}

DNA cytosine methylation is crucial for retrotransposon silencing and mammalian development. In a computational search for enzymes that could modify 5-methylcytosine (5mC), we identified TET proteins as mammalian homologs of the trypanosome proteins JBP1 and JBP2, which have been proposed to oxidize the 5-methyl group of thymine. We show here that TET1, a fusion partner of the MLL gene in acute myeloid leukemia, is a 2-oxoglutarate (2OG)- and Fe(II)-dependent enzyme that catalyzes conversion of 5mC to 5-hydroxymethylcytosine (hmC) in cultured cells and in vitro. hmC is present in the genome of mouse embryonic stem cells, and hmC levels decrease upon RNA interference-mediated depletion of TET1. Thus, TET proteins have potential roles in epigenetic regulation through modification of 5mC to hmC.

5-methylcytosine (5mC) is a minor base in mammalian DNA: It constitutes ~1% of all DNA bases and is found almost exclusively as symmetrical methylation of the dinucleotide CpG (1). The majority of methylated CpG is

found in repetitive DNA elements, suggesting that cytosine methylation evolved as a defense against transposons and other parasitic elements (2). Methylation patterns change dynamically in early embryogenesis, when CpG methylation is

essential for X-inactivation and asymmetric expression of imprinted genes (3). In somatic cells, promoter methylation often shows a correlation with gene expression: CpG methylation may directly interfere with the binding of certain transcriptional regulators to their cognate DNA sequences or may enable recruitment of methyl-CpG binding proteins that create a repressed chromatin environment (4). DNA methylation patterns are highly dysregulated in cancer: Changes in methylation status have been postulated to inactivate tumor suppressors and activate oncogenes, thus contributing to tumorigenesis (5).

¹Department of Pathology, Harvard Medical School and Immune Disease Institute, 200 Longwood Avenue, Boston, MA 02115, USA. ²Department of Chemistry and Chemical Biology and the Howard Hughes Medical Institute, Harvard University, Cambridge, MA 02138, USA. ³Division of Pediatric Hematology/Oncology, Children's Hospital Boston and Dana-Farber Cancer Institute, Boston, MA 02115, USA. ⁴National Center for Biotechnology Information, National Library of Medicine, National Institutes of Health, Bethesda, MD 20894, USA.

*To whom correspondence should be addressed. E-mail: arao@idi.harvard.edu (A.R.); aravind@ncbi.nlm.nih.gov (L.A.); drliu@fas.harvard.edu (D.R.L.)

Fig. 1. Expression of TET1 in HEK293 cells results in decreased 5mC staining. **(A)** Predicted domain architecture of human TET1 showing the CXXC-type zinc-binding domain (amino acid 584 to 624); the cysteine-rich region (Cys-rich) (amino acid 1418 to 1610); the DSBH domain (amino acid 1611 to 2074); and three bipartite nuclear localization sequences (NLS). **(B)** HEK293 cells overexpressing wild-type or mutant HA-TET1 were costained with antibodies specific for the HA epitope (green) and 5mC (red). To orient the reader, some HA-expressing cells are circled. Scale bar, 10 μ m. **(C)** Staining intensities of HA and 5mC were measured in individual nuclei. Data from HA-TET1-expressing cell populations are presented as dot plots (red), superimposed on dot plots from mock-transfected cells (blue), with each dot representing an individual cell. **(D)** Quantification of 5mC staining intensity of HA-positive cells compared with that of mock-transfected cells (set to 1). Data shown are mean \pm SEM and are representative of three experiments.

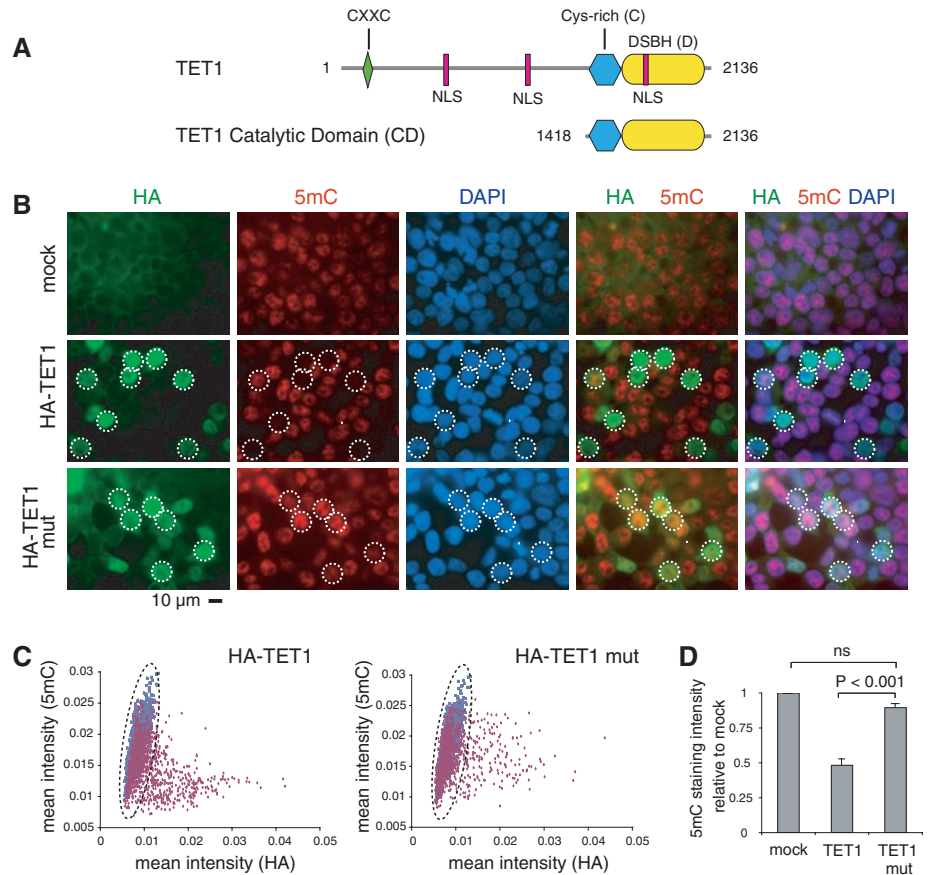
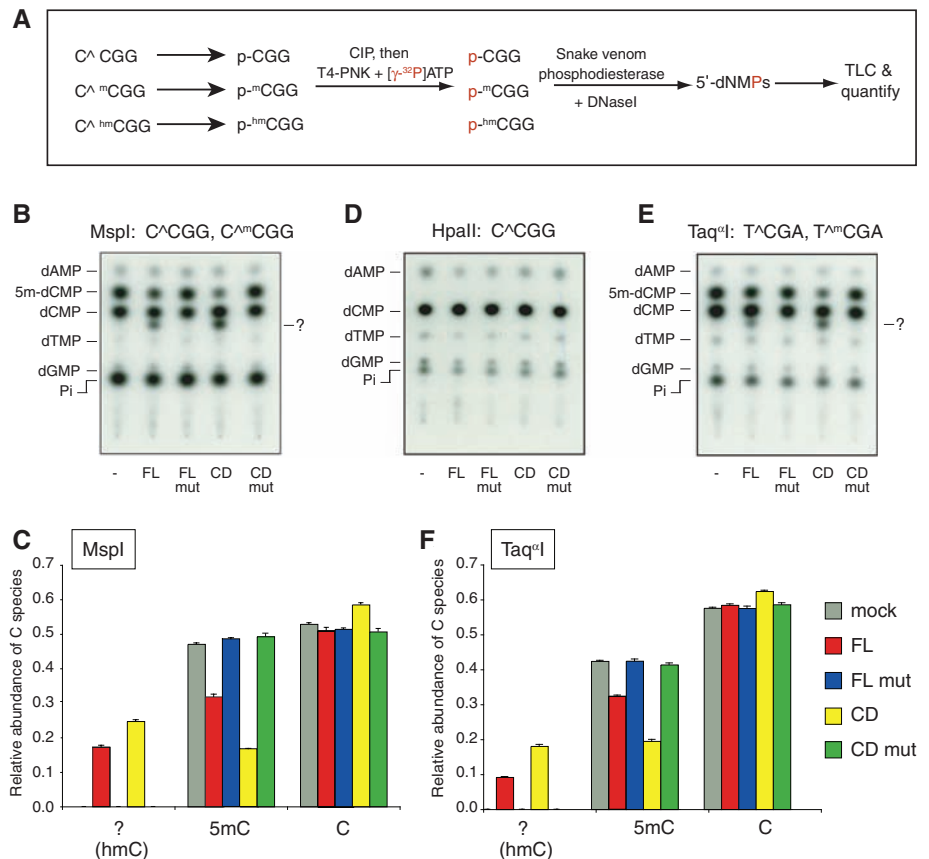


Fig. 2. Genomic DNA of TET1-overexpressing cells contains a modified nucleotide within the dinucleotide CG. **(A)** Description of experimental design. **(B to F)** Genomic DNA was purified from HEK293 cells overexpressing TET1 and cleaved with [(B) and (C)] MspI, [(D) and (E)] HpaII, or [(E) and (F)] Taq^I. The fragments were end-labeled, digested to 5' dNMPs, and resolved by TLC. A modified nucleotide (subsequently identified as hm-dCMP) is indicated by ?. Neither 5m-dCMP nor the modified nucleotide are observed when the DNA is digested with HpaII. [(C) and (F)] Quantification of the relative abundance of dCMP, 5m-dCMP, and the modified nucleotide. Data shown are mean \pm SD of three independent transfections and are representative of at least three experiments.



Trypanosomes contain base J (β -D-glucosyl hydroxymethyluracil), a modified thymine produced by sequential hydroxylation and glucosylation of the methyl group of thymine (fig. S1A) (6). J biosynthesis requires JBP1 and JBP2, enzymes of the 2OG- and Fe(II)-dependent oxygenase superfamily predicted to catalyze the first step of J biosynthesis (7, 8). Like 5-methylcytosine, base J has an association with gene silencing: It is present in silenced copies of the genes encoding the variable surface glycoprotein (VSG) responsible for antigenic variation in the host but is absent from the single expressed copy (6). We performed a computational search for homologs of JBP1 and JBP2 in the hope of identifying mammalian enzymes that modified 5mC.

Iterative sequence profile searches using the predicted oxygenase domains of JBP1 and JBP2 recovered homologous regions in three paralogous human proteins TET1, TET2, and TET3 and their orthologs found throughout metazoa ($e < 10^{-5}$), as well as homologous domains in fungi and algae (fig. S2 and SOM Text). Secondary structure predictions suggested the existence of an N-terminal α helix followed by a continuous series of β strands, typical of the double-stranded β helix (DSBH) fold of the 2OG-Fe(II) oxygenases (fig. S3) (9). A multiple sequence alignment showed that the new TET/JBP family displayed all of the typical features of 2OG-Fe(II) oxygenases, including conservation of residues predicted to be important for coordination of the cofactors Fe(II) and 2OG (fig. S3 and SOM Text). The metazoan TET proteins contain a unique conserved cysteine-rich region, contiguous with the N terminus of the DSBH region (Fig. 1A and SOM Text). Vertebrate TET1 and TET3, and their orthologs from all other animals, also possess a CXXC domain, a binuclear Zn-chelating domain, found in several chromatin-associated proteins, that in certain cases has been shown to discriminate between methylated and unmethylated DNA (10).

As a first step in determining whether TET proteins operate on 5mC, we transfected human embryonic kidney (HEK) 293 cells with full-length hemagglutinin (HA)-tagged TET1, then stained the transfected cells for 5mC and the HA epitope. Mock-transfected cells showed substantial variation in 5mC staining intensity (fig. S4; Fig. 1B, top panel; quantified in Fig. 1C), either because 5mC levels vary from cell to cell or because the accessibility of 5mC to the antibody differs among cells because of technical considerations (e.g., incomplete denaturation of DNA). Cells transfected with wild-type TET1 showed a strong correlation of HA positivity with decreased staining for 5mC, both visually (Fig. 1B, middle panel) and by quantification (Fig. 1C, left panel, and Fig. 1D). Untransfected HA-low cells showed a spread of 5mC staining intensity similar to that of mock-transfected cells (Fig. 1C, left panel; note overlapping red and blue dots at low HA intensities), whereas productively transfected HA-high cells showed uniformly low 5mC staining intensity (Fig. 1C, left panel, red HA-high dots). Cells transfected with mutant

TET1 bearing H1671Y, D1673A substitutions predicted to impair Fe(II) binding did not show decreased staining for 5mC (Fig. 1B, bottom panel; Fig. 1C, right panel; and Fig. 1D).

To determine quantitatively whether TET1 overexpression affects intracellular 5mC levels, we measured the ratio of 5mC to C at a subset of genomic CpG sites in cells expressing either full-length TET1 (TET1-FL) or the predicted catalytic domain of TET1 [TET1-CD, comprising the Cys-rich (C) and DSBH (D) regions; Fig. 1A]. HEK293 cells were transiently transfected with plasmids in which TET1 expression was coupled to expression of human CD25 from an internal ribosome

entry site (IRES). Genomic DNA from CD25-expressing cells was digested with MspI, which cleaves DNA at the sequence C⁺CGG regardless of whether the second C is methylated. The resulting fragments, whose 5' ends derive from the dinucleotide CpG and contain either C or 5mC, were end-labeled and digested to yield 5' phosphorylated dNMPs that were resolved using thin-layer chromatography (TLC) (Fig. 2A) (11).

MspI-digested DNA from cells transfected with the control vector yielded predominantly dCMP and 5m-dCMP as expected (Fig. 2B, lane 1), whereas DNA from cells expressing wild-type TET1-FL or TET1-CD yielded an additional

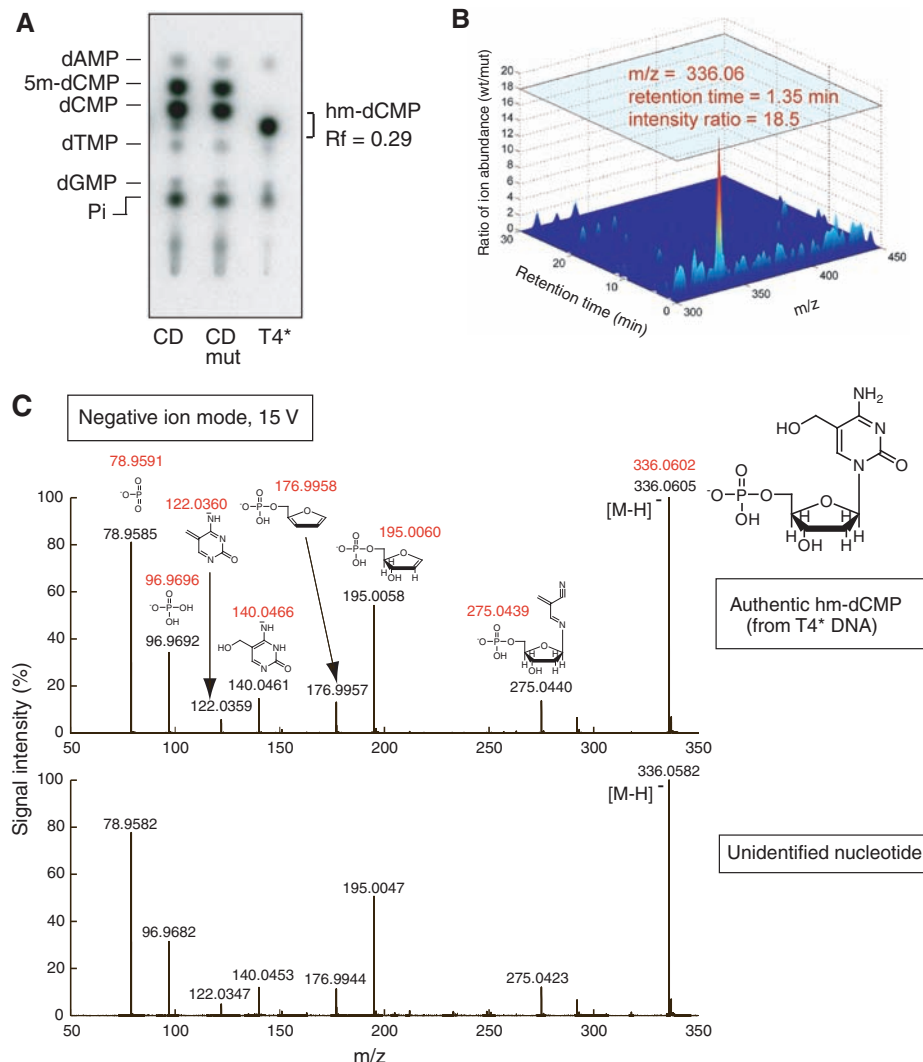


Fig. 3. The modified nucleotide is identified as 5-hydroxymethylcytosine. **(A)** Genomic DNA from T4 phage grown in UDP-glucose-deficient *E. coli* ER1656 (T4*) and HEK293 cells transfected with wild-type or mutant TET1-CD were digested with Taq^I. The fragments were end-labeled, digested to mononucleotides, and separated by TLC. The modified nucleotide present in TET1-CD-expressing cells migrates similarly to authentic hm-dCMP. **(B)** Comparison of liquid chromatography–electrospray ionization MS ions present at an R_f = 0.29 in genomic DNA from cells expressing wild-type (wt) or mutant (mut) TET1-CD. A species with an observed m/z = 336.06 was more abundant by a factor of 18.5 in the wild-type sample compared with the mutant sample. **(C)** Mass spectrometry fragmentation (MS/MS) analysis of authentic hm-dCMP (top), and the m/z = 336.06 species isolated from cells expressing TET1-CD (bottom). Expected m/z values are shown in red; observed m/z values are shown in black (anticipated mass accuracy is within 0.002 Da).

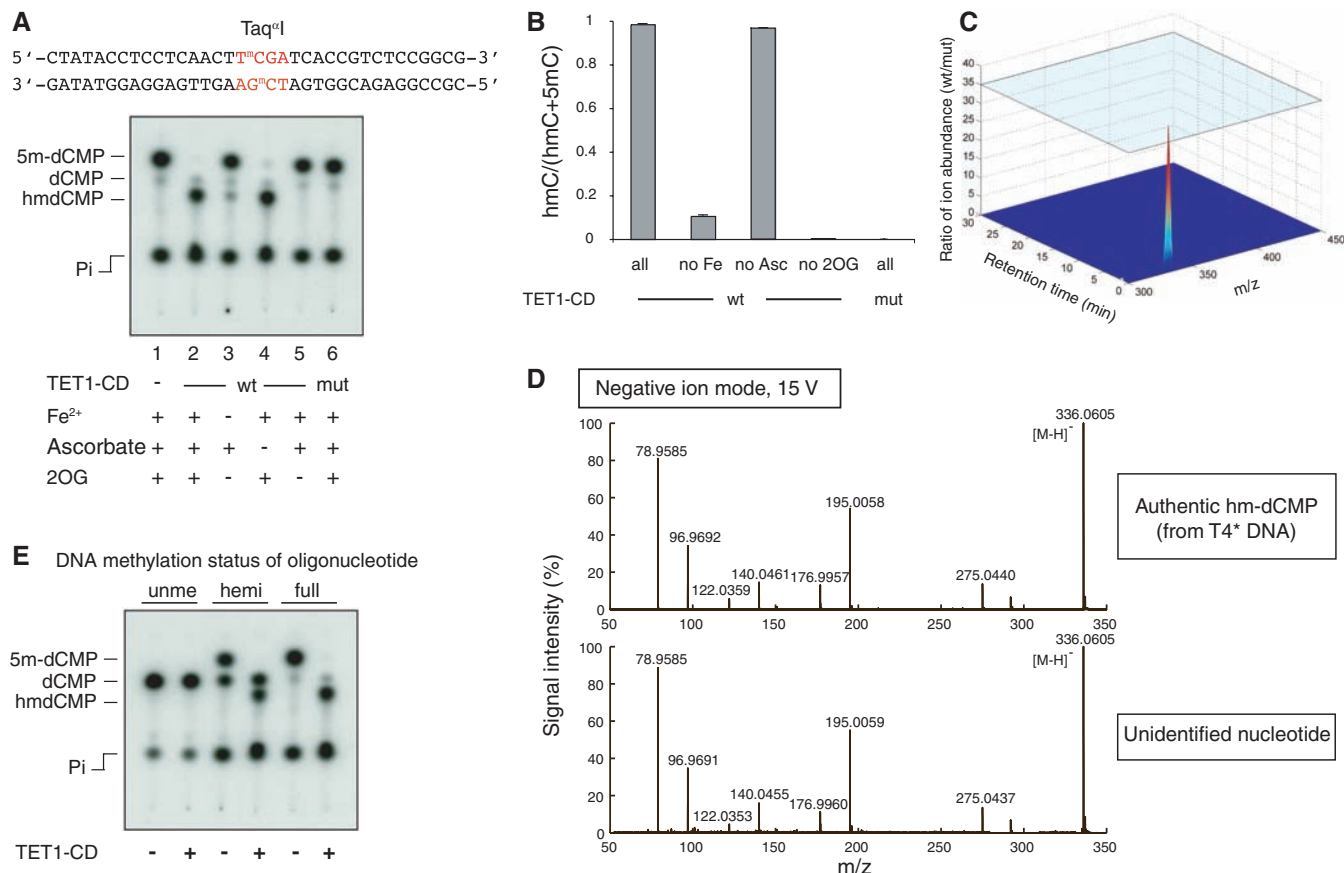


Fig. 4. Recombinant Flag-HA-TET1-CD purified from Sf9 cells converts 5mC to hmC in methylated DNA oligonucleotides in vitro. **(A)** Double-stranded DNA oligonucleotides containing a fully methylated Taq^QI site were incubated with wt or mut Flag-HA-TET1-CD (1:10 enzyme to substrate ratio). Recovered oligonucleotides were digested with Taq^QI and analyzed by TLC. The faint dCMP spot in each lane is derived from end-labeling of the C at the 5' end of each strand of the substrate. **(B)** The extent of conversion of 5mC to hmC is shown as the mean ratio [hmC/(hmC+

5mC)] \pm SD. **(C)** Comparison of species at an Rf of 0.29 in products resulting from incubation with wt or mut Flag-HA-TET1-CD. **(D)** MS fragmentation analysis of authentic hm-dCMP (top) and the nucleotide generated by Flag-HA-TET1-CD (bottom). Observed masses are shown in black (mass accuracy was within 0.002 Da). **(E)** Recombinant Flag-HA-TET1-CD is able to hydroxylate 5mC in fully methylated (full, lanes 5 and 6) and hemimethylated (hemi, lanes 3 and 4) substrates. Unme, unmethylated DNA oligonucleotide (lanes 1 and 2).

unidentified labeled species migrating more slowly than dCMP ("?", Fig. 2B, lanes 2 and 4). This new species was not detected when the DNA was digested with HpaII, the methylation-sensitive isoschizomer of MspI (Fig. 2D) but was clearly observed when the DNA was digested with Taq^QI, a methylation-insensitive enzyme that cuts at a different sequence, T³CGA (Fig. 2E). The new species was not observed in MspI- or Taq^QI-digested DNA from cells transfected with mutant TET1-FL or TET1-CD (Fig. 2, B and E, lanes 3 and 5), and its appearance was associated with decreased abundance of 5m-dCMP (Fig. 2, B and E, lanes 2 and 4; quantified in Fig. 2, C and F). In all experiments, expression of wild-type TET1-CD correlated with a small but significant increase in the abundance of dCMP (Fig. 2, C and F). Together these results suggest that the unidentified species is derived through modification of 5m-dCMP and may be an intermediate in the passive or active conversion of 5mC to C.

We used high-resolution mass spectrometry (MS) to identify the novel nucleotide. Genomic DNA was prepared from HEK293 cells overex-

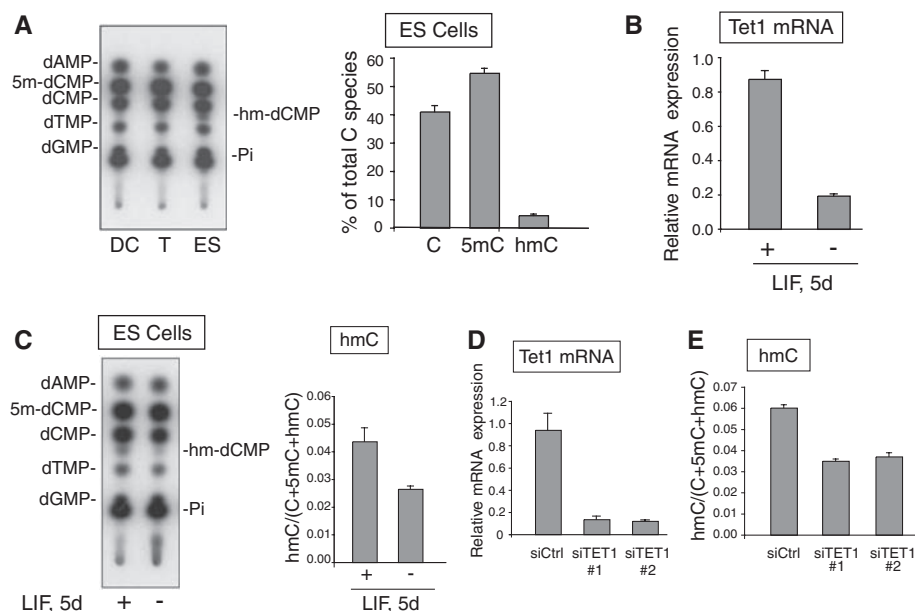
pressing wild-type or mutant TET1-CD. A singly charged species with an observed mass/charge ratio (m/z) of 336.0582, consistent with a molecular formula of $C_{10}H_{15}NO_8P^-$, was the only species migrating at the expected position on TLC that exhibited a large (by a factor of about 19) difference in abundance between the wild-type and mutant samples (Fig. 3, A and B). Based on this result, our computational analyses, and the data of Fig. 2, we hypothesized that the unidentified species was 5-hydroxymethylcytosine (hmC), produced by TET1 through hydroxylation of the methyl group of 5mC (fig. S1). As a standard, we prepared authentic hm-dCMP from unglucosylated DNA of T4 phage grown in *Escherichia coli* ER1656, a strain deficient in the glucose donor molecule UDP-glucose (abbreviated T4* DNA) (12). TLC assays showed that the novel nucleotide generated in unsorted cells expressing TET1-CD migrated similarly to hm-dCMP from T4* DNA (Fig. 3A). Tandem mass spectrometry (MS-MS) fragmentation experiments at several collision energies (15 and 25 V) in both positive and negative ion modes confirmed that the fragmentation pat-

tern of the 336.0582 dalton ion was identical to that of hm-dCMP (Fig. 3C and fig. S5).

To establish that TET1 was directly responsible for hmC production, we expressed Flag-HA-tagged wild-type and mutant TET1-CD in Sf9 insect cells, purified the recombinant proteins to near homogeneity (fig. S6A), and assayed their catalytic activity on fully methylated double-stranded DNA oligonucleotides. Wild-type, but not mutant, TET1-CD catalyzed robust conversion of 5mC to hmC and displayed an absolute requirement for both Fe(II) and 2OG (Fig. 4A; quantified in Fig. 4B). Omission of ascorbate did not result in a significant decrease in catalytic activity, most likely because we included dithiothreitol in the reaction to counteract the strong tendency of TET1-CD to oxidize (fig. S6, A to D) (13–15). Recombinant TET1-CD was specific for 5mC: We did not detect conversion of thymine to hydromethyluracil (hmU) (fig. S7).

We used high-resolution MS to demonstrate, as before, that a singly charged species at m/z of 336.0582 was the only species migrating at the expected position that differed significantly (by a

Fig. 5. hmC is present in ES cell DNA, and its abundance decreases upon differentiation or Tet1 depletion. **(A)** (Left) TLC showing that hmC is detected in the genome of undifferentiated ES cells but not dendritic cells or T cells. (Right) Quantification of the relative abundance by PhosphorImager of 5mC, C, and hmC in the genomic DNA of undifferentiated ES cells. **(B)** Tet1 mRNA levels decline by ~80% in ES cells induced to differentiate by withdrawal of LIF for 5 days. **(C)** The same differentiated ES cells show ~40% decrease in hmC levels. **(D)** Transfection of ES cells using two different RNAi duplexes directed against Tet1 decreases Tet1 mRNA levels by ~75%. **(E)** The same Tet1-depleted ES cells show ~40% decline in hmC levels. Data shown are mean \pm SD and are representative of 2 to 3 experiments.



factor of 35) in abundance when comparing substrates incubated with wild-type and mutant proteins (Fig. 4C). MS-MS experiments confirmed that the fragmentation pattern of the species produced by recombinant TET1-CD was identical to that of authentic hm-dCMP in unglucosylated T4 DNA (Fig. 4D). TET1-CD was also able to oxidize 5mC to hmC in hemimethylated double-stranded DNA (Fig. 4E).

We asked whether hmC was a physiological constituent of mammalian DNA. Using the TLC assay, we observed a clear spot corresponding to labeled hmC in mouse embryonic stem (ES) cells but not in previously activated human T cells or mouse dendritic cells (Fig. 5A). Quantification of multiple experiments indicated that hmC and 5mC constituted 4 to 6% and 55 to 60%, respectively, of all cytosine species in MspI cleavage sites (C⁺CGG) in ES cells (Fig. 5A). Tet1 mRNA levels declined by 80% in response to leukemia inhibitory factor (LIF) withdrawal for 5 days, compared with the levels observed in undifferentiated ES cells (Fig. 5B); in parallel, hmC levels diminished from 4.4 to 2.6% of total C species, a decline of ~40% from control levels (Fig. 5C). The difference might be due to the compensatory activity of other Tet-family proteins. Similarly, RNA interference (RNAi)-mediated depletion of endogenous Tet1 resulted in an 87% decrease in Tet1 mRNA levels and a parallel ~40% decrease in hmC levels (Fig. 5, D and E). Again, the difference is likely due to the presence of Tet2 and Tet3, which are both expressed in ES cells.

Together these data strongly support the hypothesis that Tet1, and potentially other Tet family members, are responsible for hmC generation in ES cells under physiological conditions (fig. S8A). CpG dinucleotides are ~0.8% of all dinucleotides in the mouse genome (16); thus, hmC (which constitutes ~4% of all cytosine species in CpG dinucleotides located in MspI cleavage sites) is

~0.032% of all bases (~1 in every 3000 nucleotides, or $\sim 2 \times 10^6$ bases per haploid genome). For comparison, 5mC is 55 to 60% of all cytosines in CpG dinucleotides in MspI cleavage sites (Fig. 5A), about 14 times as high as hmC (hmC may not be confined to CpG) (SOM Text). An important question is whether hmC and TET proteins are localized to specific regions of ES cell DNA—for instance, genes that are involved in maintaining pluripotency or that are poised to be expressed upon differentiation. A full appreciation of the biological importance of hmC will require the development of tools that allow hmC, 5mC, and C to be distinguished unequivocally (SOM Text).

As a potentially stable base (SOM Text), hmC may influence chromatin structure and local transcriptional activity by recruiting selective hmC-binding proteins or excluding methyl-CpG-binding proteins (MBPs) that normally recognize 5mC, thus displacing chromatin-modifying complexes recruited by MBPs (fig. S8B, center). Indeed, it has already been demonstrated that the methyl-binding protein MeCP2 does not recognize hmC (17). Alternatively, conversion of 5mC to hmC may facilitate passive DNA demethylation by excluding the maintenance DNA methyltransferase DNMT1, which recognizes hmC poorly (fig. S8B, left) (18). Even a minor reduction in the fidelity of maintenance methylation would be expected to result in an exponential decrease in CpG methylation over the course of many cell cycles. Finally, hmC may be an intermediate in a pathway of active DNA demethylation (fig. S8B, right). hmC has been shown to yield cytosine through loss of formaldehyde in photooxidation experiments (19) and at high pH (20, 21), leaving open the possibility that hmC could convert to cytosine under certain conditions in cells. A related possibility is that specific DNA repair mechanisms replace hmC or its derivatives with C (22, 23). In support of this hypothesis, a glycosylase activity specific for hmC was reported

in bovine thymus extracts (24). Moreover, several DNA glycosylases, including TDG and MBD4, have been implicated in DNA demethylation, although none of them has shown convincing activity on 5mC in in vitro enzymatic assays (25–27). Cytosine deamination has also been implicated in demethylation of DNA (26–28); in this context, deamination of hmC yields hmU, and high levels of hmU:G glycosylase activity have been reported in fibroblast extracts (29).

These studies alter our perception of how cytosine methylation may be regulated in mammalian cells. Notably, disruptions of the *TET1* and *TET2* genetic loci have been reported in association with hematologic malignancies (SOM Text). A fusion of *TET1* with the histone methyltransferase *MLL* has been identified in several cases of acute myeloid leukemia (AML) associated with t(10;11)(q22;q23) translocation (30, 31). Homozygous null mutations and chromosomal deletions involving the *TET2* locus have been found in myeloproliferative disorders, suggesting a tumor suppressor function for *TET2* (32, 33). It will be important to test the involvement of TET proteins and hmC in oncogenic transformation and malignant progression.

References and Notes

- M. Ehrlich, R. Y. Wang, *Science* **212**, 1350 (1981).
- M. G. Goll, T. H. Bestor, *Annu. Rev. Biochem.* **74**, 481 (2005).
- W. Reik, *Nature* **447**, 425 (2007).
- A. Bird, *Genes Dev.* **16**, 6 (2002).
- E. N. Gal-Yam, Y. Saito, G. Egger, P. A. Jones, *Annu. Rev. Med.* **59**, 267 (2008).
- P. Borst, R. Sabatini, *Annu. Rev. Microbiol.* **62**, 235 (2008).
- Z. Yu et al., *Nucleic Acids Res.* **35**, 2107 (2007).
- L. J. Cliffe et al., *Nucleic Acids Res.* **37**, 1452 (2009).
- L. Aravind, E. V. Koonin, *Genome Biol.* **2**, RESEARCH0007 (2001).
- M. D. Allen et al., *EMBO J.* **25**, 4503 (2006).
- H. Cedar, A. Solage, G. Glaser, A. Razin, *Nucleic Acids Res.* **6**, 2125 (1979).
- G. R. Wyatt, S. S. Cohen, *Biochem. J.* **55**, 774 (1953).

13. L. Que Jr., R. Y. Ho, *Chem. Rev.* **96**, 2607 (1996).
14. C. Loenarz, C. J. Schofield, *Nat. Chem. Biol.* **4**, 152 (2008).
15. L. E. Netto, E. R. Stadtman, *Arch. Biochem. Biophys.* **333**, 233 (1996).
16. M. W. Simmen, *Genomics* **92**, 33 (2008).
17. V. Valinluck *et al.*, *Nucleic Acids Res.* **32**, 4100 (2004).
18. V. Valinluck, L. C. Sowers, *Cancer Res.* **67**, 946 (2007).
19. E. Privat, L. C. Sowers, *Chem. Res. Toxicol.* **9**, 745 (1996).
20. J. G. Flaks, S. S. Cohen, *J. Biol. Chem.* **234**, 1501 (1959).
21. A. H. Alegria, *Biochim. Biophys. Acta* **149**, 317 (1967).
22. S. K. Ooi, T. H. Bestor, *Cell* **133**, 1145 (2008).
23. J. Jiricny, M. Menigatti, *Cell* **135**, 1167 (2008).
24. S. V. Cannon, A. Cummings, G. W. Teebor, *Biochem. Biophys. Res. Commun.* **151**, 1173 (1988).
25. B. Zhu *et al.*, *Proc. Natl. Acad. Sci. U.S.A.* **97**, 5135 (2000).
26. R. Metivier *et al.*, *Nature* **452**, 45 (2008).
27. S. Kangaspeka *et al.*, *Nature* **452**, 112 (2008).
28. K. Rai *et al.*, *Cell* **135**, 1201 (2008).
29. V. Rusmintrati, L. C. Sowers, *Proc. Natl. Acad. Sci. U.S.A.* **97**, 14183 (2000).
30. R. Ono *et al.*, *Cancer Res.* **62**, 4075 (2002).
31. R. B. Lorsch *et al.*, *Leukemia* **17**, 637 (2003).
32. F. Viguie *et al.*, *Leukemia* **19**, 1411 (2005).
33. F. Delhommeau *et al.*, paper presented at the American Society of Hematology Annual Meeting and Exposition, San Francisco, CA, December 9, 2008.
34. We thank K. Kreuzer for the gift of the T4 phage and *E. coli* ER1656 and CR63; Charles Richardson, Udi Qimron, and Ben Beauchamp for advice and assistance in culturing T4 phage; Melissa Call for advice on production of recombinant proteins in insect cells; and Patrick Hogan for many helpful discussions. This work was supported by NIH grant AI44432, a Scholar Award from the Juvenile Diabetes Research Foundation, and a Seed grant from the Harvard Stem Cell Institute (to A.R.); Howard Hughes Medical Institute and NIH/NIGMS

(R01GM065865) funding (to D.R.L.); an American Heart Association postdoctoral fellowship (to K.P.K.); intramural funds of the National Library of Medicine, NIH (to L.A. and L.I.); a Lady Tata Memorial postdoctoral fellowship (to H.B.); NIH award K08 HL089150 (to S.A.); NSF Graduate Fellowships (to W.A.P. and Y.B.); and a Department of Defense graduate fellowship (to W.A.P.).

Supporting Online Material

www.sciencemag.org/cgi/content/full/1170116/DC1
Materials and Methods

SOM Text

Figs. S1 to S8

References

22 December 2008; accepted 3 April 2009

Published online 16 April 2009;

10.1126/science.1170116

Include this information when citing this paper.

A Functional Role for Transposases in a Large Eukaryotic Genome

Mariusz Nowacki,¹ Brian P. Higgins,¹ Genevieve M. Maquilan,¹ Estienne C. Swart,¹ Thomas G. Doak,² Laura F. Landweber^{1*}

Despite comprising much of the eukaryotic genome, few transposons are active, and they usually confer no benefit to the host. Through an exaggerated process of genome rearrangement, *Oxytricha trifallax* destroys 95% of its germline genome during development. This includes the elimination of all transposon DNA. We show that germline-limited transposase genes play key roles in this process of genome-wide DNA excision, which suggests that transposases function in large eukaryotic genomes containing thousands of active transposons. We show that transposase gene expression occurs during germline-soma differentiation and that silencing of transposase by RNA interference leads to abnormal DNA rearrangement in the offspring. This study suggests a new important role in *Oxytricha* for this large portion of genomic DNA that was previously thought of as junk.

Oxytricha trifallax, a ciliated protozoan, is a unicellular eukaryote with two types of nuclei in the same cytoplasm. Diploid micronuclei are transcriptionally silent during vege-

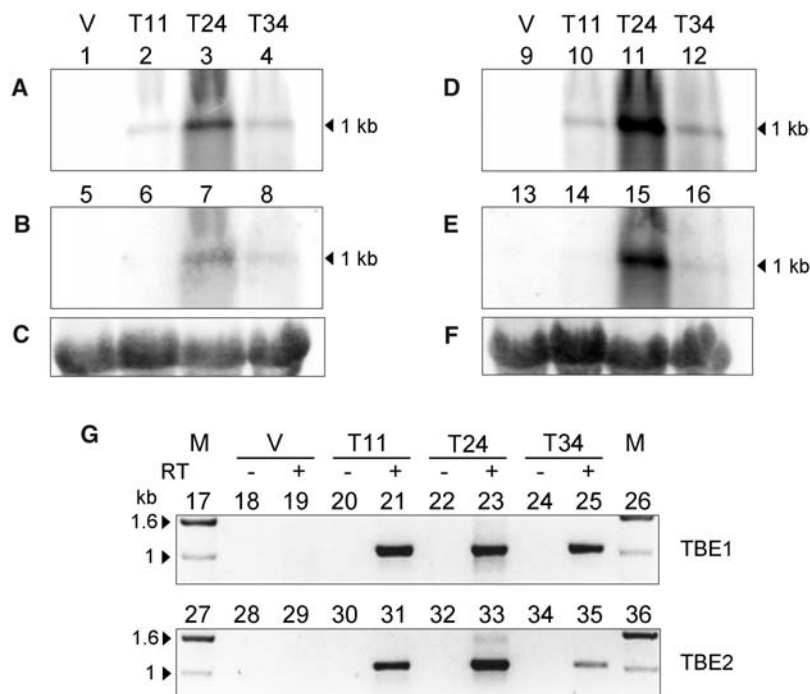
tative growth but transmit the germline genome through sexual conjugation (fig. S1). After sex, the gene-rich macronuclei that govern somatic gene expression degrade, and new macronuclei

develop from germline micronuclei. Macronuclear development in *Oxytricha* (also called *Sterkiella*) involves massive chromosome fragmentation and the deletion of thousands of copies of germline transposons (selfish DNA elements that are capable of self-replication in their host genomes) plus the destruction of intergenic DNA and noncoding DNA sequences that interrupt genes [internally eliminated sequences (IESs)]. This leads to a 95% reduction in sequence complexity, compressing the 1-Gb germline genome into a gene-dense macronuclear genome of only ~50 Mb. Sorting and reordering the hundreds of thousands of remaining short pieces [macronuclear-destined segments (MDSs)] produces mature macronuclear sequences. The resulting ~2-kb nanochromo-

¹Department of Ecology and Evolutionary Biology, Princeton University, Princeton, NJ 08544, USA. ²Department of Biology, Indiana University, Bloomington, IN 47405, USA.

*To whom correspondence should be addressed. E-mail: lfl@princeton.edu

Fig. 1. Expression of TBE transposase genes. (A to F) Northern hybridization against total RNA extracted from vegetative cells (V) as well as 11-, 24-, and 34-hour time points (T) after mixing of mating types. TBE transposase transcripts are most abundant 24 hours after mixing, when DNA rearrangements occur (22). 10 µg of RNA was loaded per lane and hybridized to ~1-kb DNA probes (23) for (A) TBE1, (B) TBE3, (D) TBE1, -2, and -3 mixed together (1:1:1 ratio), (E) TBE2 transposase, and (C and F) small-subunit ribosomal RNA (rRNA); (C) is the control for (A) and (B), and (F) is the control for (D) and (E). (G) Reverse transcription PCR of TBE1 (lanes 17 to 26) and TBE2 (lanes 27 to 36) transposase polyadenylate-containing mRNA from vegetative cells (V) and three time points (T) during conjugation (23). Plus and minus symbols indicate the presence or absence of reverse transcriptase (RT), respectively. Arrowheads indicate the size of relevant markers [1-kb ladder (Invitrogen, Carlsbad, CA)].



somes typically bear only a single gene bound by short telomeres and amplified to a high copy number (1). The remarkable degree of specificity and reproducibility of genome reorganization in ciliates relies on RNA template-guided transnuclear comparison of germline and somatic genomes (2–5). However, the molecular machinery responsible for this DNA excision and recombination remains unknown.

O. trifallax carries thousands of germline-limited transposable elements in its diploid micronucleus (6). These DNA sequences are restricted to the micronucleus and absent from the macronucleus because they are deleted during genome differentiation. Because they are ~4-kb repetitive sequences flanked by blocks of *Oxytricha* telomeric repeats (G₄T₄)₄, they have been designated telomere-bearing elements (TBEs) (7). Several lines of evidence suggest that TBEs transpose through a DNA intermediate: Apart from the presence of 3-bp insertion site duplications and inverted terminal repeats, TBEs code for a 42-kD member of a superfamily of transposases, characterized by a DDE catalytic motif (fig. S2) (8, 9). Moreover, phylogenetic evidence supports a recent origin of TBE insertions (10). *Oxytricha* TBEs comprise three known types: TBE1, -2, and -3, whose transposase genes differ 26 to 29% from each other at the nucleotide level (table S1A) while sharing high protein similarity (≥83%). Previous examination of *Oxytricha* TBE1 transposase genes identified no copies that were interrupted by stop codons or frame shifts and provided evidence of purifying selection acting on their encoded proteins (6, 8), which suggests that the encoded transposase might be responsible for the excision of TBE1 elements during macronuclear development (11, 12).

In order to test whether germline-encoded TBE transposases function in somatic DNA deletion and rearrangement, we examined the expression and function of TBE transposases, given their ability to cut and join DNA (11). First, we asked whether TBE transposase genes are expressed during macronuclear development (Fig. 1). We examined the expression of transposases from both vegetative and conjugating cells [at 11, 24, and 34 hours after the initiation of mating (mixing of mating types)], which revealed that they were expressed exclusively during conjugation; the highest expression level occurred 24 hours after mixing [most likely coinciding with polytene chromosome formation and TBE1 elimination (11)]. The presence of polyadenylated transcripts (Fig. 1G) at this stage was confirmed, suggesting that TBE expression occurs during DNA rearrangement and that transposase could therefore play a role in their elimination.

In order to determine whether transposases influence developmental DNA rearrangements, we silenced all three transposase types by microinjecting double-stranded RNA (dsRNA) into the cytoplasm at three different stages during conjugation, including at (i) early pair formation, 3 to 5 hours after the mixing of different mating types;

(ii) 10 hours after mixing, right before pair separation; and (iii) 12 to 15 hours after mixing, right after pair separation (table S2). We observed the

greatest effect when dsRNA was injected 12 to 15 hours after mixing because few cells survived and those that survived showed delayed growth.

Fig. 2. Silencing of TBE transposases leads to accumulation of aberrantly processed DNA. MDS segments (white boxes) and IESs (hatched boxes) are shown schematically and not to scale. Shown are the sequences of PCR products for *TEBPβ* between segments 2 and 7 in the progeny of triply silenced cells treated 12 to 15 hours after mixing; shown are all 32 examples of aberrantly rearranged chromosomes found among 37 sequenced clones [redundancy is indicated by the number after an x (table S2)]. Open triangles indicate locations of cryptic junctions between neighboring (pointing up) and nonneighboring (pointing down) segments on the basis of precursor micronuclear order. MIC, nonrearranged micronuclear gene sequences; MAC, expected rearranged macronuclear gene sequences.

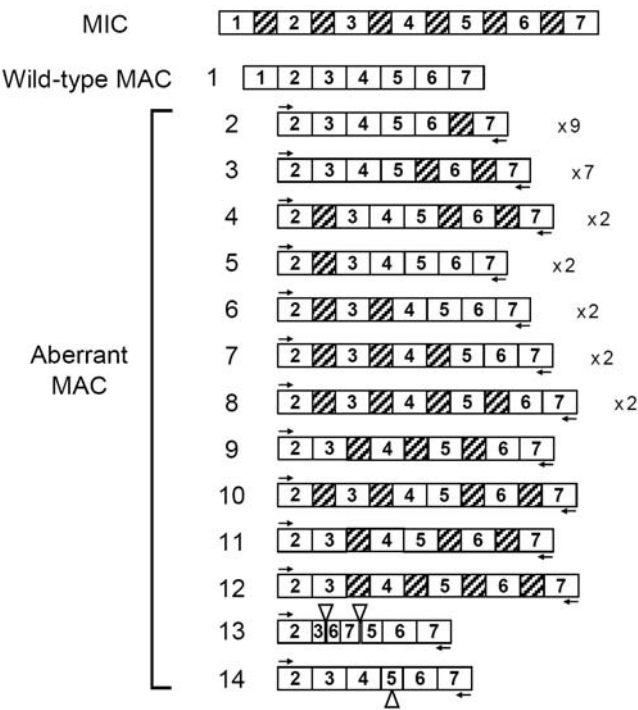
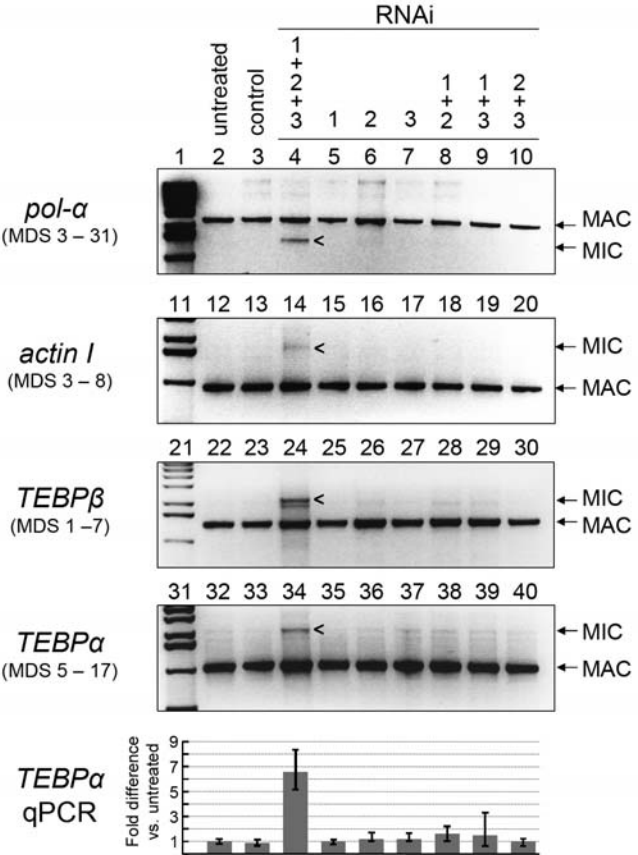


Fig. 3. RNA interference (RNAi) against TBE transposases leads to accumulation of nonprocessed DNA. PCR amplification of gene regions between two distant MDSs is shown (*pol-α* between MDSs 3 to 31; *actin 1* between MDSs 3 to 8; *TEBPβ* between MDSs 1 to 7; and *TEBPα* between MDSs 5 to 17) (23). Samples that were triply silenced (12 to 15 hours after mixing) against all three TBE transposases (lanes 4, 14, 24, and 34) show accumulation of nonrearranged (MIC) gene versions. Controls were non-treated cells (lanes 2, 12, 22, and 32) and cells injected with 184-nucleotide vector polylinker dsRNA (lanes 3, 13, 23, and 33); MAC, macronuclear; MIC, micronuclear. Quantitative PCR (QPCR) with *TEBPα* primers shows 6.55-fold more nonrearranged DNA as compared with that of the untreated control in the triple silencing example (bottom).



DNA that was extracted from the progeny of cells injected ~10 hours and 12 to 15 hours after mixing and cultured for only 1 week sometimes contained incorrect DNA rearrangements as well as increased levels of nonprocessed DNA in the new macronucleus, as revealed by polymerase chain reaction (PCR) examination of three genes: *telomere end-binding protein α subunit* (*TEBP α*), *telomere end-binding protein β subunit* (*TEBP β*), and *DNA polymerase α* (*pol- α*) (Fig. 2, fig. S3, and table S2). The cells that were injected 12 to 15 hours after mixing and harvested after 2 weeks of growth, on the other hand, evidenced no partial rearrangements, even in clones from the region of the gel corresponding to partially processed forms (in between the visible precursor- and product-sized bands) or by direct cloning of all amplified DNA, presumably because of reversion to the wild type during extended culture (5).

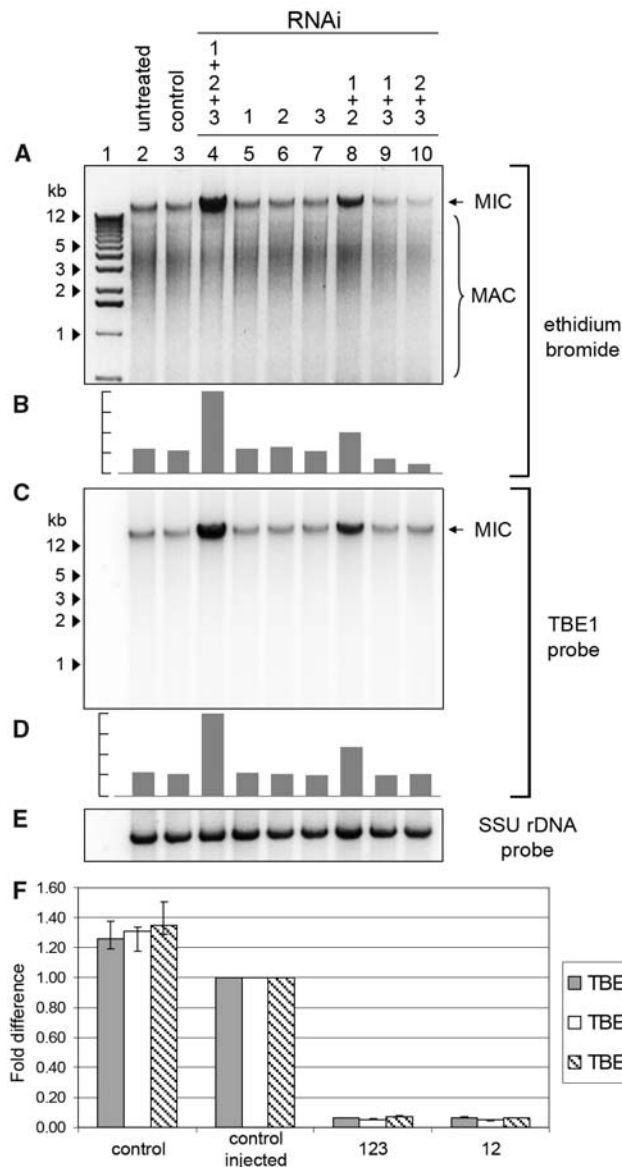
At 12 to 15 hours after mixing, we silenced each transposase type individually (TBE1, TBE2, or TBE3) as well as all three possible pairs and all three types together. Because triple silencing at 12 to 15 hours after mixing reliably inhibited rearrangements (Fig. 3), we repeated the triple silencing and the combination of TBE1 and TBE2 at this time point and also analyzed transposase mRNA levels (Fig. 4F). None of the single or other paired treatments had a strong effect. PCR at several loci in the progeny of cells triply silenced at 12 to 15 hours revealed a substantial accumulation of precursor nonrearranged versions of each gene (Fig. 3 and table S2, B and C), indicating stalled rearrangement. A weak effect was also observed after TBE1 and TBE2 were simultaneously silenced (fig. S4A). Normally the precursor, micronuclear DNA is rare and hard to detect (untreated lanes in Fig. 3 and fig. S4, A and B) relative to the macronuclear products, which have roughly a 1000-

fold amplification. The abundance of precursor-sized product in TBE-silenced cells strongly suggests an increase in the ratio of nonrearranged to rearranged DNA. This was confirmed in the progeny of triply silenced versus control cells, with nonrearranged versions of *TEBP α* displaying a 6.6- or 3.2-fold greater abundance in the two independent experiments performed at 12 to 15 hours after mixing (Fig. 3 and fig. S4).

Unprocessed germline chromosomes in *Oxytricha* are much longer than somatic molecules. Therefore, we confirmed that the progeny of triply silenced and TBE1- and TBE2-silenced cells contain more high-molecular weight DNA (limited by mobility in the gel) than do control cells (Fig. 4A and fig. S4D) and noted a fourfold increase when all TBE genes were silenced and a twofold increase when TBE1 and TBE2 were silenced (Fig. 4B and fig. S4D). In addition, we observed an increased hybridization of the high-molecular weight DNA to transposase DNA (Fig. 4, C and D, and fig. S4D), which is consistent with the hypothesis that these cells had a reduced ability to eliminate these transposons, which represent approximately 2% of the germline genome. Furthermore, we also observed no hybridization of transposase DNA to macronuclear-sized (<12 kb) molecules (Fig. 4C and fig. S4D), which is consistent with prior observations that TBE transposons are absent from macronuclear chromosomes (7, 11, 13). The silencing of the three transposase types (and to some extent TBE1 and TBE2 together) alters the efficiency of developmental DNA rearrangements, including chromosome fragmentation, and this leads to the accumulation of long nonprocessed DNA molecules. Our results suggest that germline-limited transposase genes in *Oxytricha* function in genome rearrangement.

These transposons might not merely be parasitic invaders that reduce host fitness or have little phenotypic effect (14, 15) but instead mutualists directly contributing a useful function for the organism (12), such as genomic DNA processing. This would also account for the evidence that strong purifying selection (6, 16) acts on TBE-encoded proteins (fig. S5 and table S3). Particularly striking is that all three TBE transposase groups need to be silenced to achieve the greatest effect. Given the massive level of DNA deletion and reorganization in *Oxytricha*, it is possible that the three types have either specialized or overlapping functions or that their contributions are additive. A high level of transposase activity may be necessary to facilitate thousands of simultaneous DNA rearrangements, affording an indispensable role to the large quantity of germline-limited transposable elements, which were previously considered selfish DNA or part of the dispensable genome (17). This mutualism (18) is uniquely different from other known cases of transposon domestication, such as RAG recombinase (19), piggyBac (20), or Mariner (21), in which a single transposase copy has assumed a host function. The situation in *Oxytricha* could also be viewed as a case of massive transposon domestication, in

Fig. 4. Transposase silencing leads to increased levels of nonprocessed high-molecular weight DNA and transposon retention. (A) 1 μ g total DNA from vegetative progeny of cells treated with RNAi against TBE transposases (lanes 4 to 10) as well as untreated and control cells (23); ethidium bromide staining was used. (C) DNA from (A) hybridized to a TBE1 transposase DNA probe (23). Samples that were treated with RNAi (12 to 15 hours after mixing) against all three transposases or TBE1 and -2 together (lanes 4 and 8) show increased levels of (A) high-molecular weight DNA and (C) TBE1 hybridization to high-molecular weight DNA as well as decreased levels of transposase mRNA (F). (B and D) Gray bars indicate relative amount of ethidium bromide (B) and TBE1 probe signals (D) in high-molecular weight DNA. (E) Control hybridization with a small-subunit rDNA probe. Arrowheads indicate size of relevant markers (1-kb ladder). (F) Relative transposase mRNA levels for TBE1, TBE2, and TBE3 in injected (12 to 15 hours after mixing) versus noninjected cells in an independent experiment (23). Absolute values for each transcript were obtained with QPCR (in femtograms) and normalized against the transcript level for the mitochondrial large-subunit rRNA. Transcript levels of the control injected sample were set to 1.



which thousands of unmodified transposons may have been recruited for their transposase as part of the catalytic machinery of RNA-guided genome rearrangements just before they are eliminated from the macronuclear genome. In support of this model, we found that IES excision can precede transposon elimination (fig. S6), refuting a simple indirect effect of genome rearrangements occurring only after transposon processing. Transient TBE transposase expression begins after meiosis (Fig. 1 and fig. S1) and coincides with the production of maternal RNA templates that guide rearrangement (5) as well as all events of DNA processing, including TBE transposon elimination, IES excision, and segment-reordering in the developing nucleus (22).

References and Notes

1. D. M. Prescott, *Microbiol. Rev.* **58**, 233 (1994).
2. D. L. Chalker, M. C. Yao, *Mol. Cell. Biol.* **16**, 3658 (1996).
3. S. Duhaucourt, A. M. Keller, E. Meyer, *Mol. Cell. Biol.* **18**, 7075 (1998).
4. K. Mochizuki, N. A. Fine, T. Fujisawa, M. A. Gorovsky, *Cell* **110**, 689 (2002).
5. M. Nowacki *et al.*, *Nature* **451**, 153 (2008).
6. D. J. Witherspoon *et al.*, *Mol. Biol. Evol.* **14**, 696 (1997).
7. G. Herrick *et al.*, *Cell* **43**, 759 (1985).
8. T. G. Doak, F. P. Doerder, C. L. Jahn, G. Herrick, *Proc. Natl. Acad. Sci. U.S.A.* **91**, 942 (1994).
9. Single-letter abbreviations for the amino acid residues are as follows: A, Ala; C, Cys; D, Asp; E, Glu; F, Phe; G, Gly; H, His; I, Ile; K, Lys; L, Leu; M, Met; N, Asn; P, Pro; Q, Gln; R, Arg; S, Ser; T, Thr; V, Val; W, Trp; and Y, Tyr.
10. A. Seegmiller *et al.*, *Mol. Biol. Evol.* **13**, 1351 (1996).
11. K. Williams, T. G. Doak, G. Herrick, *EMBO J.* **12**, 4593 (1993).
12. L. A. Klobutcher, G. Herrick, *Prog. Nucleic Acid Res. Mol. Biol.* **56**, 1 (1997).
13. D. J. Hunter, K. Williams, S. Carinhour, G. Herrick, *Genes Dev.* **3**, 2101 (1989).
14. W. F. Doolittle, C. Sapienza, *Nature* **284**, 601 (1980).
15. L. E. Orgel, F. H. Crick, *Nature* **284**, 604 (1980).
16. T. G. Doak, D. J. Witherspoon, F. P. Doerder, K. Williams, G. Herrick, *Genetica* **101**, 75 (1997).
17. M. Morgante, P. De Paoli, S. Radovic, *Curr. Opin. Plant Biol.* **10**, 149 (2007).
18. M. G. Kidwell, A. J. Lish, *Evolution* **55**, 1 (2001).
19. V. V. Kapitonov, J. Jurka, *PLoS Biol.* **3**, e181 (2005).
20. A. Sarkar *et al.*, *Mol. Genet. Genomics* **270**, 173 (2003).
21. H. M. Robertson, K. L. Zumpano, *Gene* **205**, 203 (1997).
22. M. Möllenbeck *et al.*, *PLoS One* **3**, e2330 (2008).
23. Materials and methods are available as supporting material on Science Online.
24. This work was supported by NSF grant 0622112 and NIH grant GM59708. We thank J. Wang for technical assistance. DNA sequences have been deposited in GenBank under accession numbers FJ666213-FJ666314 (TBE transposases), FJ545743 (ribosomal DNA (rDNA) macronucleus), and FJ545744 (rDNA micronucleus).

Supporting Online Material

www.sciencemag.org/cgi/content/full/1170023/DC1

Materials and Methods

Figs. S1 to S6

Tables S1 to S4

References

DNA Sequence Data Files S1 to S8

19 December 2008; accepted 1 April 2009

Published online 16 April 2009;

10.1126/science.1170023

Include this information when citing this paper.

MAPK3/1 (ERK1/2) in Ovarian Granulosa Cells Are Essential for Female Fertility

Heng-Yu Fan,¹ Zhilin Liu,¹ Masayuki Shimada,² Esta Sterneck,³ Peter F. Johnson,⁴ Stephen M. Hedrick,⁵ JoAnne S. Richards^{1*}

A surge of luteinizing hormone (LH) from the pituitary gland triggers ovulation, oocyte maturation, and luteinization for successful reproduction in mammals. Because the signaling molecules RAS and ERK1/2 (extracellular signal-regulated kinases 1 and 2) are activated by an LH surge in granulosa cells of preovulatory follicles, we disrupted *Erk1/2* in mouse granulosa cells and provide in vivo evidence that these kinases are necessary for LH-induced oocyte resumption of meiosis, ovulation, and luteinization. In addition, biochemical analyses and selected disruption of the *Cebpb* gene in granulosa cells demonstrate that C/EBP β (CCAAT/Enhancer-binding protein- β) is a critical downstream mediator of ERK1/2 activation. Thus, ERK1/2 and C/EBP β constitute an in vivo LH-regulated signaling pathway that controls ovulation- and luteinization-related events.

In the mammalian ovary, the female germ cells (oocytes) reside within the ovarian follicles and are surrounded by somatic cell-derived granulosa cells (GCs) and cumulus cells that have endocrine functions and control oocyte maturation. Female reproductive success depends on the growth of ovarian follicles and differentiation of GCs as well as oocyte maturation and ovulation (1, 2). Although LH plays a critical role in the initiation of ovulation and in the terminal differentiation of GCs to luteal cells that compose the corpora lutea (CLs) and produce progesterone, the precise molecular targets in these processes remain ill-defined. Cyclic adenosine 3',5'-monophosphate (cAMP) is a well-known mediator of LH action, but LH also induces expression of the epidermal growth factor (EGF)-like factors that, via activation of the EGF receptor, RAS, and extracellular signal-regulated kinases 1 and 2 [ERK1/2, also known as mitogen-activated protein kinases 3 and 1 (MAPK3/1)], may act as the intrafollicular mediators to stimulate the cumulus cell-oocyte complex (COC) expansion and oocyte maturation (3–5). However, specific role(s) of the EGF network and, more specifically, of ERK1/2 in regulating ovulation, oocyte maturation, and the global reprogramming of GCs to luteal cells have not yet been analyzed or defined clearly in vivo.

tion and ovulation (1, 2). Although LH plays a critical role in the initiation of ovulation and in the terminal differentiation of GCs to luteal cells that compose the corpora lutea (CLs) and produce progesterone, the precise molecular targets in these processes remain ill-defined. Cyclic adenosine 3',5'-monophosphate (cAMP) is a well-known mediator of LH action, but LH also induces expression of the epidermal growth factor (EGF)-like factors that, via activation of the EGF receptor, RAS, and extracellular signal-regulated kinases 1 and 2 [ERK1/2, also known as mitogen-activated protein kinases 3 and 1 (MAPK3/1)], may act as the intrafollicular mediators to stimulate the cumulus cell-oocyte complex (COC) expansion and oocyte maturation (3–5). However, specific role(s) of the EGF network and, more specifically, of ERK1/2 in regulating ovulation, oocyte maturation, and the global reprogramming of GCs to luteal cells have not yet been analyzed or defined clearly in vivo.

ERK1 and ERK2 are coexpressed in all mammalian tissues and implicated as key regulators of cell proliferation and differentiation as well as oocyte maturation in culture (6, 7). Mutant mouse models have shown that *Erk1*-null mice are viable and fertile (8), but mutation of the *Erk2* gene is embryonic lethal in mice (9). To analyze the specific ovarian functions of ERK1 and ERK2 in vivo, we crossed *Erk2^{fl/fl}* mice (10) with the *Cyp19-Cre* transgenic mice (11), and the resultant *Erk2^{fl/fl};Cyp19-Cre* mice were further crossed into the *Erk1^{-/-}* background (8), yielding *Erk1^{-/-};Erk2^{fl/fl};Cyp19-Cre* (*Erk1/2^{sc-/-}*) mice. Efficient depletion of ERK1 and/or ERK2 in the mutant GCs and cumulus cells, as well as the lack of phosphorylation of ERK1/2 in the mutant GCs in vivo, was demonstrated (fig. S1, A to C). Loss of ERK1/2 did not impair LH-mediated activation of known upstream regulators of ERK1/2 or other LH-regulated signaling molecules (fig. S1, D and E) but did block phosphorylation of the ERK1/2 target RPS6KA2 (P90RSK) (fig. S1D).

The *Erk1^{-/-}* and *Erk2^{sc-/-}* females were fertile; however, the *Erk1/2^{sc-/-}* females failed to ovulate and were completely infertile (Fig. 1A). Ovaries of adult *Erk1/2^{sc-/-}* females contained preovulatory follicles but no CLs (fig. S2A). Concentrations of estradiol in serum were elevated (fig. S2B), causing constant vaginal estrus (fig. S2C). Even in immature *Erk1/2^{sc-/-}* females treated with exogenous hormones, events associated with ovulation did not occur: No oocytes matured, as indicated by the complete lack of germinal vesicle breakdown (GVBD) (Fig. 1A); no COCs expanded (Fig. 1, B and C, and fig. S2D); no follicles ruptured to form CLs (Fig. 1, D and E); and the concentration of estradiol in serum was elevated but that of progesterone was not (Fig. 1F), indicating profound endocrine changes in the mutant mouse ovaries. GCs in the equine chorionic gonado-

¹Department of Molecular and Cellular Biology, Baylor College of Medicine, 1 Baylor Plaza, Houston, TX 77030, USA.

²Department of Applied Animal Science, Graduate School of Biosphere Science, Hiroshima University, Higashi-Hiroshima, 739-8528, Japan. ³Laboratory of Cell and Developmental Signaling, Center for Cancer Research, National Cancer Institute-Frederick, Frederick, MD 21702–1201, USA. ⁴Basic Research Laboratory, Center for Cancer Research, National Cancer Institute-Frederick, Frederick, MD 21702–1201, USA. ⁵Molecular Biology Section, Division of Biological Sciences and Department of Cellular and Molecular Medicine, University of California, San Diego, La Jolla, CA 92093, USA.

*To whom correspondence should be addressed. E-mail: joanner@bcm.edu

tropin (eCG)-primed *Erk1/2^{gc/-}* females were viable but exhibited signs of apoptosis when luteinization failed (fig. S2E).

Specific analyses of oocyte functions showed that oocytes isolated from the COCs of *Erk1/2^{gc/-}* mutant mice spontaneously underwent GVBD in culture and progressed to metaphase II stage, as did controls (fig. S3A). By contrast, when spontaneous GVBD was blocked by hypothanxine (HX), the EGF-like factor amphiregulin (AREG) stimulated GVBD in wild-type (WT) but not *Erk1/2^{gc/-}* COCs (fig. S3B). In addition, AREG stimulated expansion of COCs isolated from WT, but not the *Erk1/2^{gc/-}* mice (fig. S3C). These results indicate that the oocytes that retain ERK1/2 in the *Erk1/2^{gc/-}* mice are competent for meiotic maturation, but the cumulus cells lacking ERK1/2 (fig. S1B) fail to respond to EGF-like factors.

Furthermore, the ability of LH/hCG (human chorionic gonadotropin) to terminate GC proliferation was impaired in the *Erk1/2^{gc/-}* mice, as indicated by elevated incorporation of bromodeoxyuridine (BrdU) (Fig. 2, A and B, and fig. S4, A and B) and expression of positive cell cycle-regulatory molecules CCND2, CCNA, and E2F1 and reduced expression of CDKN1B and CDKN1A (fig. S4, C and D) in the mutant ovaries compared to controls. Thus, ERK1/2 control GC fate decisions at this critical stage of their differentiation.

To identify ERK1/2 target genes in preovulatory follicles, we analyzed gene expression profiles using RNA prepared from GCs obtained from WT and *Erk1/2^{gc/-}* mice treated with eCG for 48 hours and at 0, 2.5, and 4 hours after hCG injection because the activation of ERK1/2 peaks at 2 hours after hCG treatment (11, 12) and many genes that affect ovulation are maximally expressed by 4 hours (5). Among the 563 highly regulated LH target genes (more than fourfold, hCG at 4 hours versus hCG at 0 hours; 466 with increased and 97 with decreased expression, tables S1 and S2), 77% (376 with increased and 57 with decreased expression) lost their response to LH/hCG in the *Erk1/2^{gc/-}* cells (Fig. 3A). Two identified ERK1/2 target genes that regulate estradiol biosynthesis and activity are *Cyp19a1* (aromatase), which converts testosterone to estradiol, and *Sult1e1*, which deactivates estradiol (13). Whereas hCG turns off *Cyp19a1* expression in WT mice, *Cyp19a1* was markedly increased in the *Erk1/2^{gc/-}* cells. By contrast, hCG transiently induced *Sult1e1* in WT but not *Erk1/2^{gc/-}* GCs (Fig. 3B and tables S1 and S2), leading to inappropriately high estradiol concentrations (Fig. 1F and fig. S2B) that may adversely affect the ovary and other tissues as well (13). Conversely, two luteinization markers, *Star* and *Cyp11a1*, were substantially reduced in the *Erk1/2^{gc/-}* ovaries, consistent with the lack of CLs in the mutant mice (Fig. 2, C to F, and fig. S5, A and B).

The expression of many genes associated with COC expansion and ovulation (*Ptgs2*, *Tnfrsf6*, *Has2*, *Ptx3*, and *Pgr*) was abolished

in the *Erk1/2^{gc/-}* ovaries, as indicated by the microarray data (table S1), quantitative reverse transcription-polymerase chain reaction (qRT-PCR) (Fig. 3C and fig. S5A), and immunoflu-

orescence (fig. S5D), whereas genes encoding the two EGF-like factors *Areg* and *Ereg*, presumed mediators of LH action, were induced rapidly to normal (*Ereg*) or reduced (*Areg*) levels compared

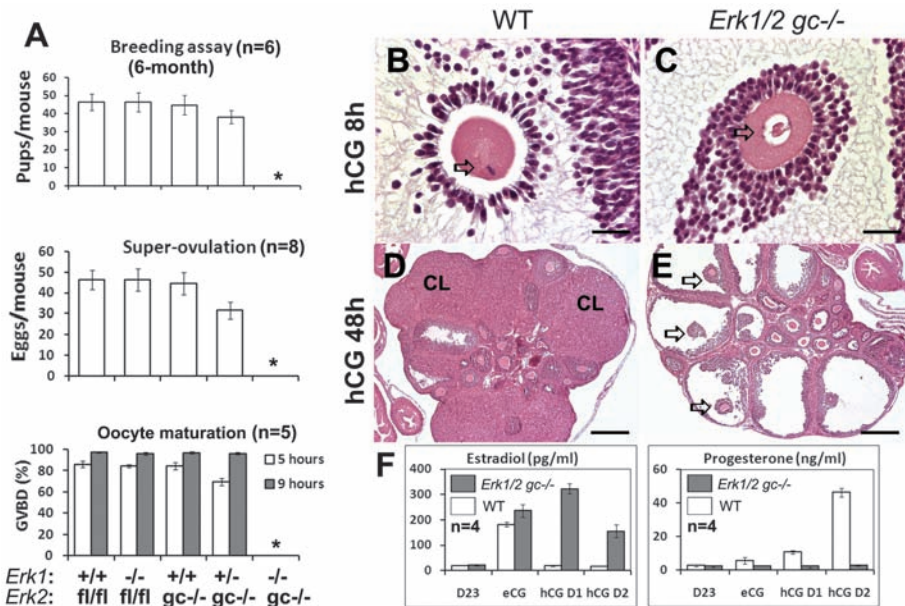
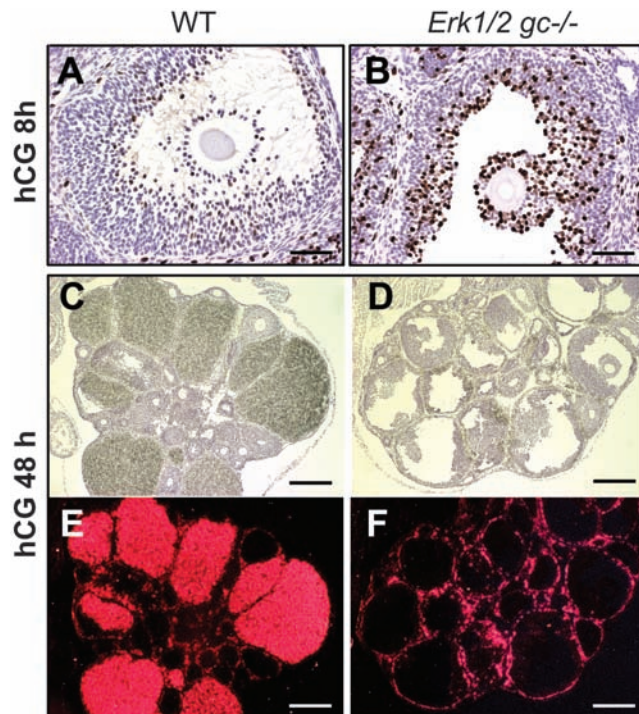


Fig. 1. ERK1/2 mediate LH-induced oocyte maturation, ovulation, and luteinization. (A) Breeding assays, superovulation assays, and oocyte maturation (germinal vesicle breakdown; GVBD) rate in the different mouse genotypes. An asterisk (*) indicates that the data point is zero. Error bars denote SD. (B to E) Hematoxylin and eosin (H&E) staining of ovaries from immature WT and *Erk1/2^{gc/-}* mice treated with hCG for 8 hours (B and C) or 48 hours (D and E). CL: corpus luteum. In (B) and (C), arrows indicate the nuclear configuration of the oocyte nucleus. Scale bars, 31.25 μ m. In (D) and (E), arrows indicate nonovulated COCs in preovulatory follicles. Scale bars, 250 μ m. (F) Changes in estradiol and progesterone concentrations in serum after hCG treatment of eCG-primed 3-week-old WT and *Erk1/2^{gc/-}* females. D23: postnatal day 23; eCG: 23-day-old female mice treated with eCG for 48 hours; hCG D1 and hCG D2: 23-day-old females treated with eCG for 48 hours followed by hCG for 24 hours (D1) or 48 hours (D2).

Fig. 2. ERK1/2 are required for the terminal differentiation of GCs during ovulation. (A and B) BrdU staining of WT and *Erk1/2^{gc/-}* ovary sections at 8 hours after hCG treatment. Scale bars, 62.5 μ m. (C to F) In situ hybridization shows the expression of *Cyp11a1* mRNA in ovaries of WT and *Erk1/2^{gc/-}* mice at 48 hours after hCG treatment. Histology of the ovaries is shown by hematoxylin staining (C and D); localization of *Cyp11a1* mRNA is shown by dark-field images (E and F). Scale bars, 250 μ m.



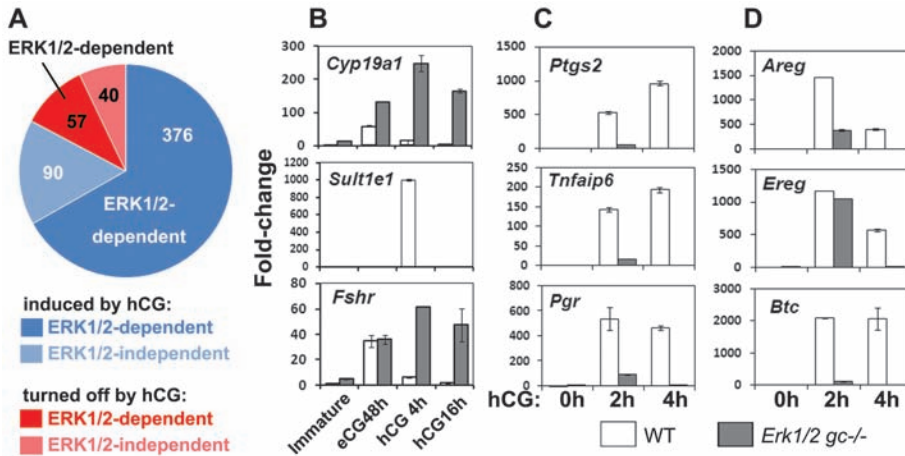


Fig. 3. ERK1/2 extensively regulate the expression of FSH/LH-target genes during ovulation. **(A)** Summary of gene expression profiling data. Genes regulated more than fourfold between 0 and 4 hours after hCG treatment were defined as LH-target genes; those that failed to respond to hCG in the *Erk1/2^{gc-/-}* cells were defined as ERK1/2-dependent genes. **(B to D)** qRT-PCR shows the expression of selected FSH/eCG and LH/hCG target genes in GCs of WT and *Erk1/2^{gc-/-}* mice after hCG treatment. Error bars denote SD.

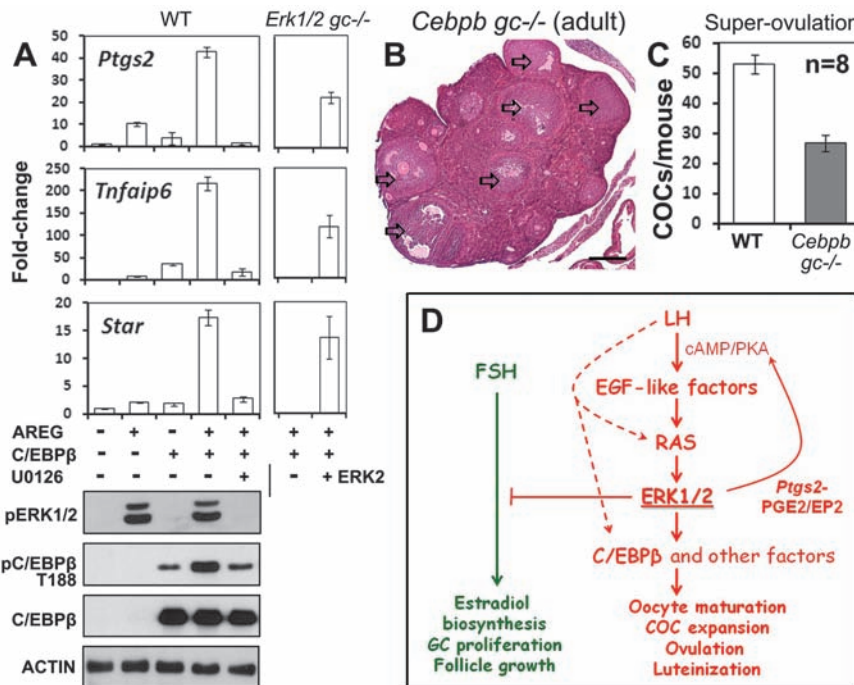


Fig. 4. C/EBP β is a key mediator of ERK1/2 activity in preovulatory GCs. **(A)** Immature WT or *Erk1/2^{gc-/-}* mice were primed with eCG for 24 hours. GCs were collected and cultured overnight, and some *Erk1/2^{gc-/-}* GCs were transfected with an ERK2 expression plasmid. The cells were then infected with an adenoviral vector encoding C/EBP β for 4 hours and further treated with AREG with (+) or without (–) U0126 for another 4 hours. Total RNA or protein was extracted. LH, hCG, and AREG downstream genes were quantified by qRT-PCR. Western blots document AREG-induced phosphorylation of ERK1/2 and C/EBP β and overexpression of C/EBP β . Error bars denote SD. **(B)** H&E staining shows the absence of CLs in the ovary of adult *Cebpb^{gc-/-}* mice. Follicles are indicated by arrows. Scale bar, 250 μ m. **(C)** The number of ovulated COCs decreased at 16 hours after hCG injection in *Cebpb^{gc-/-}* mice. **(D)** Summary. LH, cAMP, and protein kinase A (PKA) induce AREG and EREG, which activate RAS and ERK1/2. Activated ERK1/2 is required to (i) induce and activate CEBP β and genes essential for oocyte maturation, ovulation, and luteinization; (ii) maintain AREG, EREG, and BTC by inducing *Ptgs2*/PGE and activation of EP2, cAMP, and PKA; and (iii) silence the FSH-regulated program. LH may also transactivate RAS and ERK1/2 directly and regulate C/EBP β expression by other pathways. FSH and LH pathways are shown in green and red, respectively.

to controls but these levels were not sustained. By contrast, the induction of betacellulin (*Btc*) was blocked completely in *Erk1/2^{gc-/-}* ovaries (Fig. 3D). Thus, the initial induction of *Areg* and *Ereg* by LH/hCG is largely independent of ERK1/2 activation. However, the induction of *Btc* and the secondary maintenance of *Areg* and *Ereg* expression is likely dependent on ERK1/2 induction of *Ptgs2*, leading to prostaglandin E2 (PGE2) production and activation of the EP2 receptor (5).

By contrast, genes in addition to *Cyp19a1* that are expressed and/or induced by follicle-stimulating hormone (FSH) and equine chorionic gonadotropin (eCG) in GCs during preovulatory follicle development (*Fshr*, *Lhcgr*, and *Nr5a2*) (fig. S6) and normally down-regulated during the early stages of LH-induced luteinization (14) were expressed at elevated levels in ovaries of the hormone-treated *Erk1/2^{gc-/-}* mice (Fig. 3B and fig. S5C). Thus, ERK1/2 is required for suppressing the expression of FSH target genes.

Mice null for the transcription factor CCAAT/Enhancer-binding protein- β (*Cebpb*) are one of a only few knockout mouse models that show an *Erk1/2^{gc-/-}*-like ovarian phenotype (15). C/EBP β protein is increased rapidly by hCG in GCs in vivo (fig. S7, A and B), and in cultured cell lines. C/EBP β is the substrate of ERK1/2 and/or RPS6KA2 (P90RSK) (16), making C/EBP β a potential mediator of ERK1/2 in GCs. Indeed, when undifferentiated GCs were infected with an adenoviral vector encoding C/EBP β , C/EBP β was expressed, phosphorylated in response to AREG at a known ERK1/2 site and by a MEK1/2-dependent mechanism (C/EBP β -T188; Fig. 4A). Only in C/EBP β -expressing cells could AREG induce ERK1/2-dependent (U0126 sensitive) expression of target genes (*Ptgs2*, *Tnfaip6*, *Pgr*, and *Star*) (Fig. 4A and fig. S8A). AREG and C/EBP β induced the expression of LH/ERK1/2 target genes in *Erk1/2^{gc-/-}* GCs only when an ERK2 expression vector restored kinase activity (Fig. 4A). The synergistic actions of AREG and C/EBP β were compromised dramatically by an ERK1/2 site, but not P90RSK site, point mutation (fig. S8A), indicating that C/EBP β is a direct target of ERK1/2 and both constitute a critical signaling network in preovulatory GCs.

Because the GC-specific functions of C/EBP β have not been studied in vivo, *Cebpb^{fl/fl}* mice (17) were crossed with the *Cyp19-Cre* mice, generating the *Cebpb^{fl/fl};Cyp19-Cre* (*Cebpb^{gc-/-}*) mouse strain with C/EBP β depleted in GCs (fig. S7, B to D). As in the *Cebpb*-null mice (15), the adult *Cebpb^{gc-/-}* mice were subfertile (fig. S7E). CLs were absent in 70% of the adult *Cebpb^{gc-/-}* mice ($n = 10$, Fig. 4B); the number of ovulated COCs was reduced (Fig. 4C); and the expression of *Ptgs2*, *Star*, and *Cyp11a1* was decreased, consistent with impaired CL formation (fig. S7, F to G). However, hCG-induced phosphorylation of MEK1/2 and ERK1/2 was normal in ovaries of *Cebpb^{gc-/-}* mice (fig. S7D). Expression

of C/EBP β was decreased but not totally blocked in the *Erk1/2^{gc-/-}* mice (fig. S8, B and C), indicating that C/EBP β expression is regulated by additional pathways and that ERK1/2-mediated phosphorylation and activation of C/EBP β is critical. Thus, C/EBP β is a downstream effector of ERK1/2 in GCs during ovulation and luteinization. The lower penetrance of ovulation and gene expression defects in *Cebpb^{gc-/-}* mice, compared with the *Erk1/2^{gc-/-}* mice, suggests that C/EBP β is one, but not the only, critical transcription factor regulated by ERK1/2 in vivo.

The *Erk1/2^{gc-/-}* mouse model illustrates that disruption of *Erk1/2* in GCs in vivo completely derails the ability of LH to induce genes controlling ovulation, COC expansion, oocyte maturation, and luteinization without altering genes that regulate normal follicular development to the preovulatory stage (summarized in Fig. 4D). As a consequence of ERK1/2 depletion in GCs, the FSH program is extended rather than being abruptly terminated by LH/hCG. Thus, our results demonstrate in animals that the critical roles of ERK1/2 in GCs are highly selective and cell context-specific, confirming findings of in vitro studies (6, 18). Moreover, ERK1/2 are activated for a relatively short period of time (from 0.5 to 2 hours) in GCs of the preovulatory follicles exposed to LH/hCG (11, 12, 19), and this brief window of activation is necessary and suf-

ficient to reprogram preovulatory GCs to cease dividing and terminally differentiate.

The effect of ERK1/2 activation in GCs of preovulatory follicles but not in follicles at earlier stages of growth indicates that activation of these kinases is controlled tightly by specific mechanisms. Indeed, inappropriate activation of ERK1/2 in GCs of small growing follicles might disrupt normal follicular development because mice in which ovarian GCs express a constitutively active K-RAS mutant suffer impaired follicle development and premature ovarian failure (11). Thus, further understanding of the molecular mechanisms by which ERK1/2 regulate ovarian cell functions will help unravel some of the causes of ovarian pathologies and cancer, as well as lead to therapies for female infertility.

References and Notes

1. M. Hunzicker-Dunn, E. T. Maizels, *Cell. Signal.* **18**, 1351 (2006).
2. M. M. Matzuk, K. H. Burns, M. M. Viveiros, J. J. Eppig, *Science* **296**, 2178 (2002).
3. J. Y. Park *et al.*, *Science* **303**, 682 (2004).
4. M. Hsieh *et al.*, *Mol. Cell. Biol.* **27**, 1914 (2007).
5. M. Shimada, I. Hernandez-Gonzalez, I. Gonzalez-Robayna, J. S. Richards, *Mol. Endocrinol.* **20**, 1352 (2006).
6. Y. Q. Su, K. Wigglesworth, F. L. Pendola, M. J. O'Brien, J. J. Eppig, *Endocrinology* **143**, 2221 (2002).
7. Z. Chen *et al.*, *Chem. Rev.* **101**, 2449 (2001).
8. G. Pages *et al.*, *Science* **286**, 1374 (1999).
9. M. Aouadi, B. Binetruy, L. Caron, Y. Le Marchand-Brustel, F. Bost, *Biochimie* **88**, 1091 (2006).

10. A. M. Fischer, C. D. Katayama, G. Pages, J. Pouyssegur, S. M. Hedrick, *Immunity* **23**, 431 (2005).
11. H. Y. Fan *et al.*, *Development* **135**, 2127 (2008).
12. S. Panigone, M. Hsieh, M. Fu, L. Persani, M. Conti, *Mol. Endocrinol.* **22**, 924 (2008).
13. E. Gershon, A. Hourvitz, S. Reikhav, E. Maman, N. Dekel, *FASEB J.* **21**, 1893 (2007).
14. J. S. Richards, *Endocrinology* **142**, 2184 (2001).
15. E. Sterneck, L. Tessarollo, P. F. Johnson, *Genes Dev.* **11**, 2153 (1997).
16. M. Bück, V. Poli, P. vander Geer, M. Chojkier, T. Hunter, *Mol. Cell* **4**, 1087 (1999).
17. E. Sterneck, S. Zhu, A. Ramirez, J. L. Jorcano, R. C. Smart, *Oncogene* **25**, 1272 (2006).
18. S. Sela-Abramovich, E. Chorev, D. Galiani, N. Dekel, *Endocrinology* **146**, 1236 (2005).
19. E. T. Maizels, J. Cottom, J. C. Jones, M. Hunzicker-Dunn, *Endocrinology* **139**, 3353 (1998).
20. We thank J. Pouyssegur and J. Shao for providing *Erk1^{-/-}* mice and adenoviral vector of C/EBP β , respectively. This work was supported by NIH grants NIH-HD16229, NIH-HD07495, Project II (J.S.R.), Grant-in-Aid for Scientific Research No. 18688016 from the Japan Society for the Promotion of Science (M.S.), Intramural Research Program of NIH, National Cancer Institute, Center for Cancer Research (P.F.J. and E.S.), and NIH Postdoctoral Training Grant NIH-HD07165 (H.-Y.F.). The Gene Expression Omnibus accession number for microarray data is GSE15135.

Supporting Online Material

www.sciencemag.org/cgi/content/full/324/5929/938/DC1

Materials and Methods

Figs. S1 to S8

Tables S1 and S2

References

26 January 2009; accepted 20 March 2009

10.1126/science.1171396

Cell Movements at Hensen's Node Establish Left/Right Asymmetric Gene Expression in the Chick

Jerome Gros,¹ Kerstin Feistel,^{2*} Christoph Viebahn,³ Martin Blum,² Clifford J. Tabin^{1†}

In vertebrates, the readily apparent left/right (L/R) anatomical asymmetries of the internal organs can be traced to molecular events initiated at or near the time of gastrulation. However, the earliest steps of this process do not seem to be universally conserved. In particular, how this axis is first defined in chicks has remained problematic. Here we show that asymmetric cell rearrangements take place within chick embryos, creating a leftward movement of cells around the node. It is the relative displacement of cells expressing *sonic hedgehog* (*Shh*) and *fibroblast growth factor 8* (*Fgf8*) that is responsible for establishing their asymmetric expression patterns. The creation of asymmetric expression domains as a passive effect of cell movements represents an alternative strategy for breaking L/R symmetry in gene activity.

In mice and rabbits, monocilia found on cells of the posterior notochordal plate have been shown to play a crucial role in breaking left/right (L/R) symmetry (1, 2). These cilia are able to create a leftward flow of fluid in a pit-like teardrop-shaped space that is not covered by subjacent endoderm (3). The flow of fluid across this pit stimulates signal transduction that ultimately leads to the induction of asymmetric gene expression (1, 2).

In contrast, in the chick embryo, the endoderm underlying Hensen's node (a structure at

the rostral end of the primitive streak in the gastrulating embryo) exists as a continuous sheet ventral to the notochordal plate mesoderm (4), and there is no morphological pit on the ventral surface in which a flow of fluid could be established. Essner *et al.* have observed cilia at Hensen's node in earlier work (5), but these short cilia are on endodermal cells and are unrelated to the motile cilia on the mesodermal cells of the ventral node in the mouse and rabbit. The mesodermal cells at Hensen's node in the chick are devoid of cilia. In addition, the Talpid chick

mutant lacks primary cilia (6) but does not exhibit L/R asymmetry defects. Unlike in the mouse and rabbit, the chick node itself becomes morphologically asymmetric, with a marked tilt toward the left around the time the primitive streak reaches full extension at stage 4 (7, 8) (Fig. 1, A to C). Shortly thereafter, a number of small L/R asymmetric expression domains are observed to the right and left of the node (9). However, all of the genes expressed in such a manner are initially expressed in a symmetric fashion: for example, *fibroblast growth factor 8* (*Fgf8*) bilaterally along the primitive streak and *sonic hedgehog* (*Shh*) bilaterally across the top of the node until stage 4 (10) (Fig. 1, D to G). Subsequently, concomitant with the development of morphological asymmetries in the node, these gene expression patterns also become gradually asymmetric by stage 5 (Fig. 1, H and I).

To investigate cellular rearrangements that could be responsible for establishing the morphological asymmetry of the node, we performed

¹Department of Genetics, Harvard Medical School, Boston, MA 02115, USA. ²Institute of Zoology, Hohenheim University, 70953 Stuttgart, Germany. ³Department of Anatomy and Embryology, Göttingen University, 37079 Göttingen, Germany.

*Present address: Division of Neuroscience, Oregon National Primate Research Center, Oregon Health and Science University, Beaverton, OR 97006, USA.

†To whom correspondence should be addressed. E-mail: tabin@genetics.med.harvard.edu

a time-lapse analysis of cell movements at Hensen's node, randomly labeling cells by electroporation of a green fluorescent protein (GFP) reporter (11). At stage 4, as primitive streak elongation terminates (Fig. 1, K and O) but regression has not yet begun (Fig. 1, M and Q), the cells that have formed the node exhibit a definitive, albeit brief (3 to 4 hours), leftward movement [$n = 10/10$, where n represents the number of embryos analyzed; movies S1 to S3; and Fig. 1, L and P).

We next attempted to block the leftward movement of cells at the node by the use of drugs that inhibit the function of rho kinase (Rok) (Y-27632) and its target myosinII (blebbistatin). These two proteins have been shown to provide the force driving various oriented cell rearrangements in several species. After adding these drugs, gastrulation movements continued (Fig. 1R and fig. S1, B, F, and J), and most reached at least stage 6 when the notochord has formed, although as previously described (12, 13), primitive-streak regression was affected (Fig. 1T and fig. S1, D, H, and L). In these drug-treated embryos, the leftward movements of cells at the node were no longer observed (movies S4 and S5; Fig. 1S; and fig. S1, C, G, and K). Three-dimensional (3D) reconstruction of Hensen's node from stage 5 embryos that were cultured in blebbistatin or Y-27632 revealed that the node displays a more symmetrical and anteriorly extended shape as compared with control embryos (dotted lines; Fig. 2, A, B, E, and F; and fig. S2, A and B), suggesting that the cell movements we identified are responsible for the morphological asymmetry of the node. Moreover, we noted that these embryos also displayed symmetrical expression of *Shh* and FGF8 (Y-27632, $n = 16/23$; blebbistatin, $n = 17/21$; Fig. 2, G and H; and fig. S2, C and D).

Additionally, we attempted to block the leftward cell movements anterior to the node by two physical methods: (i) manually inserting individual human hairs through the primitive streak extending anterior to the node and (ii) surgically bisecting the embryos along the midline. Both manipulations also led to bilateral gene expression (fig. S3). Thus, the leftward cellular movements at the node are necessary to initiate L/R asymmetric expression domains in the chick.

It has been previously demonstrated that asymmetric expression of *Shh* and FGF8 depends on a transient, H⁺/K⁺ adenosine triphosphatase (ATPase)-dependent depolarization of membrane potential on the left side of the primitive streak, just before stage 4 (14). We cultured embryos in plates containing the H⁺/K⁺ ATPase inhibitors SCH28080 or omeprazole and found that the node displayed a symmetrical morphology comparable to the phenotypes observed with myosinII and Rok inhibitors, suggesting that in these conditions the cell rearrangements at the node did not occur properly (Fig. 2, I and J, and fig. S2, E and F). Moreover, when we performed a time-lapse analysis on GFP electroporated

embryos cultured on plates containing omeprazole, we did not observe any leftward movements at the node ($n = 3/4$) (movie S6, Fig. 1V, and fig. S1O) as were observed in control embryos ($n = 10/10$, Fig. 1, L and P, and movie S1), although the primitive streak elongated and regressed normally (Fig. 1, U to W, and fig. S1, N to P). Embryos treated with H⁺/K⁺ ATPase inhibitors exhibited symmetrical expression of *Shh* and FGF8 [as previously reported in (14)] by stage 5 to 6 (SCH28080, $n = 7/12$; omeprazole, $n = 6/7$; Fig. 2, K and L; and fig. S2, G and H). These data

show that the leftward movement at the node is downstream of the asymmetric H⁺/K⁺ ATPase activity.

The mechanism for setting up L/R asymmetric gene expression patterns at the chick node may have relevance beyond avian species. Despite the morphological conservation of the notochordal plate's ventral surface as seen in mice, rabbits, and possibly humans (15), histological analysis reveals that, similar to the chick, the cells of the pig notochordal plate do not contain cilia (Fig. 3, A to C, and fig. S4, D to J).

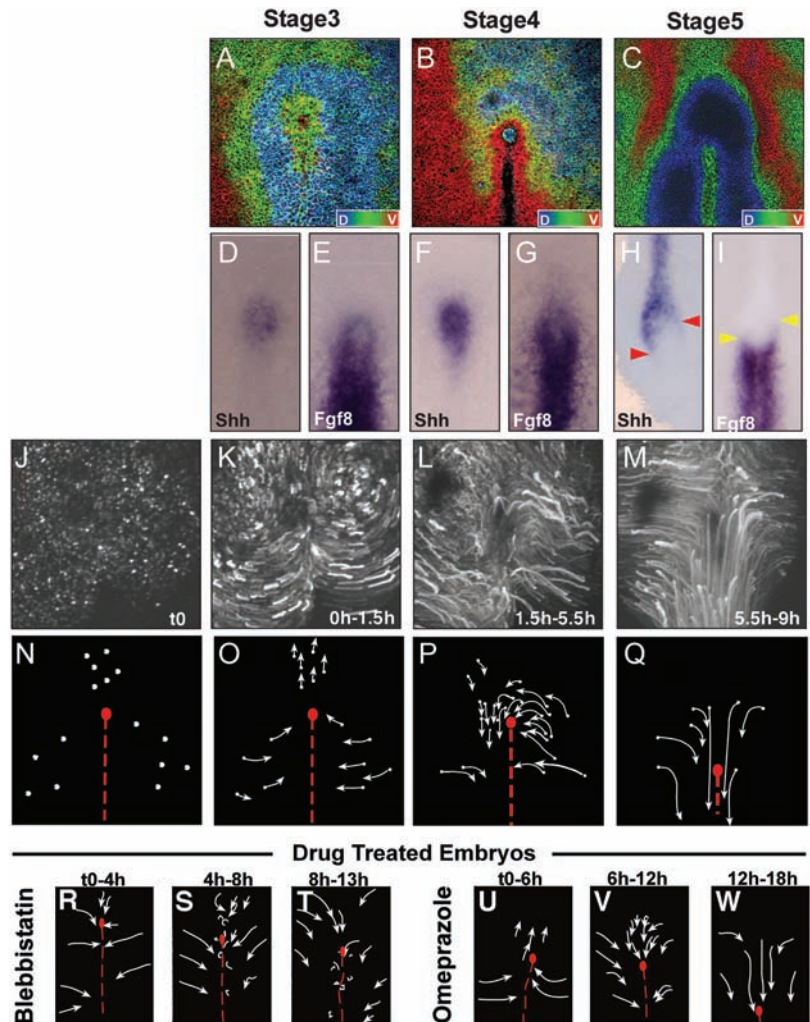


Fig. 1. Morphological and molecular asymmetries arise in conjunction with a leftward movement around the chick at Hensen's node in stage 4. (A to C) 3D reconstruction of confocal views (Z stack) of phalloidin-stained embryos at stages 3 (A), 4 (B), and 5 (C). The most dorsal (D) staining is depth coded blue; the most ventral (V) staining is shown in red. (D to I) In situ hybridizations for *Shh* [(D), (F), and (H)] and FGF8 [(E), (G), and (I)]. Red arrows, asymmetric domain of *Shh*; yellow arrows, asymmetric domain of *Fgf8*. (J to M) Time series showing movement of electroporated cells. (J) Embryos were electroporated at stage 3+, and subsequent time points are indicated in the lower right corner. 10 to 30% of cells are labeled by GFP. Cells undergo a leftward movement around the node (L). White arrows (N to Q) show the trajectories of the cells depicted in (J) to (M), respectively. In blebbistatin-treated embryos (R to T), early cell movements are relatively unaffected; however, there is no leftward movement around the node (S). Later, cells display disorganized movements, and the primitive streak fails to regress (T). In omeprazole-treated embryos (U to W), gastrulation movements are normal; however, cells from the left and right sides move symmetrically toward the node but not around it. The position of the streak and that of the node pit are illustrated by a red dotted line and a red circle, respectively.

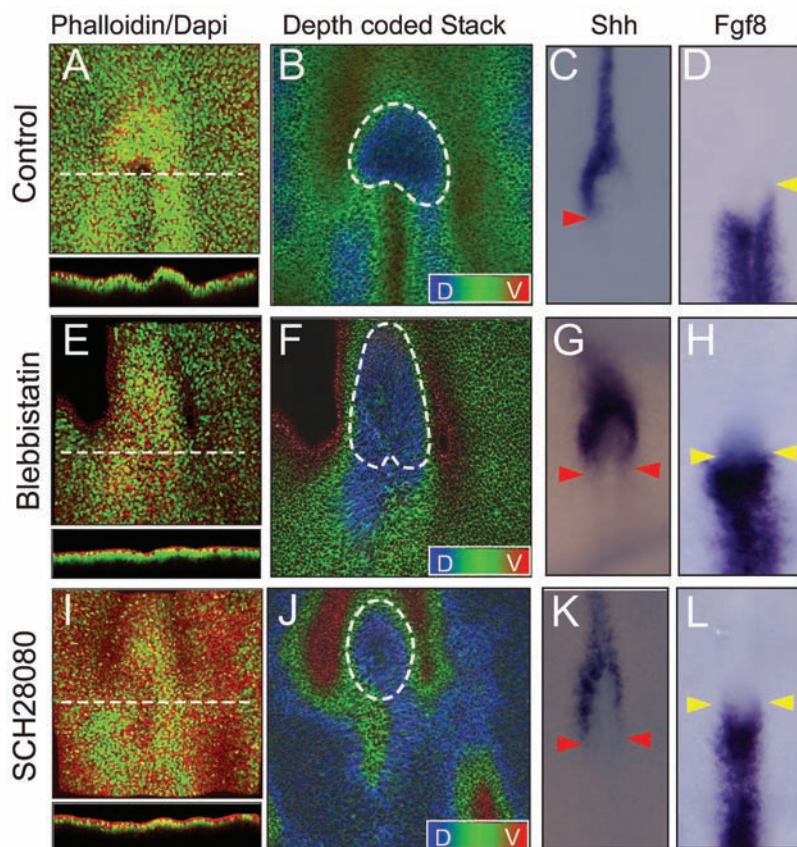
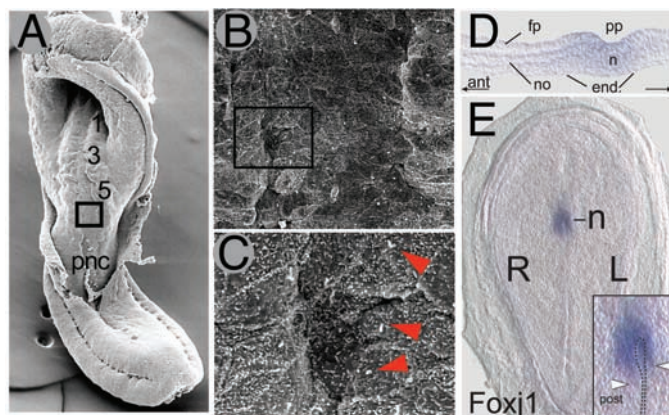


Fig. 2. Effects of myosinII and voltage gradient inhibitors on node morphology and asymmetric expression domains. (A, E, and I) 3D reconstruction of confocal views (Z-stacks) of stage 5 embryos shows the morphology of the node and the primitive streak. Lower panels represent a virtual cross section at the level of the white dotted line. (B, F, and J) Depth-coded 3D reconstruction of confocal views (Z stack) of phalloidin staining. The dorsal-most staining is shown in blue; the ventral-most is shown in red. The shape of the node is outlined by a white dotted shape. In situ hybridization of *Shh* (C, G, and K) and *Fgf8* (D, H, and L). Red arrows, extent of posterior *Shh* expression; yellow arrows, extent of anterior *Fgf8* expression.

Fig. 3. Similarities between the gastrulation node in the pig embryo and Hensen's node during chick gastrulation. (A to C) Ventral scanning electron microscopy views of a 5- to 6-somite-stage pig embryo with higher magnifications of the area surrounded by the black box [magnifications shown in (B) and (C)] of the notochordal plate and adjacent paraxial mesoderm. The endoderm forms a continuous ventral cover (that carries short, stubby cilia of 1.5- μ m length, indicated by red arrowheads) across the entire ventral surface of the embryo. pnc, prenotochordal cells. (D) A sagittal section at the level of the presumptive floor plate (fp) and notochord (no), covered by a continuous layer of endoderm (end). ant, anterior direction (leftward facing arrow); n, node. (E) The asymmetric node of a stage 5 pig embryo, marked by asymmetric expression (arrow heads) of the transcription factor *Foxj1*, demonstrating a shift of the primitive pit (pp, stippled black line). R, right; L, left; post, posterior. For more information, see fig. S4.



As in the chick, we do not observe any structure in the pig resembling the ventral node of the mouse and rabbit. Moreover, as in the chick, the cells of the pig notochordal plate are completely covered by endoderm. As a consequence, there is no space in which a flow of fluid could be generated (Fig. 3E and fig. S4, A and B). Additionally, like the chick, pig embryos have a morphologically asymmetric node displaced leftward at stage 5 ($n = 4/4$) (Fig. 3C). Like the chick and unlike the mouse, there are asymmetric gene expression domains adjacent to the node, such as *Foxj1* ($n = 3/3$) (Fig. 3A), which precede by several hours the asymmetric expression of *Nodal* at stage 6 (Fig. 3D). (*Nodal* is the first gene known to be asymmetrically expressed in mice and rabbits.)

In summary, we show here that, in chick embryos, the node is the site of cellular rearrangements that create a leftward movement of cells around it [an observation made independently by Cui *et al.* (16)]. The convergence of cells on the right edge of the node and migration away from the midline on the left thereby deform the shape of the node. This movement establishes asymmetric gene expression patterns, not through transcriptional induction or repression but rather in a passive manner by rearranging the relative orientations of cells expressing critical genes (fig. S5). Moreover, we have found that cell movements at the node arise downstream of a transient depolarization of membrane potential on the left side mediated by the activity of the H⁺/K⁺ ATPase. The symmetry-breaking event that leads to asymmetric H⁺/K⁺ ATPase activity in chick embryos remains unknown.

Previous misexpression experiments have put the genes asymmetrically expressed at the chick node into an epistatic pathway. For example, according to current models, *Bmp4* (which is expressed in very similar domains to *Fgf8*, initially bilaterally along the streak and then asymmetrically on the right side) induces *Fgf8* and represses *Shh*. *Shh* feeds back to repress *Bmp4* and induce *Nodal*, whereas *Fgf8* serves to repress *Nodal*. Our data do not contradict these previously described epistatic relations. However, because the asymmetric expression domains of these signaling molecules do not form in the absence of cell movements, we suggest that the previously described cross-regulation (for instance, the reciprocal inhibition between *Shh* and *Bmp4*) functions secondarily to sharpen borders and provide robustness once cells expressing these factors are brought into juxtaposition, rather than as a primary means of establishing their asymmetric gene expression domains.

References and Notes

1. M. Levin, *Mech. Dev.* **122**, 3 (2005).
2. A. Raya, J. C. Belmonte, *Nat. Rev. Genet.* **7**, 283 (2006).
3. J. D. Lee, K. V. Anderson, *Dev. Dyn.* **237**, 3464 (2008).
4. M. L. Kirby *et al.*, *Dev. Biol.* **253**, 175 (2003).
5. J. J. Essner *et al.*, *Nature* **418**, 37 (2002).
6. Y. Yin *et al.*, *Development* **136**, 655 (2009).

7. O. Hertwig, *Lehrbuch der Entwicklungsgeschichte des Menschen und der Wirbelthiere* (Verlag von Gustav Fischer, Jena, Germany, 1910).
8. A. Kölliker, *Entwicklungsgeschichte des Menschen und höheren Thiere* (Wilhelm Engelmann, Leipzig, Germany, 1879).
9. V. Dathe et al., *Anat. Embryol. (Berlin)* **205**, 343 (2002).
10. M. Levin et al., *Cell* **82**, 803 (1995).
11. Materials and methods are available as supporting material on Science Online.
12. F. Marlow et al., *Curr. Biol.* **12**, 876 (2002).
13. L. Wei et al., *Development* **128**, 2953 (2001).
14. M. Levin et al., *Cell* **111**, 77 (2002).
15. R. O'Rahilly, F. Muller, *The Embryonic Human Brain: An Atlas of Developmental Stages* (Wiley, Hoboken, NJ, ed. 3, 2006).
16. C. Cui, C. Little, B. Rongish, *Anat. Rec. (Hoboken)* **292**, 557 (2009).
17. We thank M. Levin for helpful suggestions for addressing the role of ion channels; R. O'Rahilly for providing information regarding human embryos; D. Rath and P. Schwartz for provision of pig embryos and assistance with electron microscopy; and C. Cui, C. Little, and B. Rongish for discussing data before publication. This work was supported by a Human Frontier Science Program fellowship to J.G., a Ph.D. fellowship from the Boehringer Ingelheim Fonds to K.F., a grant from the Deutsche Forschungsgemeinschaft

(DFG) to M.B., a grant from the DFG (VI 151-8-1) to C.V., and grant R01-HD045499 from NIH to C.J.T.

Supporting Online Material

www.sciencemag.org/cgi/content/full/1172478/DC1

Materials and Methods

Figs. S1 to S6

References

Movies S1 to S6

18 February 2009; accepted 26 March 2009

Published online 9 April 2009;

10.1126/science.1172478

Include this information when citing this paper.

A Frazzled/DCC-Dependent Transcriptional Switch Regulates Midline Axon Guidance

Long Yang, David S. Garbe, Greg J. Bashaw*

Precise wiring of the nervous system depends on coordinating the action of conserved families of proteins that direct axons to their appropriate targets. Slit-roundabout repulsion and netrin–deleted in colorectal cancer (DCC) (frazzled) attraction must be tightly regulated to control midline axon guidance in vertebrates and invertebrates, but the mechanism mediating this regulation is poorly defined. Here, we show that the Fra receptor has two genetically separable functions in regulating midline guidance in *Drosophila*. First, Fra mediates canonical chemoattraction in response to netrin, and, second, it functions independently of netrin to activate *commisureless* transcription, allowing attraction to be coupled to the down-regulation of repulsion in precrossing commissural axons.

Establishing precise midline circuitry is essential to control rhythmic and locomotor behaviors (1, 2). Conserved signals that regulate axon guidance at the midline include attractive cues such as netrins and repulsive cues such as slits, semaphorins, and ephrins (3, 4). In

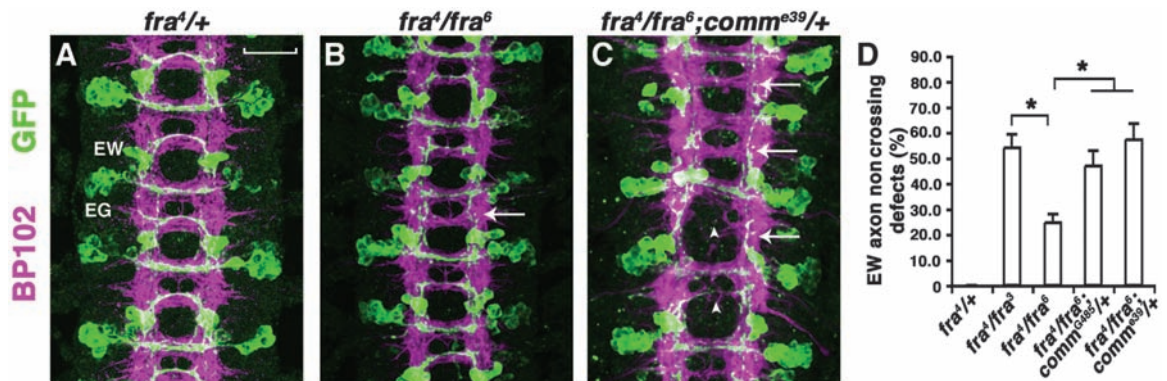
Drosophila, netrin attracts many commissural axons to the midline through activation of the frazzled (Fra), the *Drosophila* ortholog of the DCC (deleted in colorectal cancer) receptor (5–8), whereas the repellent slit and its receptor roundabout (Robo) prevent commissural axons from recrossing (9, 10). Commissureless (Comm) controls midline crossing by negatively regulating surface amounts of Robo on precrossing commissural axons (11–13). Comm is expressed transiently in commissural neurons as their axons traverse the midline, where it sorts

Robo to endosomes (12). Once across the midline, *comm* expression is extinguished, resulting in increased amounts of Robo on the growth cone. How *comm* expression is spatially and temporally regulated to gate midline crossing is unknown.

While characterizing the structural requirements for Fra-mediated axon attraction, we observed that neuronal expression of a dominant negative form of Fra (Fra Δ C) leads to a dose-dependent “commissureless” phenotype (14). Searching for candidate genes that modify this phenotype, we found that removing one copy of *comm* enhances the midline-crossing defects caused by expressing *UASFra Δ C* (fig. S1), suggesting a role for Fra in regulating Comm during midline guidance. Consistent with this idea, removing one copy of *comm* in hypomorphic *fra* mutants increases the commissural defects as shown by thin or missing commissures in many segments, as well as an increased frequency of noncrossing defects in a subset of commissural neurons: the eagle neurons (Fig. 1 and table S1). Similar genetic interactions are also observed by using additional alleles of both *fra* and *comm* (fig. S2 and table S1). These dose-dependent genetic interactions suggest that *fra* and *comm* may function in the same pathway to control commissural axon guidance.

How could Fra regulate the function of Comm? Because *comm* mRNA is up-regulated in commissural neurons as their axons cross the

Fig. 1. Genetic interaction between *fra* and *comm*. (A to C) Stage 16 *eglGal4::UASTau-MycGFP* embryos stained with MAb-BP102 (magenta) to display all central nervous system axons and anti-green fluorescent protein (GFP) (green) to visualize the eagle neurons. Anterior is up. (A) In *fra⁴/+* or *fra⁴/+; comm^{e39}/+* embryos, EW and EG neurons (white labels) project their axons across the midline in almost every segment. Scale bar indicates 20 μ m. (B) *fra⁴/fra⁶* mutants have normal commissure formation and a mild EW axon noncrossing defect (arrow). (C) Compared with *fra⁴/fra⁶*, *fra⁴/fra⁶; comm^{e39}/+* embryos have missing and thin commissures in many



segments (arrowheads), and many EW axons also fail to cross the midline (arrows). (D) Quantification of EW axon noncrossing defects. The guidance of EG axons is not affected in *fra* mutants. Error bars represent standard error of the mean. Asterisks denote $P < 0.02$ in a Student's t test.

midline and DCC has been shown to mediate netrin-induced axon outgrowth and turning through activation of the mitogen-activated protein kinase and calcineurin and nuclear factor of activated T cells (NFAT) signaling cascades (15, 16), we tested whether Fra regulates *comm* mRNA expression (17). Examination of *comm* mRNA in *fra* mutant nerve cords by real-time polymerase chain reaction revealed a 12-fold reduction of total *comm* mRNA relative to that of wild type (fig. S3). To analyze *comm* mRNA expression with single-cell resolution, we focused on the eagle neurons. At stage 14 in wild-type or *fra*⁺ embryos, when the eagle axons are crossing the midline, they have high *comm* RNA expression in their cell bodies (Fig. 2, A to C). However, in *fra* mutants *comm* mRNA is reduced in the eagle neurons that project their axons in the posterior commissure (EW) and the eagle neurons that project their axons in the anterior commissure (EG) (Fig. 2 and figs. S4 and S5).

comm mRNA reduction in *fra* mutants is unlikely to be secondary to the failure of these axons to cross the midline, because a similar reduction is observed in EWs that have normal trajectories (Fig. 2). This implies that crossing the midline is not sufficient to induce *comm* transcription. Furthermore, the down-regulation of *comm* mRNA is likely a reflection of reduced transcription, rather than reduced mRNA stability, because we detected a similar reduction of *comm* pre-mRNA expression by using a *comm* intron probe for hybridization (fig. S6). Lastly, *comm* mRNA reduction in *fra* mutants is specific to commissural neurons because *comm* mRNA expression in the midline glia is not affected (Fig. 2).

Fra has non-cell-autonomous functions (18, 19), so we tested whether Fra is required exclusively in commissural neurons to control *comm* transcription. Expressing a *UASFra-Myc* transgene in the eagle neurons of *fra* mutants not

only rescues the guidance defects of EWs as previously reported (14) but also rescues *comm* mRNA expression (Fig. 2, G to I, and fig. S4). *comm* mRNA expression is also recovered in the few EWs (1.8%) that are not rescued, and *comm* mRNA amounts are normally regulated when the EW axons are prevented from crossing the midline by misexpressing the Robo receptor, indicating that crossing the midline is not necessary to induce *comm* expression (figs. S4 and S7). During axon migration, growth cones of ipsilateral neurons extend long filopodia that reach all the way across the midline (20), suggesting that even when commissural axons extend ipsilaterally they could still have access to midline signals.

In contrast to wild-type Fra, expression of Fra Δ C in *fra* mutants does not rescue *comm* mRNA expression (fig. S8). In fact, expressing *UASFra Δ C* in the eagle neurons of wild-type animals results in a decrease in *comm* expression in EWs; an observation consistent with Fra Δ C's function as a dominant negative (fig. S9). All together, these results support a cell-autonomous requirement for Fra to activate *comm* transcription in commissural neurons as they cross the midline, and furthermore this effect is dependent on an intact cytoplasmic domain.

To test whether Fra is sufficient to induce *comm* mRNA expression, we overexpressed Fra in a subset of ipsilateral neurons, the apterous (Ap) neurons. In wild-type embryos, the Ap neurons do not express *comm*. Only stochastic expression of *comm* can be detected at late stages in these neurons (stages 16 and 17) (Fig. 3, A and C, arrows) (12). Overexpressing a *UASFra-myc* transgene in the Ap neurons frequently induces ectopic *comm* mRNA expression (16% of hemisegments contain Ap neurons that express *comm*, $n = 160$ hemi-segments) (Fig. 3, D and F, arrows). In addition, Fra expression causes the Ap axons to cross the midline in many segments (35%, $n = 18$) (Fig. 3E asterisks). Therefore, Fra is both necessary and sufficient for *comm* mRNA expression in subsets of neurons in vivo.

Because netrins are the ligands for DCC to activate downstream gene transcription during vertebrate axon outgrowth and turning, we tested whether netrins are required for *comm* transcription. Unexpectedly, there is no reduction of *comm* mRNA in the eagle neurons of *netAB* mutants compared with *netAB*⁺ siblings (Fig. 4 and fig. S8). Even in the EWs that fail to cross the midline, *comm* mRNA is expressed normally, again arguing that midline crossing is not required to induce *comm* transcription (Fig. 4, D and F, arrows). In addition, expressing either a *UASMyr-Fra-Myc* transgene that removes the entire extracellular domain of Fra (and therefore its ability to bind netrin) or a *UASFra Δ P1 Δ P2 Δ P3-Myc* transgene can also rescue *comm* mRNA expression (fig. S8). Accordingly, the midline crossing defects of the EW axons in these embryos are partially rescued, resulting in a milder phenotype (table S1). The conserved cytoplasmic P3

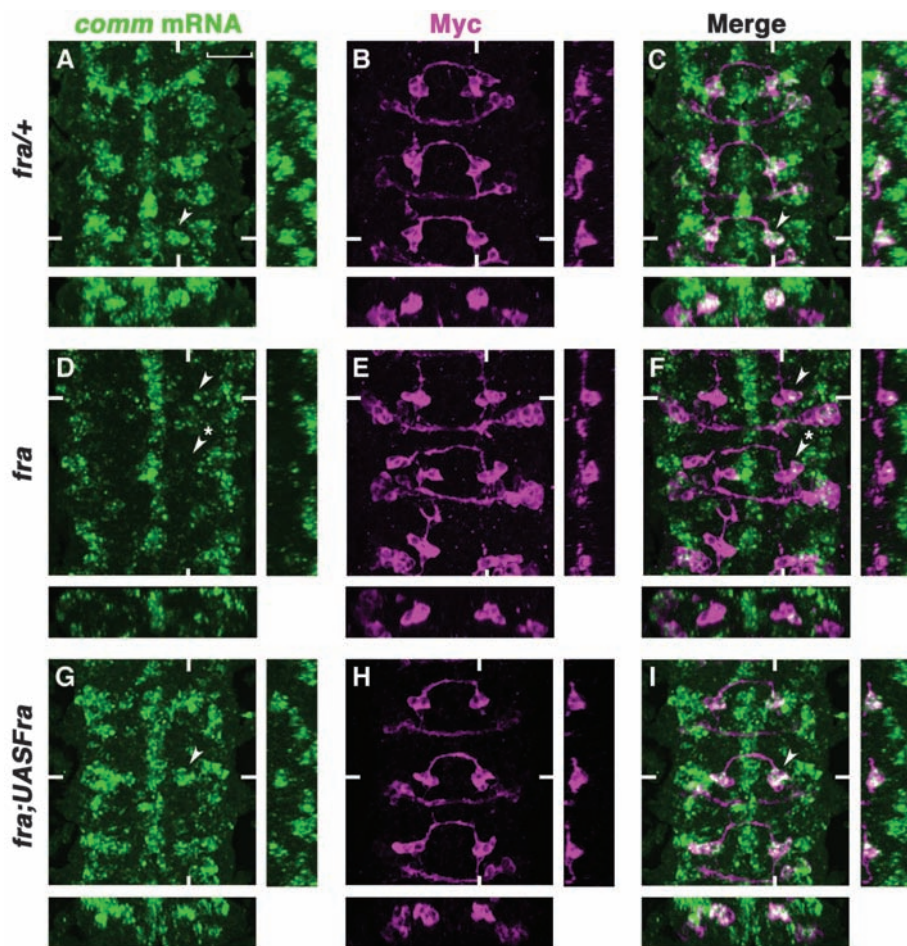


Fig. 2. Fra is required cell-autonomously for *comm* mRNA expression. (A to I) Stage 14 *eglGal4::UASTau-MycGFP* embryos double-labeled with RNA in situ probes for *comm* (green) and anti-Myc (magenta) to visualize the eagle neurons. Anterior is up. Confocal sections of the EWs are shown. White hash marks indicate the positions of the XZ and YZ sections. (A to C) *comm* mRNA expression in the EWs of *fra*⁺ embryos (arrowheads). Scale bar in (A), 20 μ m. (D to F) *comm* mRNA is reduced in the EWs of *fra*⁴/*fra*³ mutants (arrowhead, EW with crossing defect; starred arrowhead, EW that projects normally). (G to I) Expressing *UASFra-Myc* in the eagle neurons of *fra* mutants rescues *comm* mRNA expression in the EWs [(G) and (I), arrowheads].

motif of Fra is required for netrin-mediated attraction (14). Therefore, *Fra* Δ P1 Δ P2 Δ P3 loses its chemoattractive function but still retains the ability to activate *comm* transcription. These results support the idea that netrins are not the ligands for Fra to induce *comm* transcription and indicate that chemoattraction and the regulation of *comm* expression are controlled by distinct regions of the Fra cytoplasmic domain. Moreover, the transcriptional activation of *comm* appears to be independent of any of the conserved P motifs.

Together these results suggest that, to ensure midline crossing, Fra signaling has dual functions in commissural neurons: First it mediates netrin-dependent axon attraction, and second it leads to netrin-independent activation of *comm* transcription. Comm, in turn, down-regulates Robo expression on commissural axons, allowing midline crossing (fig. S10). If this model is correct, the guidance defects observed in *fra* mutants should be due to a combination of the loss of attraction and a failure to activate *comm* transcription, and at least four genetic predictions can be made. First, *fra* mutants should have more severe EW commissural guidance defects than *netAB* mutants do. Second, expressing *UASComm* transiently in commissural neurons should partially rescue the guidance defects in *fra* mutants, and these partially rescued *fra*; *UASComm* mutant animals should have similar guidance defects to *netAB* mutants. Third, *fra*, *robo* double mutants should display the same severity of defects as *fra*; *UASComm* animals. Lastly, expressing *UASComm* in commissural neurons of *netAB* mutants should have no effect on the midline crossing defects.

To test these predictions, we compared the EW axon guidance defects in the genotypes described above, and a phenotypic analysis was performed blind to genotype (Fig. 5). As predicted, the EW guidance defects in *fra* mutants are significantly stronger than those in *netAB* mutants (Fig. 5, B, F, and H, and table S1). Expressing *UASComm* in the eagle neurons of *fra* mutants partially rescues the EW guidance defects, leading to a phenotype similar to that observed in *netAB* mutants (Fig. 5, C and H, and table S1). Similarly, the EW guidance defects in *fra*, *robo* double mutants are also less severe than *fra* single mutants (Fig. 5, D and H, and table S1) (21). Lastly, overexpression of *UASComm* in *netAB* mutants does not affect the guidance defects (Fig. 5, F and G, and table S1). These observations strongly support a netrin-independent role for Fra in triggering *comm* transcription. Fra-dependent transcriptional regulation is unlikely to be the only mechanism to activate *comm* expression, because *fra* mutants have less severe commissural guidance defects than *comm* mutants.

Preventing conflicting signals at the midline from confusing navigating axons is fundamental to neuronal development. One mechanism that may allow axons to coordinate their responses to

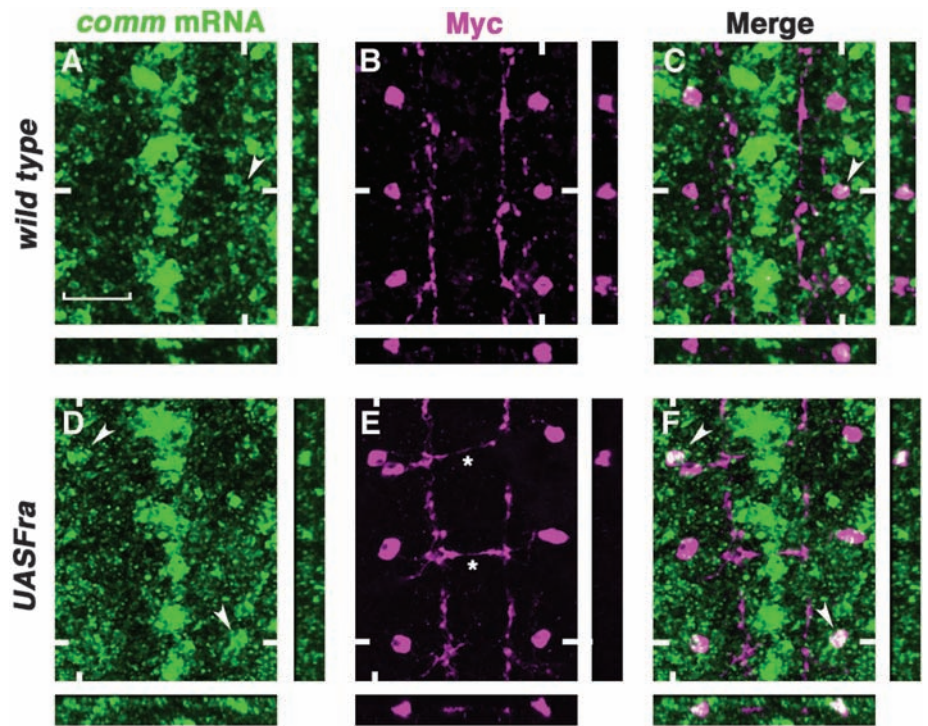


Fig. 3. Fra is sufficient to induce *comm* mRNA expression. (A to F) Stage 16 *aptGal4::UASTau-MycGFP* embryos double-labeled with RNA in situ probes for *comm* (green) and anti-Myc (magenta) to visualize the Ap neurons. Anterior is up. Confocal sections of the Aps are shown. White hash marks indicate the positions of the XZ and YZ sections. (A to C) Stochastic *comm* mRNA expression in the Ap neurons (arrowheads). Scale bar in (A), 20 μ m. (D to F) Expressing *UASFra-Myc* in the Ap neurons induces *comm* mRNA expression frequently [arrowheads in (D) and (F)] and leads to ectopic midline crossing in many segments [asterisks in (E)].

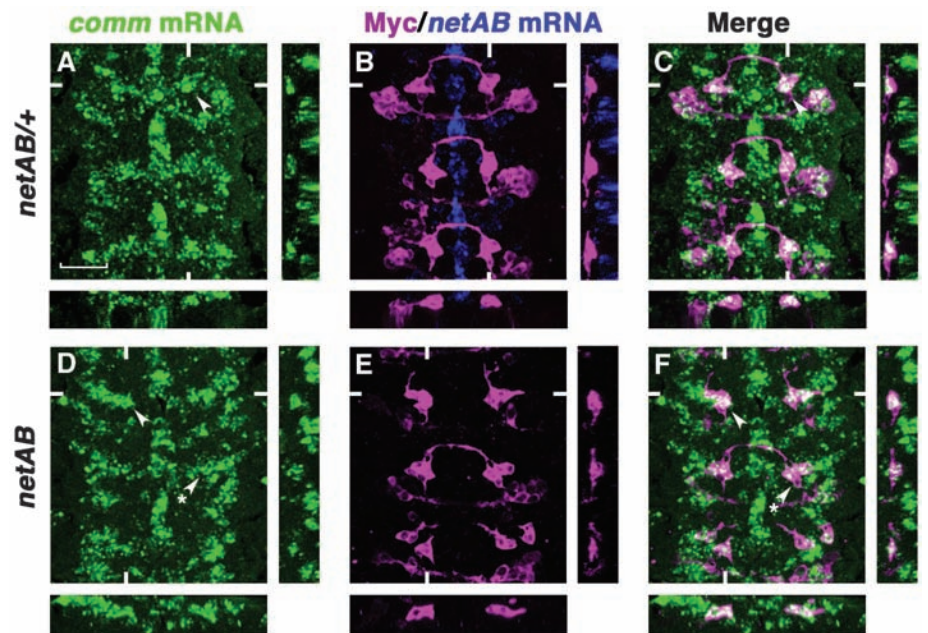
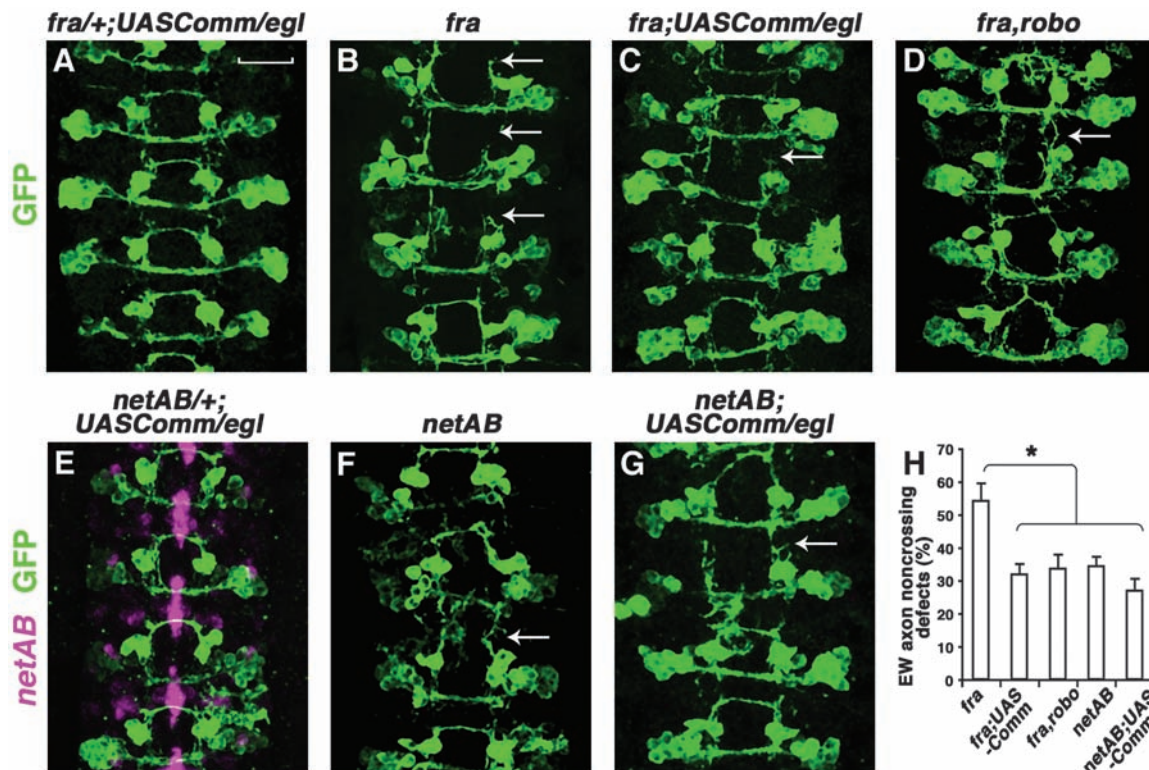


Fig. 4. Netrins are not required for *comm* mRNA expression. (A to F) Stage 14 *eglGal4::UASTau-MycGFP* embryos triple-labeled with RNA in situ probes for *comm* (green) and *netrinAB* (blue) and with anti-Myc (magenta) to visualize the eagle neurons. Anterior is up. Confocal sections of the EWs are shown. White hash marks indicate the positions of the XZ and YZ sections. (A to C) *comm* mRNA expression in the EWs of *netAB/+* embryos (arrowheads). Scale bar in (A), 20 μ m. (D to F) *netAB* mutants have normal levels of *comm* mRNA expression. Arrowheads indicate an EW that has crossing defects, and starred arrowheads indicate an EW that projects normally.

Fig. 5. Expression of Comm partially rescues guidance defects in *fra* mutants. (**A** to **G**) Stage 16 *eglGal4::UASTau-MycGFP* embryos stained with anti-GFP (green). Embryos in (**E** to **G**) were also labeled with RNA in situ probes for *netrinAB* (magenta). Anterior is up. Overexpressing *UASComm* in the eagle neurons partially rescues the EW guidance defects in *fra* mutants [compare arrows in (**B**) and (**C**)] but not in *netAB* mutants [compare arrows in (**F**) and (**G**)]. The EW guidance defects in *fra*, *robo* mutants are also partially rescued [compare arrows in (**B**) and (**D**)]. Overexpressing *UASComm* in *fra/+* or *netAB/+* does not affect the trajectories of eagle neurons in (**A**) and (**E**). Scale bar in (**A**), 20 μ m. (**H**) Quantification of EW axon noncrossing defect. Error bars represent standard error of the mean. Asterisk denotes $P < 0.001$ in a Student's *t* test.



conflicting attractive and repulsive signals has been described in cultured *Xenopus* spinal neurons, where slit induces a physical interaction between Robo and DCC (22). This direct receptor-receptor interaction silences netrin attraction, and this mechanism is proposed to prevent postcrossing commissural axons from recrossing the midline (22). Here, we provide in vivo evidence supporting a distinct mechanism to regulate axon responses: Two conserved guidance receptor signaling pathways (Fra and Robo) are coupled through a transcriptional event in precrossing commissural neurons to prevent premature repulsive responses and therefore ensure midline crossing. Although transcriptional regulation by netrin-DCC signaling is required for embryonic axon outgrowth and turning in vitro, it is less clear whether it is relevant in vivo. Here, we show that Fra signaling triggers a transcriptional event in vivo and identify a specific target gene, *comm*, a key regulator of repulsion at the *Drosophila* midline.

Surprisingly, Fra-mediated transcriptional activation is netrin-independent, raising the question of whether there is an extrinsic midline signal required to activate Fra-dependent *comm* transcription. The spatial and temporal *comm* expression pattern is tightly associated with midline crossing, strongly suggesting the existence of such a midline signal. At first glance, our finding that Fra-induced *comm* transcription can be restored by expression of a myristolated Fra cytoplasmic (myrFracyto) domain seems inconsistent

with this idea. Although it may be tempting to conclude from this observation that the regulation of *comm* is strictly ligand-independent, it is also possible (and, in our view, likely given the tight temporal window of *comm* expression) that the myrFracyto construct is either constitutively active or that it can associate with a co-receptor. Indeed, a similar construct when expressed in *Caenorhabditis elegans* leads to constitutive activity (23), and myristolated guidance receptor cytoplasmic domains have been shown to be competent to interact with co-receptors in a ligand-dependent manner (24, 25). Identifying the signals that trigger *fra* to activate *comm* transcription and determining how these events are restricted to commissural neurons are high future priorities.

References and Notes

1. M. Goulding, S. L. Pfaff, *Curr. Opin. Neurobiol.* **15**, 14 (2005).
2. D. R. Ladle, E. Pecho-Vrieseling, S. Arber, *Neuron* **56**, 270 (2007).
3. D. S. Garbe, G. J. Bashaw, *Crit. Rev. Biochem. Mol. Biol.* **39**, 319 (2004).
4. A. B. Huber, A. L. Kolodkin, D. D. Ginty, J. F. Cloutier, *Annu. Rev. Neurosci.* **26**, 509 (2003).
5. K. J. Mitchell *et al.*, *Neuron* **17**, 203 (1996).
6. P. A. Kolodziej *et al.*, *Cell* **87**, 197 (1996).
7. R. Harris, L. M. Sabatelli, M. A. Seeger, *Neuron* **17**, 217 (1996).
8. M. Brankatschk, B. J. Dickson, *Nat. Neurosci.* **9**, 188 (2006).
9. T. Kidd, K. S. Bland, C. S. Goodman, *Cell* **96**, 785 (1999).
10. T. Kidd *et al.*, *Cell* **92**, 205 (1998).

11. T. Kidd, C. Russell, C. S. Goodman, G. Tear, *Neuron* **20**, 25 (1998).
12. K. Keleman *et al.*, *Cell* **110**, 415 (2002).
13. K. Keleman, C. Ribeiro, B. J. Dickson, *Nat. Neurosci.* **8**, 156 (2005).
14. D. S. Garbe, M. O'Donnell, G. J. Bashaw, *Development* **134**, 4325 (2007).
15. C. Forcet *et al.*, *Nature* **417**, 443 (2002).
16. I. A. Graef *et al.*, *Cell* **113**, 657 (2003).
17. Materials and methods are available as supporting material on Science Online.
18. Q. Gong, R. Rangarajan, M. Seeger, U. Gaul, *Development* **126**, 1451 (1999).
19. M. Hiramoto, Y. Hiromi, E. Giniger, Y. Hotta, *Nature* **406**, 886 (2000).
20. M. J. Murray, P. M. Whittington, *J. Neurosci.* **19**, 7901 (1999).
21. D. S. Garbe, G. J. Bashaw, *J. Neurosci.* **27**, 3584 (2007).
22. E. Stein, M. Tessier-Lavigne, *Science* **291**, 1928 (2001); published online 8 February 2001 (10.1126/science.1058445).
23. Z. Gitai, T. W. Yu, E. A. Lundquist, M. Tessier-Lavigne, C. I. Bargmann, *Neuron* **37**, 53 (2003).
24. K. Hong *et al.*, *Cell* **97**, 927 (1999).
25. E. Stein, Y. Zou, M. Poo, M. Tessier-Lavigne, *Science* **291**, 1976 (2001).
26. This work was supported by NIH grants NS054739 and NS046333 to G.J.B.

Supporting Online Material

www.sciencemag.org/cgi/content/full/1171320/DC1
Materials and Methods
Figs. S1 to S10
Table S1
References

23 January 2009; accepted 16 March 2009
Published online 26 March 2009;
10.1126/science.1171320
Include this information when citing this paper.

Fictive Reward Signals in the Anterior Cingulate Cortex

Benjamin Y. Hayden,^{1*} John M. Pearson,¹ Michael L. Platt^{1,2}

The neural mechanisms supporting the ability to recognize and respond to fictive outcomes, outcomes of actions that one has not taken, remain obscure. We hypothesized that neurons in the anterior cingulate cortex (ACC), which monitors the consequences of actions and mediates subsequent changes in behavior, would respond to fictive reward information. We recorded responses of single neurons during performance of a choice task that provided information about the reward values of options that were not chosen. We found that ACC neurons signal fictive reward information and use a coding scheme similar to that used to signal experienced outcomes. Thus, individual ACC neurons process both experienced and fictive rewards.

People routinely recognize and respond to fictive outcomes, which are rewards or punishments that have been observed but not directly experienced (1–3). Fictive thinking affects human economic decisions (4) and is disrupted in disorders such as anxiety and impulsivity (5). Moreover, monkeys respond to information about rewards that they have not directly experienced (6) or were received by other monkeys (7). To understand the neural mechanisms that mediate these processes, we investigated how fictive reward information is encoded in the anterior cingulate cortex (ACC), part of a neural circuit that mediates outcome-contingent changes in behavior (8–10) and processes fictive information in humans (11). The ACC is interconnected with the orbitofrontal cortex, which mediates fictive thinking in humans (5, 12).

¹Department of Neurobiology, Duke University School of Medicine, Center for Neuroeconomic Studies, Center for Cognitive Neuroscience, Duke University, Durham, NC 27701, USA. ²Department of Evolutionary Anthropology, Duke University, Durham, NC 27701, USA.

*To whom correspondence should be addressed. E-mail: hayden@neuro.duke.edu

In our task, monkeys chose from among eight white targets arranged in a circle (13). Seven low-value (LV) targets provided small rewards (100 μ L), whereas the eighth target [high-value (HV)] provided a variable reward with a larger expected value (EV). Its value on each trial was selected randomly from six possibilities (0, 200, 267, 300, 333, and 367 μ L). Once the monkey selected a target, the values associated with all eight of the targets, represented by their colors, were revealed (Fig. 1, A and B). After a half-second delay, the monkey received the reward associated with the chosen target. On the next trial, the position of the HV target either remained in the same position (60% probability) or moved one position clockwise (40% probability).

We analyzed only those trials in which monkeys maintained fixation (90.6% of trials). Because the HV target had a greater EV than the LV targets (243 μ L versus 100 μ L), we expected that monkeys would prefer the HV target. Indeed, in a control task that explicitly cued HV location, monkeys chose it on 93.4% of trials. In the standard task, monkeys chose the HV target (45.6% of trials) more often than chance ($P <$

0.005, binomial test, Fig. 2A). Monkeys earned 165.0 μ L per trial, 88.5% of the amount earned by an omniscient observer with access to information about the value of all targets on all preceding trials (13). Monkeys chose targets adjacent to potential HV targets more often (37.7% of trials) than more distal targets (16.7% of trials, $P < 0.005$, binomial test, Fig. 2A), suggesting that they understood the probabilistic relation between the HV target on the current trial and its likely location on the next.

Large fictive rewards promote gambling in humans (14, 15); thus, we hypothesized that monkeys would likewise preferentially choose HV options after large fictive rewards. We observed this pattern in our experiment (Fig. 2B, black line, correlation coefficient $r = 0.300$, $P < 0.001$). This effect may reflect an increased willingness to switch from to a new target, as the likelihood of switching increased with larger fictive outcomes (Fig. 2C, $r = 0.199$, $P < 0.001$). One alternative explanation for these effects is that HV targets may have positive associations that influence behavior. This explanation is unlikely for several reasons. First, obtained rewards never depended on unselected targets on that trial, so any associations between these fictive stimuli and reward values would be eliminated over the thousands of training trials that preceded recording. Second, immediately after making choices, monkeys were no more likely to make a second saccade (Fig. 2D, $r = -0.02$, $P > 0.2$) nor faster to shift gaze (Fig. 2E, $r = 0.008$, $P > 0.2$) to HV fictive targets than to LV fictive targets, indicating that attention and motivation were roughly similar after all fictive outcomes. Third, we performed a control task in which the HV target remained white and a colored square appeared in the center of the monitor during the delay after the trial. This square's color did not indicate what reward could have been received (and, thus, it provided no fictive information) but had the same associations as the fictive targets.

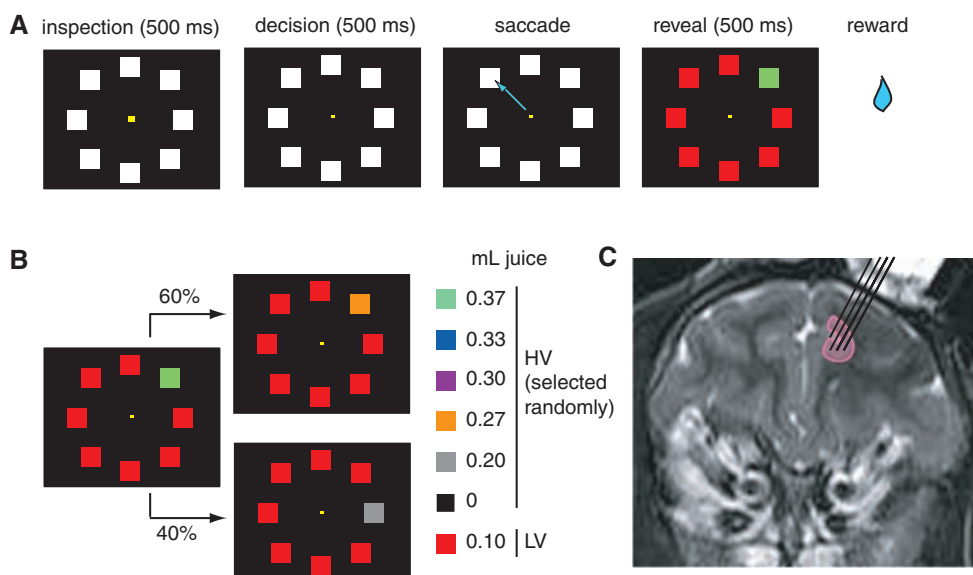


Fig. 1. Task and recording location. (A) Schematic of standard task. Fixation point and eight white squares appear; 500 ms after fixation, a monkey chooses one target, and all targets change color, revealing their value. A half-second later, a reward is given. (B) Between trials, the HV target either remains at the same position (60% chance) or moves to an adjacent position (40% chance). (C) Magnetic resonance image of monkey E. Recordings were made in the ACC sulcus.

Monkeys' choices on subsequent trials did not depend on the color of this stimulus (Fig. 2F, $r = 0.005$, $P > 0.6$).

An example ACC neuron showed clear phasic responses around the time of gaze shifts to targets; the amplitude of these responses was correlated with the size of both the experienced reward (Fig. 3A, $r = 0.056$, $P < 0.001$, the six rewards are grouped into four categories to

simplify presentation) and the size of fictive outcomes on trials when the monkey chose the LV target (Fig. 3B, $r = 0.037$, $P < 0.001$). The amplitude of phasic responses of most neurons reflected experienced reward size [$n = 46$ out of 68 (46/68) neurons, 67.7%] and was usually greater for larger rewards ($n = 39/46$, 84.8%). Responses of 50% of neurons reflected fictive reward size ($n = 34/68$); these responses were

usually greater for larger fictive rewards ($n = 30/34$, 88.2%, $P < 0.05$). A substantial proportion of neurons (35.5%, $n = 24/68$) showed tuning for both experienced and fictive outcomes; most were tuned in the same direction for experienced and fictive rewards (91.7%, $n = 22/24$). The majority of neurons showed matching tuning for experienced and fictive outcomes (97.0%, $n = 66/68$). For the population, the average response strength

Fig. 2. Fictive outcomes influence behavior. **(A)** Histogram of distance between monkeys' choices and optimal target, measured in squares clockwise (c.w.). The dashed line indicates chance performance. **(B)** Likelihood of choosing optimally increases as a function of both fictive and experienced reward outcome on the previous trial. Black, trials after choice of LV; gray, trials after choice of HV. **(C)** Likelihood of switching to new target increases with size of fictive outcome on previous trial. **(D and E)** Likelihood and latency of immediately shifting gaze to HV location are not affected by fictive reward. **(F)** Likelihood of choosing optimally is not influenced by a colored square presented during the delay between trials (red line).

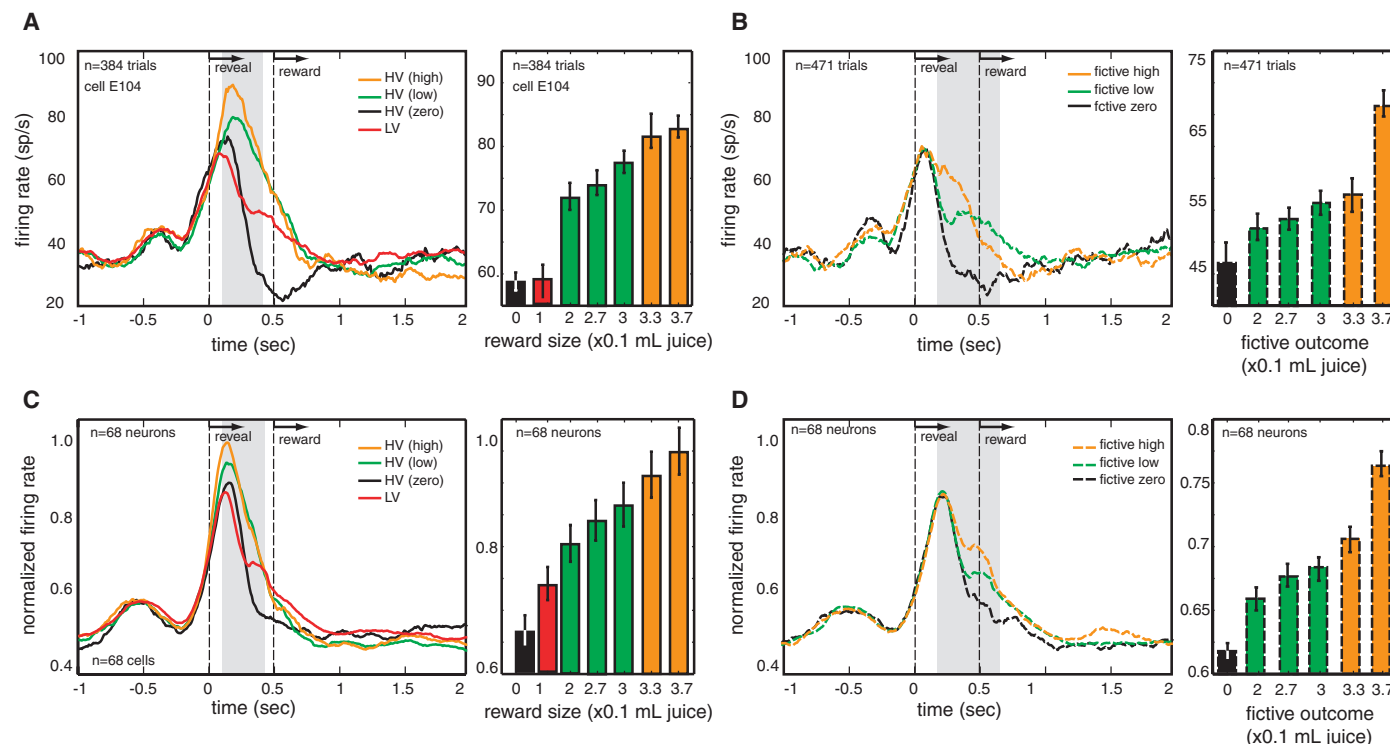
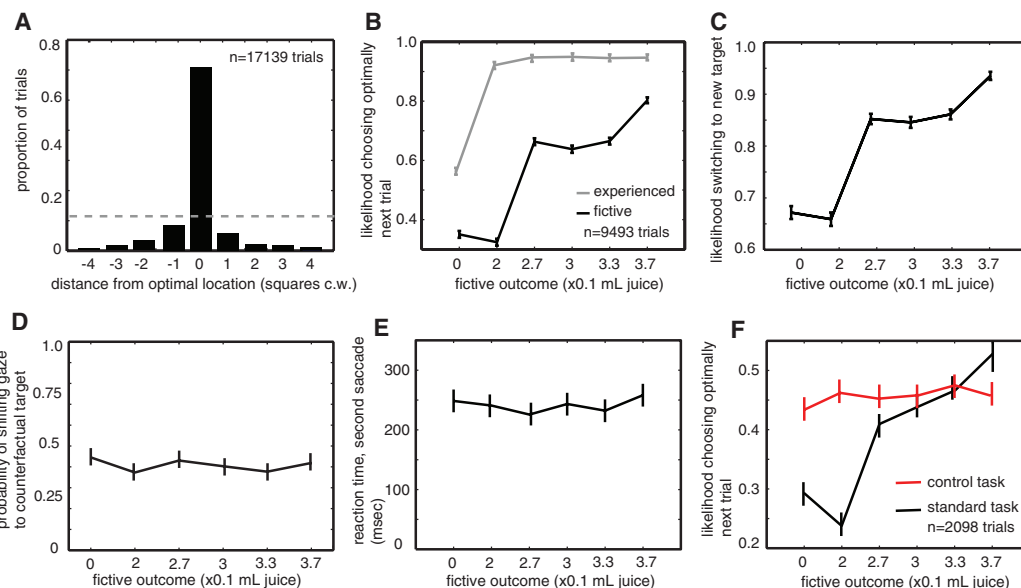


Fig. 3. ACC neurons signal both experienced and fictive rewards. **(A)** (Left) Peristimulus time histogram showing responses of example neuron after choice of HV target. Response grows with reward size. Vertical dashed lines indicate, successively, the time that outcomes are revealed and reward is given. The shaded gray region indicates the epoch used for the bar graph

showing average (± 1 SE) response of neuron for each experienced reward size. sp/s, spikes per second. **(B)** Responses of the same neuron for fictive rewards. Experienced reward was identical (100 μ L) in all cases. **(C)** Population response ($n = 68$ neurons) for experienced rewards, normalized to the maximal firing rate for each neuron. **(D)** Population response for fictive rewards.

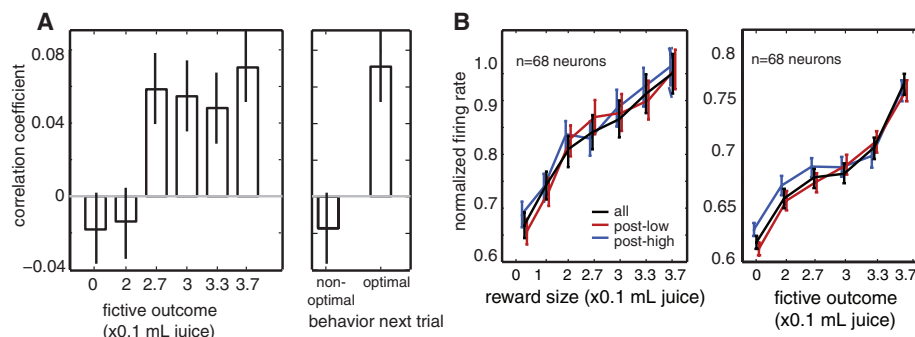


Fig. 4. Neuronal responses signal both fictive rewards and subsequent adjustments in behavior. **(A)** Firing rates after LV trials predict optimal choice on the next trial for four of the six fictive outcomes. **(B)** Neuronal responses to experienced rewards are identical on the trial that follows low (0 μ L, red line) and high (≥ 300 μ L, blue line) fictive outcomes and, thus, do not signal reward prediction errors. Error bars indicate 1 SE.

was greater for experienced rewards than for fictive reward outcomes ($P < 0.01$, bootstrap t test). These phasic neural responses are tightly coupled to gaze shifts to visual targets. These responses may thus reflect visual stimulation, reafferent oculomotor signals, or attention to the cue. The amplitude of these phasic responses carries information about the value of fictive outcomes.

To test the hypothesis that responses to fictive rewards may contribute to behavioral adjustment, we calculated the trial-by-trial correlation between firing rate and likelihood of choosing the optimal target after LV trials for all neurons (Fig. 4A). To control for the different neuronal responses to different fictive rewards, we analyzed data separately for each fictive reward. We found a positive correlation for four of the six fictive outcomes ($P < 0.001$) and no correlation for the remaining two ($P > 0.05$). These results raise the possibility that the firing rate signals subsequent changes in behavior and not fictive outcomes (16). However, a second analysis revealed that firing rates were correlated with fictive outcome preceding trials in which monkeys chose optimally ($P < 0.001$). This analysis controls for any adjustment signal, and confirms that ACC neurons do not merely predict behavioral switching. Finally, reaction times did not correlate with likelihood of choosing the optimal target across all recording sessions ($P > 0.5$, correlation test). This analysis controls for the possibility that the correlation between firing rate and adjustment merely reflects uncontrolled variations in arousal.

One alternative explanation for these data is that, by influencing behavior and thus future rewards (Fig. 2B), fictive outcomes serve as the first predictive cue of the reward on the next trial. We find this alternative explanation unlikely for several reasons. First, a choice intervenes between the time of the fictive cue and the reward at the end of the next trial, which is itself probabilistic. The value of the subsequent reward is therefore not strictly predicted by the fictive cue. Second, the reward signal would have to skip the next salient/rewarding event (the reward on the

present trial) and signal the subsequent one (the reward on the next trial); such a signal would be highly unusual and has not, to our knowledge, been observed in the ACC or any other brain area. Third, if fictive outcomes are perceived as reward-predicting cues, they should elicit faster reaction times and greater accuracy on the next trial (17). We did not observe these effects ($P > 0.5$ for both reaction time and accuracy, Student's t test). Fourth, if the reward on the next trial is larger than the value cued by the fictive outcome on this trial, we should see positive deflections in the neuronal response. Similarly, if the reward on the next trial is smaller than the value cued on this trial, we should see negative deflections in the neuronal response. However, we did not observe any dependence of HV neuronal response on previous fictive value ($P > 0.3$, Fig. 4B). Collectively, these data indicate that the behavioral and physiological correlates of fictive rewards are not an artefactual consequence of simple extended reward associations.

In summary, the most parsimonious explanation for monkeys' behavior in this task is that they recognize and respond to fictive outcomes, and responses of ACC neurons are sufficient to guide such fictive learning. Neural markers of fictive outcomes have so far been limited to non-invasive measures. Hemodynamic activity in the ventral caudate, which is connected with the ACC, reflects fictive learning signals (15), and ACC activity tracks the correlation between craving for cigarettes and fictive learning (11). The error-related negativity, an event-related potential component with a possible source in the ACC, tracks fictive outcomes (18). Here we show that the same neural circuit carries information about fictive outcomes in monkeys. Moreover, information about both experienced and fictive outcomes is encoded by the same neurons and is represented with the use of a similar coding scheme. The correlation between firing rate and behavior suggests that these neurons do not simply tag the incentive salience of a stimulus (19, 20), but also reflect neuronal processes that translate outcomes into behavior.

Thus, the ACC may integrate information about obtained rewards [probably signaled by the dopamine system (21, 22)] with information about observed rewards [presumably computed in the prefrontal cortex (23)] to derive a model of the local reward environment in the near future. These findings are consistent with the idea that the ACC represents both real and fictive reward outcomes to dynamically guide changes in behavior (9, 24–27). Such a mechanism may be crucial in complex social environments, where the behavior of others provides a rich supply of fictive information (15, 28).

References and Notes

1. R. M. Byrne, *Trends Cogn. Sci.* **6**, 426 (2002).
2. K. Epstude, N. J. Roese, *Pers. Soc. Psychol. Rev.* **12**, 168 (2008).
3. N. J. Roese, *Psychol. Bull.* **121**, 133 (1997).
4. G. Loomes, R. Sugden, *Econ. J.* **92**, 805 (1982).
5. S. Ursu, C. S. Carter, *Cogn. Brain Res.* **23**, 51 (2005).
6. D. Lee, B. P. McGreevy, D. J. Barraclough, *Cogn. Brain Res.* **25**, 416 (2005).
7. F. Subiaul, J. F. Cantlon, R. L. Holloway, H. S. Terrace, *Science* **305**, 407 (2004).
8. S. Ito, V. Stuphorn, J. W. Brown, J. D. Schall, *Science* **302**, 120 (2003).
9. S. W. Kennerley, M. E. Walton, T. E. Behrens, M. J. Buckley, M. F. Rushworth, *Nat. Neurosci.* **9**, 940 (2006).
10. J. G. Kerns *et al.*, *Science* **303**, 1023 (2004).
11. P. H. Chiu, T. M. Lohrenz, P. R. Montague, *Nat. Neurosci.* **11**, 514 (2008).
12. N. Camille *et al.*, *Science* **304**, 1167 (2004).
13. Materials and methods are available as supporting material on Science Online.
14. R. L. Reid, *J. Gambling Behav.* **2**, 32 (1986).
15. T. Lohrenz, K. McCabe, C. F. Camerer, P. R. Montague, *Proc. Natl. Acad. Sci. U.S.A.* **104**, 9493 (2007).
16. K. Shima, J. Tanji, *Science* **282**, 1335 (1998).
17. M. R. Roess, C. R. Olson, *Science* **304**, 307 (2004).
18. J. P. Goyer, M. G. Woldorff, S. A. Huettel, *J. Cogn. Neurosci.* **20**, 2058 (2008).
19. S. M. McClure, N. D. Daw, P. R. Montague, *Trends Neurosci.* **26**, 423 (2003).
20. K. C. Berridge, T. E. Robinson, *Brain Res. Rev.* **28**, 309 (1998).
21. W. Schultz, *Annu. Rev. Psychol.* **57**, 87 (2006).
22. P. R. Montague, G. S. Berns, *Neuron* **36**, 265 (2002).
23. M. F. Rushworth, T. E. Behrens, *Nat. Neurosci.* **11**, 389 (2008).
24. C. Amiez, J. P. Joseph, E. Procyk, *Cereb. Cortex* **16**, 1040 (2005).
25. S. W. Kennerley, A. F. Dahmubed, A. H. Lara, J. D. Wallis, *J. Cogn. Neurosci.* **21**, 1162 (2009).
26. R. Quilodran, M. Rothe, E. Procyk, *Neuron* **57**, 314 (2008).
27. M. Matsumoto, K. Matsumoto, H. Abe, K. Tanaka, *Nat. Neurosci.* **10**, 647 (2007).
28. P. H. Rudebeck, M. J. Buckley, M. E. Walton, M. F. S. Rushworth, *Science* **313**, 1310 (2006).
29. This work was supported by a postdoctoral fellowship to B.Y.H. (National Institute on Drug Abuse 023338), an RO1 to M.L.P. (National Eye Institute 013496), and the Duke Institute for Brain Studies. We thank K. Watson for help in training the animals and S. Heilbronner for useful discussions on the tasks. The authors declare no conflicts of interest.

Supporting Online Material

www.sciencemag.org/cgi/content/full/324/5929/948/DC1
Materials and Methods

SOM Text

Figs. S1 to S9

References

13 November 2008; accepted 12 March 2009
10.1126/science.1168488

Extinction-Reconsolidation Boundaries: Key to Persistent Attenuation of Fear Memories

Marie-H. Monfils,^{1,2*} Kiriana K. Cowansage,¹ Eric Klann,¹ Joseph E. LeDoux^{1,3,4,5}

Dysregulation of the fear system is at the core of many psychiatric disorders. Much progress has been made in uncovering the neural basis of fear learning through studies in which associative emotional memories are formed by pairing an initially neutral stimulus (conditioned stimulus, CS; e.g., a tone) to an unconditioned stimulus (US; e.g., a shock). Despite recent advances, the question of how to persistently weaken aversive CS-US associations, or dampen traumatic memories in pathological cases, remains a major dilemma. Two paradigms (blockade of reconsolidation and extinction) have been used in the laboratory to reduce acquired fear. Unfortunately, their clinical efficacy is limited: Reconsolidation blockade typically requires potentially toxic drugs, and extinction is not permanent. Here, we describe a behavioral design in which a fear memory in rats is destabilized and reinterpreted as safe by presenting an isolated retrieval trial before an extinction session. This procedure permanently attenuates the fear memory without the use of drugs.

When fearful memories are formed, they are initially labile but become progressively consolidated into persistent traces via the synthesis of new proteins (1, 2). Later retrieval of a consolidated fear memory engages two seemingly opposing mechanisms: reconsolidation and extinction (3–6). In the process of reconsolidation, a retrieved memory transiently returns to a labile state and requires new protein synthesis to persist further. During this labile state, the memory is amenable to enhancement or disruption (4, 7). The period of instability or lability, the reconsolidation window, persists for several hours after retrieval (8). Reconsolidation occurs in a broad range of learning paradigms (aversive and appetitive conditioning, explicit and implicit memory) (5, 9) and species (from snails to humans) (10, 11). Its adaptive purpose might be to enable the integration of new information present at the time of retrieval into an updated memory representation (4, 12, 13).

The possibility that reactivated memories may be modifiable was proposed many years ago (14, 15), and since then, numerous studies have demonstrated that blockade of the updating process engaged during retrieval—usually via pharmacological intervention within the reconsolidation window—prevents memory restorage and produces amnesia (loss of the specific memory that was reactivated in the presence of the drug or access to it) (4, 8, 12, 13). Thus, in the case of aversive memories, blocking reconsolidation weakens the emotional impact of a once fear-inducing stimulus by altering the molecular com-

position of the memory trace. This process generally requires the use of drugs that often cannot be readily administered to humans.

In contrast, fear extinction—a paradigm in which the conditioned stimulus (CS) is repeatedly presented in the absence of the unconditioned stimulus (US)—leads to progressive reduction in the expression of fear, but is not permanent because extinction does not directly modify the existing memory but instead leads to the formation of a new memory that suppresses activation of the initial trace (16–22). The efficacy of this inhibition, however, is strongly contingent on spatial, sensory, and temporal variables. Specifically, the reemergence of a previously extinguished fear is known to occur, in rodents and humans alike, under three general conditions: (i) renewal, when the CS is presented outside of the extinction context (17, 18); (ii) reinstatement, when the original US is given unexpectedly (19–23); or (iii) spontaneous recovery, when a substantial amount of time has passed (16, 17, 23). In clinical settings, where extinction-based exposure therapy is widely used as treatment for a number of anxiety-related disorders, including phobias and post-traumatic stress, exposure treatments are effective in some cases [e.g., (24, 25)]; however, they do not benefit everyone, and of those who do benefit, many show a return of fear due to spontaneous recovery, reinstatement, or renewal (18, 23, 26, 27).

Here, we devised an effective, drug-free paradigm for the persistent reduction of learned fear, capitalizing on differences between reconsolidation and extinction. Given that extinction training reduces the threatening value of the CS, we reasoned that when applied within the reconsolidation window (after the memory is rendered unstable by presenting an isolated retrieval trial), extinction training would result in the storage of the new nonthreatening meaning of the CS and prevent renewal, reinstatement, and spontaneous recovery, thus resulting in a more enduring re-

duction in fear relative to extinction training conducted outside the reconsolidation window. Specifically, we predicted that an extinction session presented after an isolated retrieval trial would lead to a persistent revaluation of the CS as less threatening, and/or a weakening of the stored trace or access to it, and thus would prevent the return of fear in the three aforementioned tests.

Six experiments were conducted. We first examined whether our behavioral paradigm could prevent the return of fear on a spontaneous recovery test, and if so, whether the observed effect was the result of an update during reconsolidation. We specifically designed this experiment on the basis of the premise that the lability window engaged at the time of retrieval is temporary—in rat fear conditioning, it closes within 6 hours (4)—at which time the memory is thought to be reconsolidated (4). We posited that if the interval between the isolated retrieval cue and extinction training was brief enough to enable the repeated unreinforced CSs to be presented within the lability window, then the new interpretation of the CS as no longer threatening should be incorporated during reconsolidation. If, however, the interval between the isolated retrieval trial and the beginning of extinction was outside the lability boundary, standard extinction should take place (i.e., rather than targeting the initial fear memory during its reconsolidation, a new memory would be formed in parallel with it and would act to temporarily suppress it) and fear should reemerge.

Rats were fear-conditioned using three tone-shock pairings, and were then divided into five experimental groups. Two groups had a retrieval-extinction interval within the reconsolidation window [10 min ($n = 8$) and 1 hour ($n = 8$)] and two groups outside the reconsolidation window [6 hours ($n = 8$) and 24 hours ($n = 8$)]. In addition to these four retrieval (Ret) groups, a fifth group (No Ret) was exposed to context but did not receive a CS retrieval ($n = 12$). All procedures were conducted in context A (grid floor). All groups showed equivalent freezing for the last four trials of extinction [between-subjects analysis of variance (ANOVA), $P > 0.1$; Fig. 1]. Twenty-four hours later, all groups received a long-term memory (LTM) test to assess consolidation of extinction; the groups did not differ from one another (repeated-measures ANOVA, $P > 0.1$). All groups were tested 1 month after extinction, and their freezing to the CS was compared to their respective freezing at the 24-hour time point. A repeated-measures ANOVA revealed a Group \times Time interaction, which suggested that there was a differential effect between the groups between the 24-hour LTM test and the 1-month test [$F(1,39) = 22.47$, $P < 0.0001$]. Simple main effects were then conducted to look at each group individually. The Ret groups with a retrieval-extinction interval outside the reconsolidation window, as well as the No Ret group, showed increased freezing (spontaneous recovery) relative to the 24-hour LTM test [within-subjects,

¹Center for Neural Science, New York University, New York, NY 10003, USA. ²Department of Psychology, University of Texas, Austin, TX 78712, USA. ³Department of Psychology, New York University, New York, NY 10003, USA. ⁴Nathan S. Kline Institute for Psychiatric Research, Orangeburg, NY 10962, USA. ⁵Emotional Brain Institute, New York University, New York, NY 10003, USA.

*To whom correspondence should be addressed. E-mail: monfils@mail.utexas.edu

two-tailed *t* tests; no retrieval, $t(11) = 5.225$, $P < 0.0001$; 6 hours, $t(7) = 5.671$, $P = 0.001$; 24 hours, $t(7) = 2.681$, $P = 0.031$]; however, the Ret groups with an interval within the lability window did not [within-subjects, two-tailed *t* tests; 10 min, $t(7) = 0.146$, $P = 0.888$; 1 hour, $t(7) = 1.59$, $P = 0.156$] (28). These data are consistent with an update during reconsolidation.

To more fully address whether our procedure could prevent the return of fear, we further examined its effect on two additional assays: renewal and reinstatement. Two groups of rats were fear-conditioned as described above (28). Twenty-four hours later, reconsolidation was initiated in one group by exposing the rats to an isolated retrieval trial (one tone presentation; Ret group, $n = 8$), whereas the control group was placed in the same context but was not presented with a cue retrieval (no tone presentation; No Ret group, $n = 8$). One hour later, extinction training occurred (the No Ret group was presented with 19 CSs and the Ret group with 18 CSs, in the absence of the US; that is, tones were repeatedly presented in the absence of shocks). In the Renewal experiment (Fig. 2), rats were fear-conditioned in context A and then received the retrieval, or context-only exposure, and the extinction session in context B (smooth black floor and peppermint scent) (28). Twenty-four hours later, they were tested for long-term memory in context B, and the next day were tested back in context A (renewal test). We found that the No Ret and Ret rats exhibited similar levels of freezing (a measure of fear expression) during fear conditioning (repeated-measures ANOVA, $P > 0.05$), across the last four trials of extinction (repeated-measures ANOVA, $P > 0.1$), and at the test of LTM (repeated-measures ANOVA, $P > 0.1$). When placed back in context A (the original context in which fear to the CS was acquired) to assess whether they would show increased freezing relative to the extinction context (which would be indicative of fear renewal), there was a significant Group \times Time of Test interaction, which suggested that the retrieval procedure induced a differential effect on behavior [$F(1,14) = 13.522$, $P = 0.002$]. Follow-up *t* tests revealed that whereas the No Ret group showed an increase in freezing in context A relative to context B ($P = 0.012$), the Ret group did not ($P > 0.1$).

For the Reinstatement experiment, all procedures (described above) were conducted in context A. Twenty-four hours after extinction, rats received five unsignaled footshocks and were tested for reinstatement the next day (Fig. 3). The No Ret ($n = 8$) and Ret ($n = 8$) groups froze equivalently during conditioning, extinguished at the same rate, and did not differ during the last four trials of extinction (repeated-measures ANOVAs, all tests, $P > 0.1$). There was a significant Group \times Time of Test interaction, which suggested that the retrieval procedure induced a differential effect on freezing behavior [$F(1,14) = 5.456$, $P = 0.035$]. In agreement with previous research, follow-up comparisons revealed that the No Ret rats showed increased freezing 24

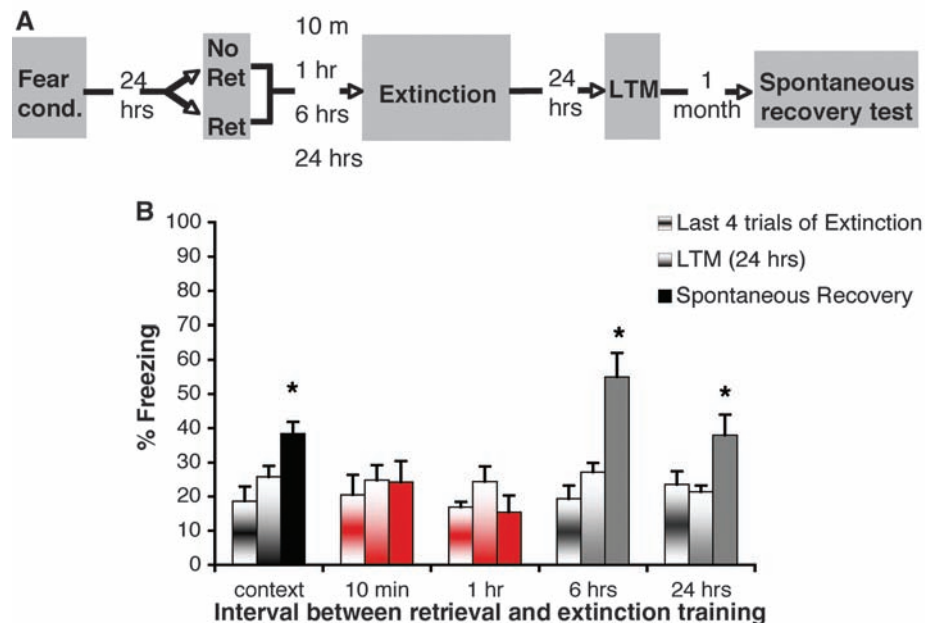


Fig. 1. Finite lability window to prevent return of fear via post-retrieval extinction. (A) Rats were fear-conditioned (Fear Cond) with three tone-shock pairings. After 24 hours, they were exposed either to an isolated cue retrieval trial (Ret) or context only (No Ret) followed by extinction training. The time interval between the retrieval trial (or context exposure, $n = 12$) and the extinction was either within (10 min, $n = 8$; 1 hour, $n = 8$) or outside (6 hours, $n = 8$; 24 hours, $n = 8$) the reconsolidation window. Twenty-four hours after extinction, all groups were tested for LTM, and 1 month later for spontaneous recovery. The gray shading represents context A. (B) All groups were equivalent for the last four trials of extinction and at the 24-hour LTM test. One month later, the Ret groups with an interval outside the reconsolidation window (gray), as well as the No Ret group (black), showed increased freezing (spontaneous recovery) relative to the 24-hour LTM test [no retrieval, $P < 0.0001$; 6-hour intertrial interval (ITI), $P = 0.001$; 24-hour ITI, $P = 0.031$]; however, the groups with an interval within the lability window (red) did not (10 min, $P = 0.888$; 1 hour, $P = 0.156$) (28). All data points show means \pm SEM. Asterisk denotes significance at the 0.05 level.

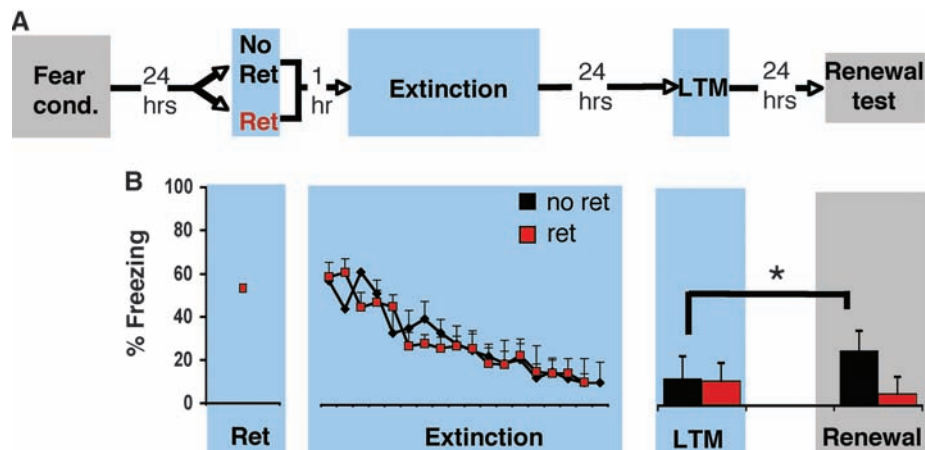


Fig. 2. Attenuation of fear memory by presenting a single isolated retrieval trial followed by an extinction session prevents renewal. (A) Rats were fear-conditioned in context A. Twenty-four hours later, they were exposed either to an isolated cue retrieval trial (Ret, $n = 8$) or context only (No Ret, $n = 8$) in context B, followed 1 hour later by extinction training in context B. Twenty-four hours after extinction, they were tested for LTM in context B. The gray shading represents context A; the blue shading represents context B (28). (B) Rats from both experimental groups froze equivalently during the LTM test (all ANOVAs, $P > 0.1$). When they were placed back in the acquisition context, the No Ret group (black) showed fear renewal ($P = 0.012$), but the Ret group (red) did not ($P > 0.1$), relative to their respective LTM tests. All data points show means \pm SEM. Asterisk denotes significance at the 0.05 level.

hours after the unsignaled footshocks (reinstatement) relative to the last four trials of extinction ($P = 0.017$), but rats in the Ret group did not ($P > 0.1$). There was no difference between the groups in pre-CS freezing (fig. S1).

We next proceeded to determine what molecular mechanism might account for the clear behavioral effect of presenting a single isolated retrieval trial before extinction training. We wanted to use a design that would allow us to examine acute retrieval-induced biochemical changes that would be taking place on a brief time scale, but that would also be predictive of

long-term synaptic plasticity, because there is an overlapping locus of plasticity for extinction and fear conditioning in the lateral amygdala (29). At initial retrieval (first CS presentation after conditioning), both reconsolidation and extinction mechanisms are engaged (5). Generally, as more CSs are presented, learning becomes biased toward extinction. In the current study, the only difference between our two experimental groups for the behavioral experiments was the interval between the first and second CSs. For these reasons, our hypothesis was that a different mechanism must be engaged early on (at the time of our

differential manipulation), and that this would lead to a different long-term outcome. It was previously shown that increasing cAMP-dependent protein kinase (PKA) signaling facilitates, and its blockade hinders, reconsolidation of fear memories in rats (7). In addition, recent rat studies show that reconsolidation after retrieval of a fear memory requires phosphorylation of GluR1 glutamate receptors at the PKA site (Ser⁸⁴⁵) (30). Phosphorylation at the Ser⁸⁴⁵ site is usually followed by GluR1 receptor insertion (30). GluR1 receptor insertion is indicative of synaptic plasticity and takes place during consolidation of fear memories (31). In addition, Hu and colleagues (32) recently showed that norepinephrine [which is known to be important for reconsolidation of fear memories in both rats (33) and humans (11)] can trigger GluR1 phosphorylation via PKA (32). In the final experiment, we therefore examined the effect of an isolated retrieval on the phosphorylation of GluR1 at Ser⁸⁴⁵ and then tested what the effect of a subsequent CS presentation would be.

We examined the effect of a single CS presentation on GluR1 phosphorylation 3 min and 1 hour after the retrieval cue, and then explored what would happen if another CS was played 3 min versus 1 hour after (Fig. 4). These time points were chosen because our two experimental groups (No Ret and Ret) show a drastically different behavioral outcome, and their only distinguishing characteristic is a different interval between the first and second CS. We hypothesized that a certain time period might be necessary for the memory trace to be destabilized. Rats were fear-conditioned, then 24 hours later received (i) context exposure only (No CS) and euthanized 3 min later ($n = 6$); (ii) a single CS retrieval and euthanized 3 min later ($n = 4$); (iii) a single CS and euthanized 1 hour later ($n = 6$); (iv) two CSs with a 3-min interval and euthanized 3 min later ($n = 6$); or (v) two CSs with a 1-hour interval and euthanized 3 min later ($n = 6$). At the time of euthanasia, the lateral amygdala was extracted, frozen, homogenized, and probed on Western blots for phospho-GluR1. We found that memory retrieval resulted in an increase in GluR1 phosphorylation at Ser⁸⁴⁵ [omnibus ANOVA across all groups, $P < 0.05$, with significant post hoc comparisons (Tukey) between the CS-3 min and No CS groups, $P < 0.05$, and between the CS-1 hour and No CS groups, $P < 0.05$]. A second CS presented 1 hour after initial retrieval resulted in dephosphorylation of GluR1 within 3 min, possibly suggesting destabilization of the memory trace, and may underlie the lack of fear reemergence observed in our behavioral experiments. This dephosphorylation of GluR1 was not simply due to the presentation of two CSs instead of one, because the presentation of two CSs with the 3-min interval used in standard extinction did not result in dephosphorylation of GluR1 (Fig. 4 and fig. S2). These results were also confirmed by enzyme-linked immunosorbent assay (ELISA)

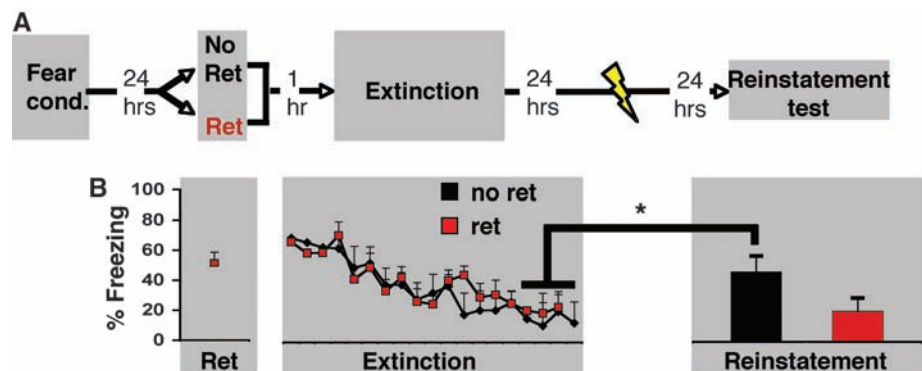


Fig. 3. Presenting a single isolated retrieval trial before an extinction session prevents reinstatement. (A) Rats were fear-conditioned. The next day, they were exposed either to an isolated cue retrieval trial (Ret, $n = 8$) or context only (No Ret, $n = 8$), followed 1 hour later by extinction training. Twenty-four hours after extinction, they received five unsignaled footshocks, and the next day were tested for reinstatement. The gray shading represents context A. (B) The No Ret and Ret groups froze equivalently to the last four CSs of extinction; however, 24 hours after the unsignaled footshocks, the No Ret group (black) showed increased freezing (reinstatement) ($P < 0.05$), but the Ret group (red) did not ($P > 0.05$). All data points show means \pm SEM. Asterisk denotes significance at the 0.05 level.

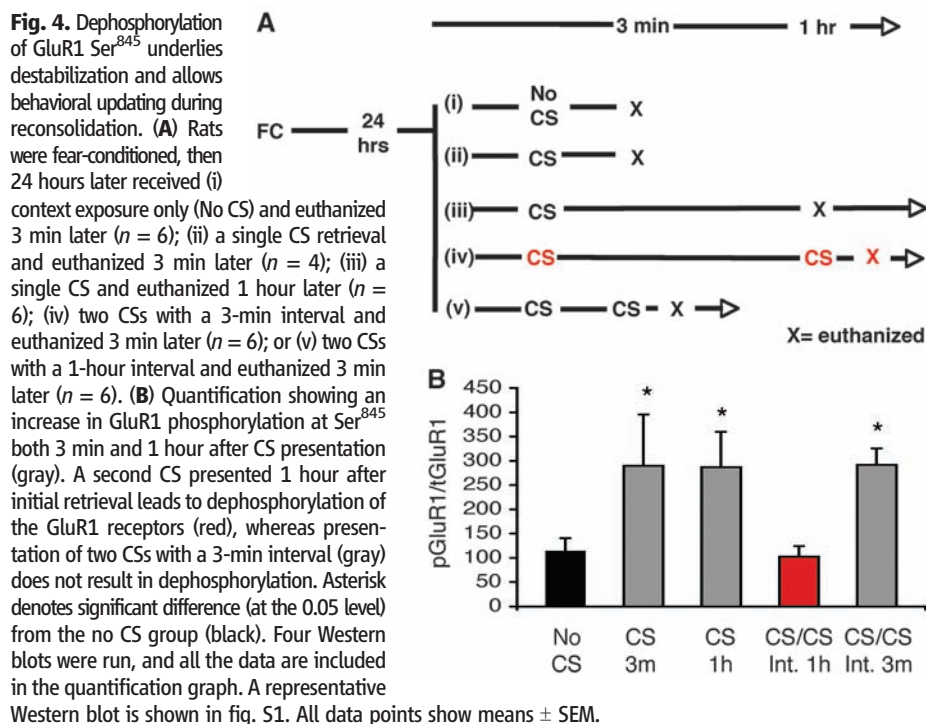


Fig. 4. Dephosphorylation of GluR1 Ser⁸⁴⁵ underlies destabilization and allows behavioral updating during reconsolidation. (A) Rats were fear-conditioned, then 24 hours later received (i) context exposure only (No CS) and euthanized 3 min later ($n = 6$); (ii) a single CS retrieval and euthanized 3 min later ($n = 4$); (iii) a single CS and euthanized 1 hour later ($n = 6$); (iv) two CSs with a 3-min interval and euthanized 3 min later ($n = 6$); or (v) two CSs with a 1-hour interval and euthanized 3 min later ($n = 6$). (B) Quantification showing an increase in GluR1 phosphorylation at Ser⁸⁴⁵ both 3 min and 1 hour after CS presentation (gray). A second CS presented 1 hour after initial retrieval leads to dephosphorylation of the GluR1 receptors (red), whereas presentation of two CSs with a 3-min interval (gray) does not result in dephosphorylation. Asterisk denotes significant difference (at the 0.05 level) from the no CS group (black). Four Western blots were run, and all the data are included in the quantification graph. A representative Western blot is shown in fig. S1. All data points show means \pm SEM.

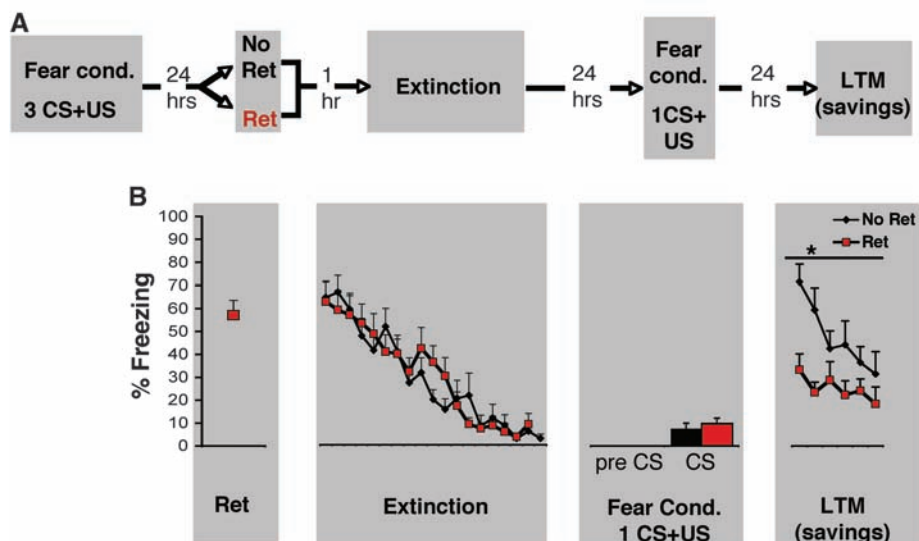


Fig. 5. Presenting a single isolated retrieval trial before an extinction session leads to less fear memory savings than extinction alone. **(A)** On day 1, rats were fear-conditioned. The next day, they received either No Ret + Ext ($n = 10$) or Ret + Ext ($n = 10$), with a 1-hour interval between the retrieval and extinction phases. Then, on the third experimental day, rats were reconditioned using a single CS-US pairing. The fourth day, we tested the groups and compared them for savings. **(B)** The No Ret group (black) froze significantly more than did the Ret group (red) during the LTM-savings test presented 24 hours after the single CS-US training session [$F(1,18) = 11.679$, $P = 0.003$]. The No Ret and Ret groups did not differ during extinction ($P > 0.1$), nor during the single CS-US pairing session ($P > 0.1$), and no significant pre-CS freezing was observed. All data points show means \pm SEM. Asterisk denotes significance at the 0.05 level.

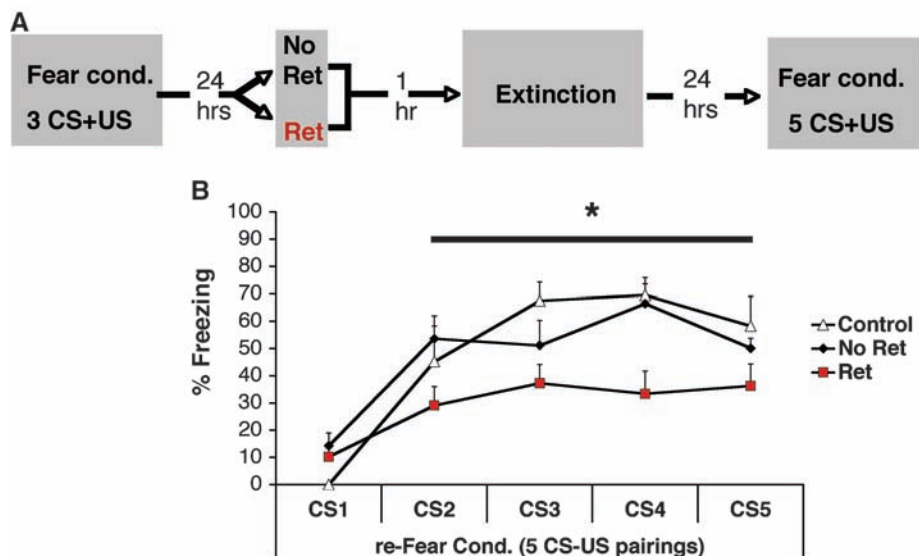


Fig. 6. An isolated retrieval trial followed by an extinction leads to a revaluation of the stimulus as safe, and retards subsequent acquisition of fear conditioning. **(A)** On day 1, rats were fear-conditioned. On day 2, they received either a retrieval (Ret + Ext, $n = 9$) or not (No Ret, $n = 14$), followed 1 hour later by an extinction session (18 CSs for the Ret group, 19 CSs for the No Ret group). On day 3, we reconditioned these groups, as well as conditioned a naïve group of rats (control, $n = 7$), using five CS-US pairings, to look at the effect of our treatment on reacquisition. **(B)** The isolated retrieval presented before extinction (Ret + Ext, red) retards reacquisition, relative to a naïve group (white) or the No Ret + Ext group (black). Repeated-measures ANOVA revealed a main effect of Group [$F(1,27) = 85.85$, $P < 0.0001$] and a Group \times Trial interaction [$F(2,27) = 55.687$, $P = 0.016$]. Simple main effect follow-up showed that the Ret + Ext group was significantly lower than the Control ($P = 0.019$) and No Ret ($P = 0.009$) groups. The Control and No Ret groups were not significantly different from one another. All data points show means \pm SEM. Asterisk denotes significance at the 0.05 level.

(fig. S3). These findings suggest that the two different treatments (Ret + Ext versus No Ret + Ext) engage different molecular mechanisms in the lateral amygdala and lead to a drastically different behavioral outcome.

To better address whether our Ret + Ext paradigm led to a permanent revaluing of the CS, we next sought to examine subsequent susceptibility to reconditioning. We performed a savings experiment, in which the initial phases were identical to the ones presented in the initial set of experiments (day 1: conditioning with three CS-US pairings; day 2: No Ret + Ext, or Ret + Ext, with a 1-hour interval between the retrieval and extinction phases). Then, on the third experimental day, we reconditioned rats through a single CS-US pairing. One additional group received the single CS-US pairing only. On the fourth day, we tested the groups and compared them for savings (six CS presentations). We found that the No Ret group froze significantly more than did the Ret group during the LTM test presented 24 hours after the single CS-US training session [$F(1,18) = 11.679$, $P = 0.003$] (Fig. 5). The No Ret and Ret groups did not differ during extinction or during the single CS-US pairing session ($P > 0.1$). These results could suggest that the initial memory has been reversed (deconsolidated), and/or that the valence associated to the CS has been permanently revalued and reencoded as safe.

To address this further, we ran one additional experiment examining the effect of our Ret + Ext manipulation on the rate of fear reacquisition. On day 1, rats were fear-conditioned using three CS-US pairings. On day 2, they received either a retrieval (Ret + Ext, $n = 9$) or not (No Ret + Ext, $n = 14$), followed 1 hour later by an extinction session (18 CSs for the Ret group, 19 CSs for the No Ret group). On day 3, we reconditioned these groups and also conditioned a naïve group of rats (control, $n = 7$), using five CS-US pairings, to look at the effect of our treatment on reacquisition. Our results suggest that the Ret + Ext treatment not only does not lead to savings, it actually retards reacquisition, relative to a group being conditioned for the first time (control) or the No Ret + Ext group undergoing conditioning (Fig. 6).

Taken together, our renewal, spontaneous recovery, reinstatement, and savings experiments point to a rather resilient decrease in fear induced by our Ret + Ext paradigm. Our GluR1 results suggest that a process taking place in the lateral amygdala may underlie this effect. Furthermore, the reacquisition experiment suggests not only that the CS no longer induces a fear response, but that it may now act as an inhibitor (similar to what we might expect from a latent inhibition paradigm). This could mean that interference during reconsolidation led to a progressive deconsolidation of the memory followed by the learning of a new interpretation of the CS, or that during reconsolidation, the new valence associated with the CS was incorporated in the updating. In either case, the initial valence conferred

by the first conditioning session no longer seems to exist in its original fear-inducing form.

In considering clinical implications, it will be important to pursue further what might underlie the retardation of reacquisition induced by our behavioral procedure because it could, in principle, result in maladaptive behaviors in some cases. Future experiments will determine whether a once fear-inducing stimulus can become simply neutral, without necessarily turning it into a safety signal. That is, it remains to be established whether the process described here involves destabilization, deconsolidation, and updating as safe, or simply destabilization and updating as safe during reconsolidation. Future studies should disambiguate “fear expression” from “fear memory” in response to our procedure, and determine the effects on other fear-related assays. Extending these findings to humans would be particularly useful in addressing questions pertaining to the subjective experience resulting from the updated stimulus.

We have shown that presenting extinction training within a reconsolidation window opened by an isolated CS prevents renewal, reinstatement, and spontaneous recovery of fear memory. This suggests that a post-consolidation behavioral manipulation can render a memory labile and rewrite and/or update it. In rodents, manipulating the intertrial interval of CS presentations during extinction (e.g., using massed versus spaced training) has been reported to yield differential effects on extinction (34), but although massed training is better in the short term, it worsens the long-term outcome (35). Thus, an important aspect of the current procedure in preventing the return of fear is that the initial CS be isolated from subsequent ones. It was also recently shown that extinction training applied shortly after fear conditioning can prevent memory consolidation and the return of fear (36). However, subsequent experiments,

in both rats and humans, that used variations of this protocol have met with limited success (37, 38). This indicates that the contingencies that function to prevent fear reemergence, either in the context of consolidation or reconsolidation, may be sensitive to subtle manipulations. Our results are consistent with the idea that an adaptive purpose of reconsolidation is to incorporate new information at the time of retrieval, and to update a memory (4, 7, 13)—in the present case leading to destabilization of the initial trace in the lateral amygdala, and the reencoding of the once fear-inducing CS as safe.

References and Notes

1. L. R. Squire, H. P. Davis, *Annu. Rev. Pharmacol. Toxicol.* **21**, 323 (1981).
2. J. L. McGaugh, *Science* **287**, 248 (2000).
3. J. L. Lee, A. L. Milton, B. J. Everitt, *J. Neurosci.* **26**, 10051 (2006).
4. K. Nader, G. E. Schafe, J. E. LeDoux, *Nature* **406**, 722 (2000).
5. M. Eisenberg, T. Kobil, D. E. Berman, Y. Dudai, *Science* **301**, 1102 (2003).
6. J. Wolpe, *The Practice of Behavior Therapy* (Pergamon, New York, 1969).
7. N. C. Tronson, S. L. Wiseman, P. Olausson, J. R. Taylor, *Nat. Neurosci.* **9**, 167 (2006).
8. S. Duvarci, K. Nader, *J. Neurosci.* **24**, 9269 (2004).
9. A. Suzuki et al., *J. Neurosci.* **24**, 4787 (2004).
10. S. Sangha, A. Scheibenstein, K. Lukowiak, *J. Neurosci.* **23**, 8034 (2003).
11. M. Kindt, M. Soeter, B. Vervliet, *Nat. Neurosci.* **12**, 256 (2009).
12. C. M. Alberini, *Trends Neurosci.* **28**, 51 (2005).
13. A. Hupbach, R. Gomez, O. Hardt, L. Nadel, *Learn. Mem.* **14**, 47 (2007).
14. J. R. Misanin, R. R. Miller, D. J. Lewis, *Science* **160**, 554 (1968).
15. R. Richardson, D. C. Riccio, M. Jamis, J. Cabosky, T. Skoczen, *Am. J. Psychol.* **95**, 67 (1982).
16. I. V. Pavlov, *Conditioned Reflexes*, G. V. Anrep, Trans. (Liveright, New York, 1927).
17. S. J. Robbins, *J. Exp. Psychol. Anim. Behav. Process.* **16**, 235 (1990).
18. M. Effting, M. Kindt, *Behav. Res. Ther.* **45**, 2002 (2007).
19. R. A. Rescorla, C. D. Heth, *J. Exp. Psychol. Anim. Behav. Process.* **1**, 88 (1975).
20. M. E. Bouton, R. C. Bolles, *J. Exp. Psychol. Anim. Behav. Process.* **5**, 368 (1979).
21. M. E. Bouton, R. C. Bolles, *Learn. Motiv.* **10**, 445 (1979).
22. R. F. Westbrook, M. Iordanova, G. McNally, R. Richardson, J. A. Harris, *J. Exp. Psychol. Anim. Behav. Process.* **28**, 97 (2002).
23. D. Schiller et al., *Learn. Mem.* **15**, 394 (2008).
24. K. Hellstrom, L. G. Ost, *Behav. Res. Ther.* **33**, 959 (1995).
25. M. B. Powers, J. A. Smits, M. J. Telch, *J. Consult. Clin. Psychol.* **72**, 448 (2004).
26. M. K. Rowe, M. G. Craske, *Behav. Res. Ther.* **36**, 719 (1998).
27. M. K. Rowe, M. G. Craske, *Behav. Res. Ther.* **36**, 701 (1998).
28. See supporting material on Science Online.
29. N. Mamiya et al., *J. Neurosci.* **29**, 402 (2009).
30. C. Blackstone, T. H. Murphy, S. J. Moss, J. M. Baraban, R. L. Huganir, *J. Neurosci.* **14**, 7585 (1994).
31. S. Rumpel, J. LeDoux, A. Zador, R. Malinow, *Science* **308**, 83 (2005); published online 3 March 2005 (10.1126/science.1103944).
32. H. Hu et al., *Cell* **131**, 160 (2007).
33. J. Debiec, J. E. LeDoux, *Neuroscience* **129**, 267 (2004).
34. C. K. Cain, A. M. Blouin, M. Barad, *J. Exp. Psychol. Anim. Behav. Process.* **29**, 323 (2003).
35. S. H. Li, R. F. Westbrook, *J. Exp. Psychol. Anim. Behav. Process.* **34**, 336 (2008).
36. K. M. Myers, K. J. Ressler, M. Davis, *Learn. Mem.* **13**, 216 (2006).
37. D. Schiller et al., *Learn. Mem.* **15**, 394 (2008).
38. S. Maren, C. H. Chang, *Proc. Natl. Acad. Sci. U.S.A.* **103**, 18020 (2006).
39. Supported by NIH grants R37 MH038774, P50 MH058911, R01 MH046516, and K05 MH067048 (J.E.L.); NIH grants NS034007 and NS047384 (E.K.); postdoctoral fellowships from the Natural Sciences and Engineering Research Council of Canada, Canadian Institutes of Health Research, and Alberta Heritage Foundation for Medical Research (M.-H.M.); and NIH doctoral fellowship F31MH083472 (K.K.C.). We thank K. Nader, M. Davis, C. Cain, J. Johansen, D. Schiller, and G. Quirk and members of his lab for helpful comments.

Supporting Online Material

www.sciencemag.org/cgi/content/full/1167975/DC1

Materials and Methods

Figs. S1 to S3

3 November 2008; accepted 23 March 2009

Published online 2 April 2009

10.1126/science.1167975

Include this information when citing this paper.

MOVING BEYOND DNA

Scientists have been playing with nucleic acids for decades. Now, with so many newly discovered molecules to explore—no longer just genomic DNA and mRNA but mitochondrial DNA, microRNA, small interfering RNA—companies and even individual researchers are coming up with newer and better ways to purify and store nucleic acids for various downstream applications. And some even have technologies that preclude the need for purification altogether.

By Diana Gitig

Isolating DNA is probably among the most basic things life scientists do. It is likely one of the first protocols they learn—undergraduates, even high school students do minipreps—and they do it constantly, no matter what they are studying. Goals as diverse as generating mutant proteins and organisms, performing microarray experiments, and crystallizing proteins all depend on purified nucleic acids. It is thus perhaps not all that surprising that companies have recognized the need and are providing different kits and technologies to meet the different requirements each application demands.

Full Automation

The immense volume of samples required for “omics” studies demands automation. **Taigen Bioscience** in Taiwan has addressed that demand with LabTurbo, their fully automated nucleic acid extraction system. According to David Daf, the president of Taigen, they chose to use spin columns because they are “the most popular method—they are traditional, reliable, and maintenance costs are low.” So customers are dealing with the same silica membrane chaotropic chemistry they are comfortable with, but Taigen has automated it to save time, labor, and plasticware. Taigen was the first to launch individual spin column automation in 2005; **Qiagen** followed with its Q system in 2007.

LabTurbo’s most unique feature is its use of vacuum manifolds in lieu of centrifugation. Daf says, “Centrifuges introduce air turbulence, which can create a cross-contamination problem. And the gravity may damage the membrane, leeching silica into the elution buffer.” Moreover, it is extremely difficult for a robotic arm to transfer samples from a linear matrix, like a 96-well plate, to a circular centrifuge chamber. LabTurbo is completely linear and has separate vacuum manifolds to further minimize cross-contamination; one for binding and washing, and another for eluting. Cross-contamination is one of the biggest issues in automated systems, and Taigen has gone to extensive lengths to prevent it. LabTurbo can be used to purify genomic DNA or total RNA, from various sources including blood, urine, viruses, plants, and cultured cells—even cigarette butts. The nucleic acids are then ready for use in any downstream application.

Qiagen has been a huge player in nucleic acid manipulation for a long time. They provide many similar products and technologies as some smaller, newer companies mentioned here: the Rotor-Gene Q is like Taigen’s LabTurbo, and QIAsafe is similar to **Biomatrix’s** SampleMatrix described below. But as Nicole York, Qiagen’s marketing communication manager, points out: “What we bring in addition is integration with our instruments as well as our global service organization.” They also have an automated polymerase chain reaction (PCR) system, QIAgility, and machines for automated nucleic acid purification.



CREDIT: ISTOCKPHOTO.COM/URBANCOW

“Goals as diverse as generating mutant proteins and organisms, performing microarray experiments, and crystallizing proteins all depend on purified nucleic acids.”

Look for these Upcoming Articles

Technologies for Gene Transfer — June 19

Label-free Technologies — September 18

Epigenetics — October 9

Inclusion of companies in this article does not indicate endorsement by either AAAS or Science, nor is it meant to imply that their products or services are superior to those of other companies.

Playing It Safe

Once DNA has been purified—regardless of how it is done—the question of how to store it remains. DNA has traditionally been stored in solution at -20°C. But freezers use a lot of energy—which is expensive and not particularly green—take up a lot of space, and can fail, with disastrous results for the samples inside and the questions they were destined to answer. Furthermore, DNA often needs to be shipped. Judy Muller-Cohn and Rolf Muller got tired of dealing with these problems, so they invented sample matrix technology, and co-founded Biomatrix.

With his high throughput genomic studies, Muller says, “I was generating 10,000 samples every week. How can you stabilize these samples in a manner that enables this workflow?” They looked to nature for inspiration. “Extremophiles live everywhere—dry valleys in the Arctic Circle and the Sahara desert, where there is no moisture in the air. These eukaryotes have DNA, RNA, and proteins that are stable for 125 years outside of a freezer,” points out Muller-Cohn. Some of these organisms, like tardigrades and brine shrimp, use anhydrobiosis—life without water—as a mechanism to prevent degradation. And so does SampleMatrix, Biomatrix’s proprietary core technology. Samples are preserved through the formation of a protective, thermostable barrier while air-drying. This barrier protects them from being degraded by heat or ultraviolet light. Samples are recovered by rehydration, and can be used immediately for various analyses. Biomatrix has several products that exploit this technology; one for DNA, one for RNA, and one for plasmids. The company can also stabilize proteins and is working on stabilizing cell lines—all using anhydrobiosis.

Mike Hogan, the founder and chief scientific officer of **Genvault**, tells a similar story. He was providing microarray analysis as a service for high throughput screens and quickly realized that clients’ shipping their DNA to him was the rate-limiting step. “Not having access to high-quality biological specimens in biobanks has held up the entire field” of genetic screening, Hogan says. He started Genvault to be “involved in all aspects of biosample management and transport. Universal genetic screening will become routine at some point in the near future,” he notes. “We are trying to position ourselves for the next era—it is like transitioning from mainframes to the Internet. Things are constantly moving rather than being stored in one spot.”

Genvault’s products are inspired by Guthrie cards, the pieces of Whatman paper that have been used to store and test neonatal blood samples for the past 60 years. GenPlates are little cups of this paper molded into 384-well plates and are used for storing crude nucleic acid material—like bacteria, blood, or plasma—dry and at room temperature for decades. GenSolve is a unique solution that facilitates recovery of samples from the FTA paper. GenTegra is an inert medium, intended to emulate bone, for dry room temperature storage and transport of purified DNA. And GenVault is currently developing a matrix to include the dry-state storage of proteins and biomarkers.

All for One and One for All

According to Nezar Rghei, a vice president of **Norgen Biotek** in Ontario, Canada, new trends such as the use of microarrays, the importance of epigenetics, and the advent of systems biology inspired their All-in-One Purification kits. This is “macromolecular



“Extremophiles live everywhere—dry valleys in the Arctic Circle and the Sahara desert, where there is no moisture in the air. These eukaryotes have DNA, RNA, and proteins that are stable for 125 years outside of a freezer.”

fractionation,” he says, rather than isolation of one component. “Molecules are interrelated and cannot be studied in a vacuum,” according to Rghei. “Once we studied expression using arrays, studying RNA was not sufficient. It became necessary to study protein simultaneously. And when they are isolated separately, there is a normalization problem.” Norgen’s columns are made of silicon carbide, in contrast to most others that are commercially available, which are just silicon. The difference means that Norgen’s matrix can bind to proteins as well as nucleic acids, and each component can be eluted sequentially, even from very small samples.

Its technology also meets the challenges posed by other discoveries, such as quantitative PCR and the discovery of miRNAs—namely, the small sizes of the samples and molecules being studied. Rghei notes that RNA species shorter than 200 nucleotides cannot be isolated in other silicon-based spin columns without the use of phenol which, in addition to being toxic, can inhibit sensitive qPCR assays. Norgen’s is “the only kit on the market that isolates all RNA species without phenol, because it has the ability to bind total RNA and miRNA in the same sample at equal rates. And these are the only kits that can isolate total RNA [mRNA, miRNA, and biomarkers in plasma, which are often products of apoptosis or other degradative processes and therefore very short] in 96-well plates.” miRNAs, large RNAs, genomic DNA, and proteins are thus eluted from a single column, without the use of phenol, chloroform, or acetone, from samples as diverse as blood, yeast, fungi, even soil and water.

Going Without

Sometimes, especially when samples are limited, the best purification is no purification at all. Or so thinks Richard Fekete, research and development manager/scientist at **Applied Biosystems**, a division of **Life Technologies**. (Life Technologies is the new company formed by the merger in November 2008 of Invitrogen and Applied Biosystems, which had previously acquired Ambion.) Applied Biosystems combined “the knowledge of RNA purification from Ambion with the real-time PCR expertise of Applied Biosystems to create one easy-to-use, validated workflow with maximum performance,” explained Fekete. The result is the Cells-to-CT product line. The sample preparation method consists of adding a proprietary lysis buffer to the sample, incubating for five minutes at room temperature, then adding the proprietary stop solution and incubating for another two minutes at room temperature. That’s it. It can be done in 96- or 384-well plates, so it is perfect for high throughput screening. Samples are **continued >**

Nucleic Acid Purification and Manipulation

Featured Participants

Applied Biosystemswww.appliedbiosystems.com**Life Technologies**www.lifetech.com**Biomatrix**www.biomatrix.com**Miltenyi Biotec**www.miltenyibiotec.com**Cornell University**www.cornell.edu**Norgen Biotek**www.norgenbiotek.com**Finnzymes**www.finnzymes.us**Qiagen**www.qiagen.com**Genvault**www.genvault.com**Taigen Bioscience Corporation**www.labturbo.com

then ready for RT-PCR, and results are equivalent to those obtained with purified RNA.

A notable feature of the Cells-to-CT kit is that it is a unique product on the market that has been optimized to prepare single cells for analysis. When starting with the genetic material from only one cell, the losses that are inherent in the washing and eluting steps traditionally used for purification can become a real issue. To avoid it, some researchers have resorted to a “homebrew” method of boiling their samples in buffer or even water. But “boiling does not free RNA from cellular structures and the high temperatures increase the chance of degradation, reducing sensitivity. Moreover, it can change the expression profile,” Fekete points out. Cells-to-CT lyses cells while inactivating RNases, which locks the expression profile at the moment of lysis. Since there is no purification, there is no loss due to heating, sample transfer, or irreversible binding to columns.

Miltenyi Biotec is known for cell separation. But as Kirt Braun, Miltenyi’s marketing manager, says: “We wanted to provide solutions for downstream applications. Our mRNA isolation allows the isolation of highly pure mRNA in 15 minutes, from as little as five cells. So the two variations of the technology [cell separation and molecular separation] work in concert to provide a more comprehensive workflow solution to the research community.”

Miltenyi’s MACS (magnetic assisted cell separation) technology allows for “one-step, in-column RNA isolation and cDNA synthesis or labeling,” according to Braun. Because purification is not a separate step in this in-column cDNA synthesis, pipetting of the sample is minimized, and so is loss of mRNA and cDNA. The technology relies on microcolumns, which Braun explains, “are comprised of a plastic housing filled with a uniform steel ball matrix. With the μ MACS mRNA Isolation Kit the binding of mRNA in solution takes seconds and does not require mixing since the MicroBeads stay in suspension due to their extremely small size.” The sample is eluted with the column still in the magnetic stand to prevent the carryover that is often a problem in other magnetic separation methods.

Yet another approach that, as its website states, “makes DNA purification irrelevant” is made by **Finnzymes**, and its name tells just about all one needs to know about it: Direct PCR. Finnzymes makes a whole slew of Direct PCR kits and protocols for use with specific starting materials, allowing PCR directly from blood, mouse ear and tail, formalin-fixed paraffin embedded (FFPE) tissues, plant leaves, bird feathers, or muscle tissues. Typically, a small volume of the sample is simply added to the PCR reaction mixture. However, Netta Fatal, Finnzymes’ marketing communications manager, qualifies: “PCR from unpurified starting material often requires more optimization than standard PCR reactions from purified DNA and may not always be suitable for all applications.” To minimize the need for optimization the company has protocols for several starting materials available on its website. “And of course we are constantly developing protocols for new starting materials to be able to serve researchers the best we can,” says Fatal.

Do-It-Yourself

But despite the availability of all of these products, some researchers are still die-hard do-it-yourself types. Carl Batt, the Liberty Hyde Bailey Professor in the Department of Food Sciences at **Cornell University**, made a PCR-based biosensor to detect microbial pathogens. His goal (which he achieved) was to make a highly sensitive and highly portable detector that could be used anywhere, not just in a laboratory setting. “What we were looking for was a purification component that could be integrated into a chip that would then be able to serve as an amplification chamber for PCR. The challenge is developing a system which would not require manual transfer of the sample from the purification to the amplification process,” says Batt.

Batt and his colleagues overcame that challenge, creating a biosensor consisting of a microchip with a region of silica-coated pillars to purify DNA linked to a region for real-time PCR. The pillars are etched into the microfluidics channel to increase its surface area. DNA binds to the pillars in the presence of the chaotropic salt guanidinium isothiocyanate, then is washed with ethanol and eluted with a low-ionic strength buffer—just like a miniprep. This lab-on-a-chip is 36 cm x 28 cm x 15 cm, and it can detect 10^4 *Listeria monocytogenes* cells in 45 minutes. “What we developed is a more controlled and certainly a more integrated approach,” concludes Batt.

Personalized medicine seems to be almost upon us. Genetic screens will become mainstream, for biomarkers to predict drug sensitivities, risk assessments, even genealogical studies. And now that the US National Cancer Institute’s Office of Biorepositories and Biospecimen Research is setting up a national biobank, like many countries in Europe and Asia have already done, the need to isolate, store, and transport nucleic acids is only going to increase with time. Fortunately, these forward-thinking entrepreneurs have anticipated that need, and developed these products to meet it.

Diana Gitig is a freelance science writer living in White Plains, New York.

DOI: 10.1126/science.opms.p0900035

Pipetting Tools

The CyBi-WellFlex and CyBi-WellFlex vario provide a unique combination of a multipipetting head, an eight-channel and one-channel pipetting tool, as well as an optional dispenser for the automation of liquid handling applications in biochemistry, molecular biology, and drug discovery. A particularly interesting innovation is the combination of the eight-channel and one-channel pipetting tool on one pipetting head, making both instantly available without time-consuming replacement. This allows automation of the process from the creation of the master mix to the simultaneous processing of a large number of samples. This ability makes it possible to combine the processing of applications, such as the replication or reformatting of complete microplates in the formats of 96-well, 384-well, and 1,536-well; the execution of dilution series; and the hit-picking in an integrated platform. The systems can be integrated into standardized flow boxes for sterile work with cell cultures.



CyBio

For information +49-36-41-351-0
www.cybio-ag.com

UV-VIS Spectrophotometer

The BioSpec-nano is a dedicated spectrophotometer for the quantitation of nucleic acids that features an automated precision drive mechanism to obtain accurate and reproducible results. The BioSpec-nano requires only 1 µl of sample (for a pathlength of 0.2 mm) or 2 µl (for a pathlength of 0.7 mm), which is pipetted onto the measurement plate. No standard rectangular cell is needed for ultrasmall volumes, although for applications that are not volume-limited, an optional rectangular cell is available. Automatic functions include sample mounting, measurement, and cleaning. The operator does not need to perform the tedious, repetitive, and inconsistent placement of the fiber-optic element or the manual cleaning required by other instruments. Sample measurement time is three seconds.

Shimadzu

For information 800-477-1227
www.ssi.shimadzu.com

Gel Visualization

SafeCloner enables safe, ultraviolet-free visualization of ethidium bromide, SYBR Green, and SYBR safe gels. SafeCloner allows DNA bands to be seen safely and clearly, using high-efficiency LED illumination and filter glasses. The use of LED illumination removes the dangers of conventional transilluminator use, such as stray ultraviolet light, which can cause retinal damage. LED illumination does not damage DNA even after long exposure times. In addition, the cloning efficiency of DNA fragments eluted from gels exposed to SafeCloner is significantly greater than that of DNA isolated from traditional ultraviolet-illuminated gels. SafeCloner's blue epi-LED illumination and special filter glass result in greater sensitivity and contrast than longer wavelength 365-nm transilluminators. SafeCloner can be used with inexpensive gel documentation products such as the Cleaver Scientific Microdoc unit.

Cleaver Scientific

For information +44-(0)-1788-565-300
www.cleaverscientific.com

Blood RNA Isolation Kit

The BiOstic Stabilized Blood RNA Isolation Kit is for the extraction of total RNA from PAXgene Blood RNA Tubes in one hour with high yields. A specially formulated wash buffer ensures reliable and complete collection of cells at the start of the protocol and a novel homogenization method provides more complete RNA solubilization for increased recovery on spin filter membranes. Deoxyribonuclease I and a high-activity buffer are

provided for on-column genomic DNA removal during the procedure. All wash buffers contain ethanol to save time and ensure reagent quality.

Mo Bio Laboratories

For information 760-929-9911
www.mobio.com

Complete DNA Profiles

A new 16-locus system makes it possible to get complete profiles from inhibited DNA samples. Forensic samples are often compromised by substances like dirt, fabric dyes, or blood, leading to inconclusive results. The robust and sensitive PowerPlex 16 HS System contains optimized buffer that makes it possible to obtain informative results even with challenging samples, achieving full profiles with higher levels of inhibitors than previously possible. In cases with very limited DNA, like touch samples, PowerPlex 16 HS is sensitive, giving complete profiles with 100 pg of DNA and interpretable data with even less sample. The newly designed product comes complete with internal lane standard in addition to hot-start Taq DNA polymerase premixed in the reaction buffer. The protocol requires fewer pipetting steps than previous systems.

Promega

For information 608-274-4330
www.promega.com

PCR without DNA Purification

Until the launch of Direct PCR, it had been virtually impossible to amplify DNA directly from starting material due to the presence of polymerase chain reaction (PCR) inhibitors. A separate DNA purification step had been needed to remove the inhibitors, which increases costs and hands-on time. Direct PCR eliminates the need for DNA purification prior to PCR and allows PCR to be performed directly from different types of starting material, including blood, mouse ear and tails, and formalin-fixed paraffin-embedded tissue. Direct PCR is based on Finnzymes' unique DNA polymerases featuring fusion protein technology, Phusion High-Fidelity DNA Polymerases and Phire Hot Start DNA Polymerase. These robust polymerases tolerate PCR inhibitors significantly better than conventional polymerases like Taq or Pfu, which can be completely inhibited by minimal amounts of PCR inhibitors. The first Direct PCR kit specifically for blood was recently launched: Phusion Blood Direct PCR Kit.

Finnzymes

For information +385-9-2472-3291
www.finnzymes.com

Electronically submit your new product description or product literature information! Go to www.sciencemag.org/products/newproducts.dtl for more information.

Newly offered instrumentation, apparatus, and laboratory materials of interest to researchers in all disciplines in academic, industrial, and governmental organizations are featured in this space. Emphasis is given to purpose, chief characteristics, and availability of products and materials. Endorsement by *Science* or AAAS of any products or materials mentioned is not implied. Additional information may be obtained from the manufacturer or supplier.



Alexander von Humboldt
Stiftung / Foundation



Shine your Light in Germany

Profit from excellent conditions for research

The Alexander von Humboldt Professorships are Germany's way of creating a beacon effect and energising its research landscape. Every year, the Alexander von Humboldt Foundation is offering ten of the world's leading researchers up to five million EUR each to create new or consolidate existing internationally visible research focus areas at German universities.

Academics of all disciplines are eligible for an Alexander von Humboldt Professorship, provided that they are established abroad and recognised internationally as top-class researchers. They will be nominated by German universities – where appropriate in cooperation with non-university research institutions. Each Alexander von Humboldt Professorship will be sponsored for a period of five years on the premise that the university presents a convincing strategy to sustain the position once the funding period

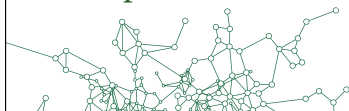
has come to an end. Accordingly, universities are asked to submit an implementation plan as part of the funding application. This will allow new, long-term research groups to be established, conducting cutting-edge (international) research.

The German Ministry of Education and Research is supporting this programme. Visit www.humboldt-foundation.de/ahp for more information. **Next closing dates for applications: 25 September 2009 and 22 January 2010**

Exzellenz verbindet –
be part of a worldwide network.

www.humboldt-foundation.de

E-mail: info@avh.de



Release The Power of Science



Science Careers Classified Advertising

For full advertising details, go to ScienceCareers.org and click For Advertisers, or call one of our representatives.

UNITED STATES & CANADA

E-mail: advertise@sciencecareers.org
Fax: 202-289-6742

Daryl Anderson

US Sales Manager
Phone: 202-326-6543

Joribah Able

Industry – US & Canada
Academic – Midwest/Canada
Phone: 202-326-6572

Alexis Fleming

Academic – East Coast
Phone: 202-326-6578

Nicholas Hintibidze

Academic – West and South Central
Phone: 202-326-6533

Tina Burks

Online Job Posting customer service
Phone: 202-326-6577

EUROPE & INTERNATIONAL

E-mail: ads@science-int.co.uk
Fax: +44 (0) 1223 326532

Tracy Holmes

Associate Director, Science Careers
Phone: +44 (0) 1223 326525

Alex Palmer

Phone: +44 (0) 1223 326527

Dan Pennington

Phone: +44 (0) 1223 326517

Susanne Kharraz Tavakol

Phone: +44 (0) 1223 326529

JAPAN

Mashy Yoshikawa

Phone: +81 (0) 3 3235 5961
E-mail: myoshikawa@aaaas.org

To subscribe to Science:

In US/Canada call 202-326-6417 or 1-800-731-4939.
In the rest of the world call +44 (0) 1223 326515.

Science makes every effort to screen its ads for offensive and/or discriminatory language in accordance with US and non-US law. Since we are an international journal, you may see ads from non-US countries that request applications from specific demographic groups. Since US law does not apply to other countries we try to accommodate recruiting practices of other countries. However, we encourage our readers to alert us to any ads that they feel are discriminatory or offensive.

Science Careers

From the journal Science



POSITIONS OPEN



The Department of Biochemistry at Vanderbilt University School of Medicine is seeking applicants for a tenure-track faculty position at the rank of **ASSISTANT, ASSOCIATE, OR FULL PROFESSOR**. The successful candidate will be expected to establish an innovative research program, educate graduate/medical students, train postdoctoral fellows, and participate in service activities within Vanderbilt and the scientific community. A generous startup package and laboratory space will be provided. The Biochemistry Department currently has internationally recognized researchers in the areas of cell signaling, cell cycle checkpoints, cancer biology, neurobiochemistry, enzymology, mass spectrometry, and structural biology. Applicants will be evaluated primarily on the strength of their research program. All research areas and experimental approaches will be considered. However, we are especially interested in candidates with interests in epigenetics, DNA repair, DNA replication, cell cycle control, or other research areas that complement the existing strengths within the Genome Maintenance Program of the Vanderbilt-Ingram Cancer Center.

Please forward a cover letter, curriculum vitae, contact information for three references, and description of research program as a single PDF file to **e-mail: marlene.jayne@vanderbilt.edu**.

Alternatively, mail hard copies of these materials to:

Biochemistry Faculty Search
Vanderbilt University School of Medicine
c/o Marlene Jayne
607 Light Hall
2215 Garland Avenue
Nashville, TN 37232

Application deadline is September 30, 2009, but applications will be evaluated as they arrive.

Women and minorities are especially encouraged to apply.

POSTDOCTORAL RESEARCHER, Department of Biological Sciences. The Department of Biological Sciences at Louisiana State University has a position available for a Postdoctoral Researcher to participate in research aimed at understanding the functions of the conserved and uncharacterized DedA membrane protein family member in *E. coli* cell division and phospholipid synthesis (see *Journal of Bacteriology* 190:4480, 2008). Position is funded for two years in the laboratory of **William T. Doerrler, Ph.D.** Required qualifications: Ph.D. or equivalent degree in microbiology or related discipline; ability to conduct independent research. Additional qualifications desired: experience in molecular biology, bacterial genetics, and/or protein biochemistry. Responsibilities: conducts research aimed at understanding the functions of the conserved and uncharacterized DedA membrane protein family member in *E. coli* cell division and phospholipid synthesis; writes grants and prepares manuscripts based on research; supervises and trains students; performs general laboratory maintenance. An offer of employment is contingent on a satisfactory preemployment background check. Application deadline is May 29, 2009, or until a candidate is selected. Apply online at **website: <http://www.lsu.systemcareers.lsu.edu>**. *LSU System is an Equal Opportunity/Equal Access Employer.*

STEM CELL BIOLOGY AND IMMUNOLOGY RESEARCH POSITION

Research Associate position available. We seek motivated researchers. Candidates who wish to pursue research on molecular processes that regulate hematopoietic stem cell function, immune regulation, or natural killer cell biology. Bachelor's degree in molecular biology, biochemistry, immunology, or related bioscience required (advanced degree a plus). Two years of laboratory experience required. Must be able and willing to work with mice. Apply to **position #025047** online at **website: <http://www.upstate.edu>**. *SUNY Upstate Medical University is an Affirmative Action/Equal Employment Opportunity/ADA Employer engaging excellence through diversity.*

POSITIONS OPEN

POSTDOCTORAL POSITION in HEPATOBIILIARY CANCER RESEARCH

A Postdoctoral position is currently available to participate in long-term NIH-funded research on the molecular pathogenesis of hepatobiliary cancer. Suitable candidates should possess a Ph.D. or M.D./Ph.D. with research experience in tumor cell biology. Expertise in cancer cell/stromal cell interactions, tumorigenicity assays, siRNA technology, and molecular biology are highly desirable. Preference will be given to candidates who are also eligible for U.S. postdoctoral fellowships and have strong communication skills in the English language. Salary levels are attractive and commensurate with experience and qualifications. Applicants should send curriculum vitae and contact information for three references to: **Dr. Alphonse E. Sirica, Professor and Division Chair, Division of Cellular and Molecular Pathogenesis, Department of Pathology, Virginia Commonwealth University School of Medicine, Richmond, VA 23298-0297. E-mail: asirica@mcvh-vcu.edu**. *Virginia Commonwealth University is an Equal Opportunity/Affirmative Action Employer. Women and minority candidates and persons with disabilities are encouraged to apply.*

FACULTY POSITION AT THE UNIVERSITY OF VIRGINIA

The Department of Pharmacology (**website: <http://www.healthsystem.virginia.edu/internet/pharmacology/>**) is seeking to fill a position at the **ASSISTANT/ASSOCIATE/FULL PROFESSOR** level. The Department has current strengths in endocrinology and in mammalian cellular and integrative neurobiology. To complement and broaden these areas of interest, we are looking for individuals who will develop a research program that utilizes any combination of modern molecular, cellular biological, and mouse genetic approaches. The position offers newly renovated space and access to state-of-the-art departmental and core facilities. A doctoral degree in pharmacology, physiology, chemistry, biochemistry, medicine, or related discipline with at least two years postdoctoral training and evidence of significant research productivity is required. To apply send curriculum vitae, a two-page document delineating significant research accomplishments and future research plans, and a list of three references (including e-mail addresses and telephone numbers) to: **Pharmacology Search Committee, Department of Pharmacology, University of Virginia, P.O. Box 800735, Charlottesville, VA 22908-0735. E-mail: pharmsearch@virginia.edu**. The position will remain open until filled. *The University of Virginia is an Equal Opportunity/Affirmative Action Employer.*

Memorial Sloan-Kettering Cancer Center – RESEARCH ASSOCIATE POSITION in Cancer Population Genetics and Genomics. Starting July 1, 2009. Focus on inherited susceptibility to cancers of the breast, ovary, colon, prostate, and lymphoma. Methodologies include whole genome association studies, population genetics, and candidate gene association studies (see, for example, PubMed ID 18326623; 18251999; 17999359). Applicant must have strong background in population genetics, molecular biology, and high throughput genotyping. Send application and three letters of reference to: **Kenneth Offitt, M.D., M.P.H., Clinic Genetics Service, Box 192, Memorial Sloan-Kettering Cancer Center, 1275 York Avenue, New York, NY 10065. Fax: 646-888-4081; e-mail: offitt@mskcc.org**. *Memorial Sloan-Kettering Cancer Center is an Equal Opportunity Employer with a strong commitment to enhancing the diversity of its faculty and staff. Women and applicants from diverse racial, ethnic, and cultural backgrounds are encouraged to apply.*



Seattle Children's HOSPITAL • RESEARCH • FOUNDATION

Neurological Surgery Associate Professor / Professor

The recently established Center for Neuroscience at the Seattle Children's Research Institute invites applications for a full-time faculty position, with the University of Washington School of Medicine Department of Neurological Surgery, at the rank of Associate Professor or full Professor, without tenure. Qualified applicants should be established investigators who are applying techniques of molecular, genetic or cellular biology to study mechanisms underlying hydrocephalus. The Center for Neuroscience at the Seattle Children's Research Institute's research vision is to restore children's health through a mechanistic understanding. The applicant's area of research interest should be complementary to the interests of current faculty working on various areas of neuroscience and bioengineering. Researchers interested in understanding CSF hydrodynamics, choroid plexus function, neuroendocrinology, brain metabolism, blood brain barrier function, brainstem neurobiology and proteomics research are particularly encouraged to apply. The successful candidate must have a M.D. and/or Ph.D. degree and have active nationally funded research grants. Level and salary will be based on applicant's qualifications and experience. Responsibilities of the position include development of an independent, extramurally funded research program, establishing a hydrocephalus section within the Center for Neuroscience and mentoring graduate and post-doctoral students and junior faculty investigators.

This position is open until filled. Address any inquiries to **Dr. Jan-Marino Ramirez, Center Director**, at nino.ramirez@seattlechildrens.org. Please send CV, a statement of current and future research interests and the names and contact information of three references to: **Wendy Kramer, Seattle Children's Research Institute, 1900 Ninth Avenue, M/S C9S-9, Seattle, WA 98101.**

For more information about Seattle Children's Research Institute, please visit:
<http://research.seattlechildrens.org>.

*All University of Washington faculty engage in teaching, research, and service.
The University of Washington is an Equal Opportunity/Affirmative Action Employer.
Women and minorities are encouraged to apply.*

UW Medicine
SCHOOL OF MEDICINE

Postdoctoral Associate

Stony Brook University's Department of Physiology and Biophysics is seeking a postdoctoral associate for stem cell research.

The function and regulation of Wnt signaling will be explored at the cellular level by using embryonic stem cells as a model system. The candidate will apply molecular biological, biochemical, and microscopic techniques in the study of the project.

Required qualifications: Ph.D. or equivalent in biological sciences. Prior experience in cell signaling with up to two years of postdoctoral training is preferred.

For a full position description, application procedures, or to apply online, visit www.stonybrook.edu/jobs (Ref. #HS-R-5795-09-04-S).

To apply, submit a cover letter and résumé to: Dr. Hsien-yu Wang, Associate Professor of Research, Department of Physiology and Biophysics, Health Sciences Center BST T5-180, Stony Brook University Stony Brook, NY 11794-8661

Fax: (631) 444-3432

Equal Opportunity/Affirmative Action Employer. Women, people of color, individuals with disabilities, and veterans are encouraged to apply.

**STONY
BROOK**



Kumamoto University

Location: Kumamoto, Japan

Open Recruitment of Young Researchers (2nd Stage)

1. Open Recruitment of Researchers (2nd stage)

- Special project researchers (all given the title of "specially appointed assistant professor")
- A maximum of 3 researchers

2. Qualification Requirements

- (1) Academic degree, etc.: Young researchers who have obtained a PhD degree within approximately the past 10 years (as of April 1, 2009)
- (2) Achievements/ability: Has outstanding research capabilities and/or research achievements in one of the specialty areas outlined at the following website: <http://sendou.kuma-u.jp/>.

3. Arrival: As soon as possible between September 2009 and October 2009

4. Period of Employment

- Those hired in stage 2 will be employed through March 2014. (Contracts will be for one year each and will be renewed once a year through March 31, 2014.)

(Note: After having gone through career advancement evaluations and after the end of one's term of employment, it is possible for one to be promoted to the position of "Associate Professor" in the Kumamoto University Priority Organization for Innovation and Excellence. A total of approximately 8 people from stages 1 and 2 will be chosen for these positions.)

5. Application Deadline: Applications must reach the university by no later than **May 29, 2009** (Friday).

6. Inquiries: Any inquiries should be made by e-mail to the Research Cooperation Section (person in charge of research strategy) of Kumamoto University at the e-mail address written below: k-senryaku@jimu.kumamoto-u.ac.jp.

Please be sure to allow enough time before the application deadline for a response to be made to you.

For details on applying, please visit the following website: <http://sendou.kuma-u.jp/>

Applications will not be accepted through our website.

FACULTY POSITION - VIROLOGY

The Department of Microbiology at U.T. Southwestern Medical Center at Dallas seeks a new faculty member in molecular virology at the Assistant Professor (tenure track) level. The appointee will be expected to develop a front-rank, competitive, independent research program that focuses on one or more aspects of the viral life cycle (host-pathogen interactions, viral pathogenesis, disruption of viral replication, command of host cell processes, viral immunology, etc.), and that will complement existing strengths in HCV, poliovirus, West Nile virus, HIV/SIV, KSHV, and viral oncogenesis. Research on any virus of medical relevance is of interest. The appointee will contribute to the teaching of medical and graduate students. Attractive start-up packages, including a competitive salary and new laboratory space, are available to conduct research in an expanding, dynamic environment. For exceptional candidates, an Endowed Scholars Program offers start-up funds of \$700,000 (plus \$300,000 towards salary support) over a four-year period. Candidates should have a Ph.D. and/or M.D. degree with at least three years of postdoctoral experience and an exceptional publication record.

Candidates please forward a c.v., three letters of recommendation, two or three representative publications, and a brief summary of future research to: **Dr. Michael V. Norgard, Chair, Department of Microbiology, U.T. Southwestern Medical Center, 6000 Harry Hines Blvd., Dallas, TX 75390-9048** (michael.norgard@utsouthwestern.edu).

U.T. Southwestern is an Equal Opportunity/Affirmative Action Employer.



Director, Therapeutics for Rare and Neglected Diseases Program

National Human Genome Research Institute

The National Institutes of Health (NIH) is seeking to recruit a dynamic and experienced senior scientist to serve as the founding director of the Therapeutics for Rare and Neglected Diseases (TRND) Program, a new effort being administered by the National Human Genome Research Institute (NHGRI) and the NIH Office of Rare Diseases Research (ORDR), in consultation with the other Institutes and Centers of the NIH. The Program will develop small molecule compounds for treating rare and neglected diseases that are suitable for human testing, beginning with chemical probes provided by the research community. The successful candidate will be expected to coordinate a first-rate research program and to work closely with other researchers, Federal agencies, and disease advocacy groups to promote the development of clinical candidates for rare and neglected diseases. They will also be expected to develop new technologies to improve success rates in the preclinical stage of the drug development process, thereby advancing the primary goal of TRND. This fully funded research position will include an ongoing operating budget, as well as positions for medicinal chemists, ADME pharmacologists and toxicologists, informaticians, and project management scientists.

Candidates must have an M.D., M.D./Ph.D., or equivalent degree, research experience in the genetics of rare diseases, demonstrated accomplishment in the preclinical development of drugs for the treatment of rare or neglected diseases, and a strong track record of scientific leadership and effective management of a major scientific program.

Interested applicants should submit their *curriculum vitae*, a description of their research experience and interest in this TRND opportunity, and three letters of recommendation through our online application system, at <http://research.nhgri.nih.gov/apply>.

The closing date for this position is June 15, 2009.

Specific questions regarding this position may be directed to Dr. Andy Baxeavanis (Search Chair) at andy@nhgri.nih.gov or by fax (301-480-2634).

DHHS and NIH are Equal Opportunity Employers and encourage applications from women and minorities.

NATIONAL HUMAN GENOME RESEARCH INSTITUTE Division of Intramural Research

U.S. DEPARTMENT OF HEALTH AND HUMAN SERVICES | NATIONAL INSTITUTES OF HEALTH | genome.gov/DIR



Department of Health and Human Services National Institutes of Health National Institute of Mental Health Tenure Track Investigator

The Division of Intramural Research Programs (DIRP), National Institute of Mental Health (NIMH), invites applications for a Tenure Track Investigator in the field of psychiatric neurobiology, to work in the Genes, Cognition and Psychosis Program (GCAP) under the direction of Dr. Daniel Weinberger, Program Director. The candidate is expected to have experience in biological studies of mental illness and to develop an independent research program in translational neuroscience research focused on understanding the molecular mechanisms of genetic risk factors associated with schizophrenia.

The candidate must have a Ph.D., M.D., or equivalent degree, and broad research experience as a molecular and/or cellular biologist and/or geneticist working with model systems of mental illness. Candidate will be provided with personnel and budget to conduct this research. Salary is commensurate with experience and accomplishments, and a full Civil Service package of benefits (including retirement, health, life, and long term care insurance, Thrift Savings Plan participation, etc.) is available.

The National Institute of Mental Health (NIMH), is a major research component of the National Institutes of Health (NIH) and the Department of Health and Human Services (DHHS), and has nation-wide responsibility for improving the health and well being of all Americans, the Department of Health and Human Services oversees the biomedical research programs of the National Institutes of Health and those of NIH's research Institutes. Interested candidates should send letter of interest, cv/bib, statement of research interests, accomplishments, and goals, together with three reference letters to: **Dr. David Goldman, Chair, GCAP Search Committee, National Institute of Mental Health, Bldg. 10, Rm. 4N-222, 9000 Rockville Pike, Bethesda, MD 20892; or by e-mail to steyerm@mail.nih.gov.** Review of applications will begin **July 20, 2009**, but applications will continue to be accepted and considered until the position is filled.


www.westernu.edu

Faculty Positions in Pharmacology available for 2009 College of Osteopathic Medicine of the Pacific

Western University of Health Sciences is a thriving center for health care and veterinary medicine education. The University's 10 year plan and core values have made the Institution a national leader for the development of interprofessional and graduate medical education. The University values a diverse institutional community and is committed to excellence in its faculty, staff and students. Western University seeks applicants of distinguished academic accomplishments who possess a passion for excellence and a proven track record of achievements.

The Department of Basic Medical Sciences provides the preclinical education for the College of Osteopathic Medicine and invites applications from highly motivated individuals for tenure-track faculty positions in pharmacology. Rank will be commensurate with experience. The successful applicants must have a Ph.D. in pharmacology or equivalent field and at least 2 years of postdoctoral experience. Preference will be given to individuals who have demonstrated excellence in teaching and significant scholarly activity with a strong potential to obtain extramural funding. Submit a current curriculum vitae and a cover letter describing your teaching experience and philosophy, your research activity and goals, and how you meet the qualifications for the position. Please include contact information for at least three references. These positions will remain open until filled.

A completed Employment Application found at:

http://www.westernu.edu/bin/hr/pdf/application_for_employment.pdf

Nissar A. Darmani, Ph.D.,
Assistant Dean for Basic Sciences and Research
Department of Basic Medical Sciences
Western University of Health Sciences
College of Osteopathic Medicine of the Pacific
309 E. Second Street, Pomona, CA 91766-1854
Email Address: ndarmani@westernu.edu

Western University of Health Sciences is an equal opportunity employer.



Program Director

Conservation of Threatened Species and Habitats

One of the world's major botanical gardens specializing in desert plants seeks an individual to direct an expanded and enhanced conservation program. The successful applicant will have (1) training in botany and the ecology of rare species (2) knowledge of conservation policy issues and governmental regulatory frameworks and (3) experience in implementing conservation measures. The Program Director will be a member of the Research Department and report to the Director of Research. Responsibilities include program development and management, collaboration with other conservation organizations and governmental agencies, and seeking extramural funding for program initiatives. Ph.D. and strong supervisory skills are required.

Send C.V., a 1-page description of your philosophical approach to conservation issues, and names and contact information of three references to: **Ms. Mary Catellier, Director of Human Resources, Desert Botanical Garden, 1201 N. Galvin Pkwy., Phoenix, AZ 85008.** Review of applications will begin **June 15, 2009** and applications will be accepted until position is filled.

An Equal Opportunity Employer.



FACULTY POSITIONS IN HEPATOBIILIARY/PANCREATIC DUCT CANCER RESEARCH

As part of its new major strategic research plan, Virginia Commonwealth University's School of Medicine in conjunction with the VCU Massey Cancer Center, a NCI-designated cancer center, is seeking applicants for full-time tenure-track faculty positions at the Assistant or Associate Professor rank to join an expanding basic and translational research initiative with a focus on the molecular pathology and target-based therapeutics of hepatobiliary and pancreatic duct cancers.

Successful candidates should possess outstanding research credentials that complement and extend our current areas of research strengths, including those focused on model systems of hepatobiliary cancer development and progression, molecular pathology and pathogenesis of cholangiocarcinoma, growth factor receptor tyrosine kinases, tumor microenvironment, and target-based cancer therapeutics. Preference will be given to candidates who have transferable NIH-R01 funding or who are likely able to successfully compete for such funding. Selected candidates will also be expected to meet institutional requirements for participating in graduate student and postdoctoral training. Individual faculty appointments will be made in appropriate basic science or clinical departments, with academic rank based on the applicant's qualifications. Successful candidates will receive a very generous start-up package, together with a competitive salary and excellent research space situated to maximize collaborative interactions. Candidates must have an earned M.D./Ph.D., Ph.D., or M.D., and demonstrate research accomplishments in the field of hepatobiliary and/or pancreatic duct cancer.

Interested individuals should submit a curriculum vitae, a summary of research interests and plans, and contact information and e-mail addresses for three professional references to: **Dr. Alphonse E. Sirica, Search Committee Chair, Department of Pathology, Virginia Commonwealth University School of Medicine, P.O. Box 980297, Richmond, Virginia 23298-0297** at asirica@mevh-vcu.edu.

Virginia Commonwealth University is an Equal Opportunity/Affirmative Action Employer. Women and minorities are encouraged to apply.



Anatomy Faculty Position

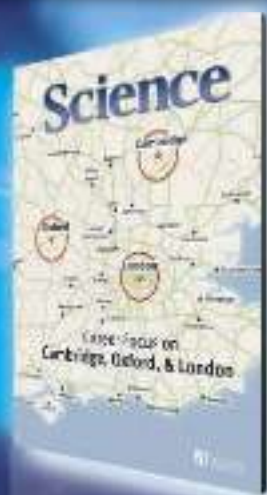
Des Moines University is currently seeking applications from qualified candidates for a tenure-track Anatomy faculty position (option for a non-tenure position also available). The successful candidate must possess a doctoral degree or be in the terminal stages of doctoral candidacy. Prior teaching experience in the anatomical sciences is strongly desired. The selected candidate will be expected to pursue independent research leading to extramural funding.

Des Moines, Iowa, a vibrant mid-sized city, with nationally recognized schools, low cost of living and cultural activities, affords opportunity for scholarly collaboration with various Midwest universities and private institutions. The mission of the anatomy department is to engage future health care providers, educators, scientists and community members in a dynamic evidenced-based discipline that fosters a professional environment of scholarly activity and service. Des Moines University takes great pride in the depth and breadth of its anatomy programs and the recent investments in both new digitally equipped dissection laboratory and scholarly research facilities.

Persons interested in this position should submit their CV, contact information for three references, and a summary statement regarding their teaching philosophy, scholarly activities and goals using the online applicant tracking system located at www.dmu.edu/employment. Please note, Des Moines University does not accept hard copy, faxed or emailed resumes. *Candidates must have current and permanent legal rights to work in the U.S.* Review of applications will begin immediately and continue until the position is filled.

For a complete job description for this position, benefits or more information on Des Moines University and its various academic programs, please visit www.dmu.edu/employment.

Des Moines University is an EOE Employer.



Career Focus on Cambridge, Oxford, and London

Issue date

26 June

Reserve ad space by 9 June

The power of *Science* is in the journal's 131,000 weekly subscribers and 700,000 weekly readers. In our 26 June issue we will use this power to highlight the state of the scientific job market in and around these renowned British seats of learning.

Bonus Distributions

Darwin Festival 2009

5–10 July, Cambridge, UK

International Society for Stem Cell Research

8–11 July, Barcelona, Spain

Contact: Alex Palmer
Telephone: +44 (0) 1223 326 500
E-mail: ads@science-int.co.uk

Science Careers

From the journal *Science* AAAS

ScienceCareers.org

At the Johann Wolfgang Goethe-Universität Frankfurt am Main are the following Professorships immediately available:

Faculty of Computer Science and Mathematics

Assistant Professorship (Juniorprofessur W1) in Computational Neuroscience - Detailed Modeling of Signaling in Neurons

a three-year temporary position with an option of prolongation for three more years

Applicants must have given significant contributions to modeling and signal processing in neurons on the cell level. You must further have contributed to the fields of image processing, numerical simulation methods and high-performance computing. The position is filled in cooperation with the Goethe Center for Scientific Computing and the Bernstein-Group Detailed Modeling of Signal Processing in Neurons.

In the context of the Frankfurt Vision Initiative (Bernstein Focus for Neurotechnology, an initiative funded by the German ministry for education and research (BMBF):

Full Professorship (W3) in Software Engineering with emphasis on biologically inspired vision systems

Applicants must have an excellent track record in the areas of software engineering and biologically inspired computer vision systems. Experiences in the management of large and complex software projects is required. The successful applicant shall closely collaborate with other groups of the Bernstein Focus. Successful acquisition of third party funding and collaborations in interdisciplinary project consortia are expected. In addition, a high commitment to teaching and University service are desired.

Assistant Professorship (Juniorprofessur W1) in Computer Vision and Machine Learning

a three-year temporary position with an option of prolongation for three more years

Applicants must have an excellent track record in the areas of computer vision and machine learning. The successful applicant shall closely collaborate with other groups of the Bernstein Focus. Successful acquisition of third party funding and collaborations in interdisciplinary project consortia are expected. In addition, a high commitment to teaching and University service are desired.

Frankfurt Institute for Advanced Science (FIAS)

Associate Professorship (W2) in Computational Neuroscience (tenure track)

The position is initially available for 5 years (tenure track). Applicants must have an excellent track record in the area of modeling the visual system with probabilistic techniques. Successful acquisition of third party funding and collaborations in interdisciplinary project consortia are expected. In addition, a high commitment to serve in the institute's self-administration is desired. The teaching obligations for this position are two hours per week. The successful candidate will also be member of the Faculty of Computer Science and Mathematics or the Faculty of Physics.

The Goethe University intends to strengthen its emphasis on complex systems research. Successful applicants shall closely collaborate with other interdisciplinary research projects and in excellence networks.

The designated salary for the position is based on "W" on the German university scale. Goethe University is an equal opportunity employer. For further information regarding the general conditions for professorship appointments, please see: <http://www.uni-frankfurt.de/aktuelles/ausschreibung/professuren/index.html>.

Applications accompanied by the usual information (CV, degrees and certificates, list of publications, details on teaching and international experience, information on successful grant applications), should be sent to: **Goethe University Frankfurt, Dean of the Department of Computer Science and Mathematics, E-Mail: dekanat@fb12.uni-frankfurt.de**. Deadline for applications is **June 15, 2009**.



The University of California, Davis, seeks an internationally recognized expert in energy efficiency science, technology or policy to lead the UC Davis Energy Efficiency Center (EEC) as faculty director and associate or full professor, and to become holder of the prestigious Chevron Chair in Energy Efficiency.

To be considered, applicants must have a Ph.D. degree or equivalent in a relevant energy-efficiency related field, outstanding leadership and administrative experience, and an excellent record of accomplishment in teaching, research, and outreach in one or more areas of energy science, technology, or policy. Demonstrated skill in obtaining overhead bearing and gift extramural funds is expected.

Applicants should visit <http://eec.ucdavis.edu/> and follow instructions for submitting on-line applications. Applicants will be asked to submit a *curriculum vitae* including publication list, three related publications, a statement of teaching and research interests, a statement describing vision and leadership experience, and the names and addresses (including e-mail and telephone numbers) of five references.

Inquiries should be directed to:

Prof. Daniel Sperling
Search Committee Chair
Institute of Transportation Studies
University of California
One Shields Avenue
Davis, CA 95616

The position is open until filled, but to ensure full consideration, applications should be received by **July 15, 2009**.

UC Davis is an Affirmative Action/Equal Employment Opportunity Employer and is dedicated to recruiting a diverse faculty community. We welcome all qualified applicants to apply, including women, minorities, individuals with disabilities and veterans.

Tenure Track Urologic Research Faculty Department of Urology

The Department of Urology at the University of Wisconsin-Madison, School of Medicine and Public Health is seeking candidates for a tenure track position in genitourinary and urologic research. The candidate will be expected to establish an independent, extramurally funded research program and to attain national recognition for accomplishment and leadership in urologic research. Responsibilities will include developing and nurturing collaborative interactions among faculty in Urology and other laboratories at UW-Madison as well as contributing to the education of Urology residents, fellows, and graduate students. Requirements include either a Ph.D. or M.D. with appropriate research experience related to genitourinary biology and/or urologic disease.

A competitive salary and fringe benefit package will be provided. Immediate enrollment in health insurance with low premiums is available for you and your family, and an outstanding retirement plan is offered. To apply, send a resume, cover letter, and salary requirements to: **Stephen Y. Nakada, MD, Professor and Chair of Urology, UW-School of Medicine and Public Health, 600 Highland Avenue, G5/339 CSC, Madison, WI 53792-3236**

UW-Madison is an equal opportunity/affirmative action employer. Unless confidentiality is requested in writing, information regarding applicants must be released upon request. Finalists cannot be guaranteed confidentiality.



Postdoctoral Positions

Fox Chase Cancer Center, a renowned Philadelphia-based NCI-designated Comprehensive Cancer Center, has several postdoctoral positions available to work on NIH funded projects in the following programs:

- **Cancer Genetics and Signaling**
- **Cancer Prevention and Control**
- **Epigenetics and Progenitor Cells**
- **Immune Cell and Host Defense**
- **Molecular Medicine**
- **Breast and Ovarian Cancers**

The Scientist's annual survey has named Fox Chase Cancer Center as one of "The Best Places to Work" for Postdoctoral Careers.

Fox Chase fosters an environment conducive to strong collaboration across all disciplines, both scientific and medical. As a postdoctoral fellow at Fox Chase, you will have the opportunity to interact with our faculty as valued colleagues in a setting built around mutual respect and collegiality.

Highly motivated candidates who can work independently are encouraged to send resume to **Dr. Jonathan Chernoff, c/o Anne Carson at anne.carson@fccc.edu**. For more information visit www.fccc.edu. Equal Opportunity Employer.

FOX CHASE
CANCER CENTER



UAB Stem Cell Institute

Department of Biochemistry and Molecular Genetics

University of Alabama at Birmingham Schools of Medicine and Dentistry

Tenure track junior positions and tenured senior faculty positions are available for investigators focused on stem cell biology, biochemistry, epigenetics and transplantation. Areas of special emphasis include, but are not limited to, mechanistic studies of stem cell self-renewal and lineage specification and mechanisms of somatic cell reprogramming to pluripotency. Nationally competitive salaries, start-up packages and space allocations will be offered to successful candidates.

UAB is a highly interactive environment with strong basic and clinical sciences. Birmingham is a beautiful and affordable city with many cultural attractions.

Applicants should send a C.V., a summary of research interests and the names of three references before **August 15, 2009** to:

Dr. Tim M. Townes
Director, UAB Stem Cell Institute
Chairman, Department of Biochemistry
and Molecular Genetics
University of Alabama at Birmingham
Kaul Genetics Building, Room 502
720 20th Street South
Birmingham, AL 35294
Email: ttownes@uab.edu

Head of Bioscience - Drug Discovery

Reference number: PI/09/21



Paterson
Institute for Cancer Research

A Bioscience Leadership position, focusing on drug discovery, is available in the Paterson Institute, one of Europe's premier cancer research centres core-funded by Cancer Research-UK (CRUK), the largest independent cancer research organisation in the world.

This is a new venture at the Paterson, so the successful candidate will be expected to participate in both the development and implementation of the strategy and tactics of this new capability, with the aim of discovering novel small molecule cancer drug candidates.

The Head of Drug Discovery Bioscience will be responsible for laboratory capabilities in cancer target validation and lead generation biology. You will recruit the bioscience team and initiate and lead collaborations to support a portfolio of projects.

The Institute supports numerous basic and translational cancer research programmes facilitated by a comprehensive range of state-of-the-art research services (see: www.paterson.man.ac.uk). Its juxtaposition to The Christie, Europe's biggest specialist cancer hospital, ensures ample opportunities for interaction across the basic to clinical research spectrum and the translation of research findings into patient benefit.

The Institute is also at the heart of the Manchester Cancer Research Centre (MCRC), an exciting development that integrates cancer research within Manchester (www.mcrc.manchester.ac.uk).

This opportunity has arisen from a new initiative, funded by CRUK, to develop a small molecule Cancer Drug Discovery capability in the MCRC. Positions are for five years initially and will be renewable, subject to successful peer review of the programme.

Essential requirements for this role include expertise in cancer biology, experience of drug discovery and target validation and also strong leadership and interpersonal skills.

Expertise in lead generation technologies and experience in the pharmaceutical sector are desirable but not essential.

If you would like to see your knowledge and experience applied to the discovery of new cancer medicines and would like to know more about this opportunity, please contact Dr Donald Ogilvie, Head of Drug Discovery (dogilvie@picr.man.ac.uk).

Applications including a CV and names of three referees should be sent to jobs@picr.man.ac.uk

The deadline for receipt of applications is 7 June 2009

www.paterson.man.ac.uk

MANCHESTER
1824

The University of Manchester



CANCER RESEARCH UK



Science Careers is the forum
that answers questions.



Science Careers is dedicated to opening new doors and answering questions on career topics that matter to you. With timely feedback and a community atmosphere, our careers forum allows you to connect with colleagues and experts to get the advice and guidance you seek as you pursue your career goals.

Science Careers Forum:

- » Relevant Career Topics
- » Timely Advice and Answers
- » Community, Connections, and More!

Visit the forum and join the conversation today!



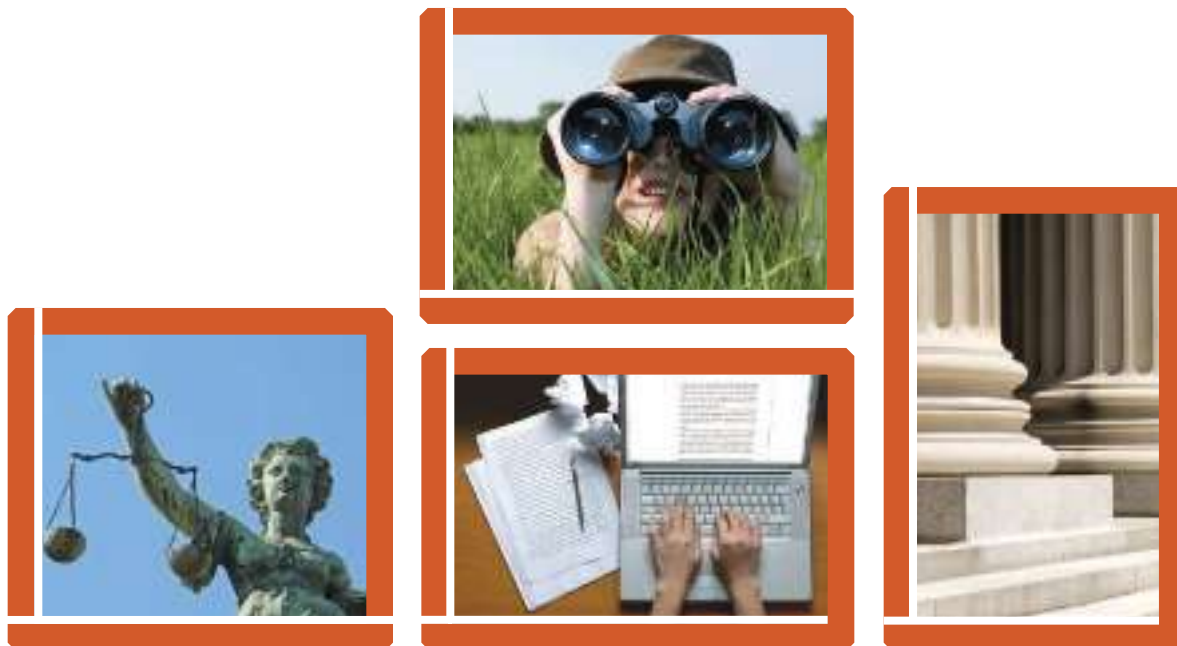
Your Future Awaits.

Science Careers

From the Journal Science



ScienceCareers.org



Nontraditional Careers: Opportunities Away From the Bench Webinar

Want to learn more about exciting and rewarding careers outside of academic/industrial research? View a roundtable discussion that looks at the various career options open to scientists across different sectors and strategies you can use to pursue a nonresearch career.

**Now Available
On Demand**
www.sciencecareers.org/webinar

Participating Experts:

Dr. Lori Conlan

*Director of Postdoc Services,
Office of Intramural Training and Education
National Institutes of Health*

Pearl Freier

*President
Cambridge BioPartners*

Dr. Marion Müller

*Director, DFG Office North America
Deutsche Forschungsgemeinschaft
(German Research Foundation)*

Richard Weibl

*Director, Center for Careers in
Science and Technology
American Association for the
Advancement of Science*

Produced by the
Science/AAAS Business Office.

Science Careers

From the journal *Science*

AAAS



Knowledge Centre for Materials Chemistry (KCMC)

Research Associate (Project Scientist)

£30,594 - £35,469 pa

You will join the Knowledge Centre for Materials Chemistry (KCMC). You should have an excellent research track record with experience in the synthesis of new oxide materials and in X-ray powder diffraction, with a PhD in chemistry, physics or materials science; excellent communication and interpersonal skills with the ability to interact with individuals at all levels within the academic and business communities. The post is available for 3 years.

The KCMC is a North West Regional Development Agency-funded activity uniting Chemistry Innovation Ltd, Science & Technology Facilities Council and the Universities of Liverpool, Manchester and Bolton to focus on delivering industry-led projects.

Job Ref: R-569322/S

Closing date: 5 June 2009

For full details, or to request an application pack, visit

www.liv.ac.uk/working/job_vacancies/

or e-mail jobs@liv.ac.uk

Tel 0151 794 2210 (24 hr answerphone)

Please quote Job Ref in all enquiries.

COMMITTED TO DIVERSITY AND EQUALITY OF OPPORTUNITY



JOHNS HOPKINS
BLOOMBERG
SCHOOL of PUBLIC HEALTH

Environmental Health Sciences

The Department of Environmental Health Sciences in the Johns Hopkins Bloomberg School of Public Health is pleased to announce two fellowship opportunities within a successful and established NIEHS funded postdoctoral training program. The mission of the training program is to actively prepare research scientists to become future leaders of individual and interdisciplinary research projects seeking to understand the role environmental exposures play in the etiology and exacerbation of human disease at the individual and population level.

Specific research opportunities are
highlighted at:

<http://www.jhsph.edu/dept/ehs/NIEHS>

Your career is our cause.

Get help
from the
experts.

www.sciencecareers.org

- Job Postings
- Job Alerts
- Resume/CV Database
- Career Advice
- Career Forum

Science Careers

From the journal *Science*



诚聘海内外优秀学者

Shanghai Changzheng Hospital is one of the top medical centers in China, located in downtown Shanghai. It has 28 clinical departments, more than 1,000 hospital beds, and serves over 800,000 outpatient visits each year. As one of the affiliated hospitals of Second Military Medical University, the hospital also has an excellent teaching staff and facilities, and possesses strong records in many areas of medical research. A new 2,000-bed expansion of the hospital in Shanghai Pudong district has been approved recently.

Changzheng hospital is seeking applications from qualified individuals for the positions of **junior and senior principal investigators** to expand basic, translational, and clinical researches. Qualified applicants will also be considered for head of laboratory and/or department. The successful candidates must have a Ph.D. or M.D. and have publications in high profile international journals (as first or corresponding author) in the last 5 years. Senior scientists with professorship (assistant, associate, full professor or equivalent), extensive research experiences, and strong record of productive independent research are preferred. The hospital will offer a generous startup package, competitive salary and benefits.

Interested individuals should send their curriculum vitae, a brief review of research plan, and name of 3 references (including address, email, and telephone) to: **Zhan Liang, Human resources, 415 Feng Yang Road, Shanghai, 20003 China. Tel: 86-21-81885086; Email: liangzhan9309@yahoo.com.cn.**



THE HORMEL INSTITUTE
UNIVERSITY OF MINNESOTA

**FIVE (5) ASSISTANT PROFESSOR/
ASSOCIATE PROFESSOR/PROFESSOR/
ENDOWED PROFESSOR POSITIONS**

The Hormel Institute, a biomedical research center of the University of Minnesota, was established in 1942 and has a long reputation in producing world class medical research. The Institute's research success has resulted in a major expansion of its research facilities and includes a new state of the art laboratory building and complete renovation of existing research facilities. The Hormel Institute offers its research scientists complete access to state of the art equipment that includes a FACS sorter; confocal microscopy; flow cytometry; and the Blue Gene/L, the world's fastest supercomputer. In conjunction with the building expansion will be the addition of five (5) new faculty positions. We are seeking applications for faculty appointments at the level of Assistant Professor, Associate Professor, Professor, and/or Endowed Professor.

Qualifications: Candidates must demonstrate the ability to establish an independent, extramurally funded program of cancer-related research that will complement ongoing programs. Preference will be given to applicants with a strong background in areas to include molecular/cell biology, protein crystallography, biological computation/informatics, stem cell, or cancer biology and a successful research record in one of the following areas: signal transduction, gene expression, functional genomics, molecular carcinogenesis, chemoprevention or other areas of cancer research. A Ph.D. (or equivalent) degree and 2 to 3 years of postdoctoral experience are required for Assistant Professor. The ability to acquire extramural funding is required for appointment of Associate Professor or Professor. For endowed professorships, the applicant should be an internationally renowned researcher with substantial external funding. Please apply online at the UMN website <http://www1.umn.edu/ohr/employment/index.html> and refer to **Requisition Number 154060 (Professor), Number 154740 (Associate Professor), or Number 154741 (Assistant Professor)**. In addition, please submit a curriculum vitae, a research plan, and the names of three references to **Dr. Zigang Dong, ambode@hi.umn.edu**.

The University of Minnesota is committed to the policy that all persons shall have equal access to its programs, facilities and employment without regard to race, color, creed, religion, national origin, sex, age, marital status, disability, public assistance status, veteran status, or sexual orientation.



**University of Saskatchewan Department of Pathology and Laboratory Medicine
Tenure Track Research Scientist/Faculty Position in Experimental Pathology**

The Department of Pathology and Laboratory Medicine, College of Medicine invites applications for a faculty position in Experimental Pathology at a rank to be commensurate with their qualifications. This appointment is part of an initiative to enhance research intensity in basic, clinical, and translational research related to cancer stem cell biology. Complementary areas of research of the Department of Pathology and Laboratory Medicine research include cell and molecular biology, immunology and microbiology, biochemistry, and correlative sciences related to cancer. Applicants must have a PhD and/or MD, postdoctoral experience, and a strong research program of relevance to cancer stem cell biology. Applicants must also demonstrate success in obtaining Health related national grant funds and have a strong track record or potential in undergraduate and graduate teaching. The successful applicant will contribute to building a cancer stem cell research program, enhancing graduate training at the College of Medicine, participate in teaching to support undergraduate MD and biomedical science programs.

The Department of Pathology and Laboratory Medicine has an accredited residency training program and is involved in the training of undergraduates, graduate students and post-graduates. The Department's broad range of clinical programs includes subspecialty aspects of pathology that are well suited to educational and research activities. The Department includes the Division of Anatomical Pathology, Clinical Chemistry, Hematopathology, Microbiology, Transfusion Medicine and Experimental Pathology.

The University of Saskatchewan is a publicly funded institution established in 1907. It has over 19,000 degree students, 4,500 employees, an operating budget of approximately \$200 million, and receives research funds in excess of \$100 million annually. It offers a full range of programs, both academic and professional, in thirteen colleges including seven in the life sciences.

An application, including curriculum vitae, and the names of three referees should be submitted by **July 31, 2009** to: **Dr. John Krahn, Head, Department of Pathology and Laboratory Medicine, Room 2841, Royal University Hospital, 103 Hospital Drive, Saskatoon, Saskatchewan S7N 0W8.**

All qualified candidates are encouraged to apply; however, Canadians and permanent residents will be given priority. The University of Saskatchewan is committed to Employment Equity. Members of designated groups (women, Aboriginal people, people with disabilities, and visible minorities) are encouraged to self-identify on their applications.

POSITIONS OPEN



**TWO FACULTY POSITIONS
(Assistant Professor)
Department of Animal Science
Texas A&M University**

The Department of Animal Science at Texas A&M University (**website:** <http://animalscience.tamu.edu>) seeks to fill two tenure track **ASSISTANT PROFESSOR** positions; one in Nutritional Genomics and one in Reproductive Biology. Successful candidates will be expected to build a vigorous, externally funded research program and to develop and teach undergraduate and/or graduate courses. A Ph.D. in the relevant field, postdoctoral experience, and evidence of outstanding research and teaching potential are required. The ability to contribute to research involving a multidisciplinary team approach using domestic and laboratory animal models is highly desirable.

We offer competitive salary and benefits package as well as start-up packages. For complete posting, application deadlines, and information on how to apply, please visit: **website:** <http://greatjobs.tamu.edu>. Review of applications will begin on June 15, 2009 and continue until successful candidates are identified and hired to start in early Fall 2009.

**POSTDOCTORAL POSITION
University of Florida**

A postdoctoral position in molecular microbial pathogenicity is available immediately to study communication, signaling and gene regulation in multispecies microbial communities (see *Mol Microbiol* 69:1153). Experience with bacterial genetics is required; expertise with protein biochemistry and confocal microscopy is beneficial. Position is supported by NIH grants. Send curriculum vitae and names of three references by e-mail to: **Dr. Richard Lamont at signal@dentall.ufl.edu**

Kansas State University, Division of Biology, has two **POSTDOCTORAL POSITIONS** available immediately in the laboratory of **Professor Gary W. Conrad** in the area of: 1) Molecular, Cellular and Developmental Biology of the Cornea and 2) Mass Spectrometry and Glycomics. These positions are supported by a four-year NIH-NEI grant. For more information on how to apply, go to **website:** <http://www.ksu.edu/biology/employment.html>. Review of applications will begin on May 20, 2009. *KSU is an Equal Opportunity Employer, and actively seeks diversity among its employees. Background check required.*

We seek a **POSTDOCTORAL LIPID BIOCHEMIST** to conduct research on the molecular basis of bacterial latency at the Burnett School of Biomedical Sciences, University of Central Florida, Orlando, Florida. Send curriculum vitae and the contact information of three references by **e-mail to: P.E. Kolattukudy, pk@mail.ucf.edu**.

The University of Central Florida is an Equal Opportunity, Equal Access, and Affirmative Action Employer. As a member of the Florida State University System, all application materials and selection procedures are available for public review.

MARKETPLACE

Oligo Labeling Reagents

↳ **BHQ®/CAL Fluor®/Quasar® Amidites**

↳ **Amidites for 5' & Int. Modifications**

↳ **Standard and Specialty Amidites**



**+1.800.GENOME.1
www.btlabeling.com**



“i can

go where the biology
takes me.”

“In research, one discovery leads to another which leads...well, who knows where? The Illumina Genome Analyzer gives me the technology to follow almost any path. Only with this system could we create the most detailed and integrated epigenome map to date for any species.”

Dr. Brian Gregory
Postdoctoral Fellow
The Salk Institute for Biological Studies

Study the genome. Epigenome. Transcriptome.
All at single base-pair resolution. Do more, and
do it better, with the Illumina Genome Analyzer.

~~Next-gen~~ Sequencing
now

www.illumina.com/sequencingSCI

SEQUENCING
GENOTYPING
GENE EXPRESSION

illumina®

economicalm.

RESEARCH. TOGETHER.

Panic is unproductive.

Let's get rational. Tough decisions lie ahead as budgets tighten. But discovery will endure. One name has been here for more than 50 years, providing stability, reliability, and quality to researchers like you: Bio-Rad.

From the beginning we have been a stable presence, offering you products that spark your imagination without burning your budget. Because great results should be within your means.

Proceed with caution. But proceed, nonetheless.

**You don't have to lose your shirt outfitting your lab.
Quite the opposite, in fact.
Visit www.bio-rad.com/economicalm/
for more information.**